DOCTOR OF PHILOSOPHY

Novel Concrete Reinforcement for Wave Energy Converters

Li, Xiaoteng

Award date:
2019

NOVEL CONCRETE REINFORCEMENT FOR WAVE ENERGY CONVERTERS

XIAOTENG LI

2019

This Thesis is submitted for the Degree of Doctor of Philosophy
To the School of Science and Engineering
University of Dundee
Scotland

Table of Contents

List of Figures

List of Tables

List of Equations

Abbreviations

Term	Definition
2D	Two-Dimensional
3D	Three-Dimensional
ACI	American Concrete Institute
ALS	Accidental Limit State
AM	Additive Manufacturing
ASTM	American Society for Testing and Materials
CC	Beams reinforced with CFRP for flexure and CFRP for shear
CFRP	Carbon Fibre Reinforced Polymer
CRI	Crack Resistance Index
CT	Computed Tomography
DFA	Desilicated Fly Ash
FRP	Fibre Reinforced Polymer
GC	Beams reinforced with GFRP for flexure and CFRP for shear
GFRP	Glass Fibre Reinforced Polymer
GGBS	Ground Granulated Blast-Furnace Slag
LCC	Load Carrying Capacity
PC	Portland Cement
PT	Post-Tensioning
PVC	Polyvinyl Chloride
RC	Reinforced Concrete
SF	Beams reinforced with aligned steel fibres
SFRC	Steel Fibre Reinforced Concrete
SLS	Service Limit State
SP	Superplasticiser
UHMWPE	Ultra-High-Molecular-Weight Polyethylene
ULS	Ultimate Limit State
WEC	Wave Energy Converter
w/c ratio	Water/Cement Ratio
XRF	X-Ray Fluorescence

Notation

A	Experimental confident
A_f	Area of longitudinal FRP reinforcement (mm^2)
A_{fv}	Area of transverse FRP reinforcement (MPa)
a	Depth of equivalent rectangular stress block (mm)
a_v	Shear span of the beam under bending (mm)
B	Experimental confident
b	Width of beam cross section (mm)
b_f	Diameter of FRP bar (mm)
C_b	Equivalent circumference of the FRP bar (mm)
c	Distance from extreme compression fibre to neutral axis (mm)
d	Effective depth(mm)
d_{max}	Slip at the maximum bond stress (mm)
d_{sf}	Diameter of steel fibre (mm)
E_c	Static modulus of elasticity of concrete (N/mm^2)
E_f	Static modulus of elasticity of longitudinal FRP reinforcement (N/mm^2)
E_{fd}	Design modulus of elasticity of longitudinal FRP reinforcement (N/mm^2)
E_{P1}	Area under the load-deflection diagram until P1 (kN·mm)
E_{P2}	Area under the load-deflection diagram until P2 (kN·mm)
E_{P3}	Area under the load-deflection diagram until P3 (kN·mm)
F_b	Tensile load in a FRP bar pull-out test (N)
F_C	Compression force developed in concrete (kN)
F_{cr}	Load at the first crack of FRP-reinforced concrete beams (kN)
F_{max}	Maximum bending load of FRP-reinforced concrete beams (kN)
F_{P1}	Load at P1 (kN)
F_{P2}	Load at P2 (kN)
F_{P3}	Load at P3 (kN)
F_T	Tensile force developed in concrete (kN)
f_c	Characteristic cylinder compressive strength of concrete (N/mm^2)
f_c'	Design cylinder compressive strength of concrete (N/mm^2)
f_{c_stress}	Cylinder compressive stress of concrete (N/mm^2)
f_f	Tensile stress of longitudinal FRP reinforcement (N/mm^2)
f_{fb}	Strength of the bent portion of FRP bars (MPa)
f_{fv}	Shear strength of the FRP reinforcement (MPa)
f_{fu}	Ultimate tensile strength of longitudinal FRP reinforcement (N/mm^2)
k	Ratio of depth of neutral axis to FRP reinforcement depth
k_1	FRP pull-out curve gradient before failure
k_2	FRP pull-out curve gradient after failure
L_{cr}	Deflection at the first crack of FRP-reinforced concrete beams (mm)
L_{max}	Maximum deflection of FRP-reinforced concrete beams (mm)

L_{P1}	Midspan deflection at P1(mm)
L_{P2}	Midspan deflection at P2 (mm)
L_{P3}	Midspan deflection at P3 (mm)
l	Bonded length of FRP bar in a pull-out test (mm)
l_{sf}	Length of steel fibre (mm)
M_{add}	Required additional moment capacity for external FRPs (N·mm)
M_n	Ultimate moment of resistance (N·mm)
V_c	Shear resistance provided by concrete (kN)
V_{cr}	Shear force at the formation of the critical inclined crack (kN)
$V_{c,f}$	Shear strength contribution from uncracked concrete (kN)
V_f	Shear resistance provided by FRP shear reinforcement (kN)
V_n	Nominal shear capacity of FRP-reinforced concrete beams (kN)
V_{sf}	Fibre volume fraction (%)
V_u	Ultimate shear force (kN)
s	Stirrup spacing or pitch of continuous spirals (mm)
z	Steel lever arm (m)
α	Safety factor of aligned steel fibres
Δ_1	Extent of the beam's load carrying capacity drop at P1 (kN)
Δ_2	Extent of the beam's load carrying capacity drop at P2 (kN)
β_1	Concrete strength factor
ε_c	Concrete compressive strain
ε_{c2}	Concrete compressive strain from Eurocode 2
ε_{cu}	Ultimate concrete compressive strain
ε_{cu2}	Concrete compressive strain from Eurocode 2
ε_f	Tensile strain of longitudinal FRP reinforcement
ε_{fe}	The lesser of the FRP design ultimate strain and a strain of 0.008
ε_{fu}	Ultimate tensile strain of longitudinal FRP reinforcement
τ	Average bond stress of the FRP bar to concrete (MPa)
$\tau_{0.05}$	Bond stress caused a slip at 0.05 mm (MPa)
$\tau_{0.10}$	Bond stress caused a slip at 0.10 mm (MPa)
$\tau_{0.25}$	Bond stress caused a slip at 0.25 mm (MPa)
τ_{max}	The maximum bond stress (MPa)
ρ_f	FRP reinforcement ratio
ρ_{fb}	Balanced FRP reinforcement ratio
η	Factor defining effective strength of concrete
η_f	Ratio of elastic modulus of FRP to elastic modulus of concrete
λ_1	Eigenvalue at *xx*-axis
λ_2	Eigenvalue at *yy*-axis
λ_3	Eigenvalue at *zz*-axis
σ_f	Flexural strength of concrete with steel fibres (MPa)
σ_{fo}	Flexural strength of concrete without steel fibres (MPa)

Acknowledgment

Firstly, I would like to express my sincere gratitude to my principal supervisor Professor Rod Jones and second supervisor Dr Moray Newlands for the continuous support of my Ph.D. study and related research, for their patience, motivation and immense knowledge. Their guidance enlightened me in all the time of research and writing of this thesis.

I would like to thank the University of Dundee and the China Scholarship Council (CSC) for providing the joint scholarship covering my entire research. Besides my supervisors, my sincere thanks also go to the Concrete Technology Unit research group, for all the academic staff, Dr Li Zheng, Dr Tom Dyer, Dr Laszlo Csetenyi, Dr Leon Chernin, Dr Michael McCarthy and Dr Judith Halliday, and all my Ph.D. colleagues, with whom it has been a great experience to work.

I thank the technician team in the Engineering Laboratories, especially Dr Gary Callon, Mr Chris Walker and Mr Cameron Anderson, for their kind assistance in carrying out my experimental work. I thank my proof-readers, Mr David Grainger, Dr Li Zheng, Dr Moray Newlands, Dr Chris Luke and Mr Gordon Ramsay, for their useful suggestions regarding this thesis. I also thank all the undergraduate and postgraduate students from the School of Science and Engineering and all the visiting students from China, France and India who joined this research project at different work stages, for the discussion and work we carried out together.

Finally, I would like to thank my family for their love and encouragement, for my parents who have encouraged and supported me to study abroad and obtain a doctoral degree, for my sister who has supported me spiritually during my writing of this thesis and for my two lovely nephews, Jinze and Jince, who have been producing so many joyful moments that I can always have a laugh at.

Declaration

I hereby declare that I am the author of this thesis; that, unless otherwise stated, all references cited have been consulted by me; that the work of which the thesis is a record has been done by me, and that it has not been previously accepted for a higher degree.

Xiaoteng Li
School of Science and Engineering
University of Dundee
Dundee, Scotland

Certificate

This is to certify that Xiaoteng Li has done his research under my supervision and that he has fulfilled the conditions of Ordinance 14 of the University of Dundee so that he is qualified to submit the following thesis in application for the degree of Doctor of Philosophy.

Professor Rod Jones
School of Science and Engineering
University of Dundee
Dundee, Scotland

Dr Moray Newlands
School of Science and Engineering
University of Dundee
Dundee, Scotland

Abstract

The experimental work programme developed in this study investigates the behaviour of novel concrete reinforcement for the wave energy converters. The reinforcement included fibre-reinforced polymer (FRP), synthetic fibres, steel fibres and ultra-high-molecular-weight polyethylene (UHMWPE). 24 cube specimens were tested using a pull-out test where no splitting was allowed to develop to examine the bond between FRP (glass and carbon) bars and concrete. 45 beam specimens were subjected to three-point or four-point bending tests where the beams were bent until their failure in order to study the structural behaviour of flexural concrete elements reinforced with internal FRPs, external FRPs as well as fibrous reinforcement. A large-scale WEC prototype was produced, and design of reinforcing this prototype with novel reinforcement was proposed.

The bond behaviour between FRP bars and concrete as well as influence of seawater ions were investigated. The shear strength contribution of FRP-reinforced concrete beams was analysed. Also, the structural behaviour of beams reinforced or strengthened with FRPs was presented and compared with estimations using existing methods. A concept of Crack Resistance Indices (CRIs) was introduced to reflect the cracking behaviour of the beams. Appropriate methods for evaluating the flexural strength of beams externally bonded with CFRPs using epoxy resin was developed. Influence of the water and seawater exposures on the CFRP strengthening capacity was also discussed.

Addition of macro-synthetic fibres to the concrete at a dosage of 20 kg/m^3 significantly improved the toughness of FRP-strengthened beams. Longitudinally aligning macro-steel fibres into concrete beams could provide the latter with competitive flexural and shear strengths. The relation between the aligned fibre dosages and the beam’s flexural strength was formulised. Influence on the flexural strength from factors of the concrete strength, addition of cementitious materials and the alignment effectiveness was also studied.

A circular Vierendeel-truss-type WEC prototype was designed and produced from precast concrete elements. Assembly of the prototype was accomplished whilst reinforcing with UHMWPE ropes remained at the proposal stage. A 3D printed concrete beam reinforced with UHMWPE ropes was also trialled.

Chapter 1 Introduction

1.1 Background

Renewable energy has turned into a dependable alternative to traditional fossil fuels for meeting an increasing demand for energy as well as for controlling the global rise in CO_2. The Scottish Government has set a target to use renewable sources to produce energy equivalent to 100% of Scotland’s gross annual electricity consumption by 2020 (The Scottish Goverment, 2017). A majority of the renewable energy already generated to date in the world comes from hydraulic, wind and solar power, while marine energy (tidal and wave) still has a distance to go before it becomes commercially viable (Perez-Collazo, et al., 2015). Wave resources are widely and substantially distributed along the Atlantic coast in Europe. Figure 1.1 shows the assessment of the European wave power in GW. The U.K. has a top assessment of an annual 120 GW enormous potential power (Lopez, et al., 2013), most of which distributes along the Scottish shores.

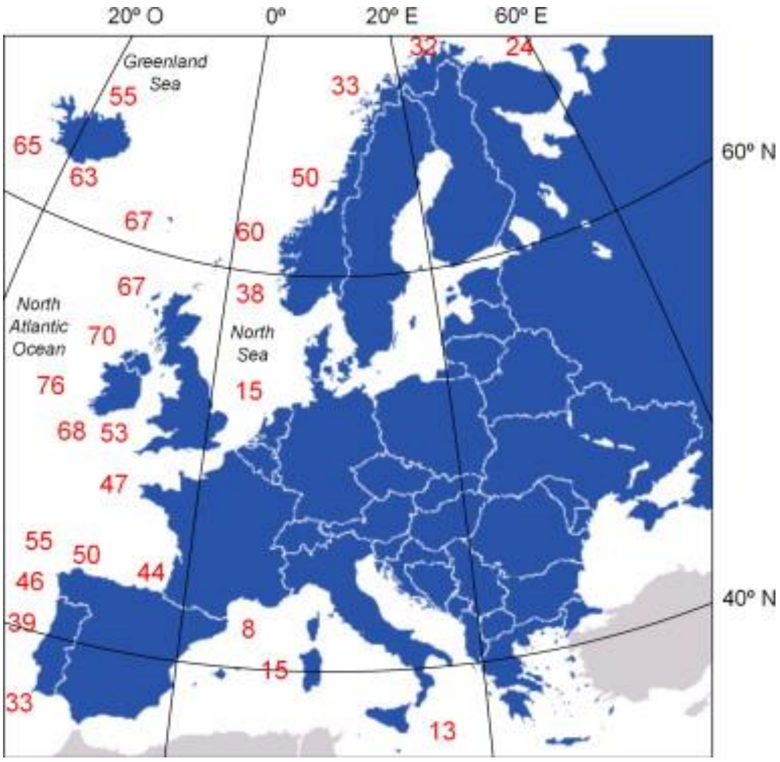

Figure 1.1 Assessment of European distribution of the annual wave power, in GW (Lopez, et al., 2013)

One of the main issues barring the development of wave power is that it is considered to not be economical. Currently, the best wave generator technology in place in the U.K. is exploiting energy at an evaluated cost of 5 pence per kWh (5300 £/MWh), which is more than 1.5 and nearly 3 times more expensive than the wind-driven turbines and large-scale coal burning technology, respectively (Ocean Energy Council, 2017). Therefore, for all engineering researches focusing on wave energy, it will always be the key drive to reduce the power-exploiting prices and, consequently, to commercialise using of this renewable power.

A huge part of the cost for exploiting wave energy is from construction and installation of the Wave Energy Converters (WECs). There are various designs of the WEC that are currently being considered (Figure 1.2). The WEC main body flexes and bends as ocean surface waves pass. It is this motion that is used to stimulate the WEC's power take-off system which is usually located at the segment connecting area and consequently to create electricity.

Existing projected WECs and prototypes have been mostly constructed in painted steel (Wave Energy Scotland, 2016). Steel is not a cheap construction material for WECs and is generally seven times more expensive than reinforced concrete (RC) (Tata Steel, 2018). Carbon steel also faces serious problems of corrosion in marine environment which will cause an extra add-on cost for device maintenance. Meanwhile, reinforced concrete has been long employed as a composite material that is commercially affordable in construction (Durpray, et al., 2010). During the building of large-scale steel-reinforced concrete structures, it is the falsework system used for temporary work restraint and support as well as the rebar bending process manufactured by the computer numerically controlled (CNC) bending that generate high labour costs.

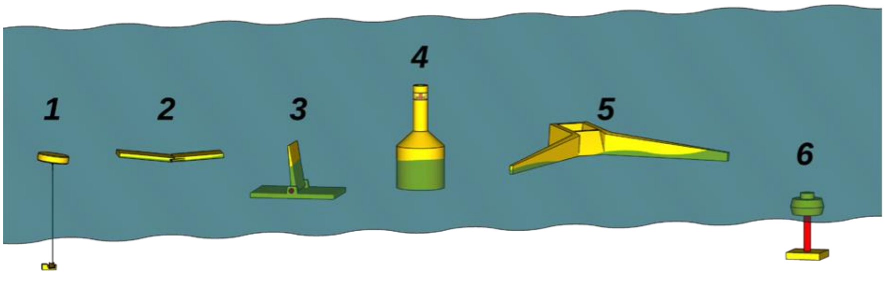

Figure 1.2 Various design concepts of the Wave Energy Converters (Quintessa, 2016)

Therefore, it is necessary to simplify these techniques and develop quicker and easier approaches to build economic and profitable WECs made of the RC material. Moreover, for the traditional RC structures in the marine environment, it is a method of largely increasing the concrete cover thickness to safe depths that is used to resolve problems of the steel reinforcement corrosion. This will not be suitable for floating or semi-submerged WEC because it increases the WEC's overall weight. The WECs are also more sensitive to the development of cracking because it is catastrophic to have any leakage within their sections.

Some novel concrete reinforcements have shown great potentials to be used in the WECs. Reinforcing and strengthening products made of the fibre-reinforced polymer (FRP) composites have been commercially available as reinforcement for concrete structures since the late 1980s. Their innovative mechanical properties, such as high tensile strength, low specific weight and corrosion resistance, make FRP reinforcement suitable for applications in the marine environment. Glass fibre- (GFRP) and carbon fibre-reinforced polymer (CFRP) are two of the most commonly used FRP materials in industry (Nanni, et al., 2014). To reinforce or strengthen concrete, GFRP has the unsatisfactory low elastic modulus (usually around 60 GPa). This means it will not be able to restrain the concrete in tension as much as conventional steel reinforcement does, and consequently will cause larger and wider cracks developing within the tensile zone. CFRP has relatively higher elasticity (around 150 GPa) but currently is still more expensive in the market, partly due to it being less popular for industry purposes. GFRP or CFRP cannot be bent once cured; however, they are light to carry and place, and easy to cut on site. GFRP and CFRP are nonferrous and noncorrosive. The glass and carbon reinforcing fibres are usually regarded as non-sensitive to moisture and sea salt ions, such as Cl^- and SO_4^{2-} (Soudki, et al., 2007; Zhou, et al., 2015), but the polymer resin matrices can reportedly absorb water (Zafar, et al., 2012) depending on their composite type. Consequently, the mechanical properties of GFRP and CFRP, such as encapsulating fibres and bonding to concrete, might be affected.

The addition of fibres into concrete mixes can provide concrete with some post-cracking load-bearing capacity and limit its crack development. Although steel fibres still corrode, it is estimated that corrosion of steel-fibre-reinforced concrete (SFRC) is less active and less harmful compared to corrosion of steel-bar-reinforced concrete in the adverse marine environment (Granju & Balouch, 2005), because fibres are usually disconnected and discontinuous in the SFRC. Corrosion of SFRC mostly happens in cracked sections and at the surface. It was reported (Balouch, et al., 2010) that when the w/c ratio is around 0.5, it is only the fibres which are embedded less than 0.1 mm deep in concrete that are susceptible to corrosion from the surface. Therefore, corrosion of steel fibres can be considered as being of minor harm. The addition of macro-synthetic fibres at high dosages (around 12 kg/m^3) is usually with the purpose of improving the post-elastic behaviour and reducing the failure brittleness.

FRP-reinforced concrete structures exhibit brittle failure types. The American FRP design guideline ACI 440.1R-06 (American Concrete Institute, 2015) defines the balanced-reinforced FRP RC flexural member as a section that fails when the FRP reinforcement reaches its design tensile strength at the same time concrete in compression starts to break. Since FRP rebar does not yield, under-reinforced FRP RC flexural sections fail in modes governed by bar rupture while over-reinforced ones are governed by concrete crushing, both of which are brittle. To provide the required pseudo-plastic behaviour for the WEC, multiple cooperative reinforcing materials including the fibres will be possibly needed. Even though this does not conform to the design principle of simplifying the fabrication and minimising the cost, it will be needed in terms of structural requirements. Therefore, it is necessary to execute laboratory experiments on small-scale specimens and optimise their test outputs, through which solutions towards constructing the less complicated and more cost-effective RC WEC can be hopefully figured out.

Thus, this research is structured to firstly conduct preliminary experiments on these novel reinforcements to collect basic information for further trials on design and development of a WEC prototype, and to provide references and guidelines for design of the FRP RC structures in the marine environment. This study also aims to develop feasible techniques that enable easy-assembly, low-cost and formwork-free manufacture of profitable WEC devices with non-steel reinforced concrete elements.

1.2 Aim and Objectives

The overall aim of this research programme is to investigate whether the use of novel concrete reinforcement could fulfil requirement of constructing RC WECs with reduced capital and maintenance costs. These reinforcing materials include several novel and non-ferrous composites, namely, GFRP, CFRP, Ultra-High-Molecular-Weight Polyethylene (UHMWPE) and macro-synthetic fibres, and macro-steel fibres. Therefore, the objectives incorporate investigating related properties of each reinforcement and determining its feasibility for application in a marine WEC device. The objectives also include studying the joint connection with structural adhesive such as the epoxy resins for FRP/UHMWP-reinforced concrete sections.

According to the experiment arrangement, the objectives of this research work could be summarised as follow:

(1) Investigate the internal GFRP/CFRP rebars' and external CFRP strands' bond to concrete and their sensitivity to chloride and sulphate attack from seawater.
(2) Estimate the mechanical and structural behaviour of concrete elements simply reinforced or strengthened with GFRP/CFRP/UHMWPE materials with outputs (i.e. load-deflection relations, crack and failure type) from the quasi-static bending test.
(3) Investigate the effects of adding macro-synthetic and aligning macro-steel fibres into concrete at designed dosages on reducing the failure brittleness and providing flexural and shear resistance, respectively, of concrete members reinforced with FRP/UHMWPE.
(4) Design a suitable and easily buildable grout-connected joint type with structural adhesive and evaluate its feasibility for being employed in the FRP/UHMWPE-reinforced concrete sections.
(5) Based on an optimisation of the achievements from aforementioned objectives, develop a large-scale concrete WEC prototype with the required hydrodynamic shape, and test its structural performance.

1.3 Scope of Study

This research focuses on comprehensive work of developing a WEC prototype that is potentially going to be made of concrete material and reinforced with available novel and non-ferrous reinforcement. The prototype is expected to possess a high strength/weight ratio with significantly reduced construction cost. Reduction of the cost and decrease of the weight can be achieved by optimising material selections, design process as well as fabrication methods, while maintenance or increase of the strength can be accomplished by employing the novel materials that are claimed to have high strength and low elasticity, e.g. FRP and UHMWPE. At the same time, efforts are also being made in attempting to improve the accidental limit state (ALS) behaviour of the WEC in which case macro-fibres made of polymer and steel are selected for investigation. This research programme is undertaken in three main phases and explores subjects from characteristic properties of the novel reinforcement to structural behaviour of flexural concrete sections reinforced with novel reinforcement, and finally development of a WEC prototype.

Phase I focuses on determining the characteristic properties of FRP bars, specifically, its bond to concrete and bond response to influence of the concrete strength and seawater ions presence. Behaviour and failure of GFRP and CFRP bars under tension and shear as well as CFRP strands under tension are also investigated.

Phase II examines the structural behaviour of flexural concrete members reinforced and strengthened separately with GFRP, CFRP, macro-synthetic and aligned steel fibres. The crack and flexural performance, load-deflection relations as well as post-failure toughness properties are obtained experimentally. Design considerations of strength and reinforcing effectiveness of these materials are evaluated.

Phases III assesses the structural behaviour of the developed WEC prototype which is a precast-and-assembled truss structure that is reinforced as well as post-tensioned with the UHMWPE ropes. The strength capacity and stress transferring reactions of this prototype are planned to be analysed according to acquired experimental data and compared with numerical modelling results.

Chapter 2 Literature Review

To achieve the aim of studying novel concrete reinforcement for WECs, reviewing work is carried out to look at available literature analysis. Design of the WEC main body is first discussed since this decides the applications of the novel reinforcement. Design of FRP-reinforced and fibrous concrete members is then presented with regards to standards and publications in Section 2.2 to 2.5. Joint design of FRP-RC members and post-tensioning of FRP bars are also reviewed considering that they might be functional in developing a concrete WEC prototype. Finally, related reference standards are listed in Section 2.8.

2.1 WEC Main Body Design and Material Selection

Currently WEC devices have been designed and fabricated in different types and shapes. The Pelamis device (Wave Energy Scotland, 2016) is composed of 5 cylindrical tubes made of painted steel (Figure 2.1) and is usually identified as an attenuator type machine. An attenuator is a floating device that operates parallel to the wave direction. The attenuator's main body structure can be in varied shapes, for example, in rectangular blocks and hemispheroidal rotators (European Marine Energy Centre, 2017). However, offshore floating devices are often subject to various and combined hydrostatic and hydrodynamic loadings, such as bending and torsion. WEC structures with a circular or elliptic cross-section can theoretically avoid potential stress concentration at a maximum extent. Elliptic cylinders are even better as they will not rotate as much as the circular ones do while floating and consequently lead to less torsion force.

When utilising reinforced concrete as the primary construction material, the converter segments can be easily cast or pre-cast in required shapes. Format of the WEC structure can be continued as the conventional shell-type. The main challenge in this regard will be ensuring the durability of the WEC, particularly, controlling cracking and avoiding water ingress. Adding steel or polymer fibres can reduce the formation and propagation of cracks (Neville, 2011), but this reduction is not a complete prevention of the occurrence of cracks, especially the macro-cracks. Considering that any macro-crack is not acceptable to keep the WEC afloat, the concrete will need to remain in compression all the time. Post-tensioning, therefore, will be essentially mandatory.

A small-scale prototype in the format of the shell-tube was previously constructed using concrete material and post-tensioned with six M10 steel tendons externally around the tube circumference (Khosravi, 2017). This prototype consisted of five tube segments that were jointed together with the epoxy resin adhesive and semi-submerged in seawater for 24 months (12 months in indoor laboratory with 1 mol/l seawater solution and 12 months near the shore in West Scotland). The prototype finally sank after the 24 months exposure owing to, as reported by the researcher, rupture of the post-tensioning steel tendons and loss of the epoxy resin at the interface among the concrete tubes and between the concrete and the end steel plates. This is a problem of corrosion and, once again, demonstrates the significance of building WECs with nonferrous or at least corroding-steel-free materials.

Another concept is proposed to use precast or the formwork-free 3D printing concrete elements, assembling and reinforcing them with novel FRP or UHMWPE reinforcement, to form a circular truss. The fibres, additionally, can be used as secondary reinforcement where shear resistance is critical or post-ultimate behaviour needs to be improved. A truss structure will be more efficient in terms of the strength-to-weight ratio and floatable if it is sheathed within an external waterproof jacket. Technologies that can fabricate the sheathing skin by using novel materials such as rotational-moulded or glass-reinforced plastics are available (Wave Energy Scotland, 2017). In such a truss structure, durability will be of negligible concern due to the extremely low risk of water ingress. Reinforcing and post-tensioning can then be primarily used for enhancing the structural behaviour of the truss element rather than controlling the cracks.

The truss structure has successful applications, e.g., the Wembley Stadium in Northwest London which was completed in 2007 and the M8 Harthill Footbridge in Lanarkshire (Figure 2.2) which was built in 2008, even though all of them are of steel. To construct a reinforced concrete truss that can be assembled simply, one potential challenge might be design of the node as the nodes will be responsible for resisting and transferring multiple forces. Numerical analysis and modelling might be helpful to pre-determine the stress distribution for the truss. If necessary, external FRP strengthening composites can also be easily bonded outside on to the nodes and other weaker parts as extra complements.

Primary requirements and potential challenges of the two proposed structure types are summarised in Table 2.1. As a conclusive review of available options, reinforced concrete material is still of great advantage in reducing the cost compared with steel, even though the final cost must encompass the assembly and post-tensioning systems. Novel FRP and UHMWPE reinforcing bars and multi-strands can be utilised as post-tensioning tendons while secondary reinforcement such as macro-steel and macro-synthetic fibres may also be needed to enhance the local shear resisting ability and extend the ALS design zone.

Figure 2.1 The cylindrical-tube-type Pelamis WEC prototype P2-001 floating on the sea (European Marine Energy Centre, 2017)

Figure 2.2 The M8 Harthill Footbridge constructed in a steel truss structure in Lanarkshire (SH Structures, 2018)

Table 2.1 Comparison of the WEC main body design: shell-tube vs. circular truss

Design Consideration	**WEC Structure Type**	
	Shell-Tube	Circular Truss
Primary Material	Reinforced concrete.	Reinforced concrete.
Primary Reinforcement	FRP rebar and strands, UHMWPE strands.	FRP rebar and strands, UHMWPE strands
Secondary Reinforcement	Macro-steel fibres, macro-synthetic fibres.	Macro-steel fibres, macro-synthetic fibres.
Purpose of Secondary Reinforcement	Control cracks and extend the ALS design zone.	Provide shear resistance and extend the ALS design zone.
Joints	Will exist.	Will exist.
Post-Tensioning	Possibly compulsory to control cracks.	Optional but recommended to reduce cost.
Crack Control	Highly required to avoid water ingress.	Averagely required.
Potential Challenges	Joint adhering.	Node design and joint adhering.
Extra Support	Not structurally.	Fabrication of the external waterproof jacket.

2.2 FRP Reinforced Concrete Flexural Members

2.2.1 FRP Application on Marine Structures and Design Guidelines

Traditionally reinforced-concrete structures in the marine environment face problems of reinforcement corrosion, which increases potential cost for extending their service life. FRP composite reinforcement has been utilised in various civil applications, the majority of which were reported to include bridge decks, retaining walls and port infrastructures (Nanni, et al., 2014). But, to the best of found knowledge, there are not yet any successful offshore floating FRP RC structures that were constructed with a complete replacement to steel reinforcement.

The Morristown Bridge located in Vermont, U.S.A., was constructed with a concrete deck slab entirely reinforced with GFRP bars in two identical layers at the top and the bottom. The deck is 230 mm thick and continuous over the 44 m-span steel girders spaced 2.36 m apart. Benmokrane et al. (2006) compared the construction details and the results from their first field loading test and concluded that both the maximum tensile strain in the GFRP bars and the maximum tensile strain in the concrete were well below the design values, revealing that the GFRP rebar provides very good and promising performance.

Applications of FRP RC in civil structure construction were also reported within the U.K., for example, the West Mill Bridge in Oxfordshire, England. This bridge was constructed in 2002 and has a span of 10 m and a width of 6.8 m. Although this is a short-span bridge, all its load-carrying elements are reinforced with only GFRP and CFRP composites. Performance of the bridge in service was examined in 2014 via principal inspection and reported as overall satisfactory with acceptable cracking resulted from local flexing and freeze/thaw cycles (Composites UK, 2014).

However, there is still little likelihood that the use of novel FRP reinforcement to replace traditional steel rebar in concrete construction is going to be widespread in the near future.

FRP composite has a disadvantage that it does not yield and remains linearly elastic until failure. Consequently, FRP-reinforced concrete members will show brittle failure modes. Design of FRP RC usually needs to be well below its maximum strength for the ultimate limit state (ULS). However, because of the usually low stiffness of GFRP, its tensile strain is still relatively large. GFRP suffers from its low elasticity. For example, at the strains at which concrete starts to crack, GFRP rebar will not be carrying significant tensile load. When the applied load increases, GFRP-reinforced concrete sections continue deforming and cracking and consequently the whole section will present a large flexural deflection. Large deflections are not structurally problematic for a WEC, but cracks might be not acceptable for a shell-tube type converter.

Another reason that limits the take-up of the FRP reinforcement application is the lack of design codes (Feeser & Brown, 2005). Despite that different national standards have been published specifying the manufacturing, test methods and properties of FRP composites (British Standards Institute, 2002; Canadian Standards Association, 2010; American Concrete Institute, 2012), it is scarcely covered in the area of design and construction of FRP RC structures.

To apply the novel FRP composites in the design of WECs made of reinforced concrete, it might be more economic and practical to follow the fundamental SLS (Service Limit State) design concepts from Eurocode 2, with special consideration on the differences of material property. Also, there are several guidelines and recommendations existing which suggest the basic design roles of FRP RC elements. As a complementary reference, this PhD. research programme has selected the following:

(1) ACI 440.1R-06 (2006), Guide for the Design and Construction of Structural Concrete Reinforced with FRP Bars, published by the American Concrete Institute (ACI).
(2) CAN/CSA-S806-12, Design and Construction of Building Structures with Fibre-Reinforced Polymers, published by the Canadian Standards Association (CSA).

Therefore, it will be highly necessary to carry out small-scale laboratorial experiments on FRP and FRP-reinforced concrete. To meet the requirements for design and constructing the hydrodynamic-shaped WEC devices, there will be several structural performances being looked for from those tests on FRP-RC flexural members:

(1) The excellent flexural strength and satisfactory tensile strain of the FRP bar and strand reinforcement;

(2) A consistent ULS behaviour that allows the section to develop reasonably large load-carrying ability;

(3) A smooth and pseudo-plastic post-ULS behaviour that enables the section to resist the spread of large cracks and to avoid sharp failure modes.

2.2.2 FRP Bond and Influence from Seawater

The bond-to-concrete of embedded FRP bars is highly dependent on their manufacturing, physical characteristics (American Concrete Institute, 2015; Ceroni, et al., 2006) as well as the environmental conditions (Yang, et al., 2016).

While the traditional steel rebar tends to be more isotropic, FRP bars are mechanically anisotropic. The polymer resin matrix is more responsible for their shear and transverse characteristics while the fibres govern longitudinal properties such as the tensile strength and stiffness. The diverse FRP composites, which usually have different polymer resins and reinforcing fibres, have different interface mechanisms between the matrix and the fibres. As a result, they might present different behaviours of bond-to-concrete.

Commercial FRP bars in the market are usually manufactured with surface deformation and preparation, e.g., surface lugging and sand-coating, to increase their bond ability. The techniques for FRP deformation have been under development and have changed recently. Unlike the traditional steel rebar, of which the design and manufacturing have been highly standardised (for example, BS EN 4449: 2005), there is a lack of design criteria specifying the manufacturing process and defining the deformation techniques of FRP bars. It is, therefore, relatively difficult to make direct comparisons among previous research results that were tested on different types of FRP specimen. But through their direct pull-out test on GFRP bars, Achillides and Pilakoutas (2004) stated that FRP bars must necessarily have a minimum height of surface preparation (rips, lugs, sand coating etc.) to develop satisfactory bond strength to concrete.

Threats from the marine environment for FRP bars embedded into concrete structures are mainly water and salts. Carbon fibres are resistant to **alkali** (Frank, et al., 2012) while glass fibres are not. Experimental data (Micelli & Nanni, 2004; Benmokrane, et al., 2017) have shown that polyester resin does not provide adequate protection for glass fibres against alkaline attack, but permanently alkali-resistant GFRP reinforcement, claimed by the manufacturer, is available in the market (Schöck, 2017). Benmokrane et al. (2017) evaluated the long-term performance of GFRP bars made separately with vinyl ester, polyester and epoxy resin by immersing them into an alkaline solution 12.8 in pH with elevated temperature for up to 5000 hours. It was found that only the polyester GFRP bars exhibited significant reductions (over 20%) of their transverse and flexural strength. The polyester GFRP bars also absorbed 18% more water than the vinyl ester and epoxy resin GFRP bars after the exposure. Non-polyester FRP bars, therefore, can still be used in situations that are exposed to alkali.

Carbon and glass fibres cannot absorb **water** (Gu, et al., 2010; Westman, et al., 2010) but water might, in the form of moisture, diffuse through the resin matrix (Sen, 2015) and affect the fibre-resin interface and consequently influence the material's bond to concrete.

Presence of the **chloride** and **sulphate** in offshore construction accelerates deterioration of the reinforcement for conventional RC structures. Seawater usually has a content of 18.98 mg and 2.65 mg of the chloride and sulphate per litre respectively (Lenntech, 2018) . These aggressive ions can be transported into concrete when liquids ingress through pore spaces in the cement paste matrix or micro-cracks (Song, 2014) and consequently cause the steel reinforcement corrosion.

CFRP is usually insensitive to chloride (Ceroni, et al., 2006; Soudki, et al., 2007). Zhou et al. (2015) carried out experimental tests on external strengthening sheets of both CFRP and GFRP with an accelerated corrosion condition simulating the coastal environment. This exposure was generated using a sulphate solution in a raised temperature (20 °C) and with cyclic wetting/drying up to 150 days while successive tests were arranged at 30-day intervals. It was found that, the CFRP did not show any evident trends of reduction in the tensile strength under this accelerated sulphate exposure while the tensile strength of the GFRP decreased by 6.6% after 150 days. The researchers also investigated the external FRP's bond-to-concrete with one type of epoxy resin adhesive and found that the bond strength of CFRP-concrete and GFRP-concrete interface decreased by 14.0%

and 14.5%, respectively, after the 150 cycles. Mechanical properties (i.e. the flexural strength and the elasticity) of the epoxy resin were measured slightly reduced but this reduction was considered unable to affect the bond failure mode; on the other hand, the concrete compressive strength decreased significantly from the peak of 60 MPa at 60 days to 32 MPa at 120 days affected by the sulphate ions. Zhou et al. (2015) concluded that sulphate attack influenced the bond behaviour between the external FRP and concrete because it dominantly affected the concrete strength rather than deteriorated the FRP or the epoxy resin adhesive.

Both chemical and physical techniques have been developed to ascertain the chloride and sulphate content in concrete, most of which are destructive. For example, the acid-soluble chloride content can be measured according to BS EN 14629: 2007 (British Standards Institution, 2007). The chemical composition of concrete can also be determined with analytical techniques such as the X-ray fluorescence (XRF) in term of its elements (see Section 3.8.3 for more explanation of the XRF technique). Both these techniques require fine ground samples hence are relatively destructive although usually only small portions of the sample are needed.

Concrete strength usually exerts noticeable influences on the bond of deformed steel bars. However, this might be different with internal FRP bars. Achillides and Pilakoutas (2004) evidenced that for concrete with compressive strength more than 30 MPa, its bond failure with FRP bars happened at the surface of the FRP. Therefore, in such concrete, the bond strength of the FRP bar is not substantially dependant on the compressive strength of concrete. However, the results of Zhou et al. (2015) are of relevance as they verified the high durability of GFRP and CFRP against sulphate attack.

2.2.3 Methods for Determining FRP Bond-to-Concrete

The bond properties of FRP bars embedded in concrete can be displayed from their bond stress vs. bar-end slip curves which are generated using a pull-out test. ACI published guidelines (ACI 440.3R-04:2004) that specified the test methods for FRPs for reinforcing or strengthening concrete structures. Their guide test method covering the determination of the FRP bars bond strength is partially modified and adopted by ASTM and published in the form of the American national standard ASTM D7913-14 in 2014.

In the guide ACI 440:3R-04, two specimen casting methods were provided: one aligning the bars with the concrete casting direction while the other aligning the bars transverse to the concrete casting direction, as shown in Figure 2.3 (b_f is the bar diameter). The bonded length, defined as the length of the test bar that directly contacts the concrete matrix, was suggested as five times the bar diameter (5×b_f). Outside the bonded area, the embedded bar should be wrapped tightly with the polyvinyl chloride (PVC) plastic film or other similar materials to prevent direct contact between the FRP bar and the concrete.

The bond behaviour will be specimen-configuration dependant, which means that the surface deformation of the FRP bar plays a noticeable role in affecting the pull-out curves. When the bonded length does not present the bond characteristics of certain types of FRP bar, it is suggested that the bonded length may be extended appropriately.

During the test, displacement of both the loaded and the free end should be measured by the linear variable differential transformers (LVDTs) or other similar measuring devices with reading accuracy of 0.01 mm.

The average bond stress should be calculated according to Equation 2.1,

$$\tau = \frac{F_b}{C_b \times l} \qquad \text{Equation 2.1}$$

where τ is the average bond stress, MPa; F_b is the tensile load, N; $C_b$is the equivalent circumference of the FRP bar, mm; and, l is the bonded length, mm.

Curves for the bond stress vs. slip at both the loaded end and the free end should also be plotted.

The ASTM standard specifies similar test methods referring to ACI 440:3R-04 except for several small modifications. However, it needs to be noted that experimental results from both ACI and ASTM methods should be used only for comparison. Neither of them can be used to estimate the design bond value or the development length for FRP bars that are embedded in flexural concrete elements for reinforcing purposes. Determination of those parameters usually use the methods for determining the bond strength of the conventional steel rebar, for example standard ASTM A944-10: 2015.

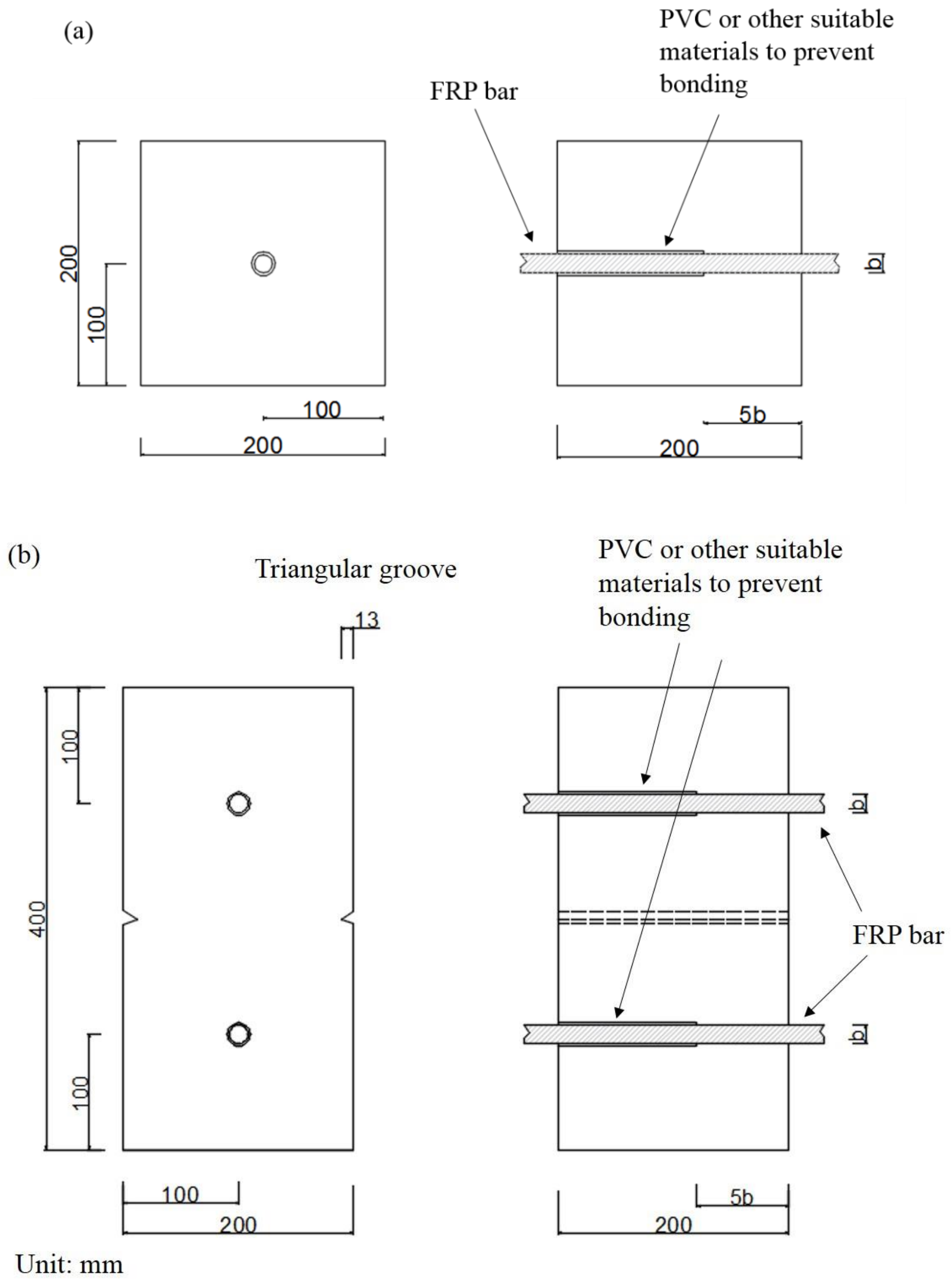

Figure 2.3 The pull-out test specimen casting methods by ACI 440.3R-04, (a) aligning the bar with the concrete casting direction and (b) aligning the bar transverse to the concrete casting direction

2.2.4 Structural Mechanics and Analysis of FRP RC

The ultimate moment capacity is one of the most important mechanics because it advises the flexural strength of a reinforced-concrete beam section. Several different approaches (American Concrete Insititute, 2006; Canadian Standards Association, 2007; Pilakoutas, et al., 2011; Torres, et al., 2012) have been developed to evaluate or predict the ultimate moment resistance as well as the short-term deflection of flexural FRP RC members. For example, standard ACI 440.1R-06 (2006) and CSA-S806-02 (2007) have both covered fundamental design principles of reinforcing concrete beams with internal FRP bars.

The flexural capacity of an FRP-reinforced flexural member is dependent on its failure mode. As FRP does not yield, the design tensile strength of the FRP bar is recommended to be used for computing the balanced reinforcement ratio. A balanced flexural section of FRP RC is expected to fail in a mode that the concrete in compression reaches its ultimate compressive strain while the FRP rebar extends to the design maximum tensile strain simultaneously. ACI 440.1R 06 (2006) proposes Equation 2.2 to calculate the balanced FRP reinforcement ratio:

$$\rho_{fb} = 0.85\frac{f_c'}{f_{fu}}\beta_1\frac{E_f \cdot \varepsilon_{cu}}{E_f \cdot \varepsilon_{cu} + f_{fu}} \qquad \text{Equation 2.2}$$

When the reinforcement ratio is greater than ρ_{fb}, the failure mode is governed by concrete crushing. In such a case, the ultimate moment resistance of the FRP RC flexural member can then be derived from Equation 2.3 to 2.5:

$$M_n = A_f f_f\left(d - \frac{a}{2}\right) \qquad \text{Equation 2.3}$$

$$a = \frac{A_f f_f}{0.85 f_c' b} \qquad \text{Equation 2.4}$$

$$f_f = \sqrt{\frac{(E_f\varepsilon_{cu})^2}{4} + \frac{0.85\beta_1 f_c'}{\rho_f}E_f\varepsilon_{cu}} - 0.5E_f\varepsilon_{cu} \le f_{fu} \qquad \text{Equation 2.5}$$

The stress level developed at the FRP bars can be determined from Equation 2.5 and used to verify the assumed failure mode.

Pilakoutas et al. (2011) proposed another evaluation approach (Equation 2.6 to 2.8) which uses the concrete compressive strength to compute the ultimate moment resistance:

$$M_n = \eta f_c' ba(d - \frac{a}{2}) \qquad \text{Equation 2.6}$$

$$\mathrm{a} = \beta_1 \frac{\varepsilon_{cu}}{\varepsilon_f + \varepsilon_{cu}} d \qquad \text{Equation 2.7}$$

$$\varepsilon_f = \sqrt{\frac{{\varepsilon_{cu}}^2}{4} + \frac{\eta\beta_1 f_c'}{\rho_f E_f}\varepsilon_{cu}} - 0.5\varepsilon_u \qquad \text{Equation 2.8}$$

And the stress developed on the FRP reinforcement is:

$$f_f = \varepsilon_f E_f = \sqrt{\frac{(E_f\varepsilon_{cu})^2}{4} + \frac{\eta\beta_1 f_c'}{\rho_f} E_f\varepsilon_{cu}} - 0.5E_f\varepsilon_u \leq f_{fu} \qquad \text{Equation 2. 9}$$

These two methods are principally based on the same analysing framework that is used for conventional steel-reinforced concrete beams and accept similar bond and stress-strain distribution assumptions. The only differences between these two approaches are their factors defining the concrete effective strength (η) and the effective height of the compressive zone (β_1). ACI 440.1R-06 (2006) takes the value of 0.85 for all η and suggests that the β_1 factor should be taken as 0.85 for design concrete strength (f_c') up to and including 28 MPa. This factor is reduced continuously at a rate of 0.05 per 7 MPa of strength greater than 28 MPa but is not taken less than 0.65. Pilakoutas et al. (2011) proposed that η and β_1 are dependent on the characteristic value of concrete compressive strength and can be determined according to the characteristic value of concrete cylinder compressive strength by Equation 2.10 and 2.11, respectively.

$$\eta = \begin{cases} 1, \; f_c \leq 50\ MPa \\ 1.0 - \frac{f_c - 50}{200}, 50 < f_c \leq 90MPa \end{cases} \qquad \text{Equation 2.10}$$

$$\beta_1 = \begin{cases} 0.8, \; f_c \leq 50\ MPa \\ 0.8 - \frac{f_c - 50}{400}, 50 < f_c \leq 90MPa \end{cases} \qquad \text{Equation 2.11}$$

When the amount of reinforcement is below ρ_{fb}, the FRP RC member is expected to fail by bar rupture and the concrete compressive strain at which the bar ruptures needs to be determined to compute the ultimate moment resistance (Equation 2.12).

$$M_n = A_f f_{fu}(d - \frac{\beta_1 c}{2}) \qquad \text{Equation 2.12}$$

$$c = \frac{\varepsilon_c}{\varepsilon_{fu} + \varepsilon_c} d \qquad \text{Equation 2.13}$$

The produce of $\beta_1 c$ in Equation 2.12 is the depth of the equivalent rectangular stress block and varies depending on material properties and reinforcing conditions for a given FRP RC section. ACI 440.1R-06 (2006) uses the simplified and, consequently, conservative method which assumes that the concrete compressive strain is at the ultimate level (0.003). Pilakoutas et al. (2011) suggested that determination of the concrete compressive strain can be achieved through an iterative procedure by solving Equation 2.14 and 2.15.

$$F_C = F_T \rightarrow bc\frac{1}{\varepsilon_c}\int_0^{\varepsilon_c} f_{c\_stress} d\varepsilon_c = A_f f_{fu} \qquad \text{Equation 2.14}$$

where f_{c_stress} is the compressive stress of concrete and can be determined using Equation 2.15. The values proposed by Eurocode 2 are used for ε_{c2} and ε_{cu2}.

$$f_{c\_stress} = \begin{cases} f_c' \left[1 - (1 - \frac{\varepsilon_c}{\varepsilon_{c2}})^n\right], & 0 \le \varepsilon_c \le \varepsilon_{c2} \\ f_c', & \varepsilon_{c2} < \varepsilon_c \le \varepsilon_{cu2} \end{cases} \qquad \text{Equation 2.15}$$

The value of β_1 is taken as 1.0 for all calculations which assumes that the concrete stress remains linear until the FRP reinforcement ruptures.

Failure modes governed by FRP rupture are usually avoided in the design of FRP RC sections as FRP does not yield. To compare the two estimating methods, calculations are made based on a sample concrete beam reinforced by $2 \times \emptyset 8\ mm$ GFRP bars, assuming that the rebar has E_f of 60 GPa and f_{fu} of 1000 MPa while the beam has a square cross-section of 100 mm by 100 mm (Figure 2.4). This flexural beam can be regarded as over-reinforced until its concrete characteristic compressive strength (f_c) reaches 90 MPa. The nominal moment capacity of this sample section can be determined using f_c, as illustrated in Figure 2.5.

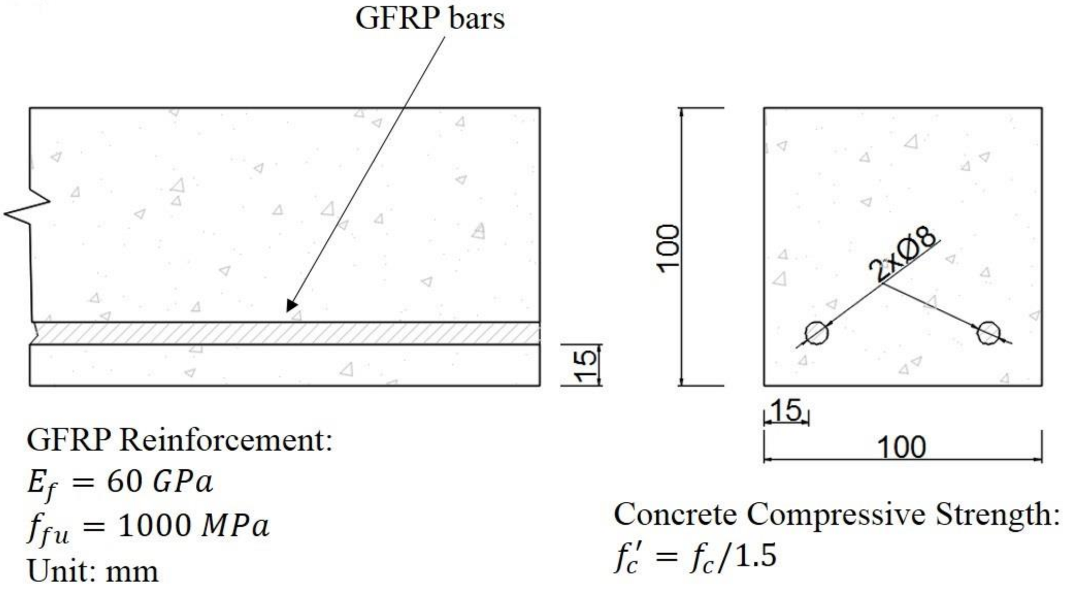

Figure 2.4 Schematic dimensions and material properties of the GFRP RC specimen used for comparing the flexural strength predications

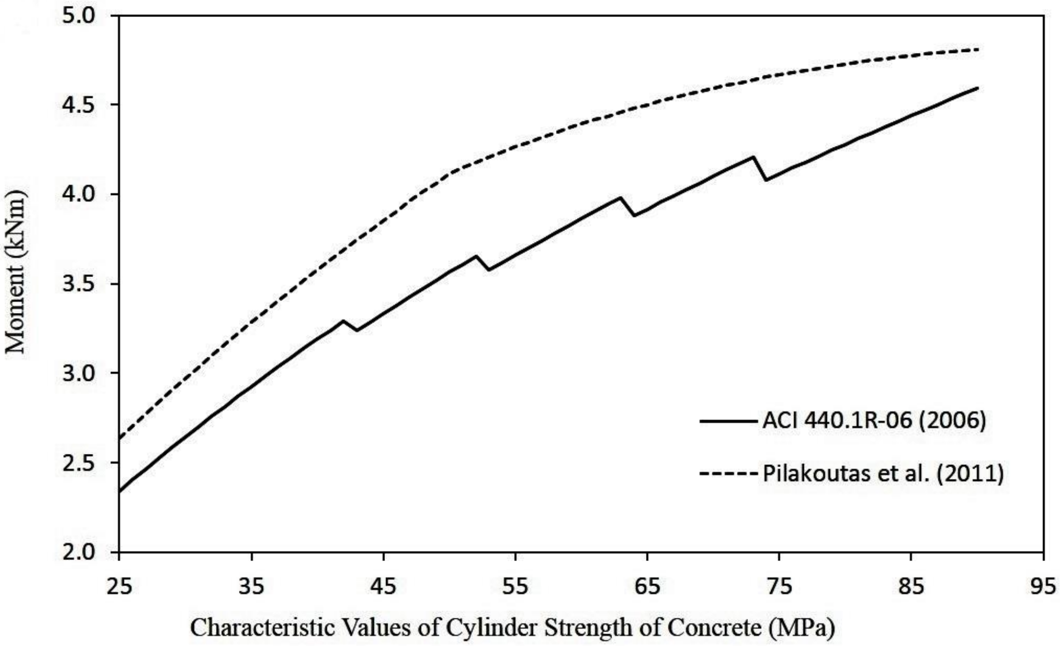

Figure 2.5 The moment predictions for FRP RC beams by the ACI and Pilakoutas et al. (2011) methods

As shown in Figure 2.5, comparing with the estimating equations proposed by Pilakoutas et al. (2011), ACI 440.1R-06 (2006) gives more conservative predictions of the nominal moment capacity, especially when the concrete compressive strength falls in the range of 45-75 MPa. However, due to the method it deals with the defining factor of concrete strength β_1 (i.e. simply reducing β_1 by an amount of 0.005 every 7 MPa), the ACI 440.1R-06 formulae present a moment resistance vs. concrete strength curve that increases unnaturally with several unsmooth connections. These connections obviously do not exist on real FRP RC beams.

With an effort to validate the prediction of the ACI formulae, Habeeb and Ashour (2008) tested two simply-supported GFRP reinforced concrete beams that were designed to fail in two different failure modes, namely, concrete crushing and GFRP bar rupture. The former was accomplished by using GFRP reinforcement ratio greater than the balanced reinforcement ratio, i.e. an over-reinforced GFRP RC beam, which is of relevance for this study. Their test results showed that the beam had an experimental value of load resistance at failure of 163.0 kN while it is 112.5 kN predicted with the ACI approaches. Similarly, Yang et al. (2012) also reported that the ACI methods underestimate the ultimate moment of their FRP bar-reinforced beams by as much as 20% or more. Hence, various previous literatures demonstrated that the ACI 440.1R-06 method could underestimate the flexural strength of FRP RC beam elements.

2.3 Externally Strengthening FRP Composites

2.3.1 Applications and Design

External FRP strengthening materials, usually in the form of plate, strip and sheet, have the advantages of easy handling and installation because of their low density and high strength. The flexural strength of reinforced-concrete beams can be increased by bonding FRPs to their tension faces. However, the increase can be affected by factors such as the bonding adhesive type and the concrete surface preparation. The Concrete Society Technical Report No.55 (2012) describes preliminary design calculations of the required additional moment capacity that can be provided by bonding FRP to concrete:

$$M_{add} = A_f \varepsilon_{fe} E_{fd} z \qquad \text{Equation 2.16}$$

where, A_f is the required area of FRP for external bonding, mm^2; ε_{fe} is the lesser of the FRP design ultimate strain and a strain of 0.008; E_{fd} is the design modulus of elasticity of FRP, MPa; z is the steel lever arm, m.

The strain of 0.008 is an empirical value at which level the bonded FRP usually starts to separate from the concrete according to Technical Report No.55.

It is worth mentioning that, as explained by the Report No.55, this preliminary calculation should only be used for situations where the load capacity of existing structures in service needs to be increased. This prediction of required FRP areas becomes less reliable when the existing sections are already heavily reinforced.

Another technical report, ACI 440.2R-08 Guide for the Design and Construction of Externally Bonded FRP Systems for Strengthening Concrete Structures (2008), does not identify any equations for computing the load capacity improvement.

Hence, design and construction of concrete structures with only external FRP composites currently still lack practical guidelines. The feasibility of utilising only externally bonded FRPs to strengthen concrete is significant for practical applications.

In an effort to investigate the behaviour of CFRP strengthened reinforced-concrete beams in a corrosive environment, Soudki et al. (2007) subjected eight steel-reinforced concrete beams that were pre-cracked at their service load then strengthened with CFRP laminates to up to 300 wetting/drying cycles with 3% NaCl solution. Three extra beams with the same reinforcing condition were kept uncracked and unexposed to chloride as a control. The reinforcement details together with the two strengthening schemes were configured by the researchers in Figure 2.6.

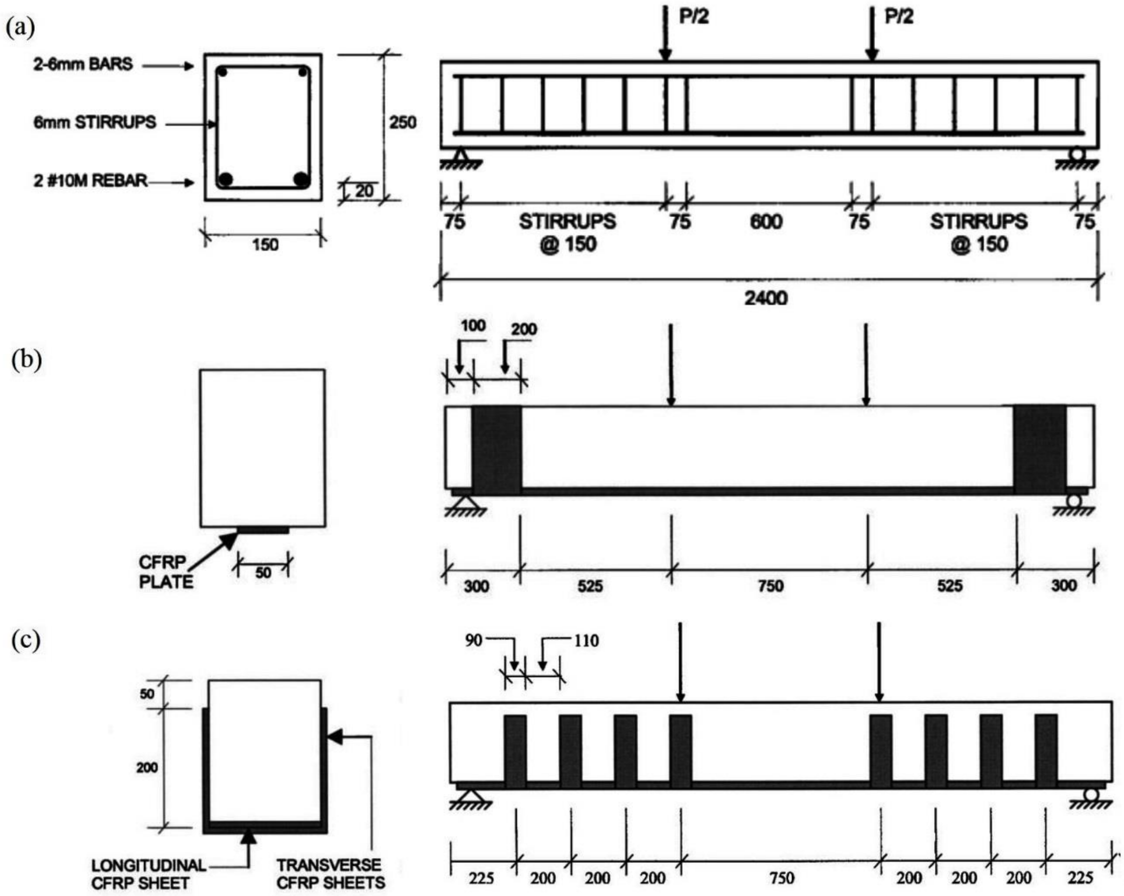

Figure 2.6 (a) Test specimen reinforcement configuration, (b) CFRP strengthening Scheme I and (c) CFRP strengthening Scheme II (Soudki, et al., 2007)

Strengthening Scheme I (Figure 2.6 (b)) used one CFRP strip bonded to the tensile face for the entire beam length and two separate CFRP sheets wrapped at the area by the two beam supports transversely and completely in the beam’s 4 faces. Strengthening Scheme II (Figure 2.6 (c)) used longitudinal CFRP sheets with the same width as the beam bonded to the bottom face and 4 separate layers of U-shaped sheet to strengthen the shear spans of the beam. These transversely bonded CFRP sheets were also expected to partly provide anchorage for the longitudinal strips and sheets in order to avoid premature debonding and prevent any premature delaminating that might happen to the concrete between the external CFRP and the internal steel rebar. These prepared specimens were tested in the four-point bending under monotonic loading at 0, 100, 200 and 300 cycles of wetting and drying respectively while control beams were at 0, 100 and 300 cycles respectively.

The results indicated that the CFRP strengthening significantly enhanced the performance of the RC beams: Strengthening Scheme I and II increased the load-carrying capacity by 97% and 115% and decreased the deflection by 21% and 42%, respectively, compared with the control beams. Regarding the simulated corrosive environment, it was found that the ultimate load capacity of the steel-reinforced beams remained nearly unaffected while the CFRP-strengthened beams decreased by11% to 28% after 300 cycles.

It was also noted from Soudki et al.'s tests that nearly all 8 CFRP-strengthened beams failed by debonding of the longitudinal CFRP, except 1 by CFRP strip rupture. However, the failure of Strengthening Scheme II beams started by delamination and rupture of the transverse U-shaped wraps and was followed by delamination of the longitudinal sheets. This previous literature suggests that use of the epoxy resin adhesive can possibly govern the failure and the flexural strength of externally bonded CFRP strengthened beams.

Soudki et al. (2007) as well as other researchers (Dai, et al., 2010; Jin, et al., 2015) advised that, under harsh environment, use of moisture epoxy resin (polyurethane prepolymer) adhesive or moisture-resistant epoxy resin adhesive might enhance the bond transfer for beams that were externally strengthened with the CFRP composites. Moisture-resistant epoxies are products that are highly resistant to aqueous and semi-aqueous systems such as moisture and hot water, when fully cured (Provatic America, 2019).

2.3.2 Epoxy Adhesive and FRP Separation Issues

The flexure strength of an FRP-strengthened concrete section generally should not be governed by the bonding adhesive, provided that the design and workmanship are both carried out in accordance with recognised standards or guidelines (The Concrete Society, 2012). However, a previous report (Dong, et al., 2013) indicated that the flexural strength of bonded FRPs could be limited by their bonding layer of the epoxy resin adhesive.

In an analysis of results from the four-point bending test on six steel-reinforced concrete beams that were additionally strengthened with external CFRP sheets, Dong et al. (2013) reported that the beams failed majorly by two modes, i.e., snapping and debonding of the CFRP sheets. The beams were externally strengthened with either one (one beam) or two layers (five beams) of flexural CFRP sheets bonded on to the tensile face of the beams as well as two strips of the U-shaped CFRP sheets bonded on to both ends of the beam near the loading supports as an external anchor. Half of the beams failed by a mode that was characterised by Dong et al. (2013) as snapping of the longitudinal CFRP sheets, while the other half were by debonding of the CFRP sheets which initiated from the mid-span or under one loading point. The adhesive utilised in their experiments was not specifically mentioned. By inspecting provided failure pictures (Figure 2.7), the designated snapping failure mode actually appears to be a combination of both debonding and material rupture. The ultimate load results measured by Dong et al. (2013) also showed random variations that appear to have no apparent relation with the failure types.

Failure at the bonded FRP-concrete interface was also experimentally investigated from the pull-out test (Toutanji & Ortiz, 2001; Haddad, et al., 2015). By viewing the load-strain responses, Toutanji and Ortiz (2001) found that all their concrete specimens bonded with FRP sheets visually failed in the same manner. This is, after the concrete initially cracked, the strain on FRP gradually increased from the cracked point to surrounding areas and at the same time separation between FRP and the concrete occurred and widened. This separation eventually led to a final fracture of the bonding interface between the FRP and concrete. No failure of the FRP composite was observed from all 12 specimens, on which surface preparation of removing the exterior mortar by either an electric sander or a water jet was applied.

Figure 2.7 Failure of beam strengthened with external CFRP sheets (Dong, et al., 2013)

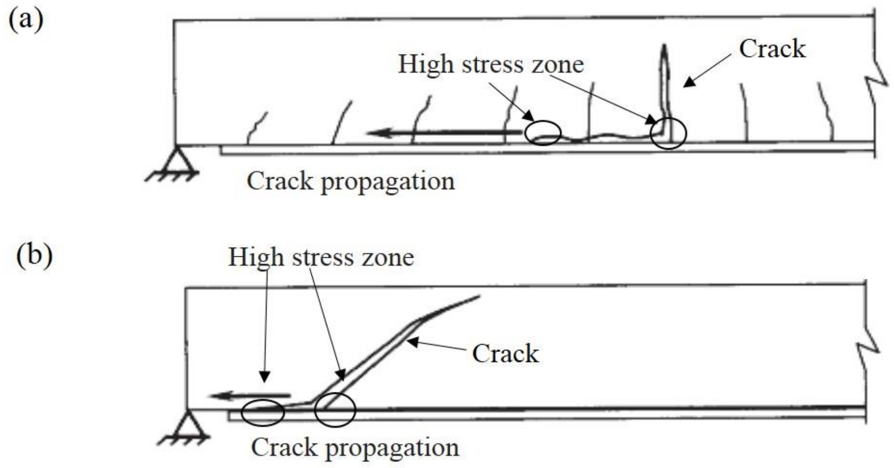

Figure 2.8 Initiation of FRP debonding in flexural strengthening: (a) intermediate flexural crack and (b) inclined crack (Triantafillou & Matthys, 2013)

Triantafillou and Matthys (2013) studied the bond and anchorage mechanisms of external FRP reinforcement and accordingly explained the causes of FRP debonding. As stated by these researchers, the bond-critical failure in the flexural strengthening system with FRPs could be categorised into two main types: FRP end debonding and intermediate crack-caused debonding. The end debonding might happen when there is insufficient anchorage capacity and occurs in the form of the FRP anchorage failure and concrete separation or concrete rip-off. If enough anchorage has been provided, debonding of the flexural FRP strengthening can still happen within the bending spans by bridging of intermediate or inclined cracks, as shown in Figure 2.8.

Therefore, it can be concluded that the flexural strength contribution of externally bonded FRPs is significantly governed by the resin adhesive because debonding usually happens prior to FRP being able to reach its designed ultimate tensile strength. Failure of the FRP-to-concrete interface will induce separation of the FRP from the concrete. In such a case, the tensile stress cannot be fully transferred to the FRP and consequently this separation will limit the development of the moment resistance for the FRP-strengthened beams.

To deal with such issues, one solution might be to carry out specific tests to physically determine the maximum force that can be transferred from concrete to the external FRP strengthening system via its bonding interface. However, this can be time-consuming and relatively inefficient considering the diversity of available strengthening and adhering materials. Alternatively, an empirical value of 0.008 for the FRP maximum strain can be used as recommended by the Concrete Society (2012). Furthermore, surface preparations of the concrete substrate are beneficial for improving the bond. Anchorage of longitudinal FRP reinforcement, which is usually in the form of transversely wrapping the beam end area with the same FRP material, is also useful for avoiding debonding that happens at, and usually starts from, the bonding ends.

2.4 Use of Macro-Synthetic Fibres

Macro-synthetic fibres are added into the concrete mix usually with the expectation of improving its toughness. This improvement will be potentially beneficial to controlling and changing the brittle failure of concrete elements reinforced with FRPs when building a WEC because the WEC is regularly subjected to combined hydrodynamic loads in the marine environment. Also, different from the ULS design, the SLS and ALS design of flexural concrete elements reinforced with FRPs are not dependent on the tensile strength of the FRP reinforcement.

The British Standard EN 14889-2 (2006) classifies the macro-synthetic fibre as polymer fibres with diameter greater than 0.30 mm and suggests that their utilisation is usually for increasing the residual (post-cracking) strength of a flexural concrete member. Typical tensile strengths and elastic moduli for commercially available macro-synthetic fibres fall in the range of 100-650 MPa and 2-10 GPa, respectively (The Concrete Society, 2007). The dosage that requires to be added in during a concrete mix varies depending on the purpose of addition. Considering the effect of fibres on reducing the workability of fresh concrete, the Concrete Society (2007) recommends that typical maximum dosages should not be more than 12 kg/m^3.

Hsie et al. (2008) added monofilament macro-polymer fibres into the concrete mixes at 9 kg/m^3 (i.e. equivalent to approximately 1% by volume fraction) and tested their effects on improving the flexural strength by the three-point bending test. The fibres had diameter of 1 mm, length of 60 mm, tensile strength of 320 MPa and elastic modulus of 5.88 GPa. As shown in Figure 2.9 (a), comparing with plain concrete, the researchers found that this addition had no considerable effects on improving the flexural strength but significantly changed the beam failure type. The plain concrete beams showed a brittle failure without any post-cracking load resistance after reaching their maximum flexural strength (around 4.7 MPa). Meanwhile, the fibrous beams had an increased maximum flexural strength of 5.5 MPa at the same deflection as the plain concrete beams. However, the failure for the synthetic-fibre-reinforced concrete beams happened without any sudden collapses. These cracked synthetic-fibrous beams also held an approximately stable load until a relatively large deflection (i.e.1 mm compared with the 0.05 mm deflection at first crack).

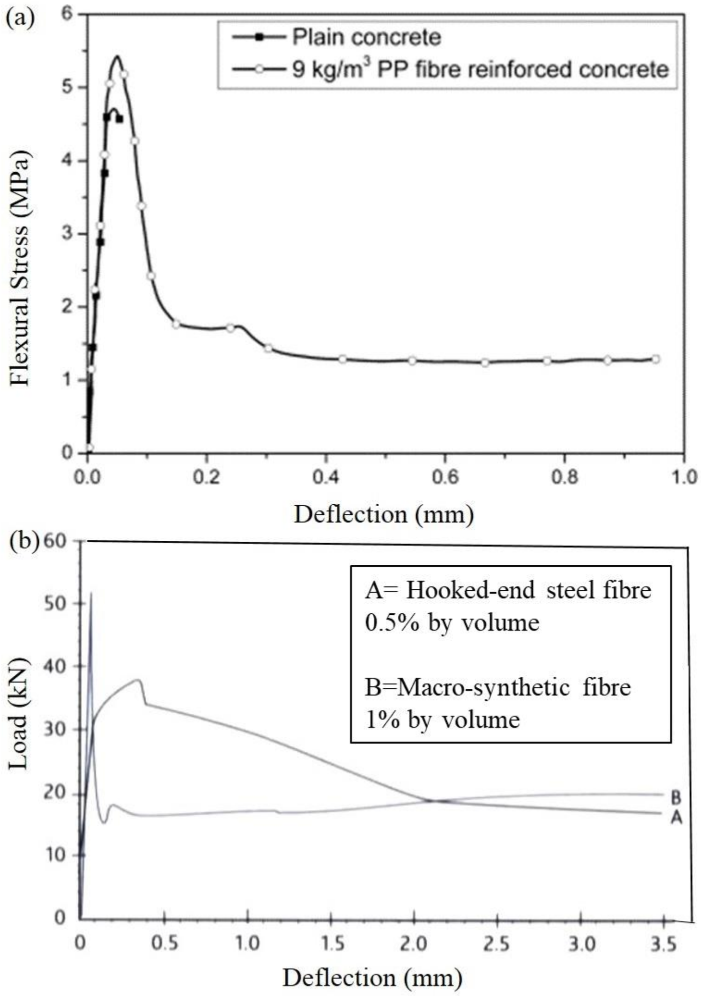

Figure 2.9 Flexural strength or load vs. deflection curves of macro-synthetic fibre reinforced concrete: (a) comparing with plain concrete (Hsie, et al., 2008) and (b) comparing with steel fibre (Ratcliffe, 2007)

Similar load-deflection behaviour was reported by Ratcliffe (2007) whose experimental curve also showed a stable post-cracking strength up to a deflection of 3.5 mm during the bending test (Figure 2.9 (b)). Concrete specimens reinforced with macro-synthetic fibres usually presented sharp load resistance reductions (Figure 2.9 (a) and Figure 2.9 (b)-B) while those with steel ones decreased more gradually (Figure 2.9 (b)-A). However, beams with these two different fibres showed close load resistance after the deflection of 2 mm, irrespective of their fibre type. Therefore, the residual strength of fibre-reinforced beams could be less affected by the fibre type but more affected by the fibre volume fraction.

In an analysis of these experimental load vs. deflection curves, the macro-synthetic fibres are believed to start picking up load at relatively small strains and perhaps can prevent the spread of cracks (Foti, 2011; Yin, et al., 2015). As the tensile stress increases, higher load can be appropriately transferred to the reinforcing fibres via concrete. However, because of the low strength and stiffness of the polymer fibres as well as the fact that the fibres do not yield, the stress drop-off after the peak load behaves proportionately sharply. The final break of the fibrous concrete beams may depend on the rupture type of the added macro-synthetic fibres at the cracked sections. In general, the failure mechanisms of the fibre are mainly dependent on its tensile strength and bond strength. Specifically, the fibre failure can be in the form of being pulled out from the concrete matrix or by fibre rupture.

Both Ratcliffe's (2007) and Hsie et al.'s (2008) results showed that macro-synthetic fibres held approximately 20-30% of the maximum strength of the fibrous beam after it failed and sustained over a proportionally large range of deflection. The residual strength of the fibrous concrete beams can be affected by factors such as the type and properties of the fibres as well as the fibre volume fraction. Though the fibre failure mechanism is still not thoroughly understood, it is clear that addition of the macro-synthetic fibres can delay the collapse of the beam.

More specifically, Hsie et al. (2008) calculated the toughness index which was a measure of the energy absorption in deflecting a beam by computing the area under a load versus deflection curve. The toughness index for concrete beams was calculated at 3δ, 5.5δ and 15.5δ where δ was the deflection at the maximum load in a bending test. These 3 indices all equalled to 1.00 for plain concrete and 3.58, 6.91 and 15.23 respectively for the 9kg/m^3

monofilament fibre reinforced beams. Similarly, Buratti et al. (2011) studied the post-cracking behaviour of their macro-synthetic fibre reinforced concrete beams which had varied fibre dosages from 2.0 to 10.0 kg/m^3 and found that the addition of fibres increased the toughness of concrete by from 5 to 10 times. The relations between the improvement of toughness and the fibre volume fraction were not correlated in their study due to lack of quantitative experimental data.

Precise calculation of the toughness requires to assume that the concrete matrix being linearly elastic-brittle, which actually does not conform to the post-ULS behaviour of the fibrous beams after their failure. However, these proposed indices are of relevance as they quantitatively demonstrate that addition of the macro-synthetic fibres has great potential in improving the concrete toughness.

2.5 Use of Macro-Steel Fibres

Steel fibres have a history of more than 50 years of being commercially utilised as an addition for concrete mixes. Steel fibres provide the concrete with multiple benefits, many of which are well estimated. For example, at required dosages, steel fibres can improve the toughness, ductility and energy absorption of the concrete, reduce the formation and development of cracks and provide a degree of post-cracking load-carrying capacity (The Concrete Society, 2007). The Concrete Society Technical Report No. 63 (2007) covers guidance and suggestions of the design of steel-fibre-reinforced concrete (SFRC) with a dosage not in excess of 80 kg/m^3. When the fibre dosage exceeds 80 kg/m^3, workability problems of the concrete and balling and clumping issues of the fibres might occur during mixing.

2.5.1 Flexural and Shear Capacity of SFRC

Adding of steel fibres at low dosages was considered to not influence the ultimate flexural strength much comparing with plain concrete (The Concrete Society, 2007). However, at higher dosages of more than 80 kg/m^3 (i.e. 1% by volume), the effects can be different.

Various research results are available regarding investigation for the effects of steel fibre addition on the mechanical properties of concrete and reinforced concrete. With respect to lower dosages under 80 kg/m^3, Altun et al. (2007) tested SFRC beams with fibre dosage at 0, 30 kg/m^3 and 60 kg/m^3 with both C20 and C30 class concrete. They found that the flexural strength of C20 concrete increased by 50% and 80% at the 30 kg/m^3 and 60 kg/m^3 dosage respectively; while for C30 concrete, it was 20% and less than 50% respectively. On the other hand, Yazici et al. (2007) tested SFRC specimens with higher dosages of 78 kg/m^3 and 117 kg/m^3 and reported that, compared with plain concrete, their flexural strength by the bending test improved by 36% and 57% respectively. The increase effects of steel fibre addition seem to be related to various other factors as well, such as the fibre aspect ratio and concrete compressive strength, but prediction modes for estimating the SFRC strength have been developed empirically (Thomas & Ramaswamy, 2007; Olivito & Zuccarello, 2010). As secondary reinforcement, addition of steel fibres is also reported to enhance the flexural behaviour and ductility of concrete beams reinforced with FRP bars (Issa, et al., 2011; Wang & Belarbi, 2011; Yang, et al., 2012).

Steel fibres, reportedly (The Concrete Society, 2007; Wilson & O'Flaherty, 2016), have the potential to resist shear force and to prevent shear failure from occurring.

One study published by Wilson and O’Flaherty (2016) investigated the effects of steel fibre dosage on the structural behaviour of SFRC beams. Their beams were cast using ultra-high strength concrete (≥120 MPa) separately with 77.5 kg/m^3 and 150 kg/m^3 steel fibre dosage. Control beams were prepared with the same mix and fibre dosages, but also with longitudinal steel rebar as the secondary reinforcement. All beams were reinforced without shear stirrups or webs. Their results show that all fibrous beams with and without secondary reinforcement failed in the flexural rather than shear mode. The beams with the 77.5 kg/m^3 fibre addition reached approximately 40% of the maximum load-carrying capacity of the beams with additional rebar, while the 150 kg/m^3 ones achieved around 45% correspondingly. Based on these results, the researchers concluded that steel fibres prevented formation of the shear failure and could be used for replacing the conventional forms of shear reinforcement.

It needs to be mentioned additionally that the shear span to effective depth ratio of a beam (a_v/d, where a_v is the beam’s shear span under bending and d is the effective depth) is another important factor affecting beam failure. Considering the usually accepted models for flexural-shear interaction, beam can be divided into deep beams of a_v/d < 2.5 and shallow beams of a_v/d > 2.5. In general, the arch action takes place in deep beams while the beam action is stronger within shallow beams. On a basis of the same classification, concrete beams with longitudinal rebar and without shear reinforcement can be divided into short beams and slender beams, similarly. However, some researcher (Slowik, 2014) also pointed out that this rule of classifying only by a_v/d is not sufficiently accurate due to the fact that members with the same a_v/d but different size and concrete strength can fail in a different mode.

The beams subject to bending by Wilson and O'Flaherty (2016) were slender beams with a_v/d of more than 5.0. Another previous study carried out by Kwak et al. (2002) tested 12 beams with different fibre content as well as different a_v/d ratio. All their beams had flexural bar reinforcement but no shear stirrups within the shear spans. 3 beams were cast with identical concrete mix (each had 64 MPa compressive strength and 0.5% steel fibre content) but different a_v/d ratios. The tested beams with the a_v/d ratio of 2.0 failed in a combined shear-flexural mode while those with 3.0 and 4.0 ratio failed in flexural mode. These results accord with the fact that the a_v/d ratio has effects on the beam failure. To particularly evaluate the influence of the fibre volume fraction, additional experiment sets were trialled with a constant a_v/d ratio but increasing fibre content. For beams with the a_v/d ratio of 3.0 and 4.0, in which the beam action should predominate, it was observed that the failure mode changed from shear to flexural when the fibre content increased from 0 to 0.75%.

Although the a_v/d ratio still seems to have a dominant influence on the failure mode, it is logical to conclude from the reviewed literature that addition of steel fibres at designed dosages can increase the shear resistance. In other words, it is feasible to design shallow and slender beams with steel fibres but without conventional shear reinforcement that can avoid shear failure.

2.5.2 Corrosion of Steel Fibres in the Marine Environment

As stated in Section 1.1, corrosion is not problematic in steel-fibre-reinforced concrete in the marine environment. Balouch et al. (2010) carried out corrosion trials on SFRC with the w/c ratio of around 0.5 and found that corrosion happened only on the steel fibres that were embedded less than 0.1 mm deep in the concrete matrix. Considering that the added fibres are randomly distributed and remain separate in the concrete, the corrosion of any single individual filament at the surface should cause negligible harm in terms of leading to concrete spalling and delamination. However, at cracked sections where the corrosion is usually more common and more serious, the impact might be different. It is the bridging function of the steel fibres at cracked sections that is responsible for the residual strength. Therefore, the sustainability of the fibre bridging might be affected if the fibres corrode.

One previous research (Granju & Balouch, 2005) was being undertaken for a duration of one year focusing on cracked SFRC exposed to an aggressive marine-like environment. After the exposure, based on the researchers' visual observation, only a light corrosion of the fibres at the cracked section happened and no concrete bursting or algae/mould growth due to the corrosion of the fibres was observed. After the visual examination, the flexural bending test was carried out on all exposed specimens. Unexpectedly comparing with the uncracked beams, the strength (both ultimate and residual) of the pre-cracked ones that were exposed for one year to the accelerated exposure was not weakened, but, increased. The researchers speculated that the gain of strength resulted from the light corrosion of fibres. This could be due to that the corrosion being too light to depress the load-carrying capacity of the SFRC meanwhile being sufficient to make the fibre surface less smooth. Consequently, slipping of the bonded steel fibres from the concrete matrix became more difficult and then the residual strength was increased.

Despite the lack of substantial conclusive experimental data and numerical models that support the practicability of employing steel fibres to completely replace the conventional reinforcement, the use of steel fibres in the marine environment is still feasible. Based on the available information, a logical conclusion can be drawn that concrete with steel fibres will not undergo any noticeable strength loss resulted from corrosion in its service life if being applied in a WEC structure.

2.5.3 Design Issues of Alignment of Steel Fibres

In machine mixing, the fibres are added during the mix and are dispersed by spreading them in an even layer over the aggregate (British Standards Institute, 2013). There are disadvantages to this adding method in terms of requiring the steel fibres to provide the concrete tensile strength. Firstly, the steel fibres are distributed throughout the depth of the beam rather than only under the nominal neutral axis where they are the most needed respecting contribution of the tensile resistance. Secondly, the added fibres are in random orientations rather than being aligned in the same direction of the maximum tensile stress. In such a case, a huge number of fibres that are in the compressive zone and in the tensile zone but have a vertical orientation component will be unfavourable. Moreover, because of the low rate of being mobilised and utilised of the randomly distributed fibres, higher dosages of the steel fibre will be needed to enable satisfactory structural behaviour of the SFRC, which can result in problems such as low concrete workability and high economic cost. The fibre distribution also has important effects on the behaviour of concrete under the tensile loading and various researches (Kang, et al., 2011; Plagué, et al., 2017) have been carried out to investigate that.

Kang et al. (2011) studied the influence of fibre distribution characteristics on the flexural strength of ultra-high-strength concrete reinforced with steel fibre in conjunction with the direction of placement. The mix had a compressive strength of around 198 MPa and a steel fibre addition of 2% by volume while the fibres were 0.2 mm and 13 mm in diameter and length respectively. The concrete was prepared with the steel fibres being randomly added during the mix, but the beams were cast with different concrete placing directions. Specifically, the concrete was placed either parallel to the longitudinal direction of the beam or transversely to the longitudinal direction of the beam. The researchers proposed three coefficients to quantitatively evaluate the fibre distribution characteristics, namely, the degree of fibre dispersion (it referred to how homogeneous the fibre distribution was), the fibre unit number and the fibre parking density. Evaluations of the fibre distribution showed that the fibres of specimens whose concrete was placed parallel to the longitudinal direction were aligned more parallel to the tensile stress direction. Based on the bending test results, the flexural strength of these better-aligned beams was 61% greater than that of the other specimens whose concrete mix was placed transversely to their longitudinal direction.

Similarly, Plague et al. (2017) experimentally evidenced that when the orientation of the steel fibre became less favourable (specifically from 39° to 54° to the direction of tensile stress in their research) in terms of providing concrete with the tensile load resistance, the flexural strength of their specimens reduced up to 33% under the uniaxial tension test.

Despite all the theoretical supports from laboratorial work, the concept of aligning steel fibres itself is not new. West (2003) and West et al. (2005) described an idea of aligning steel fibres using a magnetised fin from the vibrating screed to drag through fresh concrete. A prototype alignment device was made by West (2003) based on his idea and trialled on concrete with crimped steel fibres 25 mm in length 40 kg/m^3 in dosage. It was noticed that there were fibres remaining on the fin when it was removed from the concrete at the end of its dragging. After weighing the attached steel fibres, a conclusion was given that 97% of the steel fibres alongside the path within the magnetic field of the fin should have been settled in favourable directions, i.e. $<45°$ to the longitudinal axis. The alignment was also verified by inspecting the X-ray photographs of strip samples cut from the aligned fibrous concrete.

Other methods have also been proposed to evaluate the alignment or orientation of fibres. Alberti et al (2016) described a method of cutting concrete specimens at a required length and assessing the amount of fibres in each surface by a counting process which provided the information of the positioning of the fibres in each cut specimen. Torrents et al (2012) utilised an inductive method by measuring the self-induction change experienced by the inductance that wrapped around the specimen in the 3 coordinate axes. This magnetism method applies to steel-fibrous concrete only though.

This prototype trial confirms that the concept of aligning steel fibres in fresh concrete by using magnets is technically viable. However, in design and construction of a WEC where a large portion of fibres will be needed, the method of dragging a magnetic fin through fresh concrete to attract and align macro-steel fibres might be of restriction in practice. For example, the workability of concrete needs to be fluid enough to allow the fibres to be fully mobilised and re-accommodated; the drag speed of the fin needs to be relatively slow and well controlled to avoid steel fibres accumulating on the fin otherwise magnetic blockages will occur.

As a summary, the concept of aligning steel fibres into chosen horizontal levels within a concrete beam will be beneficial for the member’s structural behaviour, especially for the tensile strength. Alignment practice with permanent magnets has also been successfully carried out. But the techniques need to be refined and improved to allow steel fibres with larger dimensions to be aligned at higher dosages so that the objective of using aligned steel fibres to partially or maybe fully replace the steel rebar can be achieved.

2.6 Design of Joint

2.6.1 Joint Type

Joints cannot possibly be avoided in the design of a WEC due to the enormous size of the structure body. Regarding precast and 3D print concrete, it is more economic to prepare identical and repeatable components and connect them together using various available grouting materials and methods.

Different types of joints exist in concrete construction like bridges and monopile support structures. However, comparing with the various functions the joint is usually required to provide, joints in a reinforced-concrete WEC will be more responsible for transferring the flexural and shear stress. Popular types of the joint connection have been studied and compared and their arrangements are schematised in Figure 2.10. The tongue-and-groove joint will not be economically suitable because of its complexity and possible difficulty that can be encountered during the precast and grouting processes. The female-to-female (shear key) type connection was proposed by Issa et al. (2003) as capable of being used as transverse joints between precast slabs. These researchers also recommended that the joint tightness can be secured by longitudinal post-tensioning if necessary. The flat face-to-face joint is the simplest and most constructing-effective type, but it was reported (Issa, et al., 2003) that this flat shape connection could cause leakage through the joint. Leakage will not be problematic within this study for design of the truss-type WEC whose concrete

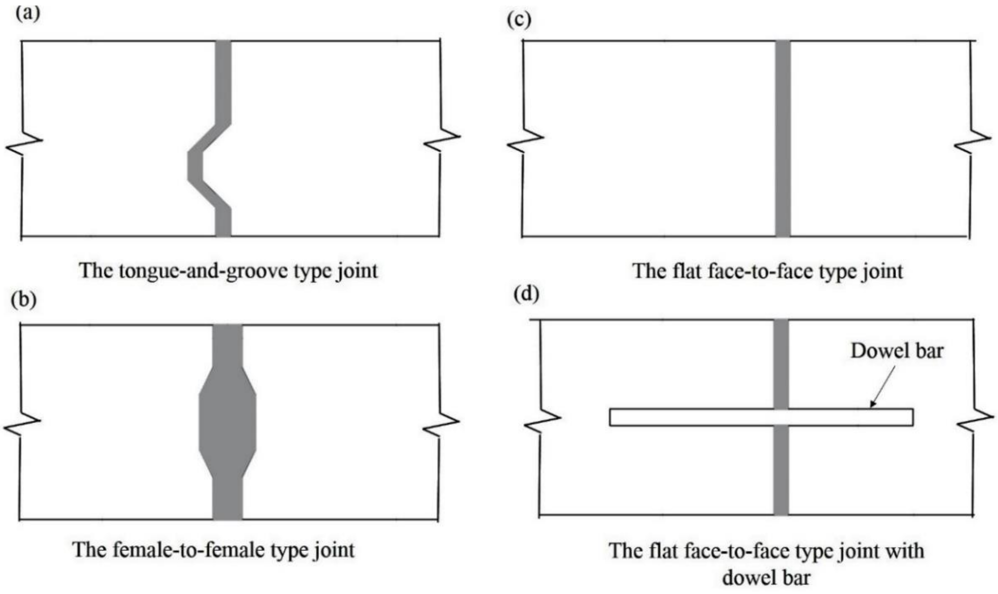

Figure 2.10 Configuration of the joints: (a) the tongue-and-groove joint, (b) the female-to-female joint, (c) the flat face-to-face joint, and (d) the flat face-to-face joint with the dowel bar

structure is planned to be shielded in a water-proof synthetic skin. When the joint bond is not sufficient, the smooth dowel bar (Figure 2.10(d)) or the deformed tie bar can be added as a supplement for the flat face-to-face joint. However, this addition obviously will make the grouting system and the segment preparation more complex and accordingly increase the expense. Therefore, from the point of view of reducing the WEC construction cost, the flat face-to-face joint type is of superior selection priority.

2.6.2 Grout Material and Joint Thickness

Both cement-based and polymer-based grout materials have been widely used in concrete construction. The epoxy resin is one of the most common structural adhesive materials in segmental bridge construction (Savvilotidou, et al., 2017). However, there are different types of epoxy resin adhesives with diverse characteristics available in industry, attributed to the fact that the molecular structure of their bases can be widely changed.

Epoxy resin adhesives usually have satisfactory grouting function between concrete and concrete (Mailvaganam, 1997; Julio, et al., 2005) and reasonable product prices, which makes them suitable for the WEC construction. Albite these adhesives may have higher requirements for surface preparation to achieve their design bond strength, it is more a matter of time consuming and labour cost. One limitation in practice can be that there are currently no effective non-destructive methods to examine and monitor the quality of the grout finish, as voids might exist within the bond and weaken the grouting. In other words, the bond strength and effectiveness of the epoxy resin adhesive will be largely dependent on workmanship.

Failure of the interface between epoxy resin and concrete under bending could be either in the concrete as a layer of concrete adhered on the epoxy resin or at the concrete-epoxy interface as the interface separation. Lau and Buyukozturk (2010) carried out the four-point bending test on sandwiched concrete prism specimens with a 2.54 mm thick epoxy layer, as illustrated in Figure 2.11 (a). In their test, the concrete had a compressive strength of 38 MPa while the epoxy resin adhesive was characterised to have a tensile strength of around 14 MPa and the Young’s modulus of 2.8 GPa. The specimens were manufactured by casting and joining two concrete blocks together and were exposed to a condition with combined moisture and elevated temperature (50°C) for 28 days. A precrack notch with a deepness of half of the block thickness was also prepared to ensure that failure happened at the concrete-epoxy interface. It was found that the failure mode changed from failure in the concrete for dry beam specimens to failure at the bond interface for specimens after the exposure. The two failure types are shown in Figure 2.11 (b).

The epoxy adhesive layer thickness such that it has no noticeable influence on the whole structure’s linear elastic fracture mechanics is the most desirable to be chosen. However, experimental researches on the influence of the layer thickness on the structural behaviour of concrete elements is particularly scarce. Peer Ph.D. work (Khosravi, 2017) within the author’s institution has been started to investigate the bond performance of epoxy resins with different thicknesses greater than 3 mm in respect of both structural and durability behaviour. Thus, thin epoxy bond, defined as the bond layer with a layer thickness less than 3 mm, is chosen as the focus for this investigation.

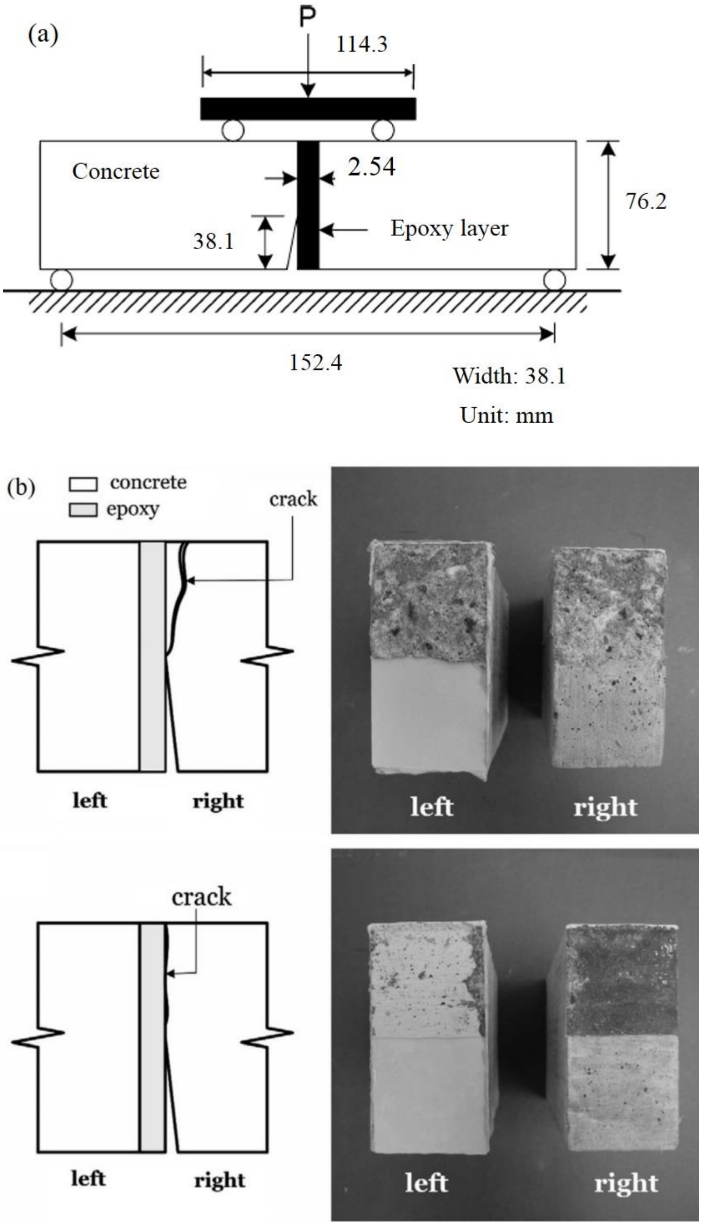

Figure 2.11 (a) The four-point bending test on the epoxy-jointed concrete prism, and (b) the two failure types of concrete failure (top) and adhesive failure (bottom) (Lau & Buyukozturk, 2010)

2.7 Post-Tensioning of FRP Reinforcement

FRP reinforcing products have been suggested for use as pre-stressing tendons in concrete structures. Post-tensioning, as a variant of pre-stressing where the tendons are tensioned after the surrounding concrete structure has been cast, enables the FRP reinforcement to meet specific design objectives. Through post-tensioning, the FRP reinforcing bars and strengthening strands will become active in tension prior to concrete cracking. Apart from improving the structural capacity by applying the initial compression on the concrete, post-tensioning also acts as a method of crack control. For a shell-tube WEC in the marine environment, crack minimisation can be important.

FRP tendons are reasonably suitable to post-tensioning because of the composite’s high strength-to-weight ratio. ACI 440.4R-04 (2004) suggests that the allowable stress in FRP tendons for pre-stressing should be typically limited to 40 to 65% of their ultimate strength due to the rupture type limitations. Due to the relatively low stiffness of the FRP, this range of allowable stress gives corresponding strain between 0.008 and 0.012. In the service stage, the posttensioned beams reinforced with FRP will deform elastically before cracking then continue deforming linearly under the increasing load until failure.

For traditional pre-stressed concrete structure construction, both bonded and unbonded post-tensioning methods exist. Fabrication of bonded tendons is generally undertaken on site and generates relatively high labour requirement for placing the tendons as well as for fitting the end-anchorage to formwork. On the other hand, unbonded post-tensioning allows the tendons permanent freedom of longitudinal movement and tendons are mostly fabricated off site. Additionally, corrosion-preventing protection will not be needed for FRP post-tensioning. Thus, in terms of reducing the construction cost for a RC WEC, unbonded post-tensioning of the FRP reinforcement is of principal advantage.

It is worth noting that the surface texture and configuration of the FRP reinforcement vary from product to product. Commercial FRP bars can be ribbed but rarely shredded, which creates extra difficulty to stress them. It is also difficult to design a safe anchorage using the traditional methods of steel anchoring (Girgle & Stepanek, 2016) because the FRP composites are heterogeneous and anisotropic. Use of mechanical anchors, such as the split wedge anchor system, introduces high compression on the FRP tendons and causes problems as FRPs are weaker in the transverse direction of the reinforcing fibres. Another FRP anchoring technique is by using bonded anchoring. A bonded anchor keeps the tendon being stressed through plain adhesion between the adherents, which in this case are the external anchor and the internal FRP tendon, and the adhesive such as epoxy resin and other similar bonding agents. Consequently, this method necessitates strong bond and rapid curing of the adhesive. Hence, as admitted by Schmidt et al. (2009), efforts are still largely needed to design and develop practicable FRP anchors in applications of external post-tensioning

2.8 Conclusions of Literature Review

The compendium of the main findings and analysed results that were involved in the literature review are summarised in this section. Firstly, the reinforced-concrete material is of advantage in potentially reducing the WEC construction cost and a form of a shell-tube or a truss enclosed with an outer skin will be beneficial in terms of strength-to-weight ratio.

Secondly, FRP reinforcement is primarily regarded as suitable to be used for reinforcing a concrete WEC, but its lower stiffness and non-yielding properties still require additional design intentions. The bond of internal FRP rebar to concrete is dependent on the product configurations and seems insensitive to sea salts. There are guidelines and literature work available to be followed for the design of FRP RC elements. External FRP strengthening products can enhance the load-carrying capacity but the enhancement might be restrained by the adhesive and also the adhering failure type.

Thirdly, addition of macro synthetic and steel fibres is of great potential in improving the toughness and strength behaviour of FRP RC components respectively. Steel fibres added in the concrete will not encounter severe or unacceptable corrosion problems in seawater exposures and, if aligned appropriately at suitable dosages, the macro-steel fibres might be able to provide significant boost in improving the shear and flexural resistance.

Finally, the joint will possibly be unavoidable in the design of a WEC made of reinforced-concrete. Post-tensioning of the FRP reinforcement seems necessary and advantageous in terms of increasing the structural capacity and minimising the crack spreading.

Moreover, the lack of national standards disadvantages the use of the FRP reinforcement and the design of FRP RC. When it comes to design calculations, the following guidelines and recommendations are selected to be primarily referenced to:

(1) FRP bars:

   (a) ACI 440.1R-06 (2006), Guide for the Design and Construction of Structural Concrete Reinforced with FRP Bars.

(2) External FRP strengthening composites:

   (a) The Concrete Society Technical Report No. 55 (2012), Design Guidelines for Strengthening Concrete Using Fibre-Reinforced Composite Materials.

(3) Macro-synthetic fibres:

   (a) BS EN 14889-2 (2006), Fibres for Concrete. Polymer Fibres. Definitions, Specifications and Conformity.
   (b) The Concrete Society Technical Report No. 65 (2007), Guidance on the Use of Macro-Synthetic Fibres for Reinforced Concrete.

(4) Steel fibres:

   (a) BS EN 14889-1 (2006), Fibres for Concrete. Steel Fibres. Definitions, Specifications and Conformity.
   (b) The Concrete Society Technical Report No. 63 (2007), Guidance for the Design of Steel-Fibre-Reinforced Concrete.

(5) Pre-stressing concrete with FRP:

   (a) ACI 440.4R-04 (2004), Pre-Stressing Concrete Structures with FRP Tendons.

The principal criteria required for the limit state design in this study are based on different codes. The ULS and SLS follow Eurocode 2 (European Committee for Standardisation, 2004). The ALS is defined as a state that ensures the structure resists accidental loads and maintain integrity and performance of the structure due to local damage, which complies with the offshore code DNV-OS-C101 (Det Norske Veritas, 2011).

When it comes to specimen preparation, small-scaled beam specimens are preferred to be used in the laboratories at the initial stage for easy handling reason. Size and scale effects in strength and failure are worth being noted. A significant relative increase in strength for smaller specimens usually exists (Litle & Paparoni, 1996) while a change in the failure mechanism was also reported (Andila-Giraldo & Pujol, 2019) being associated with the beam scales. Since a large-scaled prototype is also arranged at the final stage of this study, these effects will affect the prediction of the prototype’s performance.

Chapter 3 Experimental Programme

3.1 Introduction

This chapter describes the experimental programme which has been carried out in order to achieve the proposed aim and objectives. According to their purposes, the laboratorial work involved within this project can be divided into three phases: (1) examining the fundamental properties of the novel FRP reinforcement products; (2) investigating the structural behaviour of small-scale reinforced-concrete elements for the WEC; and (3) developing and testing a WEC prototype. Each phase involves different concrete mixes, specimen preparations and test methods, all of which will be explained in detail in this chapter.

3.2 Programme of Work

The programme of work involves three continuous processes, each of which consists of a few to several progressive stages. As a synopsis, the following Section 3.2.1, 3.2.2 and 3.2.3 summarise the research approach and methodology and outline the test methods in Phase I, II and III respectively. A comprehensive structure of this research project is also illustrated in Figure 3.1.

3.2.1 Phase I

The work in Phase I focuses on determining the related characteristic properties of the FRP rebar, more specifically, its bond to concrete and bond response to influences of the concrete strength and seawater ions. The behaviour and failure under tension and shear stresses of the FRP bar and strands are also investigated. These preliminary tests are useful for deciding whether FRP composites are applicable in a WEC structure.

3.2.2 Phase II

Based on the experimental outputs from Phase I, small-scale FRP-reinforced concrete beams (beam length less than 1000 mm) were used during the tests in Phase II. Various types of novel or non-ferrous reinforcement were applied to reinforce and strengthen the concrete elements and tested. A summary of the specimens' dimensions and reinforcing conditions is listed in Table 3.1. Test arrangement in this phase covers examinations on: (1) the load-deflection relations, reinforcing effectiveness, crack and failure of flexural concrete elements reinforced or strengthened with GFRP and CFRP, (2) solutions to the brittleness failure by adding macro-synthetic fibres at selected dosages, (3) practicability of aligning steel fibres to provide shear and tensile resistance, (4) feasibility of applying a flat face-to-face joint, and (5) trials on post-tensioning FRP reinforcement to overcome its low stiffness disadvantage. A series of experiments was arranged to achieve these objects. The experiments provide a useful basis and options for optimising and finalising the WEC prototype design in Phase III.

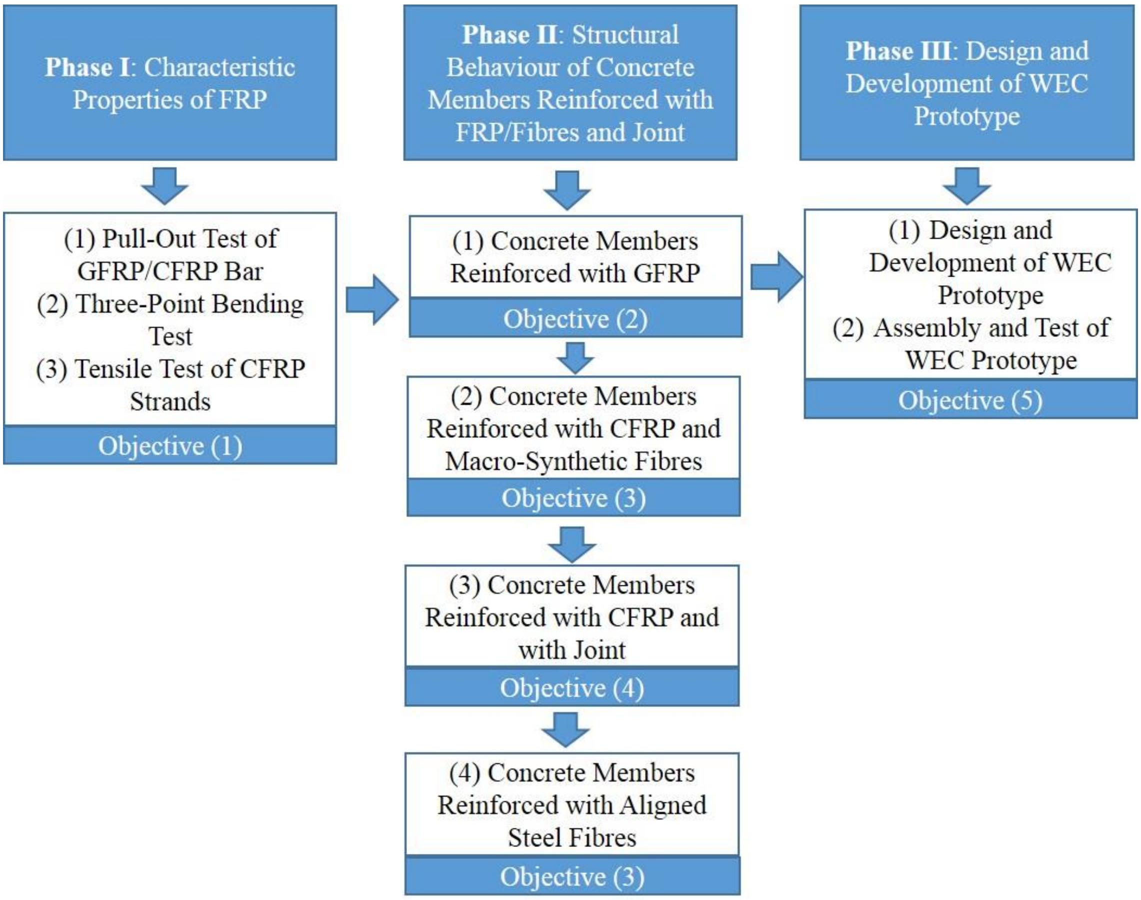

Figure 3.1 Programme of work and main research phases for this study

Table 3.1 Summary of the tests and related specimens in Phase II

Test Method	Specimen Abbreviation	Reinforcement			Beam Dimension^a, mm
		Tensile	Shear	Fibres	
Four-point bending	GC1	GFRP^b	CFRP^b	-	500×100×100
	GC2	CFRP^c	CFRP^c	-	1000×100×100
	CC1			Synthetic	
	CC2			-	
	GC3	GFRP^b	-	-	500×100×100
	SF	-	-	Steel	1000×100×100

^{a}: length×width×depth; ^{b}: rebar; ^{c}: strengthening strands

3.2.3 Phase III

Based on an optimisation of the production within Phase II, design, development as well as testing of a WEC prototype are arranged in this final work phase. Prior to the prototype, tests on its components are also carried out to understand the fundamental behaviour of a truss structure as well as to compare with numerical modelling results. Large-scale beams manufactured with 3D printing and reinforced, and post-tensioned with UHMWPE cables were also prepared and tested as a proof of concept.

3.3 Materials

3.3.1 Composition of Concrete

Cements

All cements used throughout this study were obtained in single bulk samples and stored in air-tight bags or within plastic baskets before mix. Portland cement (PC) CEM I 52.5N, conforming to BS EN 197-1 (2011), was used in this project. For most mixes, the PC was partially replaced by other supplementary cementitious material, namely, the desilicated fly ash (DFA) by 30% and the ground granulated blast-furnace slag (GGBS) by 40%. Use of the DFA and GGBS was in order to produce more eco-friendly concrete and conformed to BS EN 450-1 (2012) and BS EN 1516-1 (2006) respectively.

Aggregates

Both gravel and crushed granite were used separately as the coarse aggregate for mixes. The gravel aggregate consisted of two grading ranges, namely 4-10 mm and 10-20 mm, while the granite aggregate had only one 4-10 mm grading range. The gravel was round and smooth-edged and obtained locally in Angus. The granite aggregate was provided by Leiths Scotland Co. and obtained by the supplier from the Blackhill Quarry in Aberdeen. The fine aggregate was in a single size of 0-4 mm and obtained by a local supplier in Fife. The main physical properties as well as the particle size distribution of both the fine and the coarse aggregates are listed in Table 3.2. Measure of their particle density and water absorption was based on BS EN 1097-6 (2013).

Table 3.2 Physical properties and particle size distribution of the aggregates

Property	Fine Aggregate	Coarse Aggregate		
	Sand	Gravel	Gravel	Granite
Grading Range, mm	0/4	4/10	10/20	4/10
Shape, visual inspection	Round	Round & Smooth Edged	Round & Smooth Edged	Irregular & Angular
SSD[a] Density, kg/m^3	2650	2690	2690	2650
LBD[b] Density, kg/m^3	1640	-	-	2620
Water Absorption[c], %	0.8	0.5	0.5	1.0
Elasticity[d], GPa	-	35	50	50
	Particle size distribution- percentage of passing by mass, %			
20 mm		-	100	-
14 mm		100	93.2	100
10 mm	-	92.7	27.9	75.2
6.3 mm	100	20.8	1.1	10.3
4 mm	91.9	-		4.7
2 mm	80.6	0.3		1.3
1 mm	74.2	-		-
0.5 mm	61.3			
0.25 mm	25.9			
0.125 mm	5.9			
0.063 mm	0.6			

[a]: Saturated Surface Dry; [b]: Loose Bulk Density on an oven-dried basis; [c]: from lab-dried to SSD; [d]:data provided by suppliers.

Mixing Water

For the purpose of casting and normal curing of concrete specimens, water was obtained directly from the tap which conformed to standard BS EN 1008 (2002).

Superplasticiser

Use of the superplasticiser (SP) admixture (Master®Glenium SKY 544 from BASF) was for water reduction during concrete mixes and complied with BS EN 934-2 (2009).

3.3.2 FRP Reinforcement

Three types of FRP reinforcement were used in this research project, namely, GFRP bars, CFRP bars and CFRP strands (Figure 3.2). The GFRP bars were provided by Schöck Co. from Germany with a trade name of Schöck ComBar®. They were manufactured into bars 8 mm in diameter by the pull-extrusion process from glass fibre and vinyl ester resin. The surface of the GFRP bar was continuously ribbed with a rib depth of 1 mm but smooth without any other deformation or coating. The CFRP bars were provided by Sireg Sp.A Co. from Italy with a trade name of Carbopree®. According to its manufacturer, the CFRP rebar was made of carbon fibre impregnated into vinyl ester resin and had a surface treatment of the bar outside being coated with quartz sand and twined with a spiralling. The surface coating and spiralling, as claimed by the manufacturer, could considerably improve the bars' bond to concrete. The CFRP bars were 7.5 mm in diameter.

The CFRP strands were from Sika with a product name of SikaWrap® FX-50C. The CFRP was made of carbon fibre with thixotropic impregnating resin and was unidirectional. The fibre content of the CFRP strands was reported as not less than 50 grams per metre while the strand cross section as over 28 mm^2, values of which might vary depending on the distribution of the reinforcing carbon fibres. The CFRP were encased in plastic envelopes before use and incorporated several smaller strands that can be easily separated by hand (Figure 3.2). Use of this CFRP product was described by its suppler as mainly for near-surface-mounted flexible strengthening and serving as a fibre connector for the anchorage of FRP fabrics. Typical physical and mechanical properties of the three types of FRP reinforcement, provided by their manufacturer or supplier, are outlined in Table 3.3.

Figure 3.2 GFRP bar, CFRP bar and CFRP strands compared with an 8 mm steel bar

Table 3.3 Properties of the GFRP bar, CFRP bar and CFRP strand reinforcement (data provided by the manufacturer or supplier)

Property	FRP Reinforcement		
	GFRP Bar	CFRP Bar	CFRP Strand
Product Dimension	Ø8 mm	Ø7.5 mm	28 mm^{2} [a]
Composite Density, kg/m^{3}	2200	1600	1800
Reinforcing Fibre	Glass	Carbon	Carbon
Matrix Material	Vinyl ester resin	Vinyl ester resin	Epoxy resin
Tensile Strength, MPa	1000	2300	2100
Tensile E-Modulus, GPa	60	130	230
Strain at ULS, ‰	7.3	1.4-2.2	-

[a]: cross section area.

3.3.3 Fibres

Both macro synthetic and steel fibres (Figure 3.3) were used, separately, in this project. The synthetic fibres were from the manufacturer Adfil Co. with a trade name of Durus® S400. These synthetic fibres were embossed monofilaments 55 mm in length and 1 mm in diameter, and consequently had an aspect ratio of 55. Usage of the synthetic fibres was added directly into the concrete pan mixer at designated dosages. The Durus® S400 synthetic fibre, according to Adfil, complied to standard BS EN 14889-2 (2006).

The macro-steel fibres were provided by Maccaferri Ltd. from the U.K. and had a trade name of WIRABD® FF1. These metal filaments were cold drawn steel wire fibres with double end hooks. They were 50 mm in length and 1 mm in diameter and therefore had an aspect ratio of 50. Use of the steel fibres was described by the supplier as mainly for flooring and precast concrete. In this project, the steel fibres were added to provide shear resistance and improve flexural strength. The addition was in a method manually aligning these fibres to the longitudinal direction of the flexural beam other than being randomly distributed during mixing. Properties of the two types of fibre are listed in Table 3.4.

Table 3.4 Physical and mechanical properties of the macro synthetic and steel fibres (data provided by the manufacturer or supplier)

Property	Fibre Type	
	Synthetic Fibre	Steel Fibre
Fibre Length, mm	55	50
Aspect Ratio	55	50
Fibre Type	Macro	Macro
Fibre Size	Embossed monofilament	Smooth monofilament with double end hooks
Composite Materials	Polypropylene	Carbon steel
Composite Density, kg/m^3	905	8050
Water Absorption	Nil	Nil
Tensile Strength, MPa	-	>1100

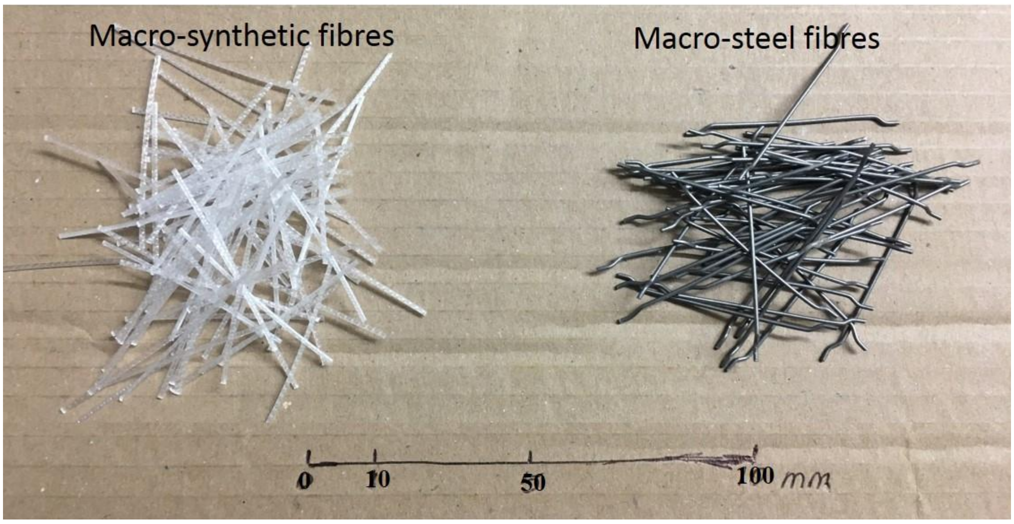

Figure 3.3 Macro-synthetic and macro-steel fibre specimens

3.3.4 Epoxy Resin Adhesive

The Sikadure®330 thixotropic-epoxy-based resin composite, supplied by Sika, was used as the structural adhesive for bonding external CFRP strengthening strands and grouting concrete/concrete joints. The Sikadure®330 adhesive consisted of a resin part A and a hardener part B, the colours of which were white and grey (Figure 3.4 (a)), respectively, before mix. These 2 parts were mixed together by 4: 1 by weight of part A: B for use and only such quantity was mixed which could be applied within its pot life. The procedures for mixing and applying the epoxy resin are listed in Table 3.5.

The ready-mixed adhesive had a uniform light grey colour (Figure 3.4(b)) and weighed 1.30 kg per litre. According to the manufacturer, at 23°C the adhesive needed a minimum of 12 hours pre-curing time and 7 days curing time to achieve its design tensile and bond strength. Once properly cured, the adhesive should have a tensile strength of 30 MPa and an E-modulus of 4.5 GPa in tension approximately.

Table 3.5 Procedures for mixing and applying of the epoxy resin adhesive

Step	Description
1	Weigh the two components as part A: part B equals 4: 1 by mass exactly and accurately;
2	Mix part A and B together for at least 3 min with a mixing spindle attached to a slow-speed electric drill until the material becomes smooth in consistency and achieves a uniform light grey colour;
3	Pour the whole mix into a clean container and stir again for approximately 1 min by hand at low speed to minimise the air entrapment;
4	Apply the ready-mixed material with a brush on to pre-prepared substrate surface, e.g. concrete, at approximate thickness of minimum 2.0 mm;
5	Joint the beams together or apply the CFRP strands for which another layer of adhesive is needed to achieve full encapsulation of the strands;
6	Allow 7 days curing before testing.

Figure 3.4 Epoxy resin adhesive before (above) and during (below) the mixing

3.3.5 Epoxy Resin Grout

The Sika AnchorFix®-1 two-component polyester anchoring adhesive was used to grout the steel dowel connectors into the concrete truss prototype. The two components were mixed at use within the provided static nozzle when injecting. Based on the supplier, this grout had an open time of 6 min and a curing time of 85 min approximately at 20°C. The AnchorFix®-1 was claimed to have a tensile strength of 12 MPa and a tensile modulus of elasticity of 4.5 GPa approximately (both 7 days, +20°C).

Figure 3.5 Injecting the AnchorFix®-1 grout into the dowel connector sockets of the prototype ring component

3.3.6 Chemical Reagents

Chemical reagents used in the project and their applications are summarised in Table 3.6.

Table 3.6 Chemical reagents used in the project and their applications

Chemical Reagents	Test Application
NaCl Solution (1 mol/l)	Chloride solution immersion.
Sodium Chloride (NaCl, salt)	Addition to concrete mix, for determining influence on FRP bond.
Calcium Sulphate Dehydrate ($CaSO_4 \cdot 2H_2O$, gypsum powder)	Addition to concrete mix, for determining influence on FRP bond.
Artificial Seawater (1 mol/l NaCl with micro-quantities of K^- and SO_4^{2-})	Accelerated exposure with cyclic wetting/drying in simulated seawater.
NaCl Standard Solution (0.05 N NaCl), $AgNO_3$ Standard Solution (0.05N $AgNO_3$), Methyl Orange Indicator, Nitric Acid and Hydrogen Peroxide (30%)	Determination of acid-soluble chloride in concrete.

3.4 Design of Concrete Mixes

The concrete mixes were all designed based on BS 8500 (2015) with consideration for the marine environment particularly. All mix designs and their applications are given in Table 3.7. The material proportions for each mix and their compressive strength growth are in Table 3.8 and Appendix A.1 respectively. Mix II and III are designed for inspecting the effects of concrete strength and ions on the FRP bond hence had different w/c ratios and additions. Mix V, VI and VII all had an S1 slump; they had low flowability but were compatible for casting concrete specimens in the laboratory with the use of the vibrating table.

Table 3.7 Concrete mixes and applications involved in this study

Mix	w/c Ratio	Strength[$], MPa	Slump[$$], mm/Class	Application
Mix I	0.38	86	90/S2	Chloride diffusion predetermination.
Mix II-1	0.40	72	100/S3	FRP bond: Influence of concrete strength.
Mix II-2	0.45	65	120/S3	
Mix II-3	0.50	56	150/S3	
Mix III-1[a]	0.45	53	100/S3	FRP bond: Influence of chloride.
Mix III-2[b]	0.47	50	20/S1	FRP bond: Influence of sulphate
Mix IV	0.43	63	120/S3	Four-point bending.
Mix V[c]	0.43	51	20/S1	Macro-synthetic fibre mix.
Mix VI	0.43	64	20/S1	SFRC: Influence of GGBS
Mix VII	0.30	80	20/S1	SFRC: Influence of concrete strength

Other materials addition: [a]: 38 kg/m^3 of salt; [b]: 51 kg/m^3 of gypsum; [c]: 20 kg/m^3 of fibres.
[$]: measured compressive strength of 100 mm cubic samples with 28 days standard curing.
[$$]: measured value of fresh concrete.

3.5 Preparation of Concrete Specimens

3.5.1 Mixing of Concrete

The procedure of concrete mixing mainly followed the steps that are specified by standard BS 1881-125 (2013). Machine mixing was applied for the whole project with a horizontal pan mixer which had a maximum capacity of 0.035 m^3 per mix. The applied mixing steps are summarised in Table 3.9.

Table 3.8 Concrete mix proportions used in this research programme

Concrete Mix	w/c Ratio	Mix Proportion									Yield Density, kg/m^3
		Water, kg/m^3	Cement, kg/m^3			Aggregate, kg/m^3			SP, %[a]	Other Material, kg/m^3	
			PC	GGBS	DFA	Sand	Gravel, 4/20 mm	Granite, 4/10 mm			
Mix I	0.38	170	225	225	-	725	1110	-	0.6	-	2455
Mix II-1	0.40	190	475	-	-	806	-	909	0.5	-	2380
Mix II-2	0.45	190	422	-	-	827	-	933	0.5	-	2372
Mix II-3	0.50	190	380	-	-	862	-	934	0.5	-	2366
Mix III-1	0.45	190	422	-	-	827	-	933	0.5	Salt, 38	2410
Mix III-2	0.47	198	422	-	-	827	-	933	0.5	Gypsum, 50	2431
Mix IV	0.43	170	280	-	120	690	-	1120	1.0	-	2380
Mix V	0.43	190	313	-	134	680	-	1091	1.0	Fibres[b], 20	2428
Mix VI	0.43	170	240	160	-	690	-	1120	1.0	-	2380
Mix VII	0.30	150	300	200	-	610	-	1120	2.0	-	2380

[a]: by mass of cementitious materials; [b]: macro-synthetic

Table 3.9 Steps for concrete mixing in this project in accordance with BS 1881-125

Step	Description
1	Add the lab-dried aggregates in the order of half the coarse aggregate, the fine aggregate and the remaining coarse aggregate and mix for 30 s;
2	Add half of the water and mix for 2 min, stop the mixer and leave the content covered for approximately 10 min;
3	Add all the cement and GGBS/DFA or fibres and mix for 30 s;
4	Mix the concrete briefly using a steel trowel to ensure homogeneity, especially for the material around the pan wall;
5	Add the SP into the remaining water and stir until it is fully dispersed then add the water and mix for around 2 min;
6	Turn the concrete over in the pan a few times using a steel trowel before sampling;
7	Carry out the slump and density test where applicable.

3.5.2 Casting and Curing of Concrete Specimens

Casting of concrete was carried out by filling the already mixed fresh concrete into the moulds with multilayers, namely, two layers for cube specimens and three layers for beam specimens. After each layer filling, vibration was arranged for compaction in accordance with code BS EN 12390-2 (2009). The top face of the moulded concrete was levelled and smoothed with a steel plastering trowel. The newly cast concrete specimens were placed under damp hessian during the first 24 ± 2 hours. After that, specimens were demoulded and then immersed into water in curing tanks with constant temperature (20 ± 2°C) until being tested or transported to their exposures where applicable.

3.5.3 Consistency and Strength of Concrete

The slump test was carried out to examine the workability and to measure the consistency of fresh concrete, the test procedure of which was in accordance with standard BS EN 12350-2 (2009). The slump value is described as the vertical distance between the top of the slumped concrete and the top of the inverted slump cone (to the nearest 10 mm). The measured slump results are given in Table 3.7 in Section 3.4.

The compressive strength of concrete was measured with 100 mm cubic samples based on BS EN 12390-3 (2009) at 3, 7, 28 and 90 (where needed) days respectively. For each strength measurement, three cubes for acceptance were subjected to the load at a rate of 7.0 N/mm^2 per second continuously until the cubes failed. The strength development curves were plotted for each mix in terms of compressive strength vs. age. Results of the compression test for all mixes at 28 days are presented in Table 3.7 in Section 3.4 while their compressive strength growths over time are plotted in Figure A.1 in Appendix A.

3.6 Preparation of Reinforced-Concrete Specimens

3.6.1 FRP Specimens for Pull-Out

A total of 8 sets of specimens were prepared for the FRP pull-out test to estimate the influence of concrete strength, chloride and sulphate ions on the bond-to-concrete of both GFRP and CFRP bars. Each set consisted of three identical samples. The specimens were prepared with FRP bars 500 mm in length embedded in the concrete parallel to its casting direction. The bars' bonded length was made as 40 mm, which was approximately 5 times the bar diameter, by sheathing its outside section that contacted the concrete matrix tightly with PVC film. The holding concrete matrices were 100 mm cubes.

During casting, the sheathed FRP bar was inserted into the moulded fresh concrete by hand until it was felt that the bar touched the bottom of the steel mould (some of them actually did not, see Figure 4.2 in Section 4.2.2). Position of the inserted bar was at the geometrical centre of the mould. Then the concrete surface was smoothed, and the mould was covered with a holding cap made of polystyrene foam to keep the inserted FRP bar standing vertically (Figure 3.6) during the concrete's pre-curing.

Accelerated methods were developed to estimate the long-term influence of chloride and sulphate ions from the marine environment on the bond of FRP to concrete. Instead of exposing the cast concrete specimens with embedded FRP bars to high concentration solutions of Cl^- or SO_4^{2-} (that usually takes at least 90 days), the Cl^- and SO_4^{2-} ions were separately added into the concrete mixes in the form of salt and gypsum respectively.

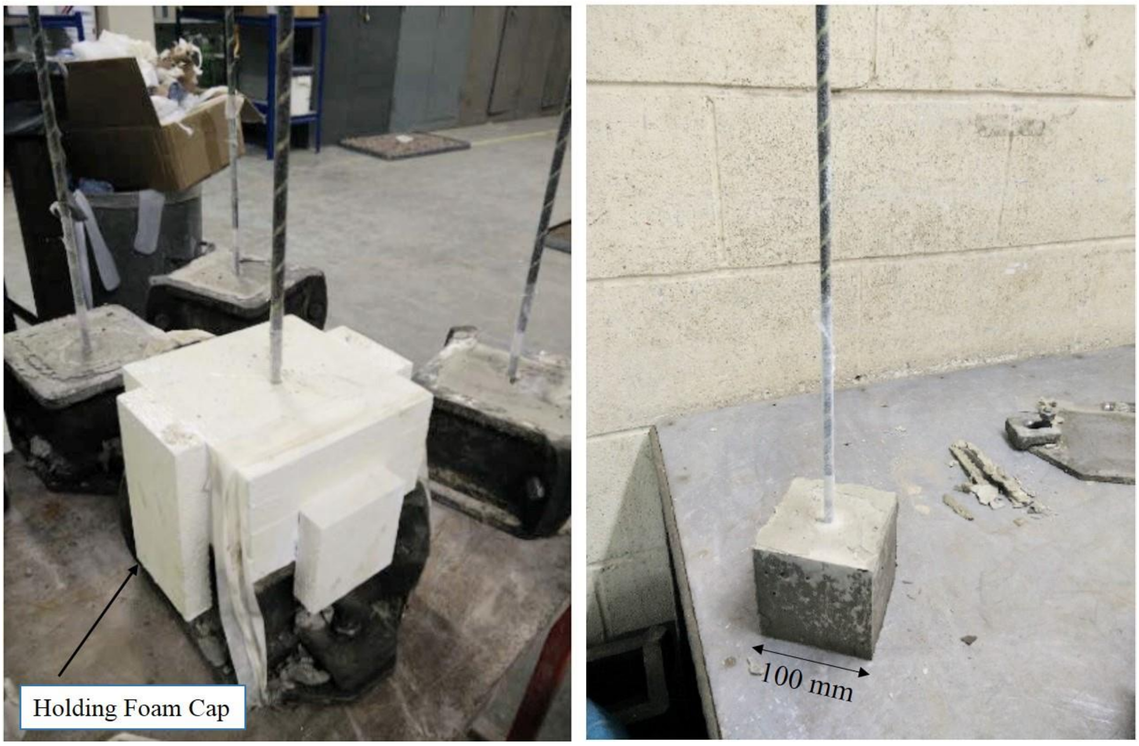

Figure 3.6 Casting of specimen for the pull-out test (left) and one specimen after being demoulded (right)

To determine the proper amount of salt needed to be added in to generate a suitable and representative level of chloride ion presence, a chloride diffusion predetermination test was carried out on concrete Mix I. This test was carried out in accordance with standard CEN/TS 12390-11: 2010 (Bristish Standard Institution, 2010) with 1 mol/l NaCl solution and lasted for 45 days. After the exposure, the acid-soluble chloride content of concrete was determined using the method from BS EN 14629:2007 (British Standards Institution, 2007). Details of the test specimen, exposure and chloride content determination are described in Appendix A.2. After a 45 days exposure, it was measured that concrete Mix I had an acid-soluble chloride content of 0.53% by mass of concrete at the surface. Various factors could affect the chloride resistance of concrete (Neville, 2011; Song, 2014) but this value was of reference in this study programme because it gave a comparison level of chloride that the FRP bars embedded in concrete might be exposed to in the marine environment. Since the FRP bars are not expected to suffer from any serious deterioration within their service life, a higher level of chloride stimulation was preferred to simulate the accelerated exposure. Therefore, addition of the sodium chloride was decided as 1.58%

by mass of concrete (i.e. 38 kg/m^3). This addition theoretically would produce a chloride content of around 0.96% by mass of concrete evenly within the concrete mix, which was approximately double the level from the predetermination test.

To determine the proper amount of gypsum needed, the American standard ASTM C452-06 (ASTM International, 2006) was referenced. This standard is for testing the potential expansion of PC mortars exposed to sulphate and recommends that the mixture of PC and gypsum should be in such proportions that the mixture has a sulphur trioxide (SO_3) content of 7.0% by mass of cement. This is not a method for estimating the sulphate attack on concrete; however, it provides a method for adding sulphate during the mix. Based on the code’s suggestion, a portion of 2.0% by mass of concrete (51 kg/m^3) gypsum was decided for the addition. Considering the very low dissolvability of $CaSO_4$, this dosage might still produce limited existence of SO_4^{2-} ions. On the other hand, adding of the gypsum at this amount might cause noticeable expansion of the concrete matrix, which is worth being noted for further analysis. Calculations for determining the gypsum addition quantity for Mix III-2 are explained in detail in Appendix A.3.

The salt was added in by dispersing it fully into the mixing water while the gypsum, in the form of fine powder, was added in by spreading it in an even layer over the aggregate after the cementitious materials. After the pull-out tests, the contents of chloride (Cl) and sulphur trioxide (SO_3) of the tested concrete specimens were also measured with the X-ray fluorescence (XRF) technique (method details described in Section 3.8.3).

3.6.2 Beam Specimens Reinforced with FRP Bars

Beam specimens reinforced with internal FRP bars were prepared mostly following the same methods of mixing, casting and curing for pure concrete specimens. The main bars or the rebar cages (with transverse FRP reinforcement) were placed in the mould with plastic spacers controlling the underneath cover thickness. All FRP bars were cut with a steel hacksaw by hand into required lengths. To fabricate the FRP reinforcement cages where applicable, the transverse FRP bars were fastened on to the longitudinal bars using plastic cable ties while all tying cables longer than needed were cut and removed.

Figure 3.7 One FRP rebar cage with transverse CFRP bars tied on to longitudinal GFRP bars with the cable ties

3.6.3 Beam Specimens Strengthened with External FRP Strands

Beam specimens strengthened with external FRP strands were prepared firstly following the same methods of mixing, casting and curing for plain concrete specimens, except that applying of the CFRP strands with the epoxy resin adhesive was arranged 7 days after demoulding. Preparation and usage of the epoxy resin adhesive have been described in Section 3.3.4.

After the 7 days initial curing in the tank, the beams were taken out of the water and left in air inside the laboratory for at least 2 hours to dry their surfaces. After the 2 hours, the beam surfaces were observed to be visually uniform and moisture-free. Where it was not moisture-free, an electric hair dryer was used additionally to dry the surface completely. Prior to applying the epoxy resin, laitance on the beams’ bonding area was removed with a steel brush as well as compressed air and the positions for adhering (usually 15-20 mm wide and 80-100 mm apart) were marked out with duct tape. Then the ready-mixed epoxy resin was applied on to the marked concrete surfaces evenly at a thickness of 2 mm approximately. The FRP strands, previously cut into required lengths with scissors, were taken out from their plastic sleeves and laid on to the applied laminating adhesive. Another layer of epoxy resin was applied over the strands and then pushed into them with

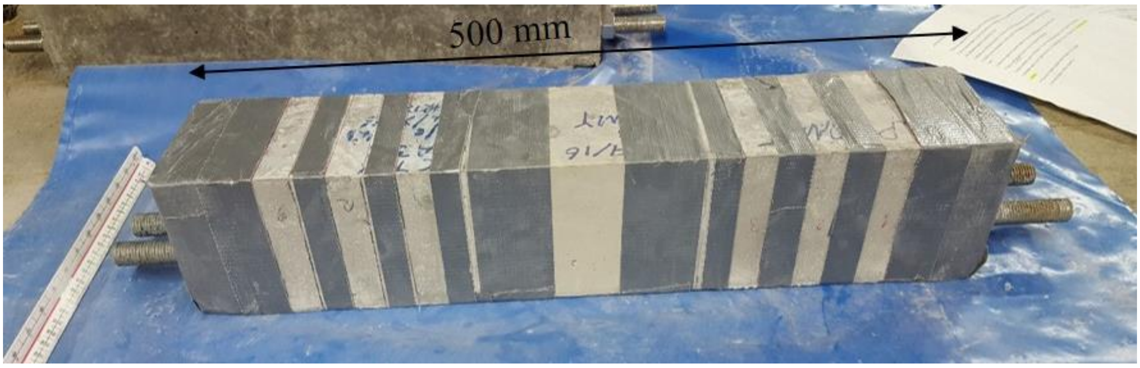

Figure 3.8 Preparation for bonding the external strengthening FRP strands

a steel brush. Finally, the epoxy resin on the FRP strands was smoothed by hand to ensure fully encapsulating of the FRP. The marking tapes were removed while the epoxy resin was still wet. The epoxied beam specimens were wrapped loosely with PVC film to reduce drying shrinkage of the concrete and left in air inside the laboratory for 48 hours, by which time the epoxy resin adhesive was supposed to have achieved 70% of its bonding strength according to the supplier. After the initial curing of the epoxy resin adhesive, the specimens were restored back to their primary curing tanks or started their planned exposures where applicable.

3.6.4 Beam Specimens with Fibres

Preparation of the fibrous beam specimens included producing beams with the randomly distributed synthetic fibres and the manually aligned steel fibres separately.

Addition of the macro-synthetic fibres followed BS EN 1881-125 (2013). To determine a suitable maximum amount of fibres that could be added in while still keeping acceptable workability for concrete to compact, a series of trial mixes was carried out prior to casting the beams. The trials covered mixes of 80 kg/m^3 fibres with 170 kg/m^3 free water content, 60 kg/m^3 fibres with increased 190 kg/m^3 free water content, and 20 kg/m^3 fibres with 190 kg/m^3 free water content. Details of these mix proportions and their measured slumps were given in Table A.2 in Appendix A.4. The process ended up finding that the last one was the only mix that was able to produce acceptable workability and compatibility. A brief analysis was also explained in Appendix A.4. Therefore, the last trial mix (i.e. named Mix V in Table 3.7) was selected for preparing the synthetic-fibrous beam specimens.

Preparation of the steel-fibre-reinforced beams involved alignment of the steel fibres. The alignment was carried out mainly by hand. Meanwhile, attempts to utilise electrical magnetisation methods to align the steel fibres were tried out but were unsuccessful. It was found that the maximum amount of steel fibres that could be placed during the mix highly depended on the aligning effectiveness. The steel fibres were added in by layer, usually two or three layers under the nominal neutral axis of the beam and one or two layers above if needed. The space between each layer was controlled at approximately 15 mm (1.5 times the maximum coarse aggregate size) to ensure enough bonding between the reinforcing fibres and the concrete matrix in order to avoid any probable delaminating between the layers under bending.

After a layer of fresh concrete was filled in the mould, sufficient vibration was provided to produce a levelled and relatively smooth surface that the steel fibres could be aligned on. The batched steel fibres were firstly placed in half round gutters 500 mm in length and 20 mm in diameter in the same direction as the gutter. These plastic gutters were made by cutting PVC pipes lengthwise into two halves. Then the half-pipe aligned steel fibres were positioned on to the levelled concrete by holding the gutter at a moderate angle and moving slowly and straight over the concrete face in the longitudinal direction (Figure 3.9). The aligned fibres were therefore transferred into the mould in the expected aligning orientation albeit still staying loosely together. Finally, the fibres were separated by hand so that they spread over the whole concrete face disconnectedly. It was noticed that the hand separating caused some fibres to stay in unfavourable orientations and left small gaps among the fibres. This disadvantage could be improved when handling more carefully yet might be unavoidable unless new aligning methods could be developed.

Inspired by West (2003) and West et al. (2005), an idea of electromagnetically aligning the steel fibres was proposed and attempted. The idea was to distribute the fibres on to a thin steel plate and use an electromagnet to temporarily magnetise the plate so that the metal fibres attach to the plate, turn over the plate and apply it to the concrete face, and switch off the power so that the plate will be demagnetised and the fibres will hopefully be left on the concrete in the way they were aligned before. In that instance, if practicable, the fibre alignment and distribution would be easier to control. To perform this proposal, a bench-like fibre holding deck was fabricated with a steel laminate 1 mm thick and 95 mm wide (Figure 3.10). A 12 V direct current (DC) electromagnet was used to produce the magnetic field. However, this electric-current-produced magnetic field was found too small and too weak to maintain the fibres at the required high quantity for this research. Multiple electromagnets would be needed to align the fibres more effectively, but concerns were expressed that these magnets might interfere with each other's field and pull the fibres into a different and undesirable distribution. It might have been worth contacting magnet specialists but, limited by time, it was decided that this electromagnetic method would not be attempted during the preparation of the steel-fibrous beams.

Figure 3.9 Transferring the aligned steel fibres from the PVC gutter to the mould

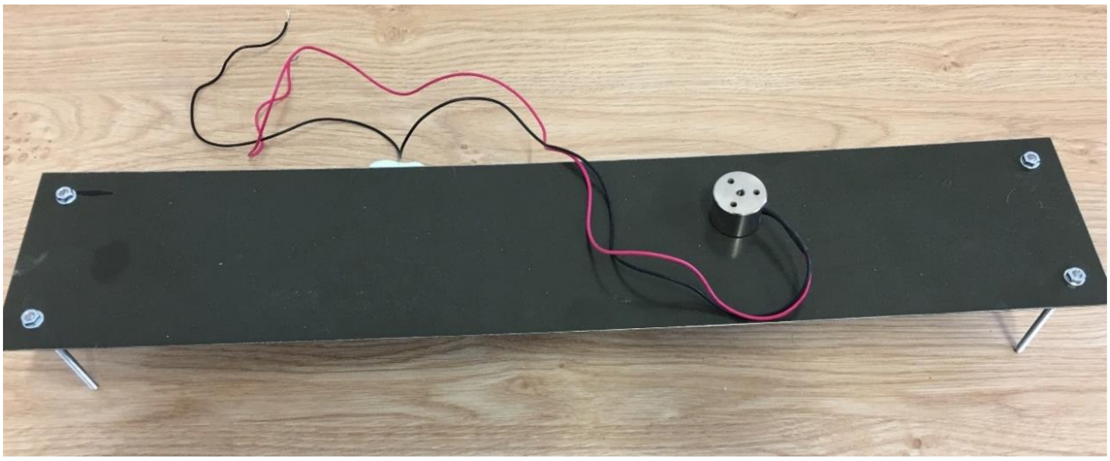

Figure 3. 10 The fabricated steel fibre-holding bench and the trialled electromagnet

3.7 Summary of Test Methodologies

As this study aimed to evaluate material properties and to develop a lab-scale prototype, it was decided that the best method was to take a mixed methods approach with physical experiments as the predominant mode and numerical modelling as a reference where necessary. Preparation and testing of all specimens were carried out in the laboratories of the University of Dundee unless otherwise specified. Quantitative tests were carried out using appropriate standardised test methods. In the case of certain tests where published standards were not suitable (due to test equipment issues) or available, modification of existing test methods or development of new methods was also applied. Validation of these methods was arranged by comparing measured results with relevant literature work.

3.8 Test Methods: Phase I

3.8.1 FRP Bar Pull-Out Test

The reference code for carrying out the FRP bar pull-out test was previously explained in Section 2.2.3. An electromechanical Instron universal test machine with a maximum load capacity of 50 kN was used to accomplish this test. A bottom supporting plate and a top bearing plate were fabricated to fasten the specimens. During the test, the bottom plate was attached to the Instron's holding base as well as connected to the top plate with bolts and nuts (Figure 3.11). Each FRP bar in test was grabbed by the clamp of the Instron at a maximum length of 100 mm. Different from ACI 440.3R-04 (2004) which suggests that slip from both the holding end and the free end of the bar should be measured, this test measured only the slip from the bar's holding end (that was automatically recorded by the Instron) because of the difference of test equipment and arrangement. Therefore, only the loaded-end-related results are presented and compared within this study. Application of the pulling force was displacement-controlled with a constant speed of 10 mm/min, which was greater than the suggestion from the reference standard (1.3 mm/min), because of the difficulty in triggering quantifiable slip at lower rates. The load was released after a slip of at least 20 mm had been measured for CFRP bars or the bonded bar was entirely pulled out of the concrete substrate for GFRP bars.

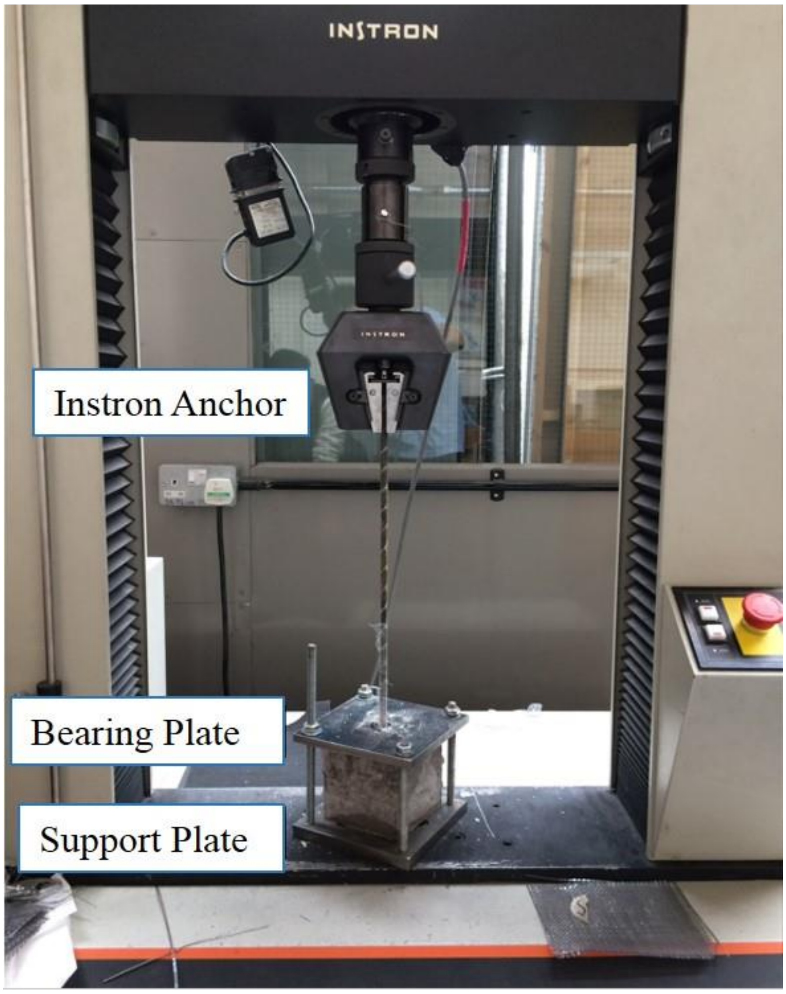

Figure 3.11 Setup for the FRP bar pull-out test with the Instron test machine

3.8.2 CFRP Multi-Strand Tension Test

One tension test was designed to judge the tensile strength of the selected CFRP strands. The American code ASTM D7565/D7565M-10 (ASTM International, 2017) describes a method for determining the tensile properties of FRP composites with both unidirectional and cross-ply pre-impregnated reinforcing fibres. However, this code is suggested as only suitable for FRP materials in the form of the laminate. For this tension test, this standard was still partially referenced regarding the loading applying rate and result calculation.

The electromechanical Instron test machine with a maximum load capacity of 250 kN was used to carry out this tension test. Considering the relatively high tensile strength of the specimen claimed by its supplier, the CFRP strands 1000 mm in length were firstly divided into four sub-portions lengthwise by separating the filaments manually. Each divided portion was also weighed to ensure they had approximately the same fibre content so that the prepared CFRP strands could be theoretically regarded as identical specimens. To apply the prepared strands, two M16 steel lifting eye-bolts were used as adaptors with one screwed to the Instron machine’s base and the other to the clamp attachment. During the test, the four portions of prepared strands were connected to the Instron by knotting them on the two eye bolts (Figure 3.12) and each one was pulled separately at a constant speed of 1 mm/min. The tensile force was released after the strand failed or an elongation of at least 20 mm had been measured. Prior to the test, the distance between the two eye-bolts was also measured when the strands were fastened and ready for being tested.

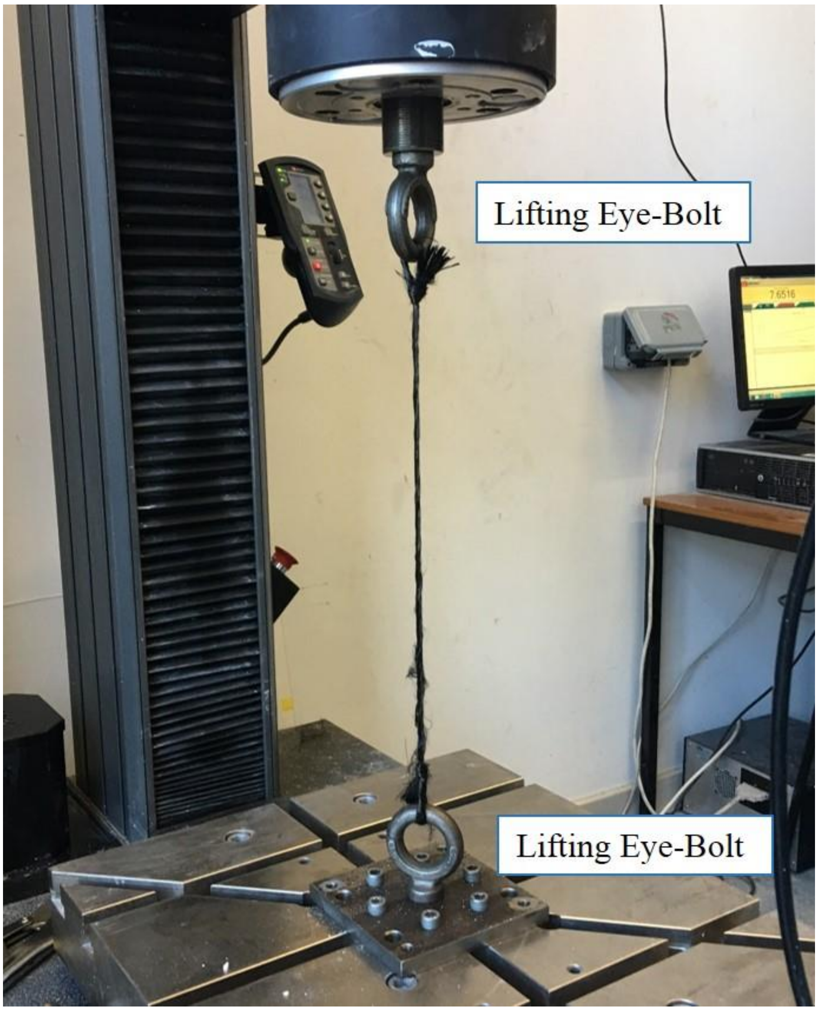

Figure 3.12 Setup for the CFRP strand tension test with the Instron test machine

3.8.3 X-Ray Fluorescence Test (Cl and SO_3)

The X-Ray Fluorescence (XRF) technique was used to determine the Cl and SO_3 content of the concrete matrix for the FRP pull-out test. The XRF is the emission of characteristic fluorescent X-rays from a material that has been excited by being bombarded with high-energy X-rays or gamma rays. The XRF spectrometer detects major elements in material for the reason that the behaviour of atoms is different when they interact with radiation (Wirth, 2019). Concrete samples with the addition of salt or gypsum were collected from the concrete holding cubes after completing the pull-out test. To collect and prepare the powder samples that could be applied in the XRF analyser, the concrete specimens were first split and opened with a hydro-splitter and hammered at the two split faces to produce sufficient small pieces from the centre of the concrete cubes to which area the embedded FRP bars were bonded. These small concrete pieces were then crushed and ground with a pestle and a mortar by hand into fine powders that were suitable for XFR spectroscopy. The powders were then collected and used for sampling (Figure 3.13). The XRF analyser machine is a Zetium® PANalytical equipment. Calculation and expression of results and analysis followed suggestions from standard BS EN 196-2 (2013).

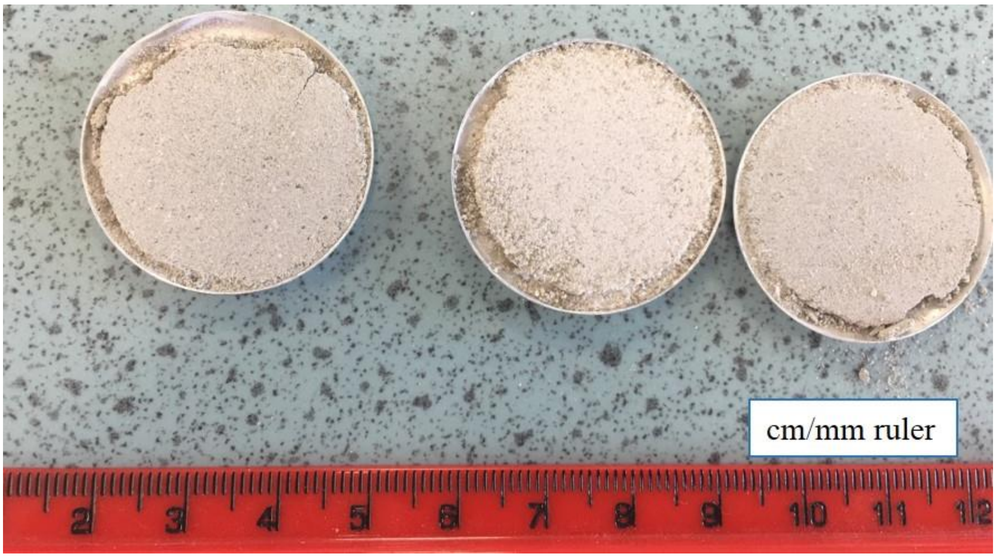

Figure 3.13 Collection and preparation of concrete powder materials for the XRF test

3.8.4 Three-Point Bending Test

The three-point bending test was only used for FRP-reinforced beams 500 mm in length and without transverse or secondary reinforcement. This test was arranged to examine the FRP bars' response to shear stress considering that FRPs are anisotropic. Mix II-1, 2 and 3 (Table 3.7) were used for preparing the test specimens. The specimen details and test setup are shown in Figure 3.14 and Figure 3.15 respectively. These prisms had two FRP bars longitudinally but without shear reinforcement. The beams had a span/depth ratio of 2.1 to ensure that the shear type failure could occur. The manually controlled AVERY machine was used for applying the load at a load-controlled speed while dial gauges were used to measure the beam's midspan deflection. The development length of these GFRP bars is not provided by their manufacture and it is taken as 100 mm and 40 mm both ends under the three-point and four-point (Figure 3.16) bending respectively, where relevant.

ACI 440.3R-04 stated that the development length of FRP bars, l_{bf}, can be expressed as a function of the bar diameter, the concrete strength and the bar design tensile strength with a constant for a particular type of FRP bar. This constant is dependent on the physical properties of the bar and needs to be decided specially via tests. Alternatively, ACI 440 also provided a conservative design estimate, assuming that the dependency of l_{bf} on the bar diameter is linear:

$$l_{bf} = \frac{1}{18.5} b_f f_f \qquad \text{Equation 3.1}$$

where b_f is the FRP bar diameter.

According to Equation 3.1, these straight FRP bars need a development length of around 330 mm (nearly $42b_f$) conservatively. Therefore, these beams with longitudinal FRP bars will have insufficient anchorage theoretically, which is worth being noted for analysis.

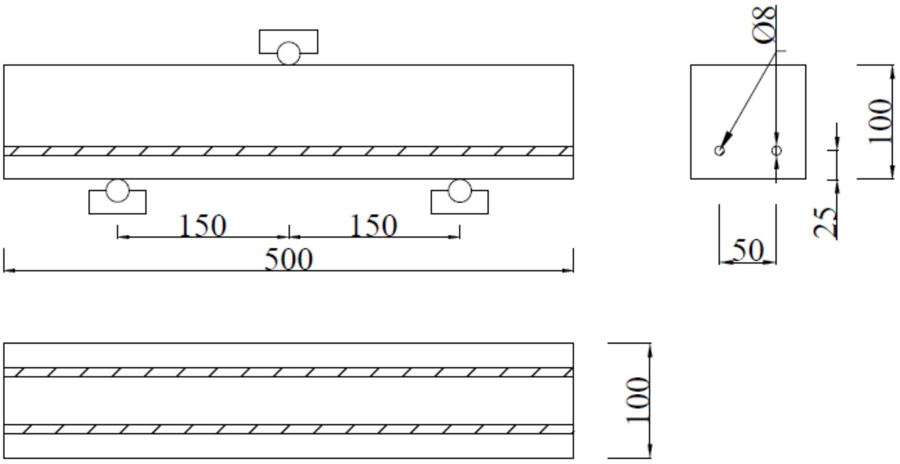

Figure 3.14 Geometric and reinforcement details of the test specimen

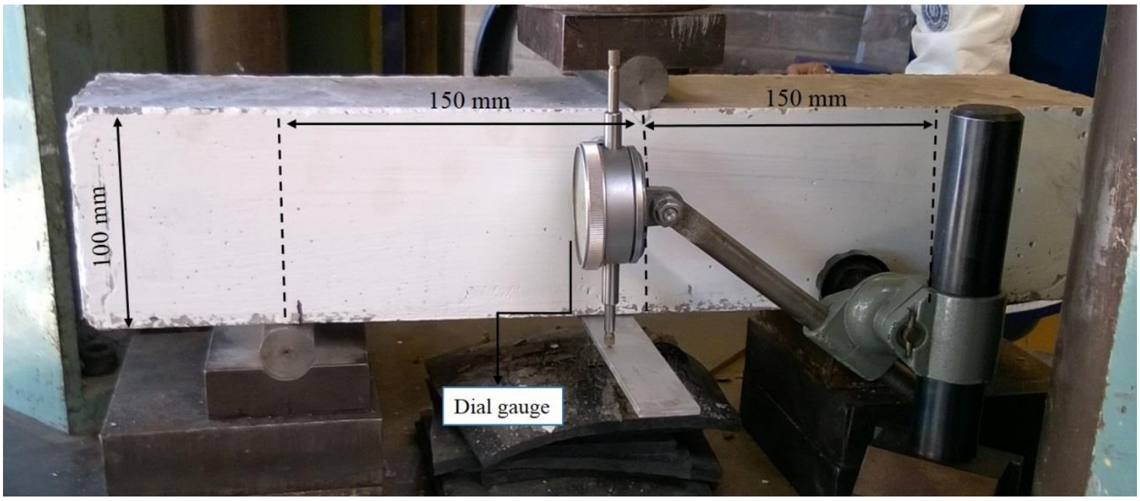

Figure 3.15 Test set up of the three-point bending test with the AVERY machine

3.9 Test Methods: Phase II

3.9.1 Four-Point Bending Test

The four-point bending test was used for most of the beam specimens that required the flexural bending test, which specifically included beams reinforced with FRP bars, beams strengthened with CFRP strands, beams with joint, the fibrous beams and the PT beams with GFRP. Test method of the four-point bending was generally the same on the various specimens. This section only covers descriptions of the concrete specimens reinforced with FRP bars whereas additional details of other aforementioned beams are explained under their categories in the following sections. The four-point bending test was carried out using the Instron machine for all beam specimens in Phase II except the PT beams (they were with the AVERY machine as the dial gauges were easier to install). Applying of load via the Instron machine was all displacement-controlled with a constant rate of 1 mm/min. Load and deflection were automatically measured and recorded by the Instron machine that connected to a programmed computer system.

The FRP-reinforced beams had 2 GFRP bars 8 mm in diameter longitudinally for flexure and internal CFRP bar ‘sticks’ or externally wrapped CFRP strands transversely for shear. The sticks were tied on to the longitudinal bars with plastic ties while the CFRP strands were bonded to the beam surfaces with the epoxy resin adhesive. The CFRP strands were wrapped on all four sides of the beam, defined as a ‘fully-wrapped’ type, with overlapping on the top side to assist anchoring of the wrapping. These FRPs were designed to provide shear resistance and to enable flexural failure. Geometric and reinforcement details of the 2 types of FRP RC beams are presented in Figure 3.16 while test setup of the four-point bending test is shown in Figure 3.17.

GFRP RC with CFRP 'sticks' for shear

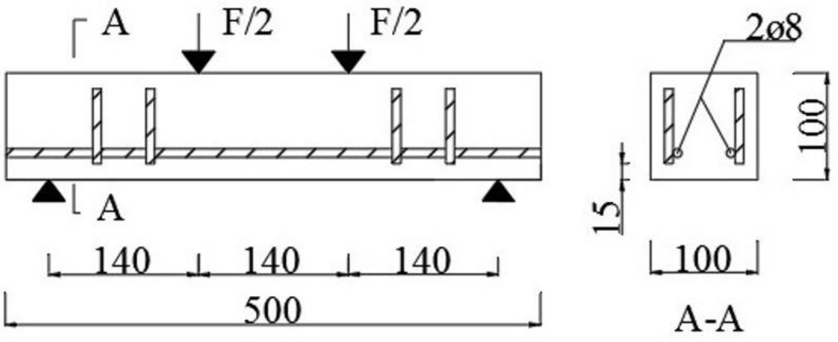

GFRP RC with CFRP strands for shear

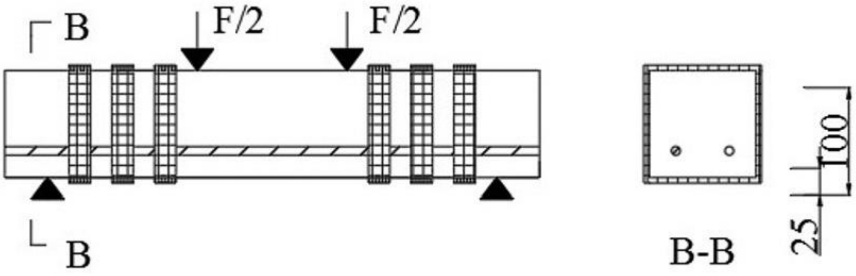

Figure 3.16 Geometric and reinforcement details of the beams reinforced with FRP

Figure 3.17 Test setup of the four-point bending test with the Instron machine

3.9.2 Flat Face-to-Face Joint and Marine Exposures

The joint was fabricated by jointing two 500×100×100 mm beams together face to face with the epoxy resin adhesive approximately 3 mm in layer thickness. Therefore, that was a flat face-to-face type of joint. After applying the epoxy resin on the ends, the two sub-beams to be jointed were kept standing vertically so that the adhering materials could be cured evenly and parallel to the two connecting end sides by the force of gravity and might reduce the air voids within the adhering material. The jointed beams were around 1000 mm in length and strengthened with only external CFRP strands. Applying of the CFRP strands was arranged 24 hours after grouting of the joint. Based on their wrapping conditions, the 9 jointed beams could be divided into 3 groups: under-reinforced (CC2.1), balanced (CC2.2) and over-reinforced (CC2.3). Strengthening details of the three groups are schematically shown in Figure 3.18.

The jointed and reinforced beams were cured in three different exposure conditions, namely, in air, fresh water and cyclic wetting/drying simulated seawater, for a duration of 90 days. Each exposure had three beam specimens with one from each reinforcing condition. The beams cured in air were wrapped with PVC film to reduce their drying shrinkage. The cyclic wetting/drying curing process involved a wetting process by fully immersing the beams into an artificial seawater (i.e. 1 mol/l NaCl solution) for 6 hours and a drying process by pumping the seawater out from the exposure tank and leaving the specimens drying naturally in air for 18 hours (Figure 3.19), and repeated for 90 cycles. When ready, the exposed beams were subjected to the four-point bending test using the Instron machine with a maximum loading capacity of 250 kN (Figure 3.20).

(a) CC2.1 Beams

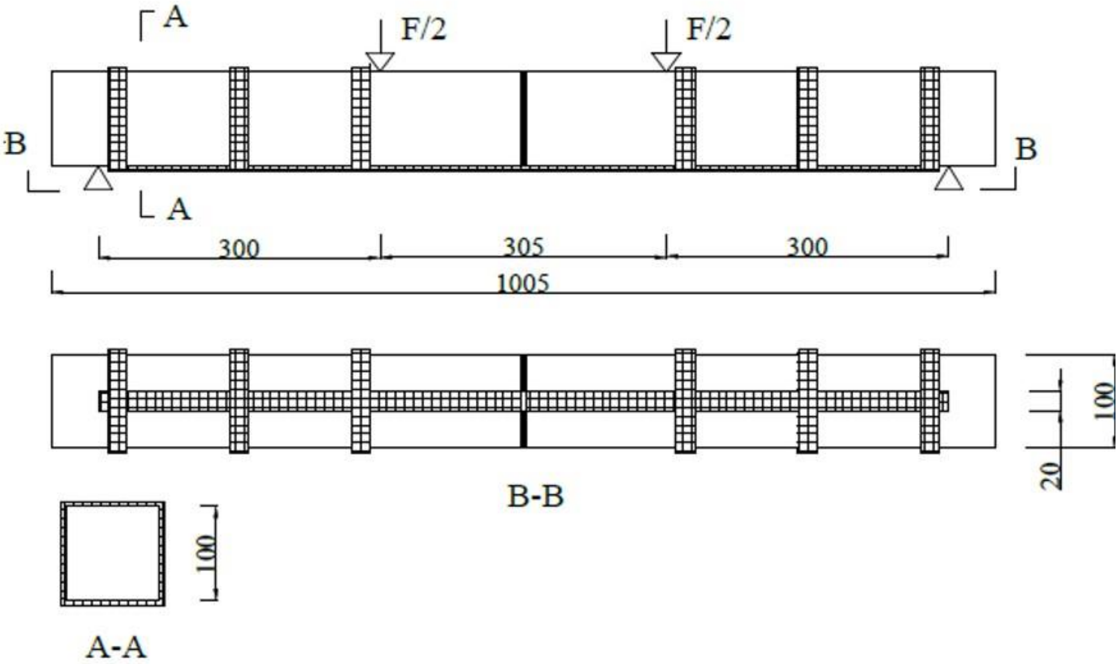

(b) CC2.2 Beams

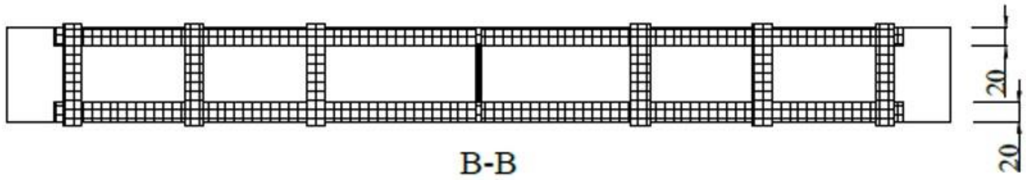

(c) CC2.3 Beams

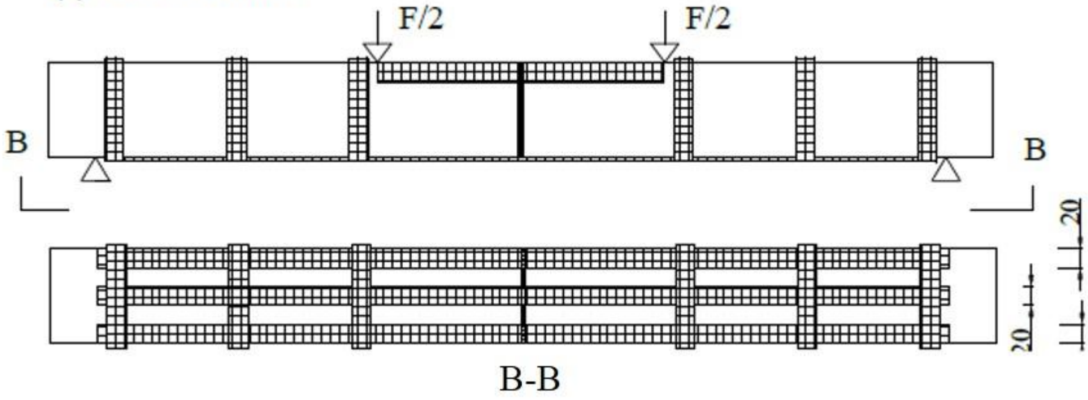

Figure 3.18 Geometric and strengthening details of the CFRP beams with the joint

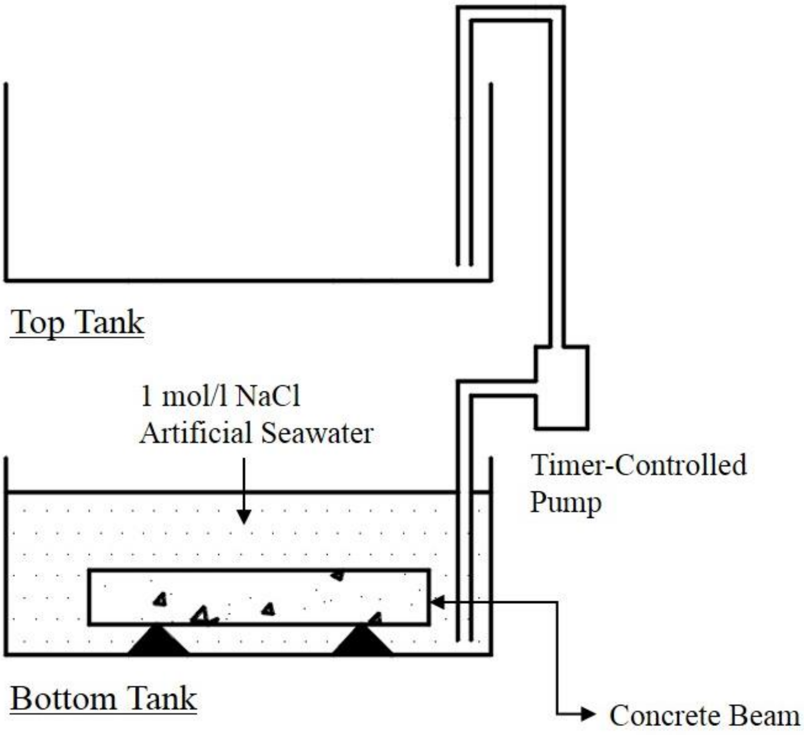

Figure 3.19 Schematic arrangement of the cyclic wetting/drying exposure with artificial seawater

Figure 3.20 Test setup of the jointed CFRP beam specimen

3.9.3 Macro-Synthetic Fibre Reinforced Beams

The mix for macro-synthetic fibre reinforced beams had an addition of macro-synthetic fibres 20 kg/m^3 in dosage and the fibrous beams were strengthened with only external CFRP strands, both longitudinally and transversely (Figure 3.21). These beams could be regarded as under-reinforced according to the computation and classification method of reinforcing conditions by standard ACI 440.1R-06 (2006). A set of three beams 1000 mm in length was prepared in total and subjected to the four-point bending test with the Instron machine.

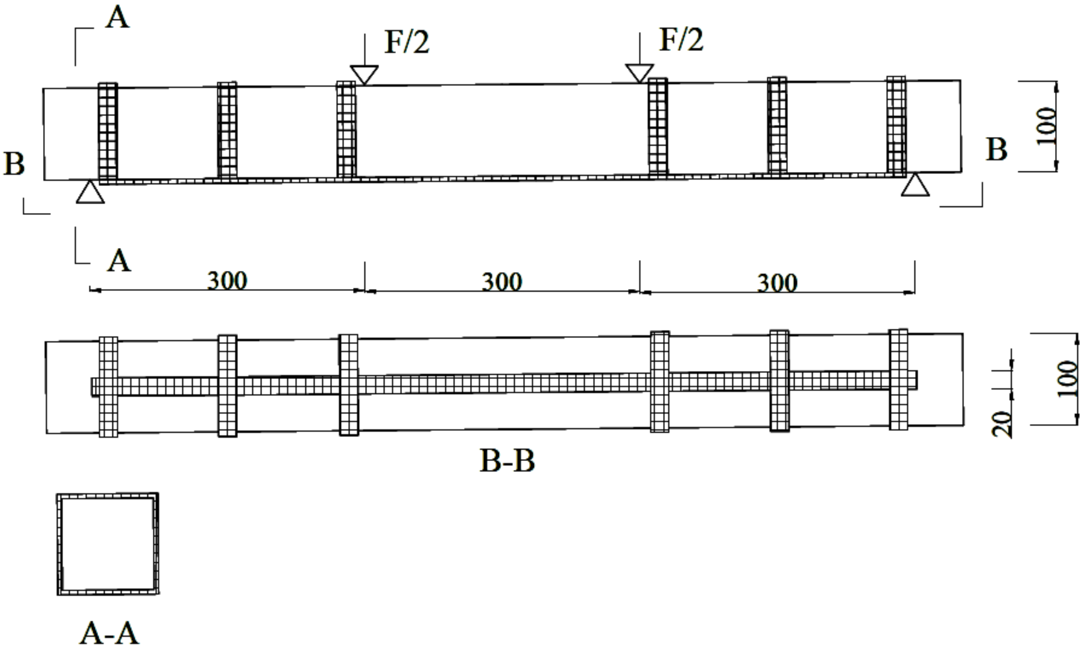

Figure 3.21 Geometric and reinforcement details of the synthetic fibrous beams

3.9.4 Aligned Steel Fibre Reinforced Beams

A total of 4 different types of beams reinforced with aligned steel fibres were prepared and subjected to the four-point bending test with the Instron machine. Categorisation of these beams according to their fibre dosage and shear reinforcement conditions are given in Table 3.10 while the fibre distribution by manual alignment is shown in Figure 3.22. It can be seen that not all fibres were settled in the longitudinal direction. The space between every two layers of aligned steel fibres below the nominal neutral axis was kept between

15-20 mm and 25 mm above the nominal neutral axis approximately. In the shear spans, SF2 beam had ‘fully-wrapped’ CFRP multi-strands for extra external strengthening while SF1.2 beams had a layer of the steel fibres aligned above the neutral axis at an equivalent quantity of 15-18 kg/m^3 per shear span. A comparison beam was also cast with steel fibres in 3 layers but randomly distributed to investigate the influence of the alignment.

Table 3.10 Details of the beam specimens with aligned steel fibres

Type	Mix	Number of		Dosage[b],	Shear Reinforcement	
		Beams	Fibre Layer [a]	kg/m^3	CFRP Strands	Steel Fibres
SF1.1	IV	1	2	80	-	-
SF1.2		2	3	120	-	✓
SF1.3		3	4	160	-	-
SF2		1	2	80	✓	-
SF3	VI	1	3	120[c]	-	-
SF4		3	3	120	-	-
SF5	VII	3	3	120	-	-

[a]: in tensile zone only; [b]: exclude the fibres for shear if present; [c]: not aligned but in layers.

Figure 3.22 Alignment of the steel fibres as a layer in the casting mould

3.9.5 Computed Tomography Scan of CFRP Bond and Fibre Alignment

Computed Tomography (CT) scanning was arranged to check the bonding of CFRP and the effectiveness of steel fibre alignment. Cubic specimens 100 mm in dimensions were used for scanning both. The CFRP specimens were saw-cut from the beams strengthened with CFRP strands after the bending test while the fibrous specimens were casting-prepared with two layers of aligned steel fibres. The two layers of steel fibres were placed manually at designated depths without using the gutter due to the mould size difference. The Nikon® XT H225 scanner was used to emit X-rays and generate the 3D tomography images. This scanner could reconstruct a three-dimensional volumetric representation of the tested samples by capturing sequential two-dimensional X-ray images and rotating the samples through 360 degrees. The scanner had a 2000×2000 pixel flat panel director which allowed it to measure samples 400×400 mm maximally in size. For this test, these cube samples were positioned 1130 mm away from the radiation source (Figure 3.23) and were scanned with reconstructed X-ray images 50 μm in resolution (that was the smallest distance distinguishable between adjacent pixels for this test).

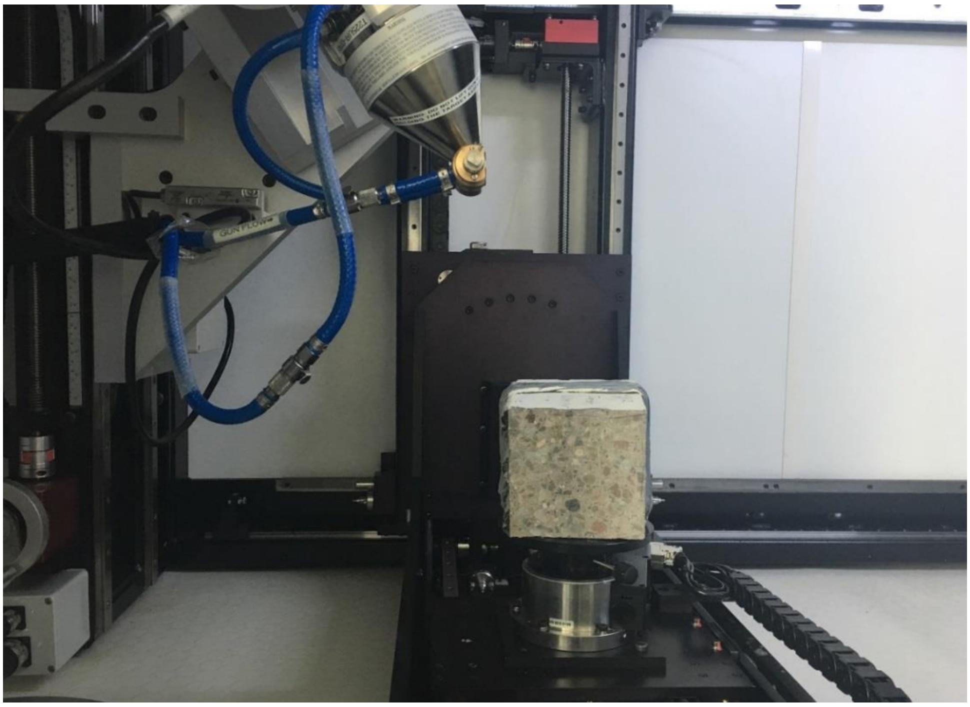

Figure 3.23 Setup of the CFRP representative cubes for CT scanning (before the radiation was turned on)

3.9.6 Post-Tensioning Trial of GFRP Rebar

Practical standards that give technical advice on post-tensioning FRP bars are with very limited availability although some codes (American Concrete Institution, 2011; Canadian Standards Association, 2007) have been published with descriptions of calculating the stress that can be post-tensioned to the FRP bars. Standard CSA S806-02 (2007) states that pre-stressing should not exceed 35% of the design tensile strength of the FRP bars.

To prepare the beams to be post-tensioned, the GFRP bars were wrapped with PVC film to achieve separation between the bars and their surrounding concrete, and allow slippage. The available hydraulic jacks in the laboratories are too small in terms of the diameter to be used to post-tension these GFRP RC specimens. An alternative solution was made by hollowing and threading the outside of the steel bars 16 mm in diameter and using them as anchors together with M16 matching nuts and washers (Figure 3.24). These hollowed anchors had 10 mm inner diameter and were bonded to the GFRP bars at the two end faces of the beams using the epoxy resin adhesive. The M16 nuts were for applying post-tension while the washers were for spreading the stress and preventing the concrete from bursting.

Each hollowed anchoring connector had a length of 50 mm and a thread count of 23; therefore, each thread was approximately 2.17 mm in length. The anchoring nuts were applied tightly against the concrete and marked so that their move might be recorded. As the nuts were hexagonal and every six sides' move would make a full thread revolution of 2.17 mm, each sixth theoretically moved the GFRP bars by approximately 0.36 mm. Therefore, a move of 4/6 of a revolution or four sides would cause the bar to be pulled against the concrete by 1.45 mm and induce a stress of approximately 140 N/mm^2 (20% prestress loss), which was around 30% of the long-term tensile strength of the GFRP bars.

Post-tensioning was trialled 28 days after demoulding and prior to subjecting the beams to the four-point bending test. During the PT, the first trial with a move of 6 nut sides caused the GFRP bar to snap (Figure 3.25) possibly because of high stress concentration upon the connecting area as well as the anisotropy of the GFRP composite. Therefore, for further specimens, the nut was only turned by 3 sides rather than 4 at each end. A cracking sound was heard while applying the tension, which was speculated to be fracturing of the GFRP. Considering the failure to accomplish post-tensioning GFRP bars, the hypothesis was advanced that the designed separation was insufficient and ineffective, i.e. wrapping the GFRP bars with only PVC film for PT could result in stress concentration to the GFRP bars. The GFRP material, as an anisotropic material, was also sensitive to such stress that was different from its fibre reinforcing direction. Albeit relatively unsuccessful, the post-tensioning forces were still calculated from the moves of the anchoring nuts. After the PT trial, these beams were subject to the four-point bending test with the AVERY machine (Figure 3.25).

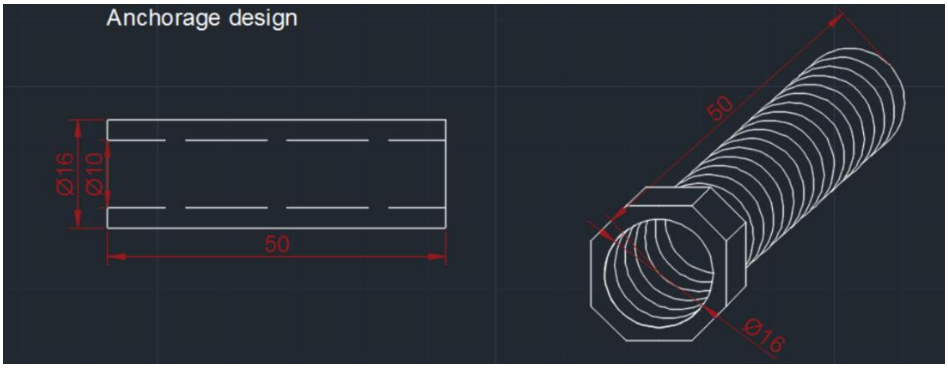

Figure 3.24 Design of the steel anchor for post-tensioning GFRP bars

Figure 3.25 Snap of the GFRP bar after post-tensioning

3.10 Test Methods: Phase III

3.10.1 Design and Production of Prototype

Design and production of the WEC prototype covered subjects including determining the form and scale of the prototype, manufacturing and reinforcing methods as well as details of the dowel connector arrangement between assembly segments.

Considering that techniques of fabricating a large-scale water-proof skin with materials such as GRP for floating structures are already available (Wave Energy Scotland, 2017), the structure of the prototype was decided as a circular truss type rather than a shell-tube type. Fundamental analysis and comparison of the truss structure were first carried out between a Vierendeel truss and a Pratt truss (Figure 3.26). The Vierendeel truss was designed to have 5 hoop sections and 6 longitudinal sections while the Pratt truss also had 5 hoop rings but 6 helix sections in order to avoid potential shear failures of the straight longitudinal members. Numerical modelling of these 2 forms of truss was arranged using the ABAQUS® software based on the four-point bending test to pre-decide their stress and strain distribution as well as to predict possible failure types. According to the finite element analysis (FEA) results (Figure 3.28), the longitudinal members of the Vierendeel truss will be exposed to high levels of shear stress under the bending, which potentially can cause the structure to fail in shear during the test. However, fabrication of the helix sections of the Pratt truss will be highly dependent on 3D printing because of their curved complex shape. Communications were liaised with Loughborough University but, due to the relatively large amount of work to build a large-scale prototype as well as the limited timeline of this project, the Pratt truss was finally shortlisted as a backup option. Another alternative design was the modified Wembley-Arch-style Pratt truss with four pairs of rectangular longitudinal members in the form of the V-knot (Figure 3.27), in which case stress may be transferred similarly as for the Pratt truss.

The truss dimensions were initially selected to be 4000 mm in length and 725 mm in outer diameter, which was approximately 1.5 times larger than Khosravi's (2017) Pelamis-type prototype. However, after consulting specialists in structural engineering (Quoceant Ltd.) and precasting (Plean Precast Ltd.), manufacture of the V-knot segments for the modified

Wembley-Arch style Pratt truss appeared to demand relatively complex requirements in preparing the formwork to produce the V-end part where the segment was also designed to be connected to the hoops with dowel connectors. Eventually, design of the truss was finalised as shown in Figure 3.29 schematically while AUTOCAD® drawings of the truss structure, the components (hoop rings and longitudinal sections) and arrangement of the reinforcement and dowel connectors are shown in Figure 3.30, 3.31 and 3.32.

Reinforcing of the truss was initially designed to use UHMWPE ropes lengthwise through the longitudinal beams. However, due to the difficulties in acquiring UHMWPE products from the overseas supplier as well as the timeline of this research project, Ø5 mm carbon steel tendons were selected as the tensile reinforcement for initial assembly.

Considering that the overall weight of the truss was preferred to be under 1000 kg so that assembling and testing of the prototype could be relatively easily handled in the lab, the number of the rings was reduced from the initially designed 5 to 3 and the load applying method was changed from the four-point to the three-point bending. To avoid potential shear failure occurring in the longitudinal beams under the bending test, each section was extended to 1500 mm in length with a cross-sectional area of 130×150 mm (Figure 3.31). As shown in Figure 3.32, the 3 hoop rings were designed to be 920 mm in outer diameter and 650 mm in inner diameter with a rectangular cross-section of 150×150 mm.

Casting of the designed components was carried out commercially by Plean Precast Ltd. using C40 concrete. The prototype components were precast (Figure 3.33 and 3.34) in 3 batches. After the 7-day initial curing on the precast site, all components were transported to the laboratories of the University of Dundee for assembly and testing.

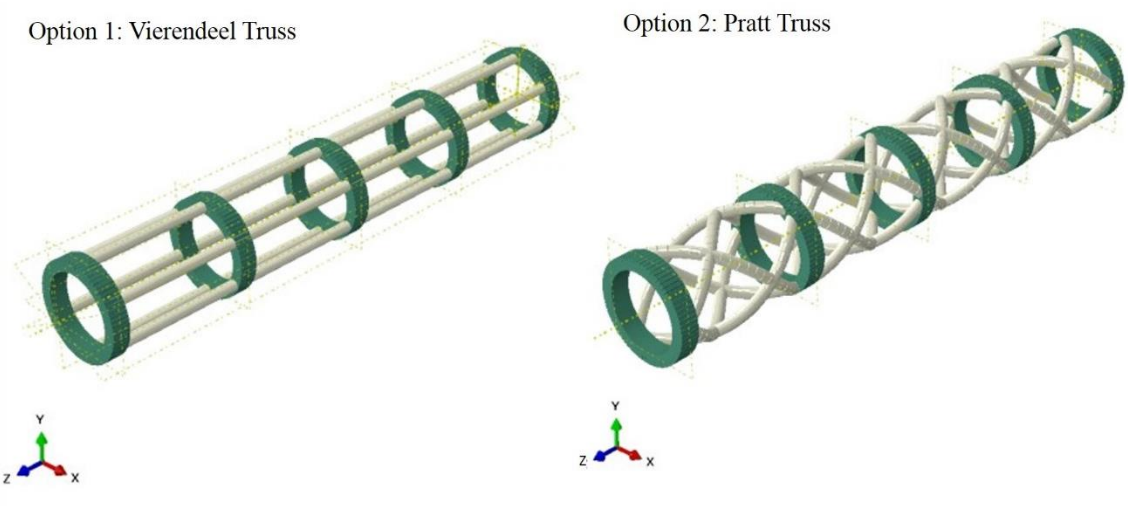

Figure 3.26 Design of the prototype structure: the Vierendeel truss (left) and the Pratt truss (right)

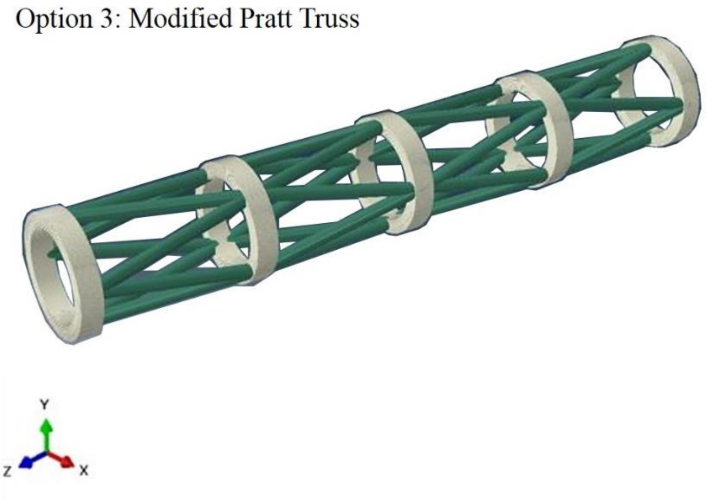

Figure 3.27 Design of the prototype structure: the modified Wembley-Arch style Pratt truss

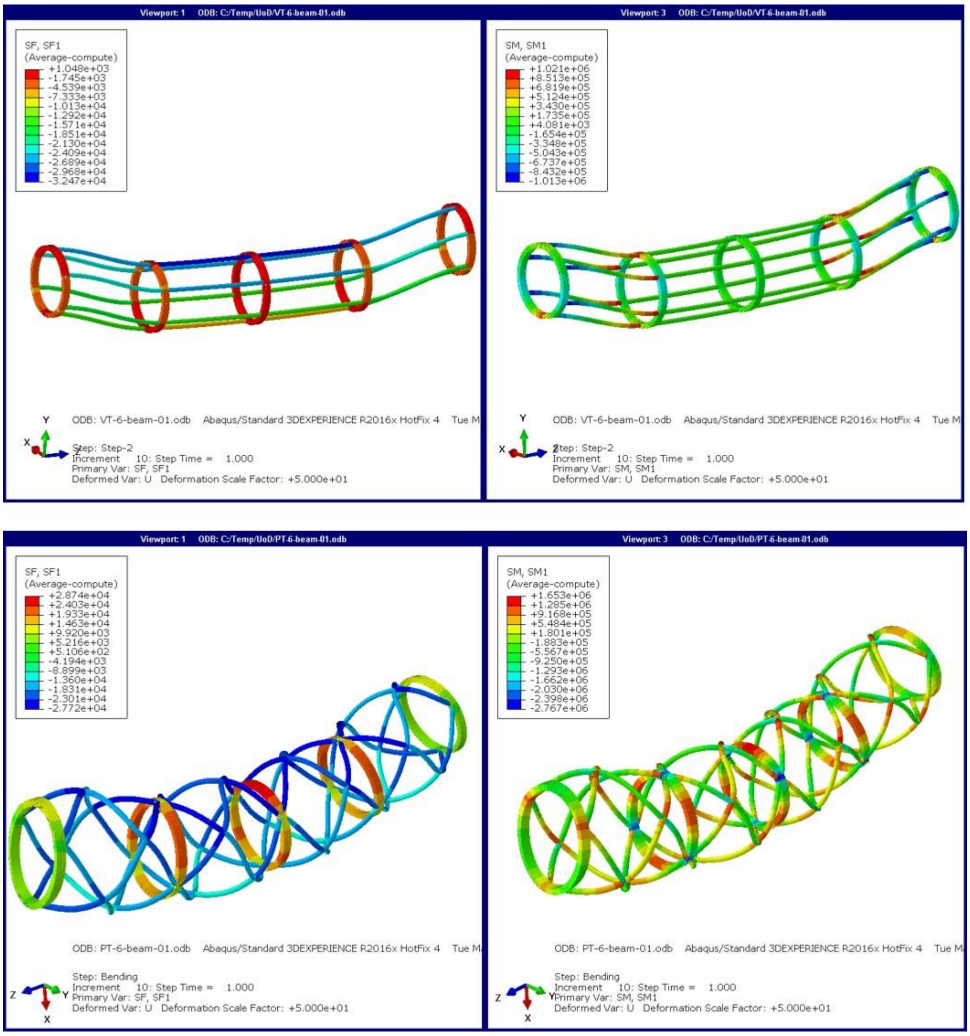

```
Viewport: 1     ODB: C:/Temp/UoD/VT-6-beam-01.odb
SF, SF1
(Average-compute)
 +1.048e+03
 -1.745e+03
 -4.539e+03
 -7.333e+03
 -1.013e+04
 -1.292e+04
 -1.571e+04
 -1.851e+04
 -2.130e+04
 -2.409e+04
 -2.689e+04
 -2.968e+04
 -3.247e+04
ODB: VT-6-beam-01.odb    Abaqus/Standard 3DEXPERIENCE R2016x HotFix 4    Tue M
Step: Step-2
Increment     10: Step Time =    1.000
Primary Var: SF, SF1
Deformed Var: U   Deformation Scale Factor: +5.000e+01
```

```
Viewport: 3     ODB: C:/Temp/UoD/VT-6-beam-01.odb
SM, SM1
(Average-compute)
 +1.021e+06
 +8.513e+05
 +6.819e+05
 +5.124e+05
 +3.430e+05
 +1.735e+05
 +4.081e+03
 -1.654e+05
 -3.348e+05
 -5.043e+05
 -6.737e+05
 -8.432e+05
 -1.013e+06
ODB: VT-6-beam-01.odb    Abaqus/Standard 3DEXPERIENCE R2016x HotFix 4    Tue M
Step: Step-2
Increment     10: Step Time =    1.000
Primary Var: SM, SM1
Deformed Var: U   Deformation Scale Factor: +5.000e+01
```

```
Viewport: 1     ODB: C:/Temp/UoD/PT-6-beam-01.odb
SF, SF1
(Average-compute)
 +2.874e+04
 +2.403e+04
 +1.933e+04
 +1.463e+04
 +9.920e+03
 +5.216e+03
 +5.106e+02
 -4.194e+03
 -8.899e+03
 -1.360e+04
 -1.831e+04
 -2.301e+04
 -2.772e+04
ODB: PT-6-beam-01.odb    Abaqus/Standard 3DEXPERIENCE R2016x HotFix 4    Tue M
Step: Bending
Increment     10: Step Time =    1.000
Primary Var: SF, SF1
Deformed Var: U   Deformation Scale Factor: +5.000e+01
```

```
Viewport: 3     ODB: C:/Temp/UoD/PT-6-beam-01.odb
SM, SM1
(Average-compute)
 +1.653e+06
 +1.285e+06
 +9.168e+05
 +5.484e+05
 +1.801e+05
 -1.883e+05
 -5.567e+05
 -9.250e+05
 -1.293e+06
 -1.662e+06
 -2.030e+06
 -2.398e+06
 -2.767e+06
ODB: PT-6-beam-01.odb    Abaqus/Standard 3DEXPERIENCE R2016x HotFix 4    Tue M
Step: Bending
Increment     10: Step Time =    1.000
Primary Var: SM, SM1
Deformed Var: U   Deformation Scale Factor: +5.000e+01
```

(SF:Section force component in *N*; SM: Section bending moment in *N•m*)

Figure 3.28 Numerical modelling (by J. Benzie from Quoceant Ltd.) outputs of the truss load distribution under the four-point bending

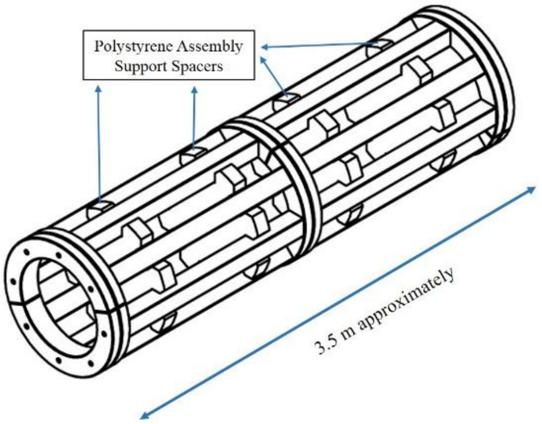

Figure 3.29 Finalised design of the WEC prototype in a Vierendeel type with shear keys

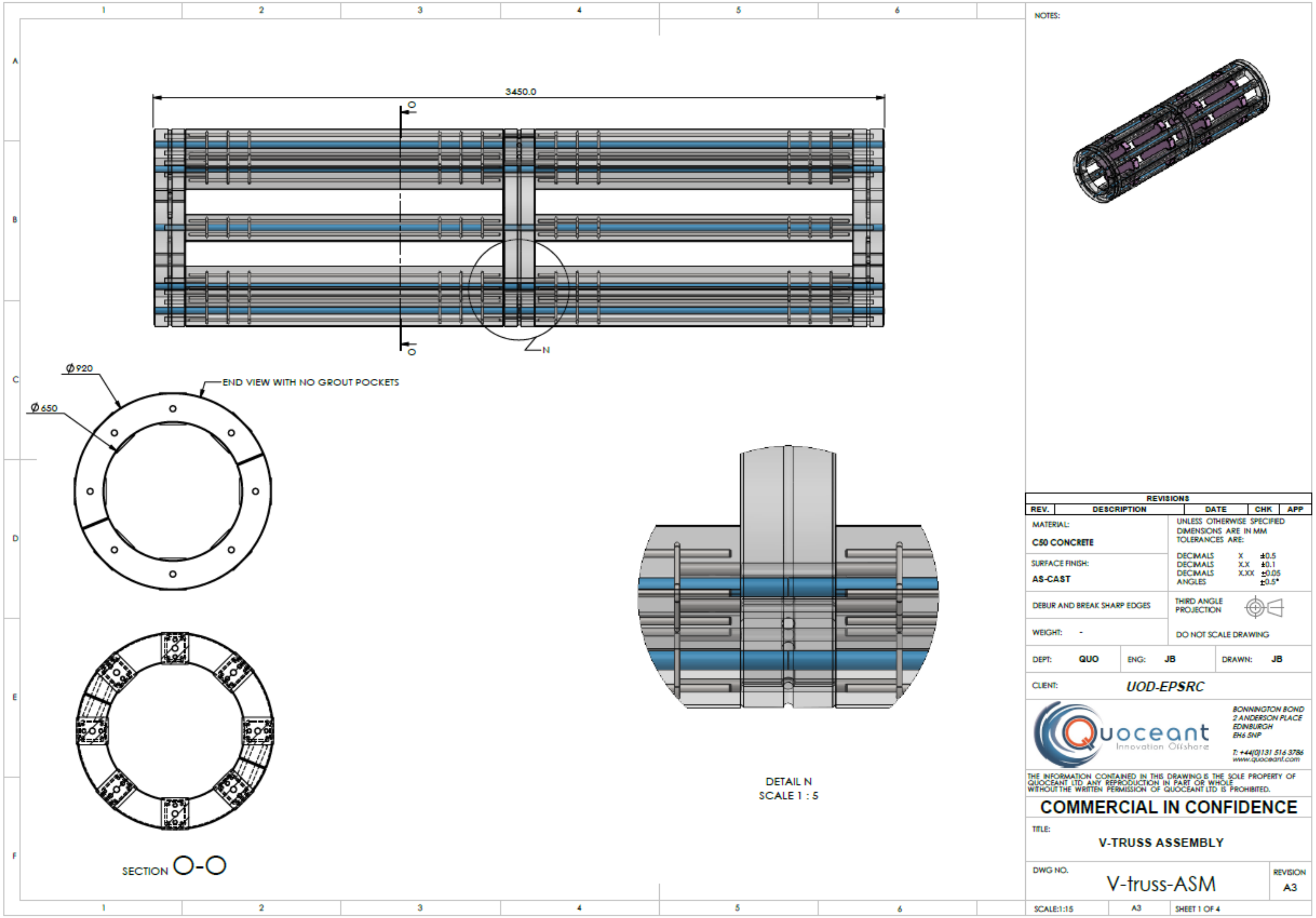

Figure 3.30 AUTOCAD® drawing (by J. Benzie from Quoceant Ltd.) of the designed prototype structure

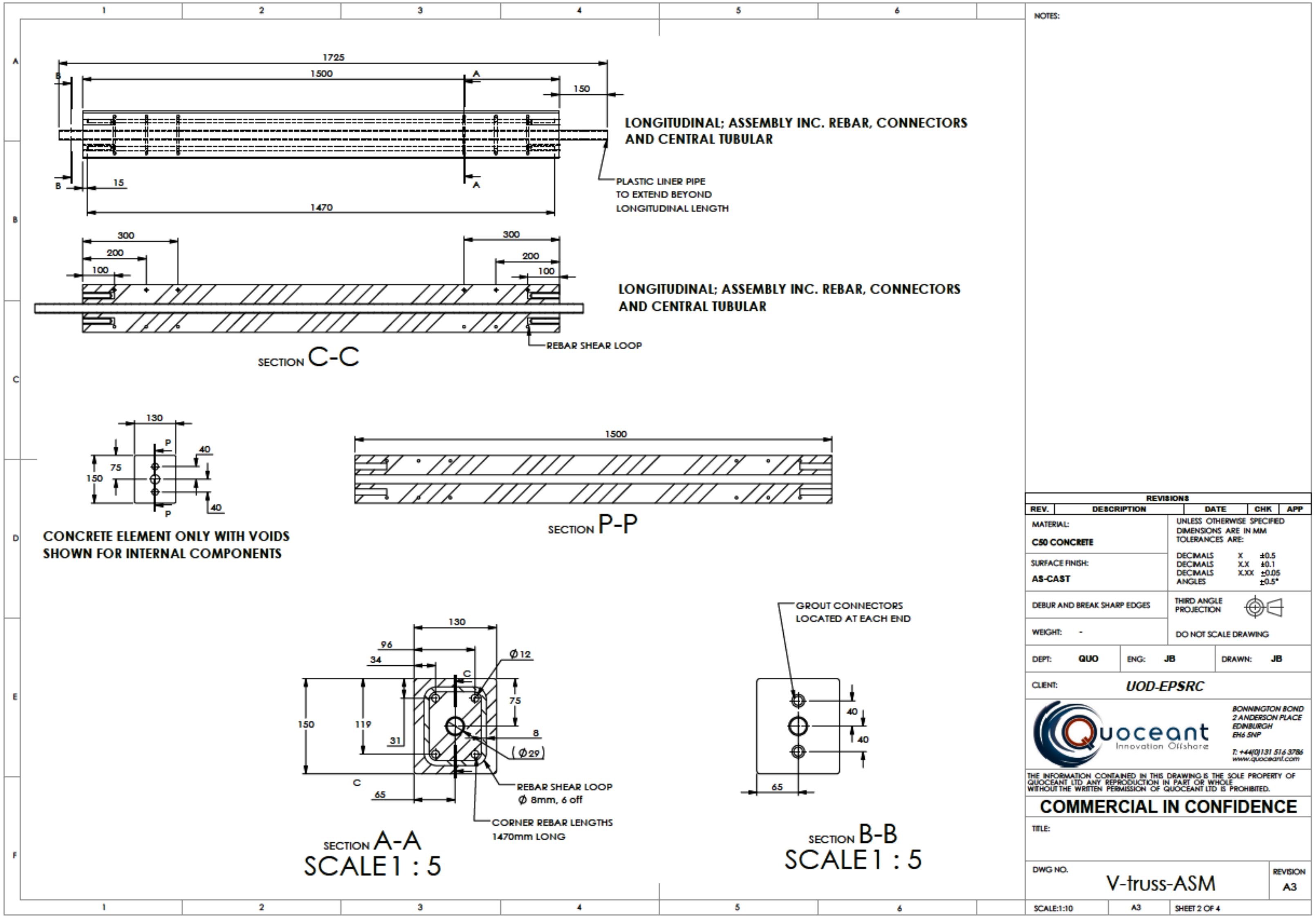

Figure 3.31 AUTOCAD® drawing (by J. Benzie from Quoceant Ltd.) of the longitudinal component for the prototype

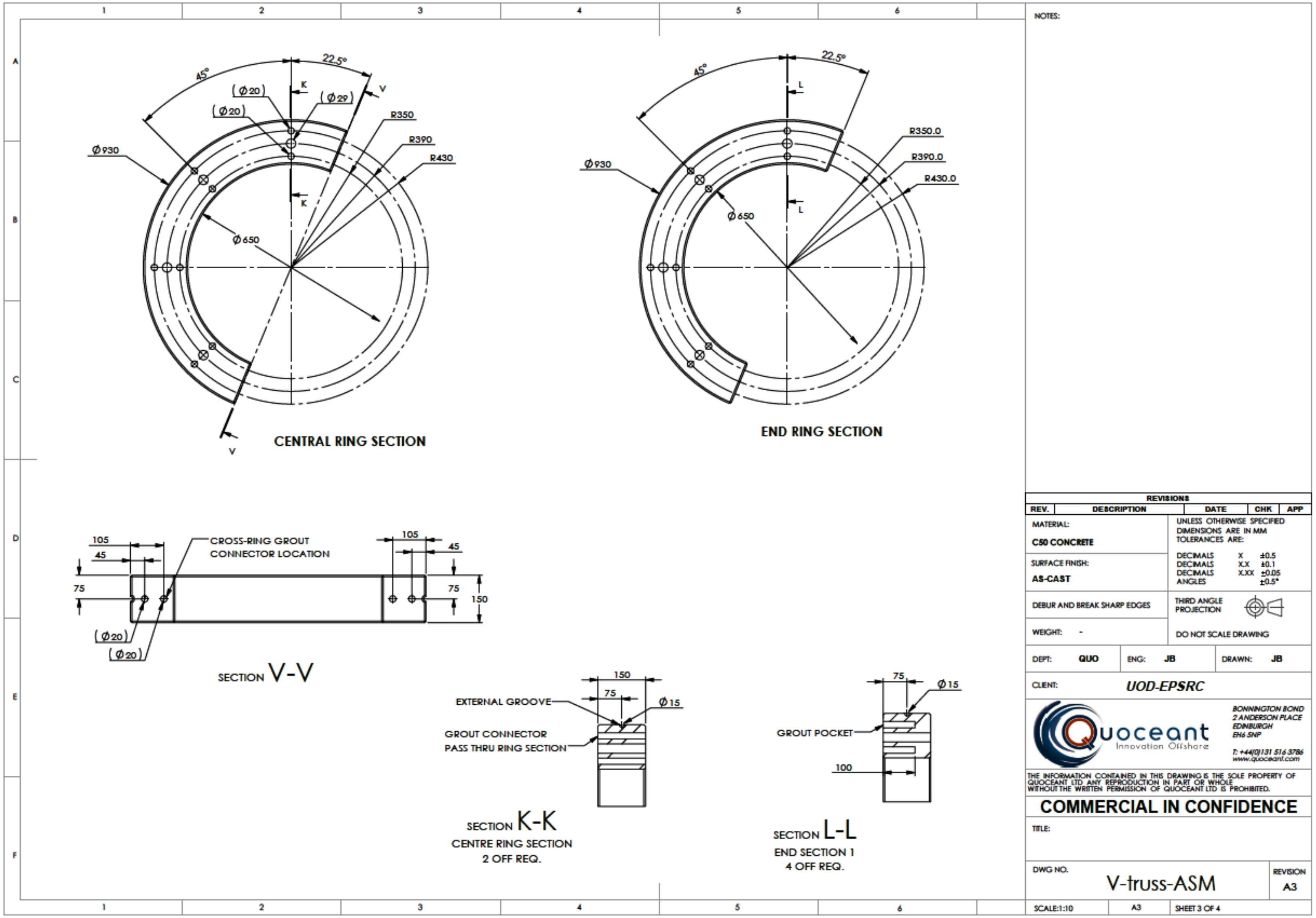

Figure 3.32 AUTOCAD® drawing (by J. Benzie from Quoceant Ltd.) of the hoop component for the prototype

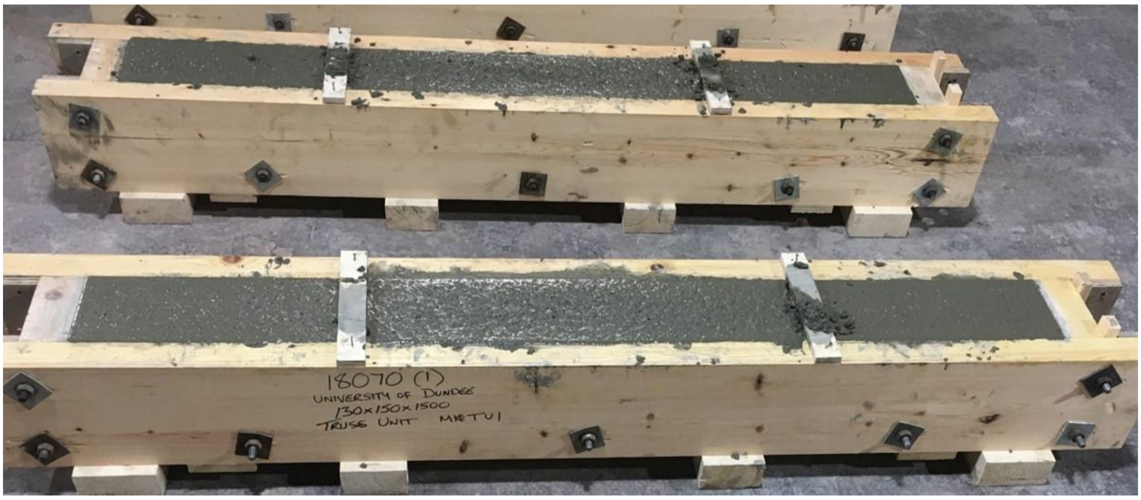

Figure 3.33 Precast of the longitudinal components in Plean Precast Ltd.

Figure 3.34 One half ring component after demoulding in Plean Precast Ltd.

3.10.2 Proof of Concept with Additive Manufacturing

Additive manufacturing (AM) was arranged to prove the idea of repetitively 3D printing concrete elements suitable for being assembled and post-tensioned for a WEC structure. A beam 1500 mm in length and 150×130 mm in cross-section was manufactured without any reinforcement in the 3D printing laboratory of Loughborough University. The beam was arranged to have a 20×10 mm rectangular space longitudinally in the cross-sectional centre (Figure 3.35) for further unbonded post-tensioning. Attempts to align steel fibres between concrete layers during printing were also carried out but it was found less stiff concrete mixes needed to be particularly developed to flow around and properly encase the fibres. Hence, the idea of AM beams with aligned steel fibres was not corroborated. This beam was transported to the University of Dundee afterwards (Figure 3.36) for post-tensioning with UHMWPE ropes as well as testing.

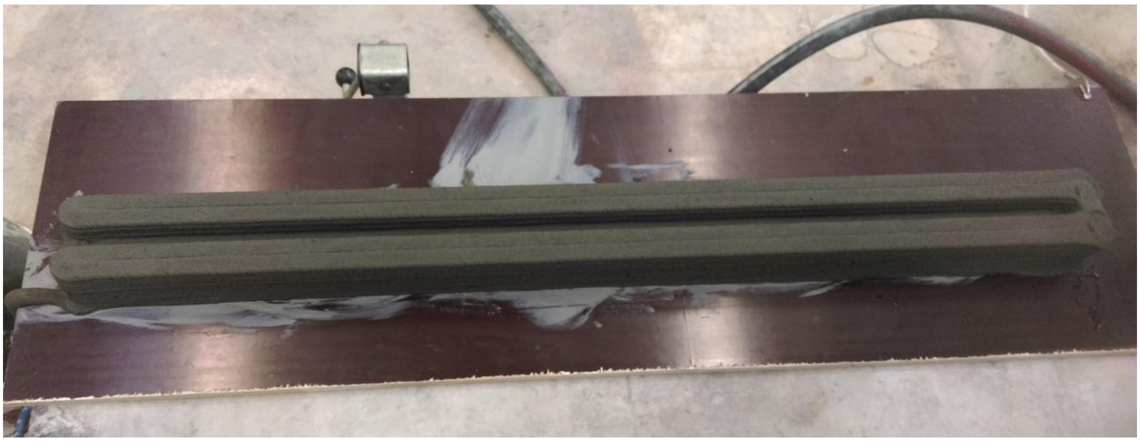

Figure 3.35 3D printing of the beam with space left in advance for novel reinforcement

Figure 3.36 The 3D printed beam arrived at the University of Dundee laboratories

3.11 Summary

Preparation of the specimens discussed in this chapter with their test methods/applications are summarised in Table 3.11. A brief discussion regarding the test arrangement was also given below.

Table 3.11 Summary of specimen preparation and test methods

Specimen Preparation	Test Method/Application
FRP specimens for pull-out	FRP bar pull-out test/FRP bond
CFRP multi-strands	Strand tension test/Material properties
Ground concrete powder	XRF Test/Cl and SO_3 content determination
Beam reinforced/strengthened with FRP	Three- or four-point bending test/Structural behaviour
Post-tensioning of GFRP	Four-point bending test/-
Beam with macro-synthetic fibres	Four-point bending test/Fibre addition
Beam with electromagnet-aligned steel fibres	Failed/-
Beam with manually aligned steel fibres	Four-point bending test/-
Cut concrete cubes	CT scanning/Steel fibre distribution
Design and production of the prototype	-/WEC prototype design and test
AM beam with aligned steel fibres	Not trailed/-
AM beam with pure concrete	Four-point bending/WEC prototype design

The FRP bar pull-out test regarding influence of concrete strength was an inappropriate arrangement. With restricted access to the test machine, all specimens for the FRP pull-out were prepared on one occasion when the CFRP bars (rather than GFRP ones) were expected to have a higher bond strength. Given the failure types of these bars (presented and discussed in Section 4.22), higher strength concrete should have been arranged with the GFRP bars to investigate its influence. However, the designed concrete strength for a WEC prototype would be around 60 MPa. The GFRP bar pull-out test is still informatic.

Chapter 4 Characteristic Properties of FRP Composites

4.1 Introduction

The work in Phase I mainly focuses on determination of the bond and shear response of the GFRP and CFRP bars as well as the tensile strength of the CFRP strands. According to the experimental results, analysis and discussion are carried out covering these aspects. The results from the pull-out test on the designed groups are analysed and compared to additionally estimate possible influences from the concrete strength and sea salt ions. The shear strength of concrete members reinforced with FRP bars is tested using the three-point bending test and compared with those reinforced with steel ones. The designed tension test for the CFRP strands also provides evaluation of the material's strength and rupture properties.

4.2 Bond-to-Concrete of FRP Bars

4.2.1 Bond Behaviour

The bond behaviour, in terms of the bond stress vs. bar end slip, for both GFRP and CFRP bars was obtained. As explained previously in Chapter 2, different mechanisms exist at different stages of the bond system between the reinforcing bar and the concrete substrate. The bond stress vs. bar slip curves for the tested FRP bars (both GFRP and CFRP, using specimens from Section 3.6.1) are illustrated in Figure 4.1. Additionally the average bond stress caused slips at 0.05, 0.10 and 0.25 mm ($\tau_{0.05}$, $\tau_{0.10}$ and $\tau_{0.25}$ respectively) and the maximum bond stress (τ_{max}) and the slip at the maximum bond stress (d_{max}) are calculated and given in Table 4.1. During the phase between when measurable slips can be observed and the maximum bond stress being achieved, bond of the FRP bar is usually governed by combined mechanisms including chemical adhesion, physical friction and mechanical interlocks (Achillides, 1998). The bond behaviour of the FRP bar at this stage can be affected by its surface deformation; hence, the deformation effectiveness of FRP bars can be verified with the pull-out test.

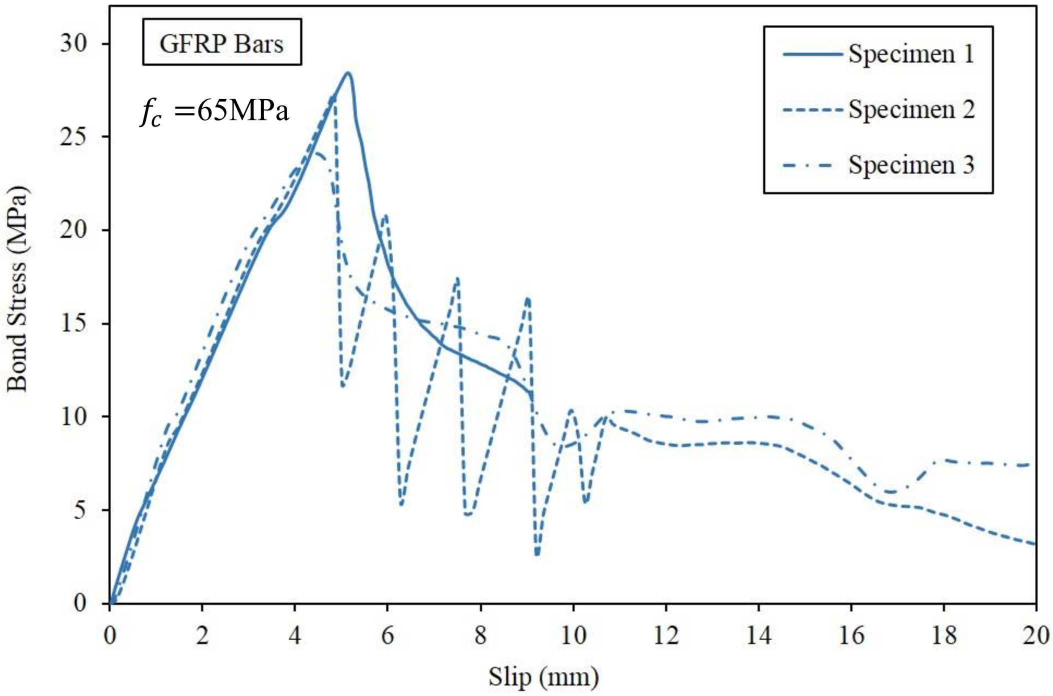

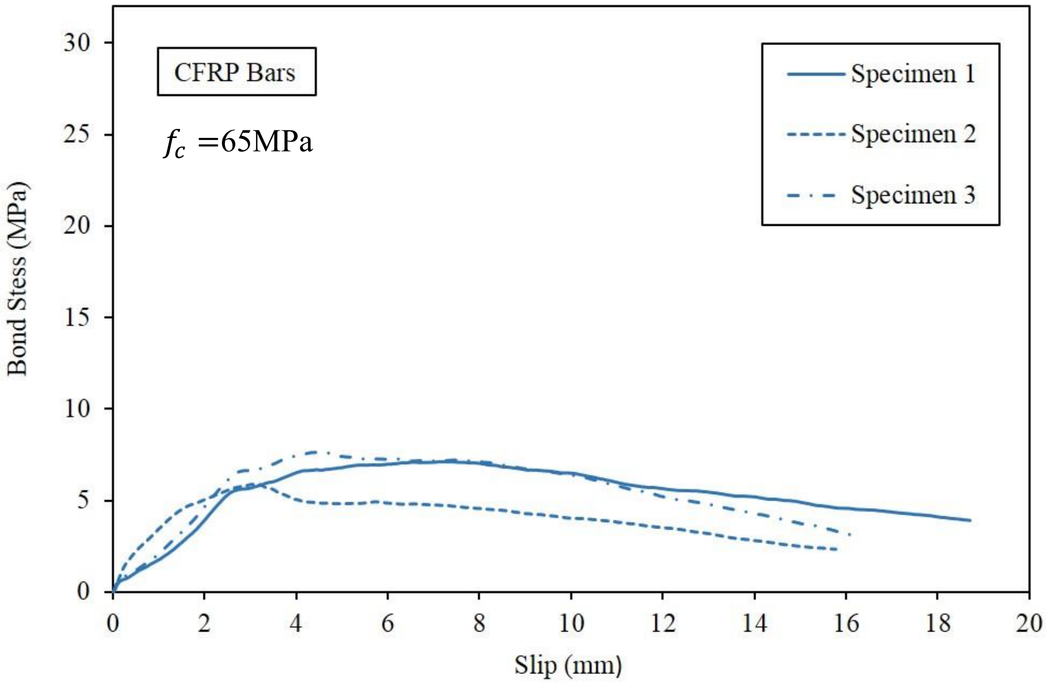

Figure 4.1 Bond-slip curves for GFRP (above) and CFRP (below) bars with 0.45 w/c ratio concrete

Table 4.1 Average bond stress and curve gradients of FRP bars via the pull-out test

Bar Type	Bond Stress, MPa					Slip, mm	Gradient[a]	
	$\tau_{0.05}$	$\tau_{0.10}$	$\tau_{0.25}$	τ_{max}	Residual	d_{max}	k_1	k_2
GFRP	0.2	0.5	1.4	26.8	9.4	4.9	5.5	-9.3
CFRP	0.2	0.5	1.0	6.9	4.1	3.4	2.1	-0.3

[a]: k_1 and k_2 was obtained from the liner part of the stress vs. slip curves before and after the maximum stress respectively.

As seen from the curves in Figure 4.1, the loaded end slipped nearly at the beginning of loading. Prior to measurable slips, there is a phase that the chemical adhesion between the bar and the surrounding concrete is the main mechanism resisting the external load. This bond resistance provided by the adhesion, in the case of conventional steel bars, is assumed to be around 0.5-1.5 MPa (Achillides & Pilakoutas, 2004), which is quite small. However, it is difficult to determine the adhesion accurately because the accuracy of slip measurement at the beginning is affected by many factors such as the local bending of non-perpendicular embedded bars and the clamping tightness. Also, distinguishing slips from the bar elongation at the beginning of the pull-out test can rarely be expected to be accomplished exactly. Therefore, it was decided to disregard the initial period until the adhesion broke for this pull-out test. That was accomplished by subtracting only the bar elongation from the measured displacement. In the calculations of bar elongation, the bars were assumed to elongate linearly under the applied direct tensile stress.

The two types of FRP bars showed very different bond behaviour at both pre-maximum and post-maximum strength stages. The GFRP bars (8 mm in diameter) presented a bond strength almost 4 times greater than the CFRP bars (7.5 mm diameter) while the slip of the GFRP bar at the maximum bond stress was only around 40% higher than that of the CFRP bars. FRP bars with a smaller diameter usually have better adhesion. Hence the bond difference could be because of their surface deformation. The two tested types of FRP bars showed similar bond stress development up until a measured slip of 0.10 mm. After that, the GFPR bars presented much stronger bond resistance with regard to the same slip.

The initial slope of the bond-slip curves for GFRP bars was much stiffer than CFRP bars. This is partially related to the difference of the elastic moduli of the two FRP materials.

However, the CFRP bars, which had an elasticity about 3 times higher than the GFRP bars, showed a curve gradient nearly 60% less than the latter. It appears, apart from the elastic modulus, the initial slopes are influenced by other parameters. This issue is examined and discussed later combining with the failure type. After the maximum bond stress, the GFRP bars (except Specimen 2) had an abrupt and quick decrease of their bond strength while the CFRP bars reduced more gradually and slowly. The residual bond strength is defined as the average strength when the curve gradient fell below -0.2. For the GFRP bars, their residual bond strength during the post-maximum period remained 35% of the bond strength while for CFRP bars this value was around 60% relatively. The post-maximum behaviour was partially dependent on the surface deformation of the bars. The deformed ribs on the GFRP bar appeared to be effective in improving the bond but since the GFRP bars had a smooth surface without coating, the frictional stress developed at their interface during the post-maximum stress part was relatively low. The difference in the bond behaviour of GFRP Specimen 2 could be the result of inaccurate sample preparation, i.e. the bar was not perpendicular to the concrete substrate.

Comparing with the GFRP bar, the high-modulus and high-cost CFRP bar presented less satisfactory bond resistance and bond strength. Even though the residual bond strength of the CFRP bar was adequate, the low maximum bond stress would possibly restrict its load transference when reinforcing concrete.

4.2.2 Bond Failure Type

In the pull-out test, all FRP bars failed in the designed pull-through mode without any noticeable signs of splitting appearing on their concrete cubes. Therefore, the concrete cubes had provided sufficient confinement of the embedded FRP bars to enable the bars to reach their maximum bond stress. After the FRP bars were pulled through, the concrete cubes were split in the centre for a better observation of the bond interface behaviour. The FRP bars and the opened concrete cubes are shown in Figure 4.2. The ribbed GFRP bar had a smooth surface and failed in a mode that the surrounding concrete was sheared off while no obvious fracture of the deformed bar surface occurred. In such a failure mode, theoretically, the bond strength would be mainly governed by the strength of the concrete.

Figure 4.2 Failure of the pull-out test specimens after splitting the concrete cubes: (a) GFRP bars and (b) CFRP bars

The CFRP bars presented a visually different failure mode in that the bond failed mainly at the interface between the surface sand coating and the successive layers of fibres. After splitting the cubes, it was observed that the sand coating of the CFRP bar together with its twined spiralling were left and attached to the surrounding concrete while the interior fibres were unsheltered and pulled through the concrete substrate. This was a failure mode of the surface deformation being sheared off. In such a failure mode, the bond strength of the FRP bars was controlled by the shear strength among successive layers of fibres or by the shear strength of the bar deformation. The surface deformation of the tested CFRP bar (that was the quartz sand coating and the twined spiralling) was an effective solution to increase its bond to concrete. However, it was the bond strength between the surface deformation and the interior layer of fibres which was weaker than the bond-to-concrete that controlled the failure mode and consequently governed the bond strength.

4.2.3 Influence of Concrete Strength

Influence of the concrete strength on the bond during an FRP bar pull-out is related to the failure type (Theriault & Benmokrane, 1998; Arias, et al., 2012). If sufficient confinement is provided to a smooth and ribbed bar in the pull-out test, shear cracks develop between the bar ribs and the surrounding concrete before the bar fails in the pull-through mode. For steel bars with such a failure mode, the bond strength is mainly dependant on the strength of the surrounding concrete (Achillides & Pilakoutas, 2004). For concrete with strength of more than 50 MPa, this might be different. The GFRP bars were not observed to have any surface material sheared-off (Figure 4.2 (a)) with the tested concrete substrate (65 MPa in strength), which means they were able to develop relatively high bond ability.

As previously stated in Section 3.11, influence of the concrete strength was investigated using only CFRP bars and a series of concrete mixes with measured compressive strength of 56, 65 and 72 MPa. Figure 4.3 shows the percentage of decrease and increase of the bond stress and bond-slip curve slopes in comparison with the 65 MPa concrete. During the early stage of measurable slip up to 0.25 mm, the relation between concrete strength and the bond behaviour appeared indirect. Both the 56 MPa and 72 MPa concrete caused decrease and increase of the bond at different levels of slip. This could be partly due to the difficulties of accurate measuring of the bond stress at the beginning of the test. Compared with 65 MPa concrete, the 56 MPa concrete had a 5-10% decrease of the bond strength and the bond-slip initial slope (k_1) while for the 72 MPa concrete, that was an increase by 15% and 39% respectively.

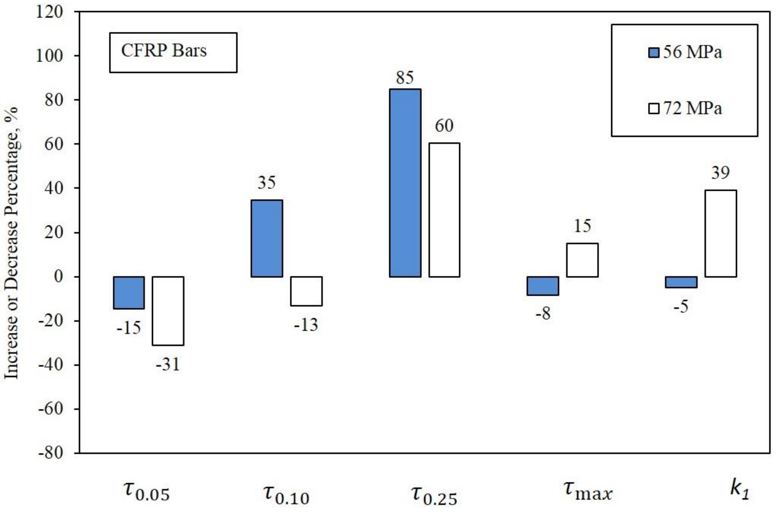

Figure 4.3 Percentage of decrease and increase of bond stress and curve slopes of CFRP bars in 56 MPa and 72 MPa concrete compared with 65 MPa concrete

Considering the visual observations of the CFRP bar, the bond failure appeared to happen at the interface between the surface deformation and the successive layers of fibres. In such a mode, the bond strength of FRP bars should theoretically not depend on the value of concrete strength. However, in this test, it appeared that the failure of CFRP bars was also partly controlled by the surface deformation. Higher strength concrete was denser. Therefore, the surrounding substrate could have provided higher confinement to these embedded CFRP bars and consequently resulted in a small but noticeable increase of the measured bond strength. The same explanation possibly applies to the change of k_1 as stronger concrete caused a stiffer initial curve slope.

4.2.4 Influence of Chloride and Sulphate

Influences of chloride and sulphate on the bond behaviour of both GFRP and CFRP bars were examined. Compared with the control specimens, the designed exposures resulted in an additional presence of Cl and SO_3 at the content of 0.7% and 2.0% respectively, based on the XRF results. The Cl and SO_3 content as well as the concrete compressive strength of each group are given in Table 4.2. It is worth noting that the content values were assessed according to determination of elemental composites. The real content of chloride and sulphate ions under each exposure might be not the same but still relatively proportional to the measured elemental composite quantities.

Table 4.2 Cl and SO_3 content and concrete compressive strength of each exposure

Specimen	Cl Content, %	SO_3 Content, %	Concrete Strength, MPa
Control	Nil	1.7	65
Chloride Exposure	0.7	1.7	52
Sulphate Exposure	Nil	3.7	50

Compared with the control specimens, changes of the bond stress and curve slope of both sets under their designed exposures were calculated and expressed as a percentage. The increase and decrease for the GFRP and CFRP bars are illustrated in Figure 4.4 and 4.5 respectively. For the GFRP specimens, both the chloride and the sulphate exposure were measured to have induced decreases in the initial bonding up to $\tau_{0.25}$. The decreases at the slip of 0.05 mm were significantly large (over 50%) for both exposures and gradually declined to around 10% at the slip of 0.25 mm. The bond strength for GFRP bars under both exposures was measured as nearly unchanged while the chloride-exposed bars even showed a 16% rise. The concrete strength for both exposures decreased by around 15 MPa (20% approximately) compared with the control specimens due to the addition of sodium chloride or calcium sulphate. However, as analysed in Section 4.2.3, the concrete strength is believed to have positive influence on the bond strength of these ribbed GFRP bars because of their failure mode. Therefore, the initial bond stress of GFRP bars could be weakened by either the presence of Cl^- and SO_4^{2-} or the decrease of the concrete strength, or both. The failure of the exposed-bars was observed to be the same as non-exposed ones in Figure 4.2 (a) after splitting the concrete cubes. The presence of ions can be regarded as unable to result in any noticeable deterioration of the GFRP material for the simulated exposures. The initial slopes from the bond stress-slip curves also only showed negligible variation (less than $\pm$10%) under both exposures. Hence, it can be suggested that the tested GFRP bars presented adequate resistance under the simulated chloride and sulphate exposure, albeit their initial bond appeared to be much weakened.

On the other hand, the CFRP bars displayed a different and less systematic behaviour in terms of the bond strength and stiffness changes. Under the chloride exposure, the CFRP bars firstly showed a sharp reduction in $\tau_{0.05}$ by over 60% then this reduction decreased to around 20% for $\tau_{0.10}$ during the initial development stage of the bond stress. For $\tau_{0.25}$ and τ_{max}, however, it was an increase of nearly 60% and 25% respectively. Under the sulphate exposure, the CFRP bars also showed decreased $\tau_{0.05}$ and $\tau_{0.10}$ but only slightly by around 10% and significantly increased $\tau_{0.25}$ by 60%. The maximum bond strength of the CFRP bars under the sulphate stimulation showed a slight decrease of 8%. The initial slope of the stress-slip curves under both exposures was approximately double compared with the control specimen, which means that addition of the chemical reagents affected their elastic behaviour. Additionally, the addition of gypsum at such a designed quantity in this test can lead to the chemical reaction with C_3A and C-S-H and produce the mineral ettringite which is volume expansive and usually causes small cracks within the concrete. These micro-cracks might be responsible for the bond stress drops at the initial period, but this lacks experimental evidence.

As a summary, the chloride and sulphate ions potentially from the seawater can affect the bond stress development of the tested GFRP and CFRP bars at their initial bonding level but cannot reduce their final bond strength. However, this influence was possibly caused by affecting the bonding mechanisms rather than by deteriorating the FRP materials. The GFRP and CFRP bars also presented different sensitivities to the exposures and the GFRP bars were less sensitive to and less influenced by the addition of Cl and SO_3.

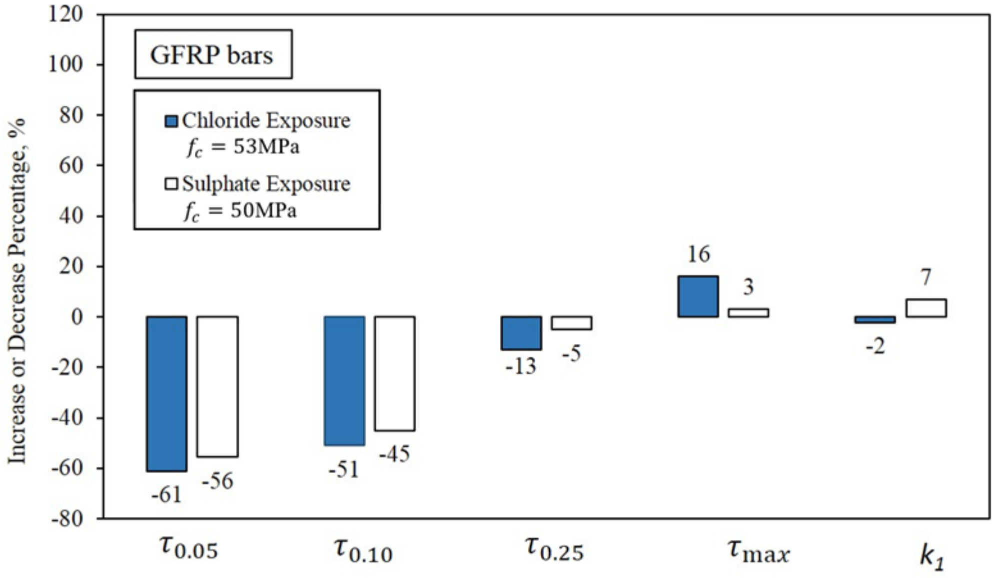

Figure 4.4 Influence of the addition of chloride and sulphate in the bond of GFRP bars

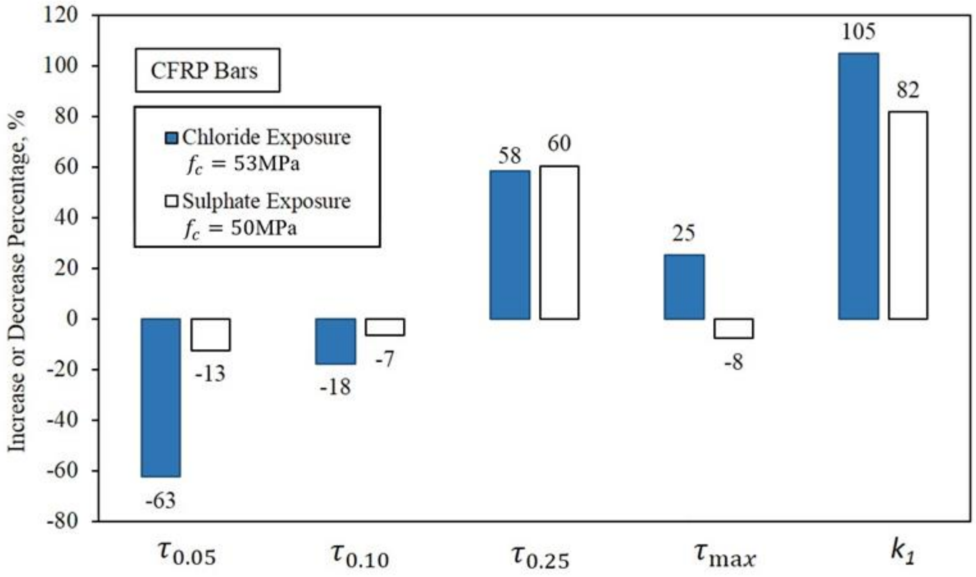

Figure 4.5 Influence of the addition of chloride and sulphate in the bond of CFRP bars

4.3 Response of FRP Bars to Shear

4.3.1 Shear Strength and Failure Type

The response of FRP bars to shear was examined (using specimens in Section 3.6.2 and test method in Section 3.8.4) considering that FRP is anisotropic and weaker in transverse directions compared with longitudinal directions. Consequently, the shear strength of concrete members reinforced with FRP bars longitudinally may differ from those with steel ones. Via the three-point bending test, all the designed specimens longitudinally reinforced with FRP bars and steel bars (control specimens) failed in shear mode mainly due to the arranged low ratio of span-length/effective-depth (around 2.1). A typical failure and crack pattern of the tested FRP specimens is shown in Figure 4.6. For equivalent amount of tensile reinforcement, the lower elastic modulus of FRP bars usually results in a lower longitudinal reinforcement stiffness than the steel bars. In this section, the factor $A_f E_f$ (that is the cross-sectional area of the tensile reinforcement multiplied by the elastic modulus of the tensile reinforcement) is used as the main variable for comparing test results. The shear force at formation of the critical inclined crack (V_{cr}) and the ultimate shear strength (V_μ) for each group are given in Table 4.3 while their applied load vs. span deflection curves are provided in Appendix B2.

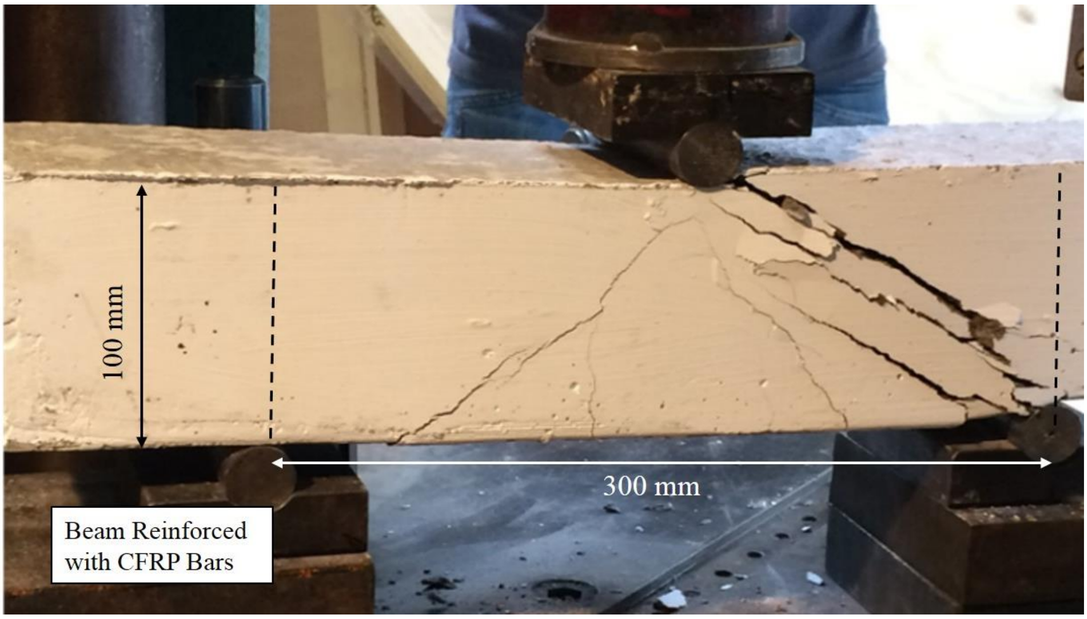

Figure 4.6 Failure and development of diagonal cracks of the CFRP beam specimen under the three-point bending test

Table 4.3 Test results from the three-point bending test (66 MPa concrete strength)

Tensile Bar	Diameter, mm	E_f, GPa	$A_f \cdot E_f$, kN×10^6	V_{cr}, kN	V_μ, kN	$V_\mu/(A_f \cdot E_f)$, ×10^{-6}	$(\tau_{max}.A_f \cdot E_f)/V_\mu$ kN×10^6
GFRP	8.0	60	3.0	7.1	16.5	5.5	4.9
CFRP	7.5	130	5.7	10.8	23.8	4.2	1.6
Steel	6.0	200	5.7	9.7	20.3	3.6	-

The crack pattern for all tested specimens was roughly the same. Micro-cracks occurred first in the centre from the underneath side under the load-applying point then inclined shear cracks occurred and grew wider and deeper diagonally to the beam's compression zone and caused the failure. In this test, the critical inclined crack was defined as the crack whose inclination had become more than 45 degrees to the vertical and was spreading towards the load-applying point while spreading over the nominal neutral axis. The beam specimens with GFRP bars had a value of $A_f \cdot E_f$ that was only around 50% of the beams with CFRP and steel ones. However, the V_{cr} and V_μ values of the GFRP beams reached more than 70% and around 80% respectively of the steel ones. The beam specimens with CFRP bars whose $A_f \cdot E_f$ was approximately the same as the steel beams also showed V_{cr}

and V_μ values that were 10-20% higher than the steel ones. The parameter $V_\mu/A_f \cdot E_f$ also showed this ratio difference. Considering the bond behaviour and strength differences in Section 4.2.1 between GFRP and CFRP bars, another parameter $(\tau_{max}.A_f \cdot E_f)/V_\mu$ was used in Table 4.3 to show the relation between the bond strength of the FRP bars and the shear contribution. It can be seen that the GFRP bars had a $(\tau_{max}.A_f \cdot E_f)/V_\mu$ that is more than 3 times greater than the GFRP bars, which is probably due to their bond failure difference. Therefore, the shear strength of concrete beams reinforced only with tensile FRP bars could be regarded as very sensitive to the bond failure mode of these bars.

The post-failure performance of the three types of specimens was also different. When the inclined cracks reached to the top face of the beam, in which case there was no shear contribution from uncracked concrete any more except the aggregate interlock, the shear stress was mainly applied to the tensile reinforcement. The steel rebar, as a reference, had sudden and abrupt bar rupture under the force of shear and possibly torsion as well while the break of the FRP bars, on the other hand, was more gradual and more ductile. When the load was maintained after the failure, the FRP reinforcement had apparent longitudinal slips. The GFRP bars had bond breaks in the form of big horizontal cracks occurring between the tensile FRP bar and its surrounding concrete (Figure 4.7) while the CFRP bars usually broke in the way of the reinforcement delamination at cracked sections of the beam (Figure 4.8).

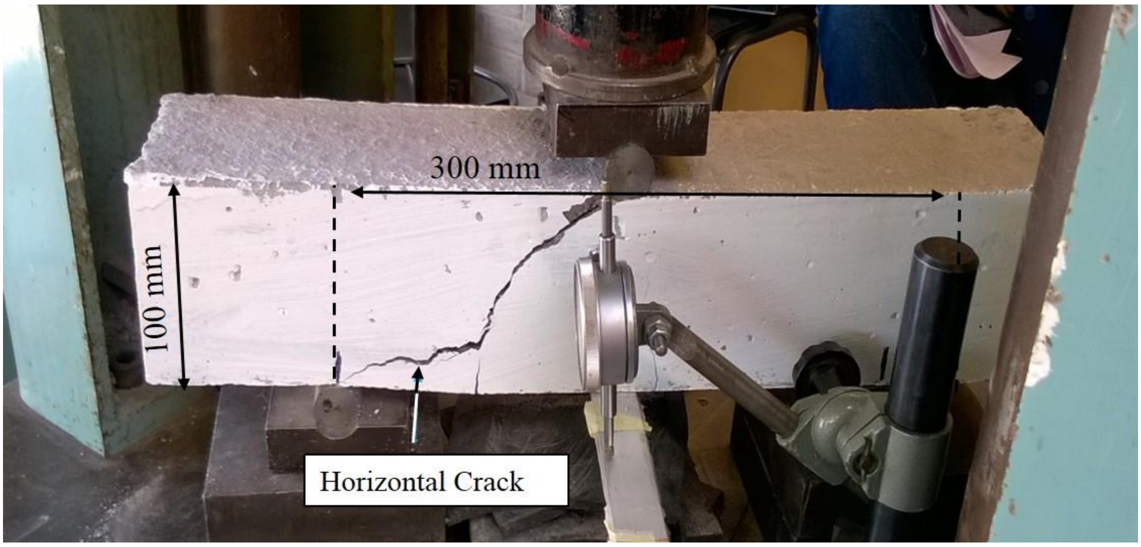

Figure 4.7 Failure of the GFRP beam specimen with the horizontal bond crack

Figure 4.8 Rupture of the CFRP bar at cracked sections of the beam in the form of material delamination

4.3.2 Shear Contribution of Uncracked Concrete

For a concrete beam reinforced with FRP bars, flexural cracks will spread deeper towards the compression zone and wider inclined cracks will form compared with a concrete beam reinforced with steel ones, due to the difference of the stiffness. Deeper cracks reduce the compression zone and wider cracks are believed to decrease the aggregate interlock mechanism (Tureyen & Frosch, 2002), both of which can theoretically result in reduction of shear resistance provided from concrete. For concrete members reinforced with steel bars and without shear reinforcement, contribution to shear strength from the uncracked concrete can be estimated according to Eurocode 2 (British Standard Institution, 2005); meanwhile, for FRP-bar-reinforced concrete members (singly reinforced, rectangular cross-sections), ACI 440.1R-06 recommends that the contribution can be calculated with Equation 4.1.

$$V_{c,f} = 0.4k\sqrt{f_c'}bd \qquad \text{Equation 4.1 (a)}$$

$$k = \sqrt{2\rho_f n_f + (\rho_f n_f)^2} - \rho_f n_f \qquad \text{Equation 4.1 (b)}$$

where b is the web width, mm; n_f is the ratio of elastic modulus of FRP bars to elastic modulus of concrete.

Comparison is made between estimated shear strength with the ACI 440.1R-06 method and tested results from this study. In this study, instead of the design strength, the concrete characteristic compressive strength is always used for computing the flexural and shear strength of concrete members at the ULS where applicable. As shown in Figure 4.9, for both GFRP and CFRP beams, the estimations are far below the measured results, i.e. only around 20% of the test data.

To propose suitable approaches to computing the shear strength, two series of concrete beams with the same GFRP bars longitudinally but different concrete strength were tested additionally using the same bending method. The applied load vs. span deflection curves for these two additional sets with concrete strength of 56 MPa and 72 MPa are shown in Appendix B.2. Based on analysis of the relation between measured shear resistance and the concrete strength (Figure 4.10), a modification factor k_a is advanced for improving the estimation accuracy of the shear strength based on the ACI 440.1R-06 method. For the beam specimens longitudinally reinforced with GFRP bars, the shear resistance provided by the uncracked concrete at the ULS can be more accurately computed with Equation 4.2 (a) – (c):

$$V_{c,f} = 0.4kk_a\sqrt{f_c}bd \qquad \text{Equation 4.2 (a)}$$

$$k = \sqrt{2\rho_f n_f + (\rho_f n_f)^2} - \rho_f n_f \qquad \text{Equation 4.2 (b)}$$

$$k_a = 0.03f_c^{1.25} \qquad \text{Equation 4.2 (c)}$$

The expression of k_a is for keeping the format of Equation 4.2 (a) the same as Equation 4.1. The computed shear strength according to this modified Equation 4.2 (a), compared with the experimental results from the three-point bending test, is shown in Figure 4.9. Unlike the substantial level of conservatism from ACI 440.1R-04’s Equation 4.1, Equation 4.2(a) can estimate the shear strength more accurately. It is worth noting that computation of the modified Equation 4.2 uses the characteristic compressive strength of concrete, therefore larger safety factors will be additionally needed if using these formulae for the SLS design. Furthermore, the level of estimation accuracy for Equation 4.2 might also depend on the characterisation of FRP reinforcing bars. The suggested modification will not be universal and cannot properly be applied directly to the CFRP-bar-reinforced beams.

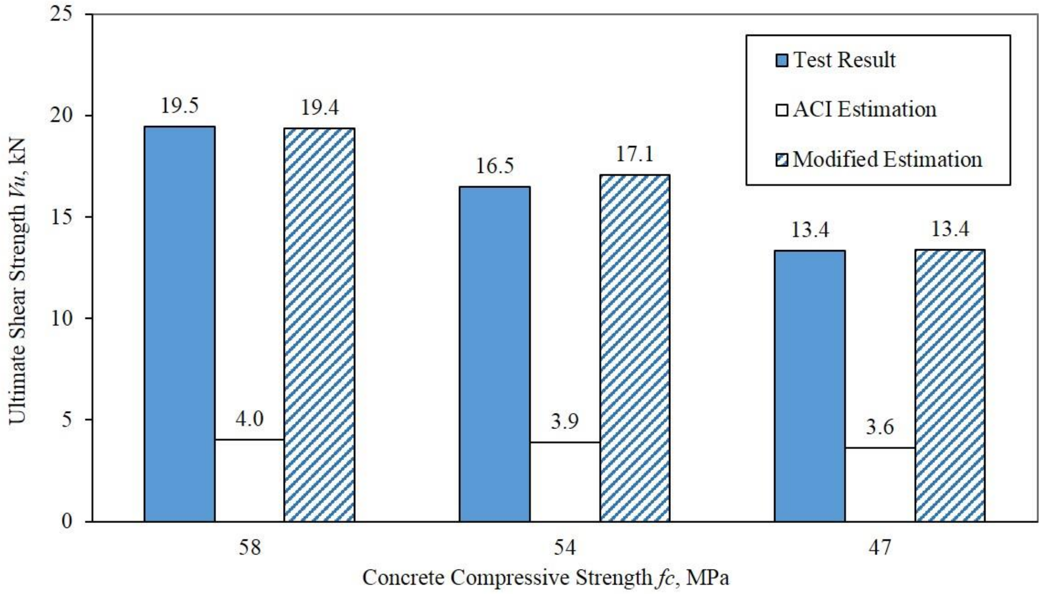

Figure 4.9 ACI and the modified estimations for beam specimens reinforced with tensile GFRP bars

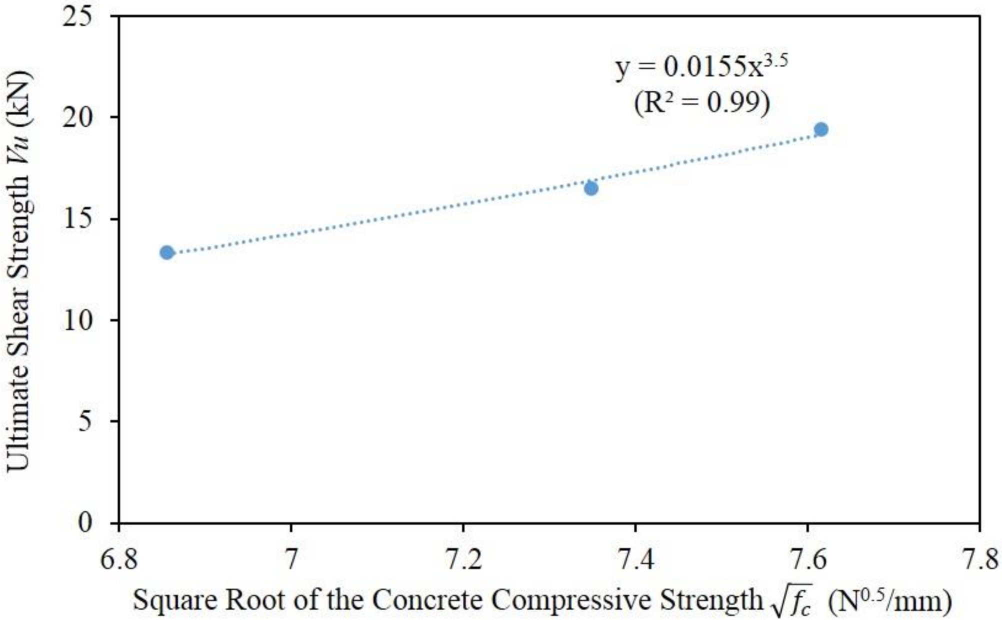

Figure 4.10 Relation between the measured ultimate shear strength and the concrete compressive strength

4.4 CFRP Strands under Tension

Through the designed tensile test (Section 3.8.2), the maximum tensile stress of the tested CFRP strands was obtained. It is worth noting that all the test specimens failed in sections near their top tying knots (Figure 4.11) rather than in the centre part where it is usually regarded as the gauge section for determining the modulus of elasticity. That was possibly because stress concentration formed near the knot. Therefore, the measured tensile load and elongation cannot be used for accurately computing the tensile strength and elastic modulus of the CFRP. However, the failure type and maximum tensile stress are still relevant to estimate the composite's properties. Based on the test results, the CFRP strands had a maximum tensile strength of 440 MPa on average before failure. The value is not comparable to that claimed by the manufacturer (2100 MPa). Both strength values are used in Chapter 5 for predicting the flexural capacity of beams externally strengthened with such CFRP strands so that the tensile strength provided by the CFRP can be double-checked. The post-failure behaviour of the CFRP strands was also favourable in terms of reducing the failure brittleness of a concrete member strengthened with CFRP strands. As seen in Figure 4.12, the CFRP composite could still hold a load that is 40-60% of the maximum load after its failure and sustained over a relatively long period with the load gradually reducing.

Figure 4.11 Test setup (left) and failure (right) of the CFRP strands under the tensile test

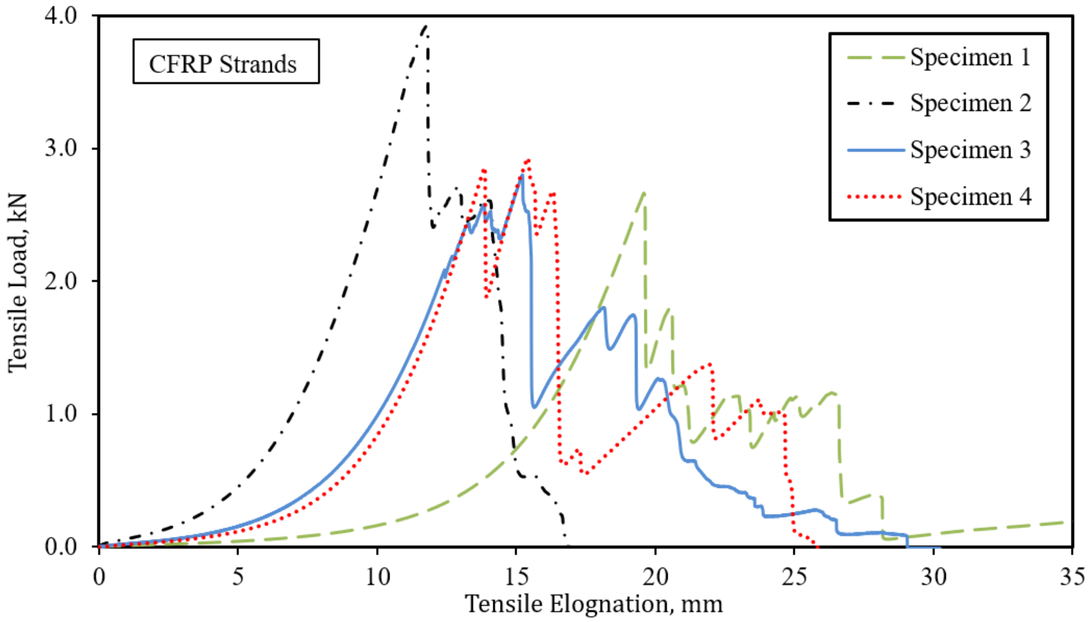

Figure 4.12 Tensile load vs. elongation curves of the CFRP strands under the tensile test

4.5 Summary

Comparisons between the selected types of FRP bars are first carried out according to their test behaviour and results in order to determine a more suitable bar reinforcement for the succeeding tests in Phase II. It was observed from the pull-out test that the GFRP bars generally had a bond strength and an elastic stiffness about 3 and 1.6 times greater than the CFRP ones respectively. However, during the post-failure period, the CFRP bars presented a slower and more gradual reduction of the bond stress than these GFRP bars because of their surface deformation difference. The sand coating and twined spiralling surface deformation of the CFRP bars was noticed to be effective in improving their bond between the concrete and the bar, but it was also observed that the bond between the coating and the interior fibres was weaker and more responsible for the bond failure of CFRP bars. Considering the significance of bond for concrete members reinforced with tensile bars, the more economic GFRP bars were chosen as of priority in selection.

The concrete compressive strength (at the range of interest for this study, 50-75 MPa) was believed to have no significant influences on the bond of the CFRP bars but might affect the bond strength of these GFRP bars. This can be explained based on their bond failure. The GFRP bars were found insensitive to the presence of chloride and sulphate ions in concrete and presented nearly unaffected bond strength and stiffness property albeit their bond mechanisms at the initial stage appeared weakened. The CFRP bars behaved relatively more sensitively to the ions, especially at the initial stage, but were still only slightly affected. No visual deterioration of the FRP composites was observed under the chloride and sulphate exposures.

Concrete beams reinforced separately with GFRP and CFRP bars presented comparative and reasonably large shear strength provided by their uncracked concrete sections. The final ruptures of the FRP bars were usually in the form of noticeable slips or delamination of the composite rather than abrupt bar breaks, which is favourable for the ULS and ALS design. The ACI 440.1R-06 (2006) underestimates the shear contribution provided from the uncracked concrete ($V_{c,f}$) of a beam reinforced with FRP bars. One modified equation is introduced based on the experimental data for the tested type of GFRP bar:

$$V_{c,f} = 0.4kk_a\sqrt{f_c}b_w d$$

where $k = \sqrt{2\rho_f n_f + (\rho_f n_f)^2} - \rho_f n_f$ and $k_a = 0.03f_c^{1.25}$

The concrete strength factor k_a is added additionally compared with the ACI 440.1R-06 method. Dependence of reinforcement characterisation for this equation was not verified within this study due to the lack of enough data.

Finally, the CFRP strands were tested to reveal a lower tensile strength than that claimed by their manufacturer but had favourable ductile post-failure behaviour.

Chapter 5 Structural Behaviour of Concrete Reinforced with FRPs and Synthetic Fibres

5.1 Introduction

The work in Phase II focuses on the structural behaviour of concrete members reinforced or strengthened with different novel FRP reinforcement and fibres. Based on outputs from the quasi-static bending test, mechanical behaviour of these beams is discussed as well as compared. Design recommendations of both flexure and shear strength are also presented for FRP- and synthetic-fibre-reinforced concrete members.

5.2 Behaviour of Concrete Reinforced with FRP Rebar

5.2.1 Crack and Failure Modes

The labelled GC1 and GC2 beams (specimen details in Figure 3.16 of Section 3.9.1) were longitudinally over-reinforced with GFRP bars while GC1 beams had vertical CFRP bar ‘sticks’ for shear and GC2 beams had external fully-wrapped and overlaid CFRP strands. Compared with GC1 beams, GC2 developed wider flexural cracks and the cracks were spread more towards the top face of the beam. A representative behaviour of cracking for GC1 and GC2 are shown in Figure 5.1 and 5.2 respectively. Both sets of GFRP-reinforced concrete beams presented similar patterns of crack development and spreading. The first crack always occurred in the beam’s constant-moment span and afterwards more micro-cracks originated from the underneath where the principal stresses were the greatest. These cracks spread upwards over the nominal neutral axis of the beam and grew wider while the applied bending load was increasing. The cracks were mainly vertical flexural cracks which were mostly parallel to, or slightly inclined from, the beam’s transverse axis. Visually no shear cracks occurred in the shear spans since both GC1 and GC2 beams were designed to have theoretically sufficient shear resistance. The crack spacing for both beam sets was also similar with all beams finally having two or three big flexural cracks formed in their bending span.

Both GC1 and GC2 beams failed in a typical bending failure mode that the concrete at the top compression zone started to crush from under the load-applying points since they were all designed to be over-reinforced. However, the GC2 beams suffered more severe damage in that a big horizontal crack formed between the two load-applying points as a layer of concrete (around 10-15 mm thick) separated from the main body of the beam (Figure 5.2). This could be because the transversely fully-wrapped CFRP multi-strands provided additional confinement to the beam and had comparatively restricted the development of its flexural deflection. No debonding or rupture of the CFRP strands was visually observed after the failure, which demonstrated that the tested CFRP strands had the potential to provide appropriate shear resistance.

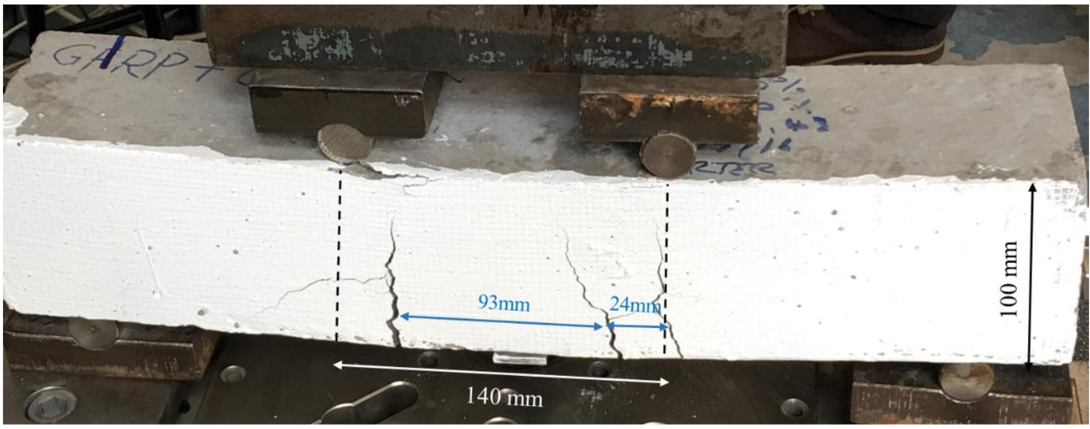

f

Figure 5.1 Crack and failure of the GC1 beam

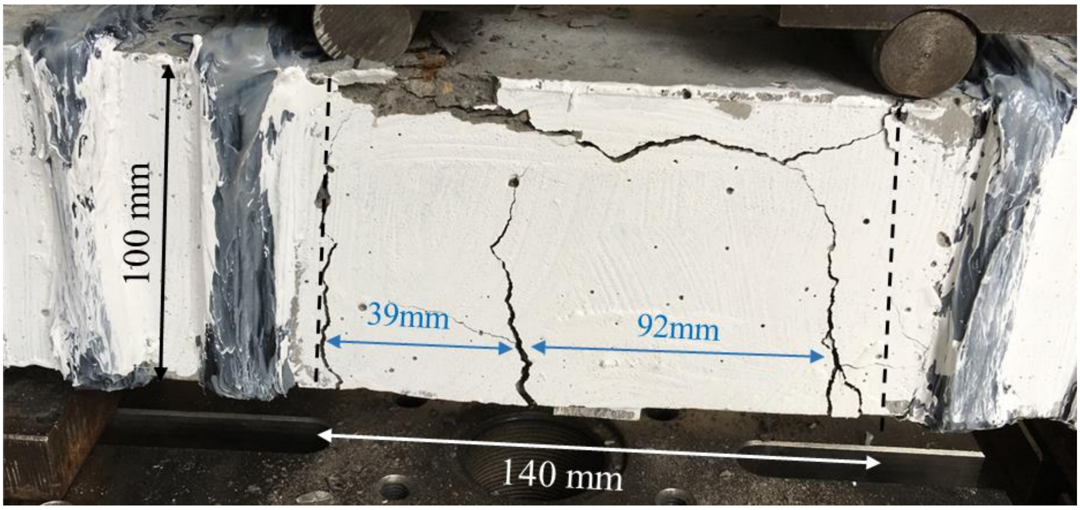

Figure 5.2 Crack and failure of the GC2 beam

5.2.2 Load-Deflection Behaviour

Structural behaviour of the GC1 and GC2 beams tested in flexure is presented in terms of the measured load-deflection as well as the computed moment-curvature curves at their midspan section in Figure 5.3 and 5.4 respectively. The structural response of each beam in terms of the measured load and deflection at its first crack, at the maximum load and at the eventual rupture is given in Table 5.3 in Section 5.5 where comparative discussions are carried out for all beams reinforced or strengthened with FRP from this study. Average values of the measured first crack load and deflection (F_{cr} and L_{cr} respectively), the maximum load (F_{max}) and the deflection at the maximum load (L_{max}) are presented in Figure 5.5 below. As shown, the flexural load capacity of GC1 and GC2 beams was nearly the same, since both sets failed in flexure thanks to the two forms of shear reinforcement behaving effectively in providing required shear resistance. However, the deformability of the GC2 beams appeared slightly more controlled compared with GC1. The deflection of GC2 beams at the first crack and at the maximum load was around 25% and 8% less than the GC1 beams respectively. These reductions, with the previously viewed failure difference, support the idea that the fully-wrapped CFRP strands provide confinement to the concrete beam and consequently reduce its flexural deflection.

Additionally, it is observed from the load-deflection curves that a few load-resistance drops (from 2 to 4 individually) happened before the beams reached their maximum load resistance by which time they were regarded as failed. All beams presented one drop at occurrence of their first crack and a few more afterwards while the applied bending load was increasing. These drops are named as the Load-Carrying Capacity (LCC) Drop for further analysis and are more specifically discussed in Section 5.5.

5.2.3 Behaviour of Post-Tensioned GFRP-Reinforced Beams

The post-tensioned GFRP reinforced beams (specimen details in Section 3.9.6) also broke in a flexural failure mode and were measured to have an improved load resistance at their first crack level but a reduced maximum load resistance at the failure. A brief discussion of the PT beams’ behaviour is given in Appendix C.4

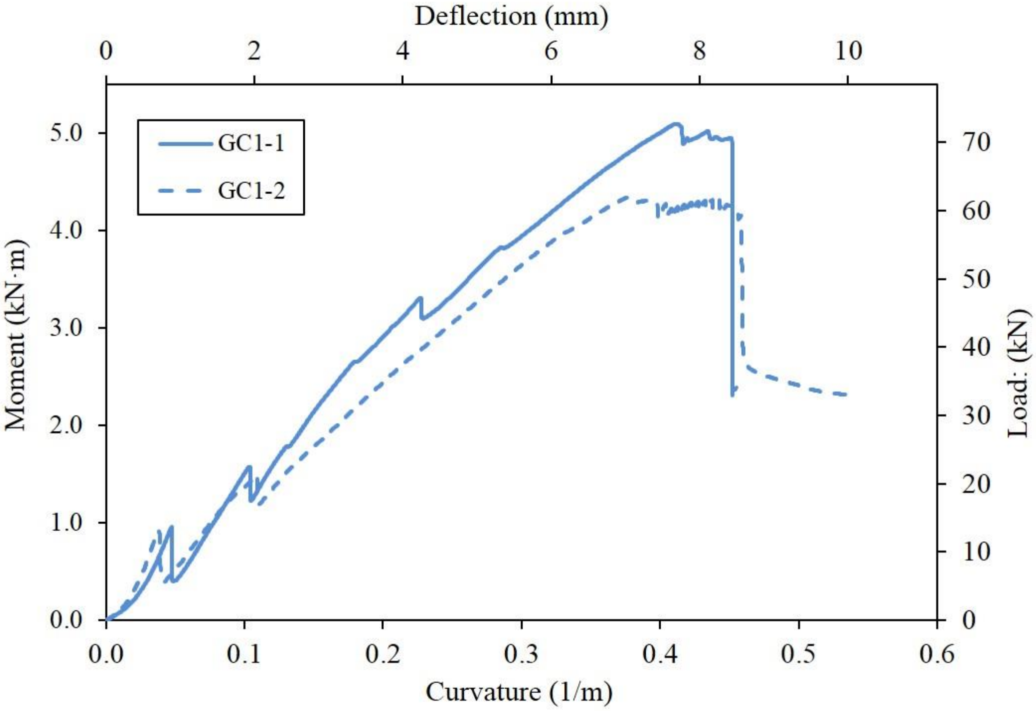

Figure 5.3 Load-deflection and moment-curvature curves at midspan of GC1 beams

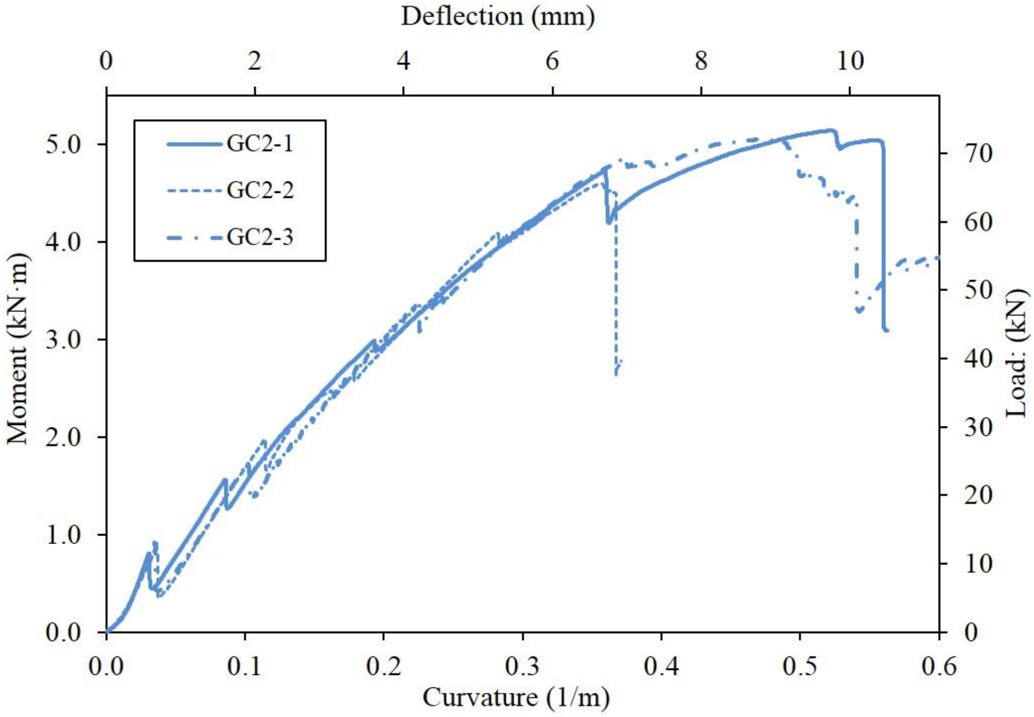

Figure 5.4 Load-deflection and moment-curvature curves at midspan of GC2 beams

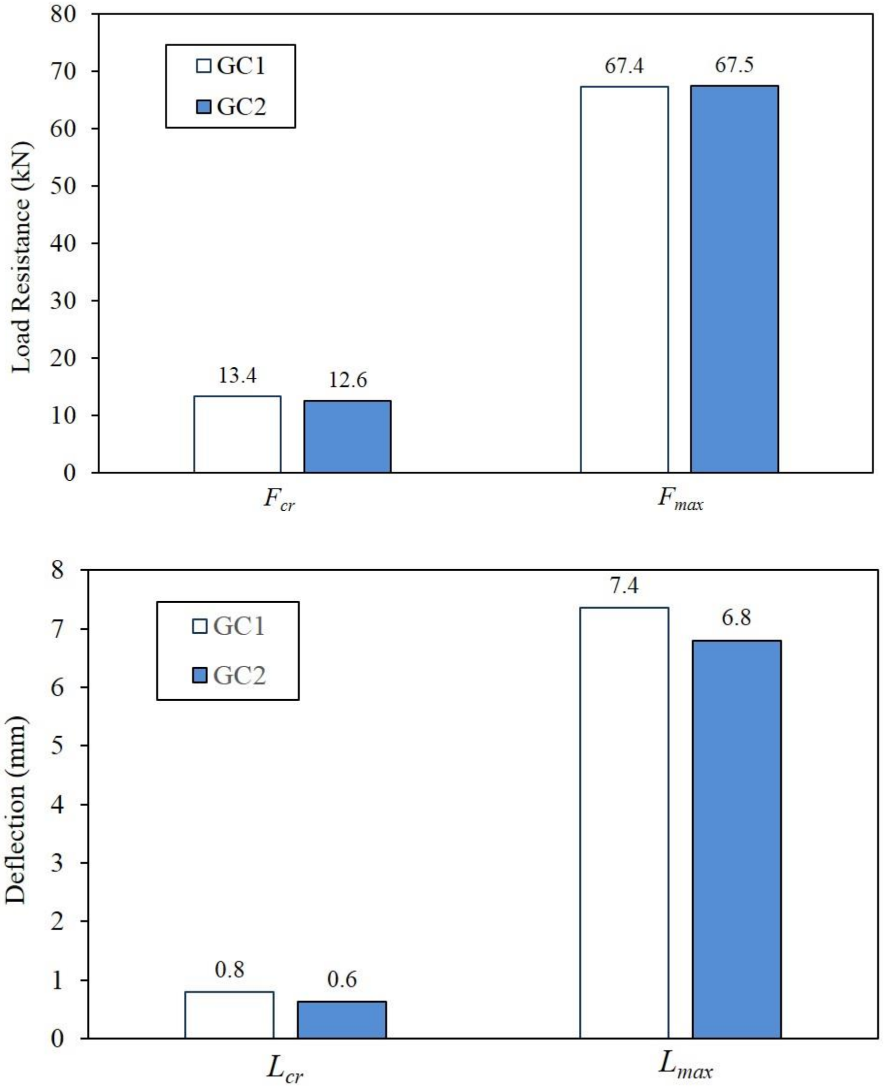

Figure 5.5 Load and deflection at the first crack and at the failure of GC1 and GC2 beams

5.3 Behaviour of Synthetic-Fibrous Concrete Strengthened with CFRP

5.3.1 Crack and Failure Mode

The synthetic-fibrous beams (specimen details in Section 3.9.3) were strengthened with the external CFRP strands and were categorised as the CC1 specimens. These beams were designed to be under-reinforced providing that the selected epoxy resin adhesive worked effectively in transferring tensile and shear stresses and was able to maintain the same strain as its two adhering substrates. It needs to be noticed that under-reinforced concrete beams reinforced or strengthened with FRPs are usually avoided for design because of their potential brittle failures such as abrupt rupture of the FRP reinforcement. However, in this study, these CC1 beams were prepared to mainly estimate the influence of the addition of synthetic fibres. When the beams are under-reinforced, the longitudinal FRP reinforcement will be able to develop a tensile stress that approaches the maximum design (and maybe characteristic) tensile strength of the FRP and, consequently, big flexural cracks will form in the bending zone. These flexural cracks are essential for investigating the mobilisation of the added macro-synthetic fibres because it is believed (The Concrete Society, 2007) that the added macro-plastic fibres are only be active in providing tensile contribution when ample cracks exist.

Crack response of the three tested fibrous beams at their failure is shown in Figure 5.6 schematically. Their initial cracks appeared at roughly the same location as GC1 and GC2 beams and these cracks increased in size and gradually propagated towards and over the nominal neutral axis of the beam while the applied load was increasing. Based on only visual inspection, it was hard to determine whether these initial micro-cracks originated before the external FRP started to debond or after. Formation of micro-cracks from the extreme fibre can possibly induce debond of the epoxy resin adhesive since it was applied to the bottom face of the beam and, consequently, affect the tensile strength contribution of the bonded CFRP strands. In this test, all tested CC1 beams failed in a flexural mode (Figure 5.7) in that the longitudinally bonded FRP strengthening system broke. The break could be theoretically caused by either failure of the bond between CFRP and concrete or rupture of the CFRP composite under tension, or a combination of both. Through visual examination after the failure, it was noticed that at the pure bending span, disengagement of the longitudinal CFRP strands happened from the concrete face and in a way that the applied layer of epoxy resin adhesive was nearly all left attached to the CFRP strands rather than on the concrete. The failure mode is vital for determination and prediction of the design tensile strength of the employed CFRP strengthening system. In a case where the epoxy resin adhesive separates prior to CFRP reaching its design tensile strength, the flexural resistance provided by the CFRP reinforcement will not be as much as the CFRP is assumed and expected to be. To review this particular issue, possible maximum strains of CFRP in tension and concrete in compression are computed according to the measured load and deflection results. The calculation process is explained in Section 5.5.1 while the computed result is that the CFRP tensile and concrete compressive strain at failure are 500 and 5000-5600 microstrain ($\mu\varepsilon$) respectively. The selected CFRP composite was claimed to have a tensile strength of 2100 MPa and an elastic modulus of 230 GPa, which would have allowed it to hold a maximum tensile strain of 9000 $\mu\varepsilon$. However, the actual tensile strain developed in the CFRP at the failure was only around 60% of that notional value. Therefore, the disengagement of the CFRP, which was highly responsible for the beam failure, was more likely to be mainly in the form of separation between the adhesive and the concrete surface.

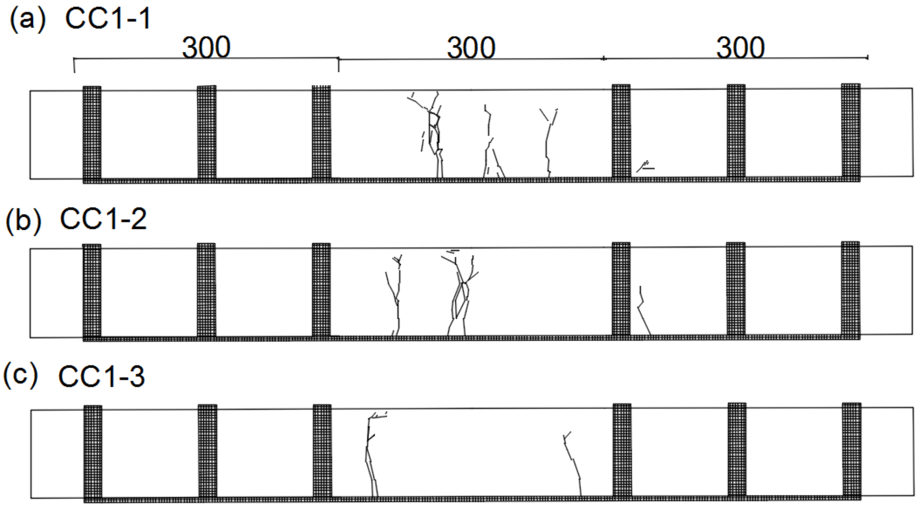

Figure 5.6 Crack response at failure of the tested fibrous beams: (a) CC1-1, (b) CC1-2 and (c) CC1-3

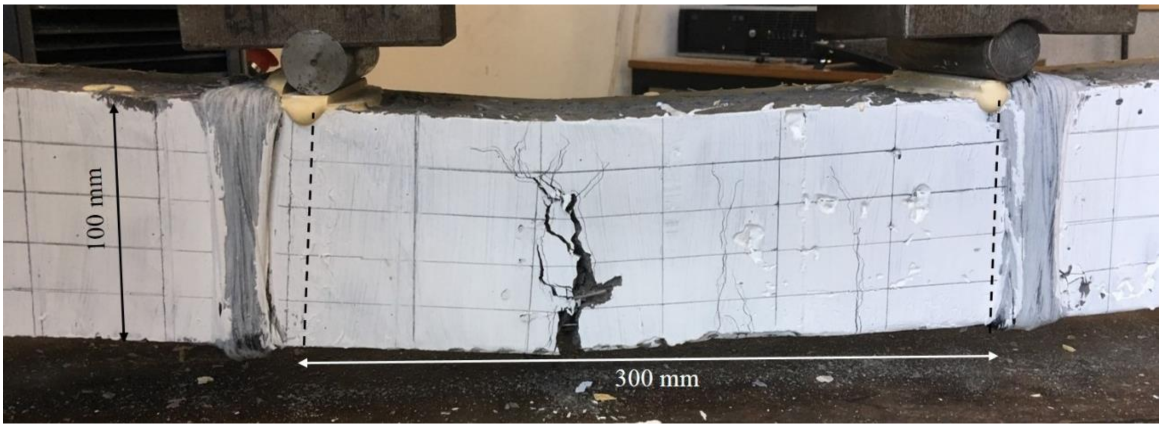

Figure 5.7 Failure of the macro-synthetic fibrous beam strengthened with CFRP strands

5.3.2 Load-Deflection Behaviour

Structural behaviour of the CC1 fibrous beams tested in flexure is presented in terms of the measured load-deflection as well as the computed moment-curvature curves at the midspan section in Figure 5.8. The mechanical response of each tested beam in terms of the measured load and deflection at its first crack, at its maximum load and at its eventual rupture is also given in Table 5.3 in Section 5.5. The average load capacity of CC1 beams was measured to be 5.8 kN and 7.8 kN at the first crack and at the failure respectively. Therefore, occurrence and development of the flexural cracks affected the growth of the beams' load resistance since the maximum flexural strength was only around 30% higher than that at the first crack. This can be explained that development of flexural cracks led to the bonded longitudinal CFRP strands starting to separate from the beam at locations where these cracks initiated. Once the separation had reached a critical magnitude, the external CFRP strengthening system would fail in providing sustainable tensile resistance and consequently the beam broke. After the failure, 2 of the 3 tested fibrous beams had relatively sharp drops of load resistance by around 30% while one (Specimen CC1-2) was by a smaller amount of less than 5%. This variation could be related to the separation conditions of the CFRP in the pure bending zone since CC1-2 visually had a less serious debonding issue. Following the drop at failure, the beams experienced a gradual recovery of their load capacity which can be described as the load resistance being maintained at a relatively high level (50-60% of the maximum strength) and slightly recovering to around 80% of the maximum strength. This recovery was also sustained over a proportionately large range of beam deforming (i.e. a deflection of more than 20 mm compared with the deflection of 3.1 mm at failure) without any brittle collapses of the concrete member. This experimental performance demonstrates that addition of the macro-synthetic fibres can significantly improve the post-failure behaviour of beams strengthened with CFRP.

The moment-curvature measure was used as the main axes while the load-deflection one as the secondary for CC1 beams since these beams had different dimensions with GC1 and GC2. Figure 5.8 (CC1) also used different scales from Figure 5.3 (GC1) and 5.4 (GC2) to present the data more clearly.

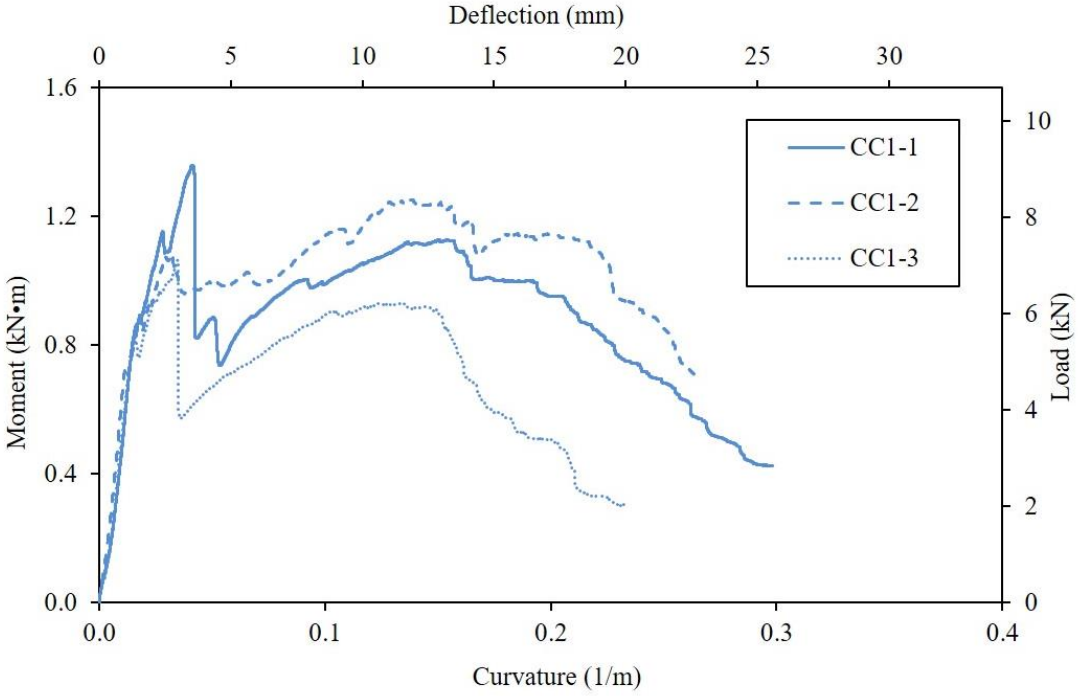

Figure 5.8 Load-deflection and moment-curvature curves at midspan of CC1 beams

5.4 Behaviour of Concrete with Thin Epoxy-Resin-Connected Joint

The beams strengthened with external CFRP had a joint connected with the epoxy resin adhesive (specimen details in Section 3.9.2) and are categorised as the CC2 beams. More precisely, they are classified as 1, 2 and 3 for their reinforcing condition of being under-, balanced and over-reinforced and A, W and S for their exposure history of being in air, in fresh water and in the artificial sea water, respectively. For example, Beam CC2.1-A represents an under-reinforced sample that had an exposure history of being in air.

5.4.1 Crack and Failure Modes

The CC2.1 and CC2.2 beams mainly had an interfacial failure mode of the joint without developing any big flexural or shear cracks while the CC2.3 beams were in a mode that combined both joint failure and formation of macro-cracks. On the other hand, specimens with the same reinforcing condition but subjected to different exposures mostly presented similar failure modes. Hence, the simulated three exposures appeared to have negligible influence on the cracking and failure behaviour of these jointed beams. It was also noticed that the CC2.1 beams generally failed in a mode that a few small diagonal cracks occurred from the bottom face of the beams nearby the joint (e.g., Figure 5.9 for Beam CC2.1-A) prior to the joint snapping. It was possibly due to the local adhering stress of the epoxy resin being relatively strong at the early stage of bending that these small ‘flexural’ cracks were dragged to propagate diagonally. Similarly, Beam CC2.2-W (Figure 5.10) also had a diagonal crack near its joint interface and this crack caused partial debonding of the longitudinal CFRP strands epoxied to the beam’s bottom face. After occurrence of these cracks, and while the applied load was increasing, the joint started to open and break. So, the concrete/concrete interface connected with the epoxy resin was still a weaker part of the beam where cracks would propagate at or nearby, and subsequently caused the beam to fail under bending.

The CC2.3 beams showed less severe joint failure and developed bigger flexural cracks in the pure bending zone but not alongside the connection (Figure 5.11 for Beam CC2.3-S). Those designed over-reinforced beams longitudinally had three bonded CFRP strands on the bottom face and two shorter ones on the front and back face of the beam separately. The two shorter portions were expected to provide additional restraints over the interface. Based on the behaviour and failure type of the joint, the arranged conjunct CFRP strands appeared to be effective in reducing the interfacial failure and controlling the formation of cracks at and near the epoxy resin adhesive layer.

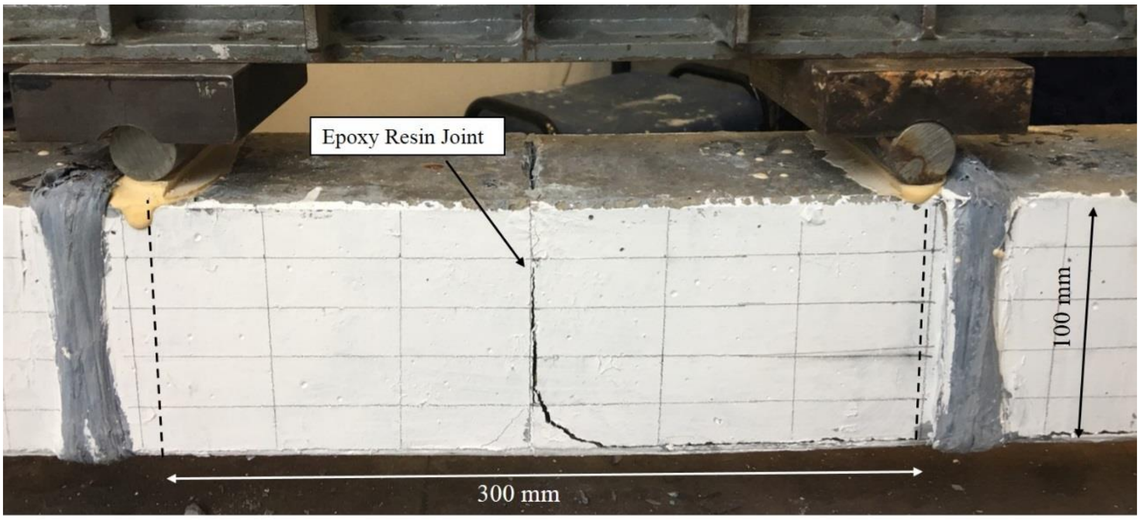

Figure 5.9 Crack and failure of the under-reinforced and air-exposed Beam CC2.1-A

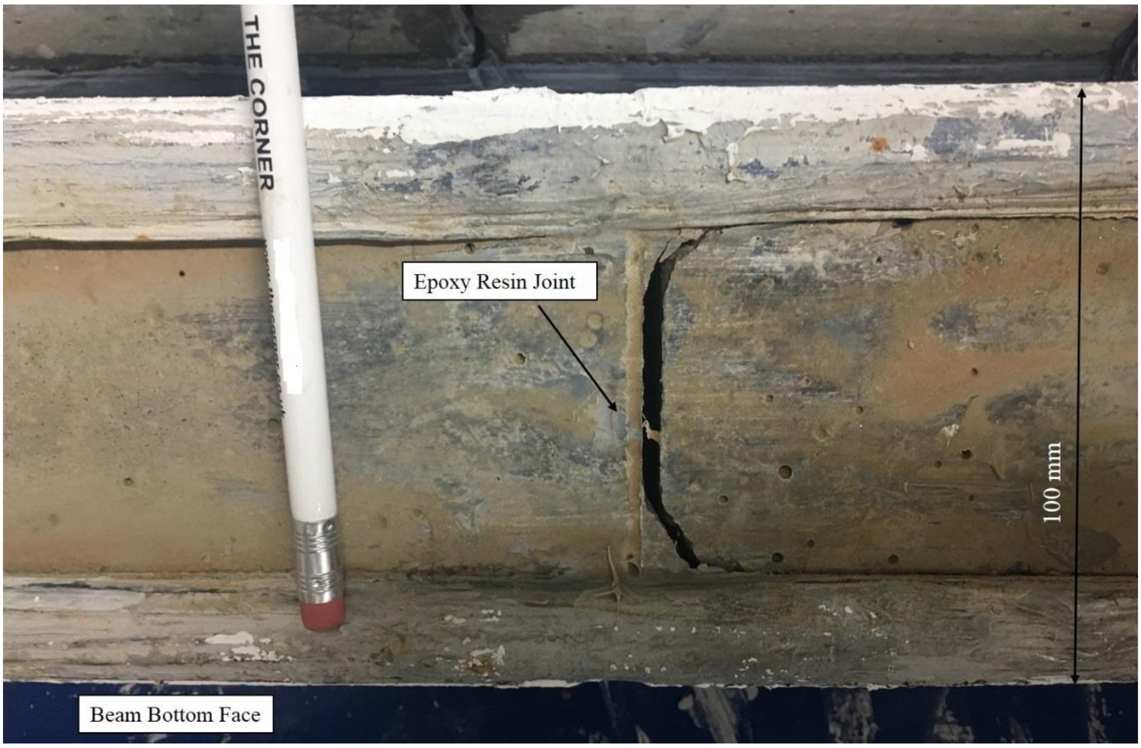

Figure 5.10 Crack and failure of the balanced and fresh-water-exposed Beam CC2.2-W

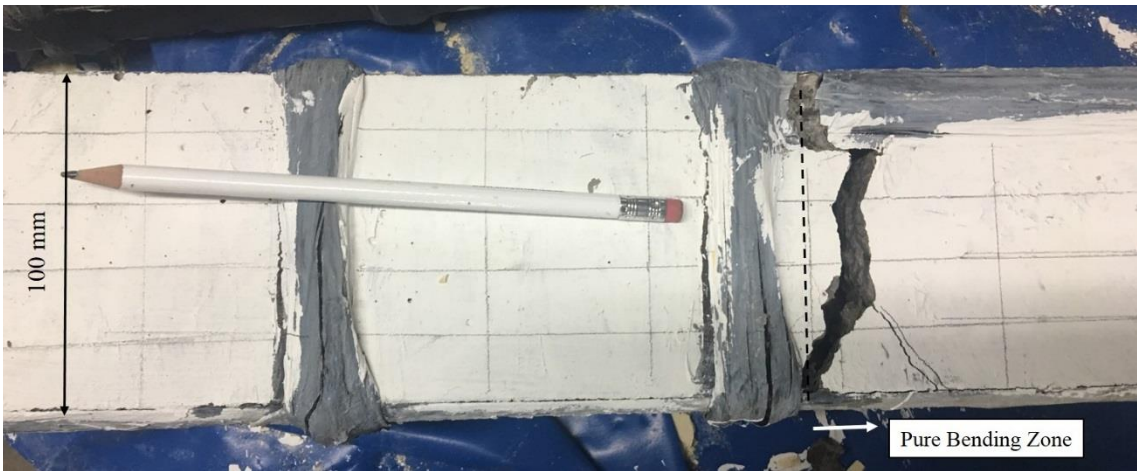

Figure 5.11 Crack and failure of the over-reinforced and seawater-exposed Beam CC2.2-S

5.4.2 Load-Deflection Behaviour

The structural behaviour of the jointed beams tested in flexure is also presented in terms of the measured load-deflection and computed moment-curvature curves at their midspan section in Figure 5.12, 5.13 and 5.14 for beam series CC2.1, 2.2 and 2.3 respectively. The structural response of each tested beam in terms of the measured load and deflection at its first crack, at its maximum load and at its eventual rupture is given in Table 5.3 in Section 5.5 as well as diagrammed in Figure 5.15 below for comparison and discussion of their mechanical behaviour. As shown in Figure 5.15, both the exposure condition and the reinforcement ratio influenced the load resistance at the failure of tested beams. For beams with the same CFRP reinforcing condition, it appeared that the ones exposed in air were measured to generally have the highest flexural capacity under the bending test (for CC2.1 beams, it was CC2.1-S instead) while the ones exposed in fresh water were the lowest. More specifically, the air-exposed beams generally showed a maximum flexural load capacity 45-60% higher than fresh-water-exposed ones with the same reinforcing condition. Beams subjected to the cyclic wetting/drying exposure in the artificial seawater exhibited greater variation of their maximum load resistance compared with the other two exposures. For example, for CC2.1 beams, the maximum load resistance of CC2.1-S was slightly greater than CC2.1-A while for CC2.2 and CC2.3 beams, the load resistance of seawater-exposed beams was around 70-80% of the air-exposed ones. On the other hand, while the number of the tensile CFRP reinforcements increased from 1 to 2 and 2 to 3, all beams under each exposure showed improved load resistance. For instance, the maximum load resistance of the air-exposed beams increased by 180% and around 20% while their tensile CFRP strands changed from 1 to 2 and 2 to 3 respectively. Beams longitudinally strengthened with one CFRP strand were designed to be under-reinforced while those with two and three should be nearly balanced and over-reinforced. However, considering that the failure of the beams was in a mode that the epoxy resin joint separated rather than concrete in the top compressive zone crushed, calculation of the balanced reinforcement ratio and classification of the reinforcing conditions might not be accurate. Therefore, the increase of load resistance should be mainly attributed to the supplementary confinement provided by the bonded CFRP strands to the joint. This increase also demonstrates that the designed type of joint was limiting the flexural strength development of the tested beams and consequently wrapping system of the three strands was the optimum for these jointed beams.

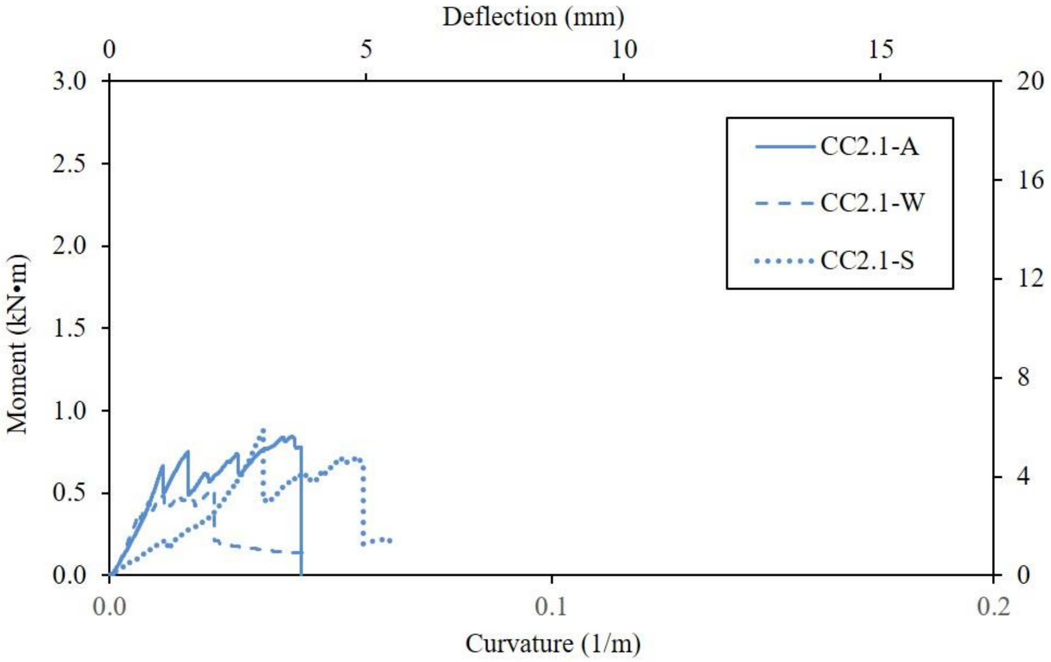

Figure 5.12 Load-deflection and moment-curvature curves at midspan of CC2.1 beams

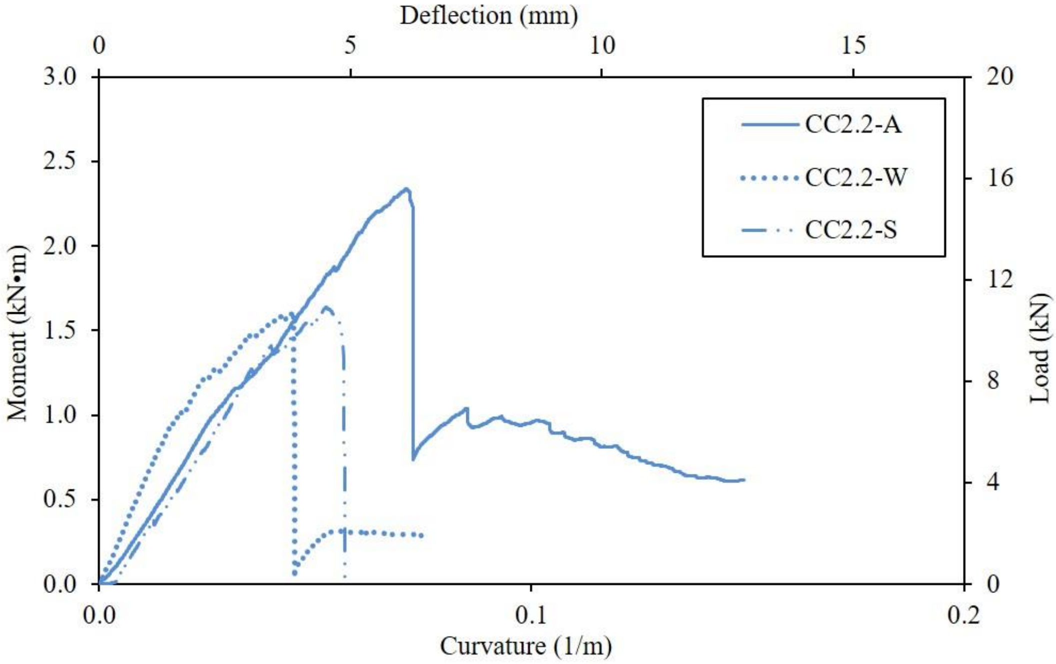

Figure 5.13 Load-deflection and moment-curvature curves at midspan of CC2.2 beams

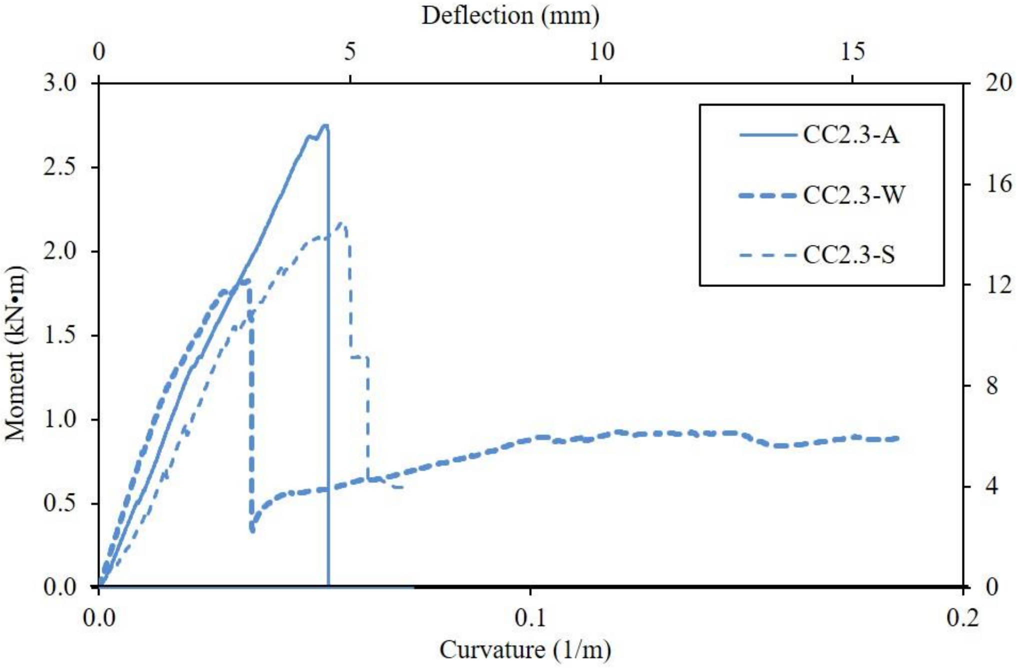

Figure 5.14 Load-deflection and moment-curvature curves at midspan of CC2.3 beams

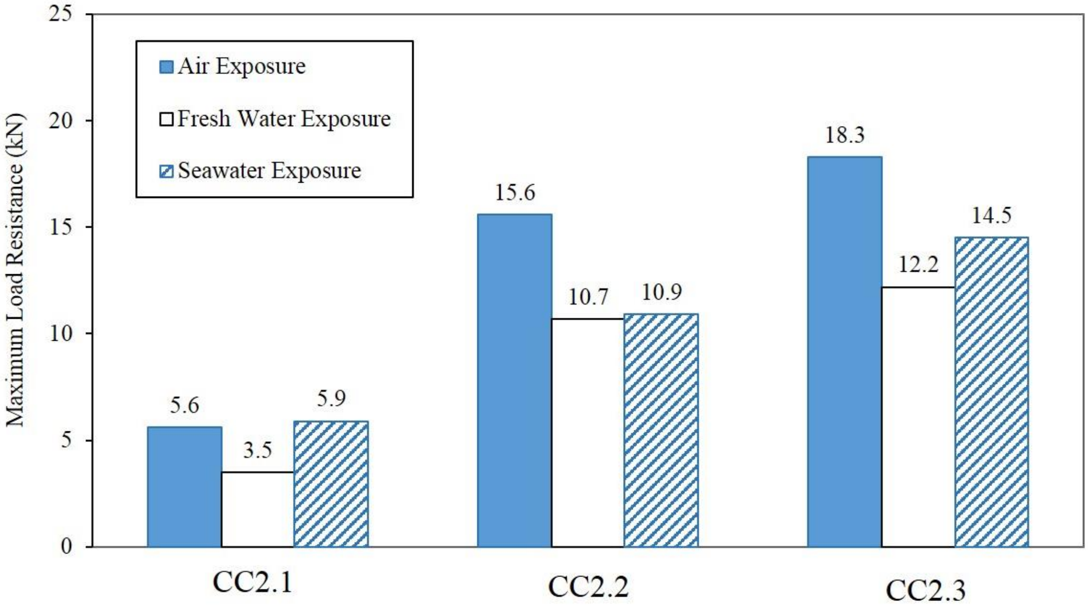

Figure 5.15 Load resistance at the failure of all jointed beams

5.4.3 Joint and Influence from Seawater

The CC2 beams had a thin epoxy-resin-connected joint which was designed to investigate the practicability of simply applying a flat face-to-face type of joint to flexural concrete members reinforced with FRP as well as to estimate the potential risks this joint might be exposed to in a marine environment. As a comparison reference, the polymer-fibrous CC1 beams previously discussed in Section 5.3 had the same tensile CFRP reinforcement ratio and exposure history as Beam CC2.1-W. CC2.1-W was tested to have a maximum load resistance of 3.5 kN with a deflection of 2.0 mm at the maximum load, which were less than half and around 65% of that from the fibrous beams respectively. Variables between these two beams included the concrete strength, addition of macro-synthetic fibres and presence of the joint. The concrete for CC2.1-W was measured to have a compressive strength of 63 MPa which was about 20% stronger than the fibrous mix. However, both CC1 and CC2.1-W were under-reinforced and designed to fail in a mode not by crush of concrete in compression. Accordingly, the concrete strength can be regarded as having negligible effects on the maximum load resistance at the failure in this test. Addition of macro-synthetic fibres is also considered as making nearly no contribution to the flexural capacity of the beam before concrete substantially cracks (The Concrete Society, 2007; Issa, et al., 2011). Therefore, it can be deduced that the designed flat face-to-face type of joint connected with the epoxy resin limited the development of the flexural load capacity for concrete members externally strengthened with CFRP.

Influence of the seawater is examined based on the measured load resistance and analysis of the CT scanned images. Beam CC2.1-A and CC2.1-S also had the same reinforcement ratio as the fibrous beams except that CC2.1-A was exposed in air while CC2.1-S was in the cyclic wetting/drying artificial seawater. CC2.1-A was tested to have a maximum load resistance of 5.6 kN and a deflection at failure of 3.6 mm. The load and deflection were around 80% of, and slightly over than, that of the fibrous beams respectively. Meanwhile, CC2.1-S resisted a maximum load of 5.9 kN and had a deflection at failure of 3.0 mm. The results from both CC2.1-A and CC2.1-S were higher than the fresh-water-exposed CC2.1-W (Figure 5.15). Logically the exposure conditions appeared to have affected the flexural strength of the beams externally strengthened with CFRP. Two factors could be responsible for this difference: presence of water and the sea salt ions. As previously reviewed in Section 2.2, CFRP and the epoxy resin are usually insensitive to seawater ions. Therefore, the designed exposures were not likely to cause any significant material deterioration or strength reduction on the CFRP. Additionally, CT images (test method in Section 3.9.5 and Appendix C.3) show that voids existed within the CFRP strengthening system (Figure 5.16). Based on calculation of the porosity, the defect volume ratio of the seawater-exposed sample was 15% greater than the fresh-water-exposed one (Table 5.1). Although the defect volume ratios for the three exposure conditions varied but they were overall under 1.5%. Therefore, the curing condition was probably a more important factor affecting the strength while the sea salt ions appeared to be less relevant. Consequently, it can be inferred that the bonding strength of the epoxy resin adhesive between concrete/concrete and concrete/CFRP can be affected by the curing condition, more specifically, the history of being exposed to water. This conforms to literature work reported by Zafer et al. (2012) that mechanical properties of epoxy resin adhesive reduce in water contributed to mainly by swelling of the composite caused from water absorption. From this test, it behaved in such a way that this reduction could be lessened when the epoxy resin adhesive is initially cured in air longer than 48 hours.

CC2.2 and CC2.3 beams were designed to be balanced and over-reinforced respectively. The maximum load resistance of CC2.2-S and CC2.3-S at the failure was measured as 10.9 kN and 14.5 kN respectively and CC2.2-A and CC2.3-A was 15.6 kN and 18.3 kN respectively. Correspondingly, for beams with the same CFRP reinforcing condition, the air-exposed ones showed a maximum load resistance about 30% greater than those cyclic-seawater-exposed while the fresh-water-exposed beams were the lowest.

Table 5.1 Calculated defect volume ratio of CFRP-strengthened concrete samples under different exposures

Exposure Condition	Air	Fresh Water	Cyclic Wetting/Drying Seawater
Defect Volume Ratio[1], %	1.39	0.96	1.11

[1]: including the concrete substrate.

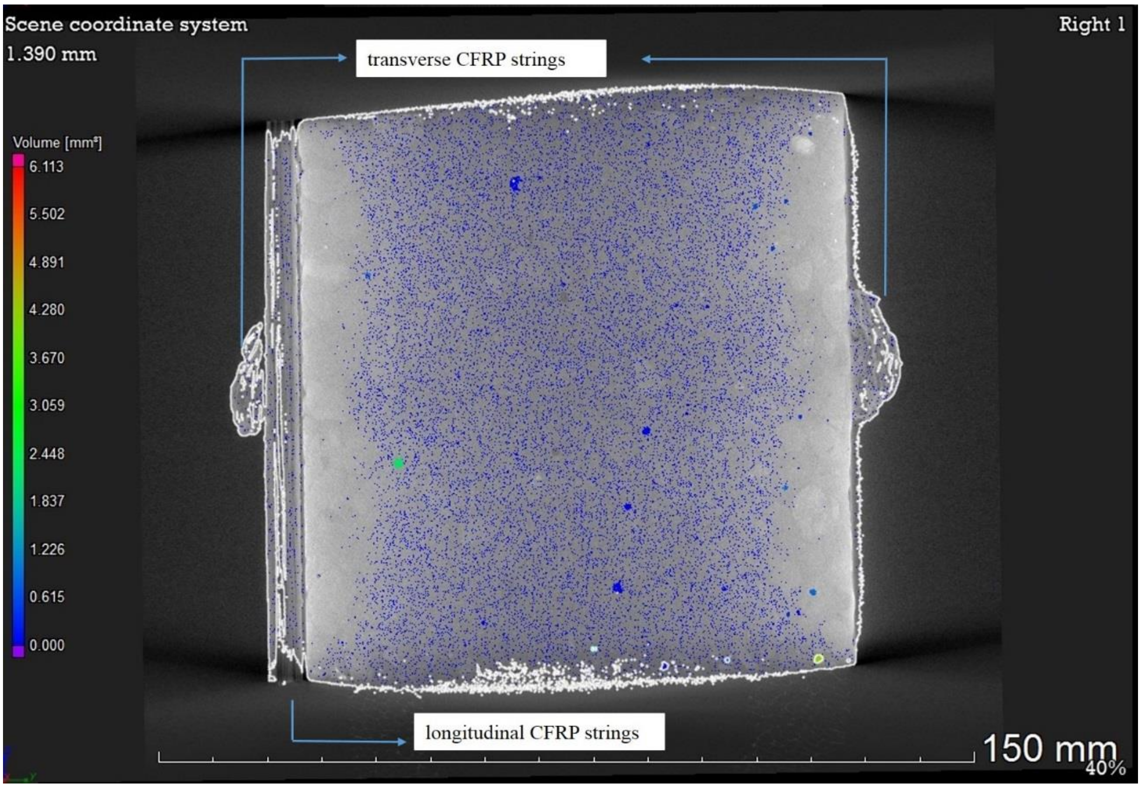

Figure 5.16 Results of porosity analysis for the cyclic-seawater-exposed CC2.3-S beam

5.5 Structural Analysis of FRP-Reinforced Members

5.5.1 Prediction of Ultimate Moment and Maximum Strain

The ultimate moment of tested FRP-reinforced beams is calculated utilising the prediction methods previously explained in Section 2.2 based on their tensile reinforcing conditions. The predicted results from both ACI 440.1R-06 (2006) and Pilakoutas et al (2011) method are given in Table 5.2 while the main calculating process is described in Appendix C1. On the other hand, possible maximum strains of the concrete in compression and the FRP reinforcements in tension at the beam failure are also estimated. The strain estimation is based on the same assumptions as ACI 440.1R-06 (2006) about such conditions as FRP reinforcement bond, stress distribution, calculating simplification etc. More specifically, the concrete compressive strain, ε_c, and the reinforcement tensile strain, ε_f, at the beam failure can be decided by solving the following binary quadratic formulae (Equation 5.1) with MathWorks® MATLAB software:

$$0.85\varepsilon_c E_c b \frac{\varepsilon_c}{\varepsilon_c+\varepsilon_f} d\beta_1 = \varepsilon_f E_f A_f \qquad \text{Equation 5.1}$$

with the following condition according to the mechanical properties of FRP and concrete:

$$\begin{cases} 0 < \varepsilon_c \ll 0.003 \\ 0 < \varepsilon_f \ll \varepsilon_{fu} \end{cases}$$

where ε_{fu} is the ultimate tensile strain of the FRP reinforcement.

Equation 5.1 is a mechanical equilibrium in terms of the compressive force provided by concrete (left part) and the tensile force provided by the FRP reinforcement (right part). Due to the lack of adequate boundary conditions, it is a range of solutions that is deduced from Equation 5.1. However, this range still provides an approximation of the possible tensile and compressive strain that the FRP and the concrete might have achieved at the beam failure under the bending test, respectively.

As shown in Table 5.2, both ACI 440.1R-06 (2006) and Pilakoutas et al. (2011) method underestimated the ultimate moment capacity of beams longitudinally reinforced with GFRP bars (GC1 and GC2). The ACI method was more conservative and had estimations approximately 20% less than the measured results. For the beams externally strengthened with CFRP strands (CC1 and CC2), both methods had estimations around 4 times greater than measured results for under-reinforced beams (CC1 and CC2.1) and around 3 times greater for over-reinforced ones (CC2.2 and CC2.3). Therefore, these methods which are recommended for beams reinforced with internal FRP bars appear to be not suitable for being directly adopted to compute the flexural strength of beams bonded with external FRP strands.

Two circumstances can be attributed to the prediction difference for beams strengthened with CFRP. Firstly, the bond-to-concrete mechanism for internal GFRP bars and external epoxy-resin-adhered CFRP strands is different. It is assumed that such perfect bond exists between CFRP and concrete that allows the longitudinally bonded CFRP to develop high tensile stress under the bending, based on the prediction assumptions. However, restricted by the failure type, the tensile CFRP multiple strands of the under-reinforced CC1 and CC2.1 beams were maybe not able to stress and strain as much as they were assumed in design. For example, ACI 440.1R-06 (2006) used the ultimate tensile strain of the CFRP composite (i.e.9100 $\mu\varepsilon$ based on the manufacturer-provided data) to figure the ultimate moment capacity of CC1 beams. However, as shown in Table 5.2, the actual maximum strain of the CFRP in tension was possibly between 5000-5600 $\mu\varepsilon$. This value matches the maximum tensile strain of the epoxy resin adhesive (around 6000 $\mu\varepsilon$). Secondly, the tensile strength of the CFRP strands might be not as strong as the manufacturer claimed. If using the measured 400 MPa strength from Section 4.4, the moment resistance of CC1 can be computed with the Pilakoutas et al. (2011) method as 0.9 kN·m, which is close to the measured results. Therefore, it appears that these existing methods cannot appropriately predict the flexural strength of beams externally strengthened with CFRP strands. Consequently, the formulae for computing the balanced CFRP reinforcement ratio would also be inaccurate. This calculation issue of the flexure design is more specifically discussed in Section 5.7.

Table 5.2 Measured and computed values of the ultimate moment and strains at failure

Series	Ultimate Moment, kN·m			Computed Strain at Failure, microstrain ($\mu\varepsilon$)	
	Experimental	ACI	Pilakoutas et al.	Concrete	Reinforcement
GC1	4.7	3.8	4.4	<2100	<6800
GC2	4.9	3.8	4.4		
CC1	1.2	5.4	5.6	500	5000-5600
CC2.1-A	0.9	5.3	4.2	400-450	2400-3000
CC2.2-A	2.3	7.7	5.5	≤400	<5200
CC2.3-A	2.8	8.9	6.5		

5.5.2 Crack Resistance Indices and Load-Carrying Capacity Drops

The developing and spreading process of cracking is essential for a floating device made of reinforced-concrete, especially for a non-truss structure. The process influences design of serviceability, durability as well as survivability under some accidental conditions such as storm hits and ship collisions. Accordingly, the concept of Crack Resistance Indices (CRIs) is introduced to reflect the cracking characteristics for flexural concrete members reinforced with FRP.

To chart the flexural response of the concrete beams reinforced or strengthened with FRP, the measured load-deflection curves are simplified and systematised according to their structural behaviour with designated points. These points include the first crack point (P_1), the failure point (P_2) and the collapse point (P_3). Figure 5.17 shows the simplified curves for the tested 4 series of FRP-reinforced beams in this study. The proposed CRIs include two factors representing the cracking behaviour of flexural concrete members reinforced with FRP at its ULS level (CRI_1) and at ALS level (CRI_2) respectively. Measures of the cracking should be related to common structural properties such as the load resistance, midspan deflection and area under the load-deflection curve which represents strength, deformability and energy absorption (toughness) respectively. Therefore, the two indices are proposed to be defined and expressed as follow:

$$CRI_{1L} = \frac{F_{P2} \cdot L_{P2}}{F_{P1} \cdot L_{P1}} \qquad \text{Equation 5.2 (a)}$$

$$CRI_{2L} = \frac{F_{P3} \cdot L_{P3}}{F_{P2} \cdot L_{P2}} \qquad \text{Equation 5.2 (b)}$$

or, from an energy point of view,

$$CRI_{2E} = \frac{E_{P2}}{E_{P1}} \qquad \text{Equation 5.3 (a)}$$

$$CRI_{2E} = \frac{E_{P3}}{E_{P2}} \qquad \text{Equation 5.3 (b)}$$

where F_{P1}, F_{P2} and F_{P3} are the load at P_1, P_2 and P_3 respectively; L_{P1}, L_{P2} and L_{P3} are the midspan deflection at P_1, P_2 and P_3 respectively; and E_{P1}, E_{P2} and E_{P3} are the area under the load-deflection diagram at P_1, P_2 and P_3 respectively.

It is worth noting that toughness measure at the ALS is different from the calculated E_{P3} aforementioned because the FRP-reinforced beams have had a nonlinear load-deflection behaviour after P_2. However, E_{P3} is used in this discussion since the CIRs are introduced for behaviour comparison rather than capacity scaling. Therefore, CRI_1 can be regarded as a parameter representing the range of serviceability design for an FRP-reinforced beam between when it starts to crack and before it reaches the ULS; meanwhile CRI_2 reflects the impact tolerance and energy absorption ability for the beam under the ALS.

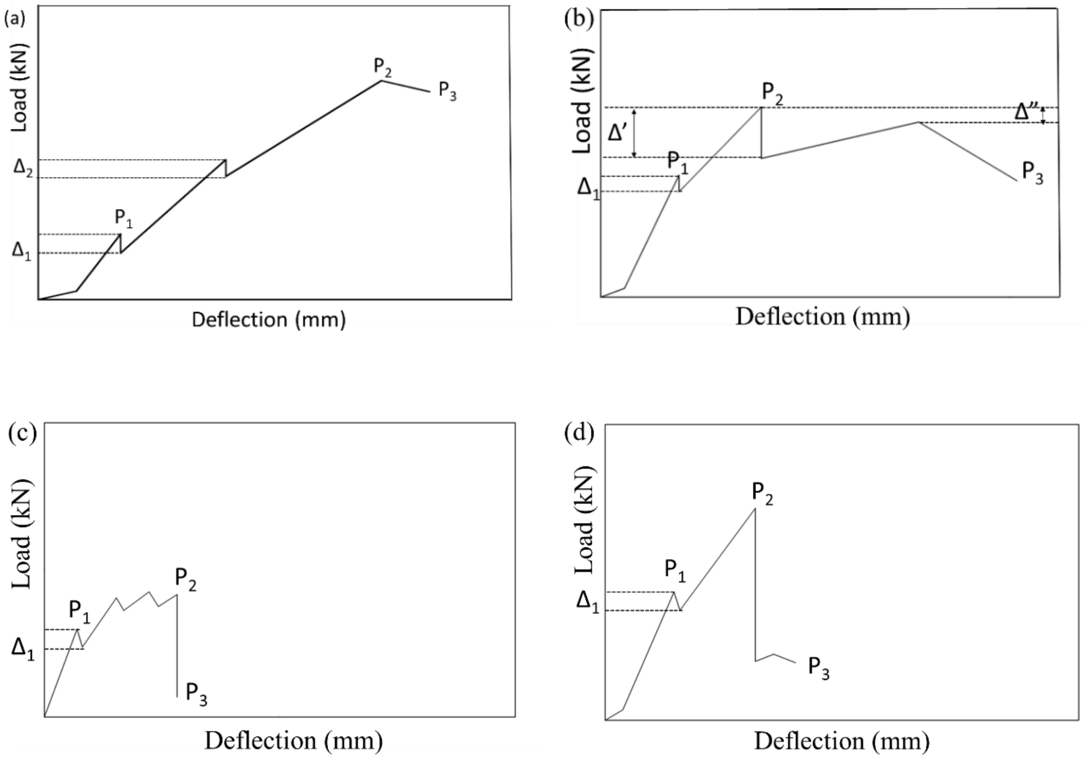

Figure 5.17 Simplified load-deflection curves of tested beam series: (a) GC1 and GC2, (b) CC1, (c) CC2.1 and (d) CC2.2 and CC2.3

The computed CRIs are presented in Table 5.3 together with data of load, deflection and area under the load-defection curve. As shown, the GFRP-reinforced beams present large CRI$_1$ but low CRI$_2$ which is only slightly above 1.0. When CRI$_2$ equals to 1.0, the flexural member fails in a brittle mode that the beam collapses once it reaches the ULS strength. This is usually caused by rupture of the FRP reinforcement for over-reinforced flexural sections. This type of failure is catastrophic for a floating WEC structure. On the other hand, the beams strengthened with CFRP strands mostly exhibited relatively small CRI$_1$, which means they have limited design range for the ULS in terms of controlling cracks. The addition of synthetic fibres at a dosage of 20 kg/m^3 or equivalently 2.2% by volume fraction of concrete enhanced the ALS behaviour of beams strengthened with external CFRP strands. This improvement is presented as an LCC recovery in Figure 5.8 and can be quantified as a CRI$_2$ parameter of more than 6.0 while the jointed beams (CC2.1) with the same reinforcing condition is only less than 2.1. Compared with CC1 beams, the CRI$_1$ data from CC2.1 beams with various exposures are all relatively higher albeit they varied individually. This indicates that the designed face-to-face joint connected with a thin layer of the epoxy resin adhesive structurally worked without shrinking the design range of the SLS for the tested under-reinforced concrete beams strengthened with CFRP strands.

It was noticed that tested beams reinforced with GFRP and strengthened with CFRP both experienced an LCC drop (Δ_1) at occurrence of their first crack while GFRP-reinforced beams also underwent another (Δ_2) before reaching the ULS. Measurement of Δ_1 and Δ_2 is defined as the amount of dropped load resistance divided by the maximum resistance that the beam had reached prior to the drop (i.e. F_{P1} and $F_{\Delta 2}$ for Δ_1 and Δ_2 respectively). Based on this definition, the computed results are expressed in percentage and charted as the histogram in Figure 5.18. It can be seen that GFRP-reinforced beams have Δ_1 drop by more than 50%, which means that loss of their flexural strength due to formation of the first crack was more than half. Considering that the elastic modulus of GFRP and concrete were under the same order of magnitude (i.e. 60 GPa and roughly 10 GPa respectively), it is rational to see this enormous loss of LCC at the first crack. When the concrete started to crack, the stiffness of the reinforced beam as a composite would reduce and a stiffness reduction by around 15% would occur if a perfect bond existed between GFRP rebar and concrete. However, the actual tensile elasticity of GFRP bar under bending might be less than the claimed datum due to such issues as bond and stress transferring. This might have resulted in Δ_1 being much higher than the theoretically calculated 15%. The GFRP-reinforced beams presented another LCC drop when the applied load achieved roughly 50% of the beams’ maximum load resistance, yet by approximately 10-20%. This might be attributed to the succeeding development of cracks and, with reference to previously discussed bond behaviour of GFRP bars in Section 4.2, the debonding between concrete and GFRP rebar. By contract, beams strengthened with CFRP strands had less noticeable Δ_1 and did not experience any Δ_2 drops. More specifically, CC1 beams experienced an LLC drop of Δ_1 by less than 5% while the jointed CC2.1 beams with the same reinforcing condition underwent the Δ_1 by nearly 20% due to the lower maximum load resistance of the latter.

Table 5.3 CRI factors of all tested beams and load, deflection and area under the load-deflection curve at P1, P1 and P3

Beam	P1			P2			P3			Load-Defection Appr.		Energy Appr.	
	F_{P1}, kN	L_{P1}, mm	E_{P1}, kN·mm	F_{P2}, kN	L_{P2}, mm	E_{P2}, kN·mm	F_{P3}, kN	L_{P3}, mm	E_{P3}, kN·mm	CRI_{1L}	CRI_{2L}	CRI_{1E}	CRI_{2E}
GC1-1	13.7	0.9	4.4	72.8	7.7	96.4	70.7	8.5	299.8	45.5	1.1	21.9	3.1
GC1-2	13.1	0.7	3.4	62	7.0	229.0	59.2	8.6	322.7	47.3	1.2	66.8	1.4
GC2-1	11.5	0.6	2.5	67.4	6.7	250.3	60.1	10.5	509.4	65.4	1.4	100.5	2.0
GC2-2	13.2	0.7	3.7	65.6	6.7	244.2	62.0	6.9	256.3	47.6	1.0	66.9	1.0
GC2-3	13.2	0.6	3.2	69.4	7.0	263.3	65.5	9.7	450.3	61.3	1.3	81.5	1.7
CC1-1	6.0	1.6	4.5	9.0	3.6	19.9	5.0	20.0	126.4	3.4	3.1	4.4	6.4
CC1-2	5.9	1.6	5.2	7.2	2.8	13.3	6.2	20.0	140.3	2.1	6.2	2.6	10.5
CC1-3	5.5	1.4	3.5	7.1	3.0	13.6	2.0	20.0	92.9	2.8	1.9	3.9	6.8
CC2.1-A	4.4	1.0	1.9	5.6	3.5	13.2	1.7	3.7	14.2	4.5	0.3	6.9	1.1
CC2.2-A	8.7	3.2	14.4	15.6	6.1	49.9	5.4	10.0	66.7	3.4	0.6	3.5	1.3
CC2.3-A	9.2	2.0	9.0	18.3	4.5	44.5	1.5	4.6	45.3	4.5	0.1	4.9	1.0
CC2.1-W	2.5	0.6	0.6	3.5	2.0	4.9	1.1	3.0	6.0	4.7	0.5	8.2	1.2
CC2.2-W	6.1	1.4	4.3	10.7	3.8	26.0	0.9	3.9	26.3	4.8	0.1	6.0	1.0
CC2.3-W	8.8	1.6	7.8	12.2	3.0	22.4	4.3	5.3	31.8	2.6	0.6	2.9	1.4
CC2.1-S	1.4	1.1	0.8	5.9	3.0	6.3	4.7	4.8	13.5	11.5	1.3	7.9	2.1
CC2.2-S	8.5	3.0	11.3	10.9	4.5	25.6	1.3	4.9	29.3	1.9	0.1	2.3	1.1
CC2.3-S	4.8	1.3	2.8	14.5	4.8	40.0	4.0	6.0	48.0	11.2	0.3	14.3	1.2

P1: First crack point; P2: Failure point; P3: Eventual collapse point. Appr. = Approach

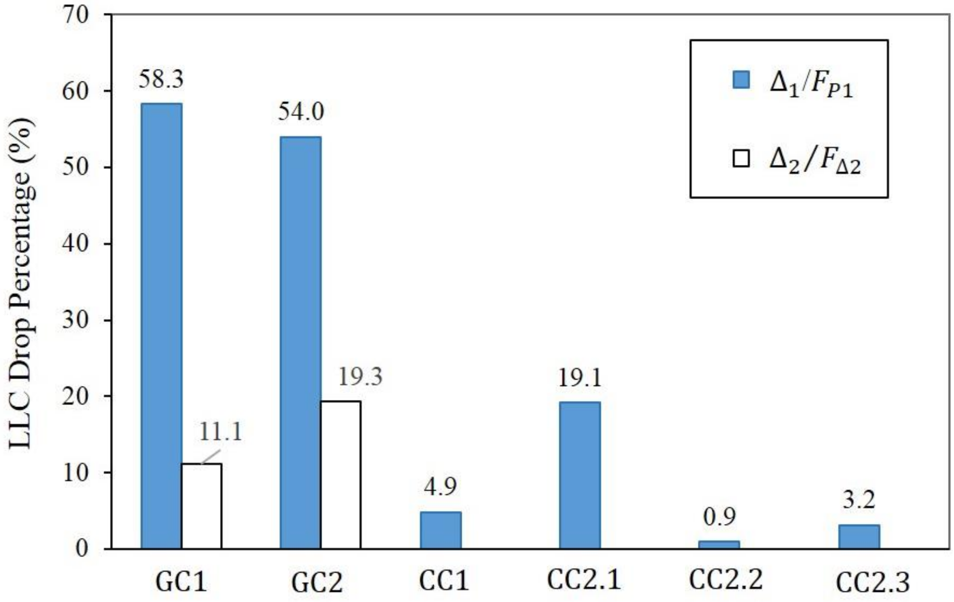

Figure 5.18 LCC drop percentage for beams reinforced or strengthened with FRP

5.5.3 Prediction of Shear Resistance

Similar to conventionally reinforced concrete sections, the nominal shear capacity of an FRP-reinforced concrete member (V_n) should be the sum of the shear resistance provided by concrete (V_c) and by the FRP shear reinforcement (V_f) (American Concrete Insititute, 2006). According to ACI 440.1R-06 (2006), the shear resistance of V_f can be computed from Equation 5.4 and 5.5:

$$V_f = \frac{1}{s} A_{fv} f_{fv} d \qquad \text{Equation 5.4}$$

$$f_{fv} = 0.004 E_f \le f_{fb} \qquad \text{Equation 5.5}$$

where *s* is the stirrup spacing or pitch of continuous spirals, mm; f_{fb} is the strength of the bent portion of FRP bar, MPa;

The concrete shear capacity (V_c) of flexural members reinforced with GFRP rebar as the main tensile reinforcement can be evaluated with Equation 4.2 proposed by the author previously in Section 4.3.2. According to Equation 4.2 and 5.4, the computed values of shear contribution of V_c and V_f are listed in Table 5.4 meanwhile the computing details are explained in Appendix C.2.

Table 5.4 Calculated shear resistance contribution of concrete and FRP shear reinforcement

Beam	Shear Resistance Contribution, kN		Shear Resistance, kN	
	V_c	V_f	V_n	Measured
GC1	16.0	27.9	43.9	33.7
GC2	16.0	36.8	52.8	33.8

As illustrated above, the two tested types of CFRP shear reinforcement (internal CFRP ‘sticks’ and external CFRP strands) should have provided shear resistance approximately 30-50% greater than the applied maximum shear load. This prevented these GFRP-reinforced beams from failing in shear. Additionally, the V_c shear contribution provided from concrete for GC1 is evaluated to be around 3.7 kN with the ACI 440.1R-06 (2006) method. In such a case, the shear resistance of the flexural member would be insufficient (31.6 kN, less than the measured 33.7 kN) and the beams would have failed in shear but they did not. This fact also supports the point that Equation 4.1 underestimates the shear contribution from the uncracked section of an FRP-reinforced flexural member.

5.6 Synopsis of Structural Behaviour of FRP-RC Members and Joint

(1) Reinforcing concrete with GFRP rebar for flexure

Reinforcing concrete with GFRP bars for flexure behaved in a structurally feasible way albeit the reinforced members usually developed large deflection and big flexural cracks. If designed to be over-reinforced, these concrete sections can fail in a mode governed by concrete crush in compression, but it is still a sharp failure type.

(2) Strengthening concrete with external CFRP strands for flexure

Strengthening concrete with external CFRP strands and epoxy resin as the bonding agent was relatively unsatisfactory for providing flexure mainly because of the lower stiffness of the adhesive material, hence the insufficient bond between CFRP and concrete. It is not logically feasible to bond external CFRP strands longitudinally to the underneath face of flexural concrete members as the only or main tensile reinforcement to provide high tensile strength, because flexural cracks starting from the extreme fibre in tension can usually result in debonding between CFRP strands and concrete. Once debonding starts, the strengthening effects of CFRP strands will be strongly affected.

(3) Reinforcing concrete with FRP for shear

Reinforcing concrete with internal CFRP bars and external CFRP strands for shear were both satisfactorily effective. If sufficient shear reinforcement is provided, GFRP bars can resist shear stress at the designed levels. The fully-wrapped external CFRP strands with suitable anchorage can also provide required shear resistance as well as extra confinement against the flexural deformation of the concrete member; if there is no big shear crack formed, debonding of the fully-wrapped CFRP strands does not usually occur.

(4) Reinforcing concrete with macro-synthetic fibres

Reinforcing concrete with macro-synthetic fibres randomly distributed as the secondary reinforcement at required dosages was effective in terms of improving toughness and increasing energy absorption capacity at the post-ULS, however the synthetic fibres at a high dosage can usually take a large amount of volume for mixing.

(5) Thin concrete-concrete joint with epoxy resin adhesive

The flat face-to-face type of joint grouted with a thin layer of epoxy resin adhesive was relatively incapable of providing moment resistance when without any dowels. Bond with epoxy resin as the grouting material is also critical because debonding can easily happen within the concrete/epoxy interface. However, this separating issue can be comparatively ameliorated by bonding additional CFRP strands perpendicularly to the joint direction.

5.7 Design Considerations of Flexure and Shear

5.7.1 Flexural Design Considerations

Flexural strength of reinforced concrete sections containing internal GFRP bars can be properly determined with the existing methods. The methods recommended by ACI 440.1R (2006) and Pilakoutas et al. (2011) provide predictions of the flexural strength approximately 20% and 10% less than the measured results respectively; however, this is reasonably conservative.

Flexural strength of strengthened concrete sections with CFRP strands externally bonded with the epoxy resin adhesive cannot be accurately determined with the aforementioned methods. However, these methods can be modified with consideration of limits of the epoxy resin and influences of the tensile crack development. According to the structural behaviour of the tested beams, the maximum design tensile stress of the CFRP strands should be computed from Equation 5.6 and 5.7 instead:

$$f_{fu} = \varepsilon_{fu} E_f \qquad \text{Equation 5.6}$$

$$\varepsilon_{fu} = min\{\varepsilon_{epoxy,}\ \varepsilon_{cfrp}, 0.005\} \qquad \text{Equation 5.7}$$

where ε_{epoxy} is the maximum tensile strain of the epoxy resin adhesive and ε_{cfrp} is the maximum tensile strain of the bonded CFRP; 0.005 is the computed maximum strain of bonded CFRP in tension from the under-reinforced CC1 beams (Table 5.2).

The Concrete Society Technical Report No. 55 (2012) suggested a value of 0.008 for the computed maximum strain of bonded CFRP in tension in Equation 5.7. From this study, it is found that a maximum tensile strain of 0.005 exists due to the limit of the epoxy resin adhesive.

The values of f_f and ε_f determined with Equation 5.6 and 5.7 should be used for figuring the balanced reinforcement ratio with Equation 2.2 proposed by ACI 440.1R-06. Based on the reinforcing condition, the flexural strength can then be computed with the same formulae suggested by ACI 440.1R-06 (2006) or Pilakoutas et al. (2011). Additionally, considering that voids are known to exist within the bonded CFRP strands from the CT images (Figure 5.16), a safety factor of 1.3 needs to be taken for the tensile reinforcement area (A_f). This value is proposed based on analysis of the area of the voids over the area of the strengthening strands whose details are explained in Appendix C.3. However, the confidence level of this safety factor is not validated in this section and might be depended on the material manufacturing and applying method.

According to the modifications, the balanced reinforcement ratio of the flexural concrete members externally strengthened with CFRP strands should be 1.3% rather than 0.5%. Therefore, the CC2.2 and CC2.3 beams should be regarded as under-reinforced as well.

Based on the new classification and calculation methods, the ultimate moment resistance of CC1 is re-evaluated to be 2.6 kN·m, while the jointed CC2.1, CC2.2 and CC2.3 beams are 2.6, 5.2 and 7.8 kN·m respectively. The modification still provides predicted values around 2 times greater than the measured results. This difference between the theoretical calculation and experimental behaviour demonstrates that externally strengthening CFRP strands at the underneath face of flexural concrete beams is relatively ineffective in terms of providing flexure strength. As previously discussed, the tensile strength of the CFRP composite might be not as great as the supplier has claimed. If using the measured tensile strength of CFRP in Section 4.5 (i.e. 400 MPa) but the same modified computing method of the maximum tensile strain (Equation 5.7), the ultimate moment resistance of CC2.1, CC2.2 and CC2.3 is computed to be 0.9, 1.8 and 2.7 kN·m respectively, which is close to the measured results (Figure 5.19).

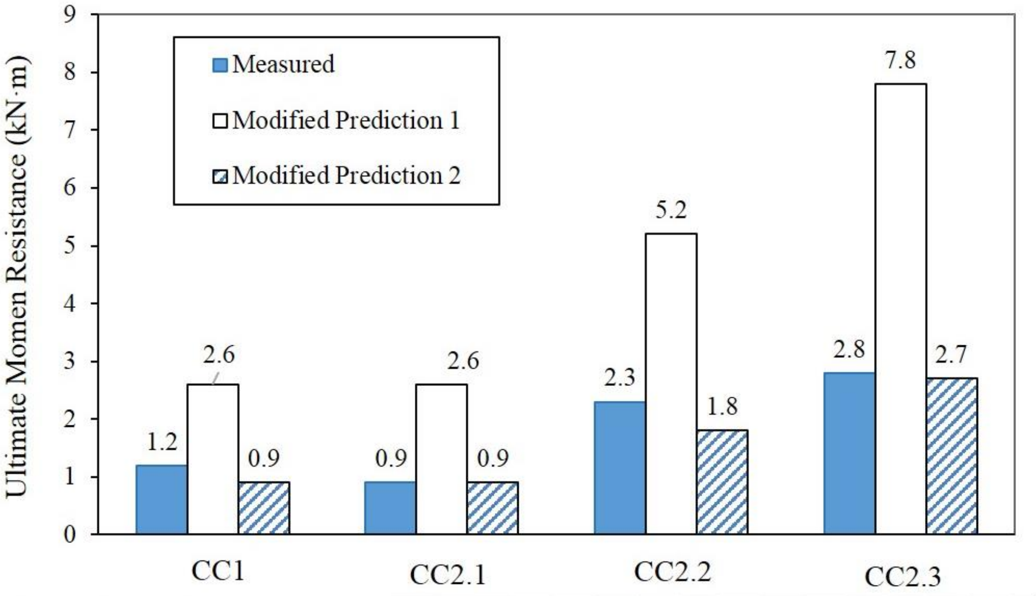

Modified Prediction 1: Pilakoutas et al (2011) Method; Equation 5.6 and 5.7 for f_{fu} and ε_{fu} respectively;
Modified Prediction 2: Pilakoutas et al (2011) Method; Measured f_{fu}; Equation 5.7 for ε_{fu};

Figure 5.19 Modified prediction of the ultimate moment of CFRP-strengthened beams

5.7.2 Shear Design Considerations

For flexural concrete members reinforced with longitudinal GFRP bars for flexure and CFRP bar ‘sticks’ or bonded CFRP strands for shear, the shear strength contribution of the FRP shear reinforcement can be appropriately evaluated with the formulae proposed by ACI 440.1R-06 (2006); meanwhile the shear strength contribution of longitudinal FRP reinforcement in term of dowel action and of uncracked concrete should be computed using the modified method. Therefore, the shear strength of FRP-reinforced members can be evaluated as:

$$V_n = V_c + V_f \qquad \text{Equation 5.8}$$

where $V_c = 0.4kk_a\sqrt{f_c}b_w d$ and $V_f = \frac{1}{s}A_{fv}f_{fv}d$

5.8 Summary

It is observed from the quasi-static load-deflection results that flexural concrete beams reinforced with GFRP bars were able to reach their designed ultimate strength level while the beams externally strengthened with CFRP were not, because of the limit of the epoxy resin adhesive in transferring tensile stress and strain. The failure of GFRP-reinforced flexural beams was brittle. A flat face-to-face type of joint with a thin epoxy resin layer (around 3 mm) was relatively unsatisfactory in structurally connecting concrete beams because of the lower elasticity of the grouting material and its potentially weak bond of concrete/concrete if the concrete surface was not specifically prepared. Beams reinforced or strengthened with FRPs usually presented declines and recoveries of their load carrying capacity at the occurrence of their first crack. Beams reinforced with GFRP bars also had a few more declines and recoveries before the ULS level, which was possibly due to the low stiffness of the GFRP and gradual bond failure when the applied load was increasing. This should be an awareness to be covered for design but not yet currently. It is also observed that development of the bond strength of the epoxy resin material was relatively sensitive to its curing condition and history where curing in both fresh and seawater could generally decrease the bond strength of the adhesive compared with in air.

A concept of the Crack Resistance Indices (CRIs) is introduced to estimate the structural performances in the post-ULS stage of concrete members reinforced or strengthened with FRPs to evaluate their toughness behaviour and energy absorption capacity at the ALS. The addition of macro-synthetic fibres at designed dosage can prevent the FRP-reinforced beams from failing in a sharply brittle mode and significantly improves the toughness. The toughness improvement can be quantitatively assessed by means of the proposed CRI parameters. Current design guidelines and literature recommendations underestimate the flexure strength of concrete beams reinforced with GFRP bars while for concrete beams strengthened with external CFRP multi-strands, the estimation needs to be modified with consideration of the adhesive behaviour. CFRP bars and external CFRP strands were both practical in providing shear resistance without suffering from any serious material rupture or bond separation. Their shear strength contributions could be properly evaluated by the ACI 440.1R-06 (2006) guide.

Chapter 6 Structural Behaviour of Concrete Reinforced with Aligned Steel Fibres

6.1 Introduction

The structural behaviour of flexural concrete sections reinforced with aligned steel fibres, influence of the fibre dosage, alignment effectiveness, concrete strength and GGBS are discussed in this chapter. According to the test objectives, the aligned fibrous beams are divided into 5 groups and named as SF1 (includes SF1.1, 1.2 and 1.3), SF2, SF3, SF4 and SF5 respectively. SF1 contained beams with varied fibre dosages ranging from 80 kg/m^3 to 160 kg/m^3. SF2 had one beam with externally bonded CFRP strands in its shear spans to investigate influence of different types of shear reinforcement. SF3 had one beam with steel fibres at a total dosage of 120 kg/m^3 but randomly distributed in three layers while SF4 and SF5 were designed to estimate influence of the GGBS and concrete strength respectively. Details of these aligned fibrous specimens are given in Section 3.9.4.

6.2 Structural Behaviour of Concrete with Aligned Steel Fibres

6.2.1 Crack and Failure Mode

SF1.1, 1.2 and 1.3 had 2, 3 and 4 layers of aligned steel fibres respectively. Within each layer was spread an amount of 400 g of steel fibres, which was equivalent to 40 kg/m^3 by dosage. Therefore, these beams had total fibre additions around 80, 120 and 160 kg/m^3 respectively. Additionally, SF1.2 and SF1.3 had their first layer of fibres aligned from the bottom face of the beam while SF1.1 started from a depth of 15 mm. As a reference, one concrete beam, reinforced with an Ø10 mm carbon steel rebar for tension and three steel stirrups 100 mm apart in each shear span, was also produced and subjected to the bending test. Design of this reference beam was according to Eurocode 2.

These 3 sets of beams together with the traditionally steel-bar-reinforced control beam all failed in a flexural failure mode. Figure 6.1 presents a cracking pattern of one beam from SF1.3 at the failure. As can be seen, it was mainly big flexural cracks that developed in the middle pure-bending zone and led to the beam failure. For SF1.2 beams, a few small diagonal cracks also occurred close to the load-applying point in the shear span. However, these cracks generally developed after the beam failed and while the beam continued deforming. These shear cracks were relatively narrow in width even though they also spread over the nominal neutral axis eventually at the ALS. On the other hand, compared with the control beam, cracks of the fibrous beams were generally wider which suggested that the latter were less stiff than the conventional steel-bar-reinforced beam. These load-deflection curves discussed in the following Section 6.2.2 also presented this difference in terms of the curve slope stiffness.

SF1.2 and SF1.3 both had 1 layer of aligned fibres at the very bottom face of the concrete and some of these steel fibres were not completely covered by mortar. On exanimation it was observed that minor corrosion occurred at those uncovered fibres after the 28-days curing in water. Since the fibres were not connected, corrosion happened to only some of the individual filaments (Figure 6.2) and was not in a mass of flaking coating in the way that steel rebar usually rusts. Therefore, the minor corrosion can be considered as having negligible influence on the flexural strength of the beams. No delamination of concrete between the bottom face of the beam and the first layer of aligned fibres happened during the bending test. Since the steel fibres did not yield, the beams broke in a mode that the fibres were pulled out from the concrete substrate within cracked sections at the ALS state (Figure 6.3).

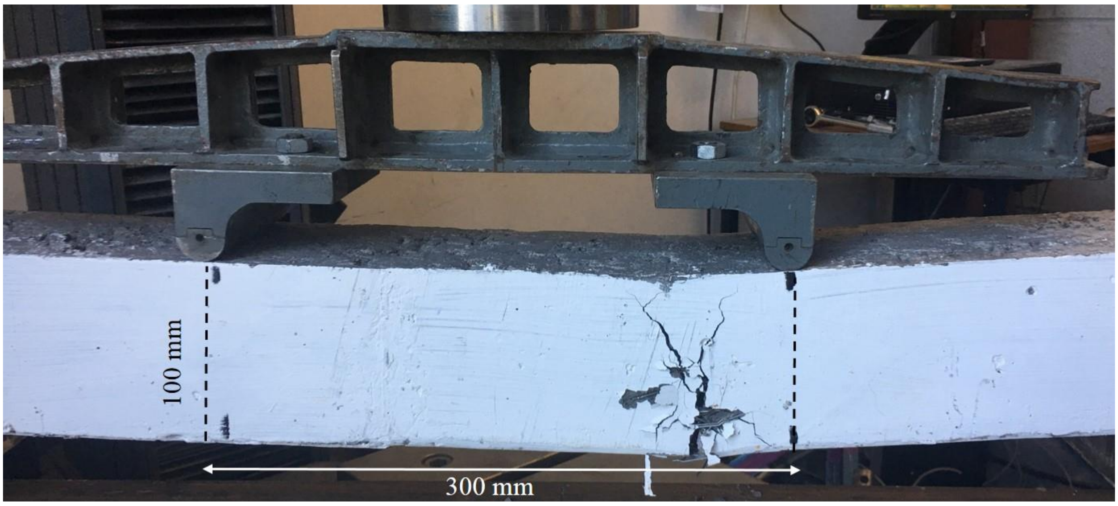

Figure 6.1 Crack and failure of the concrete beam reinforced with aligned steel fibres

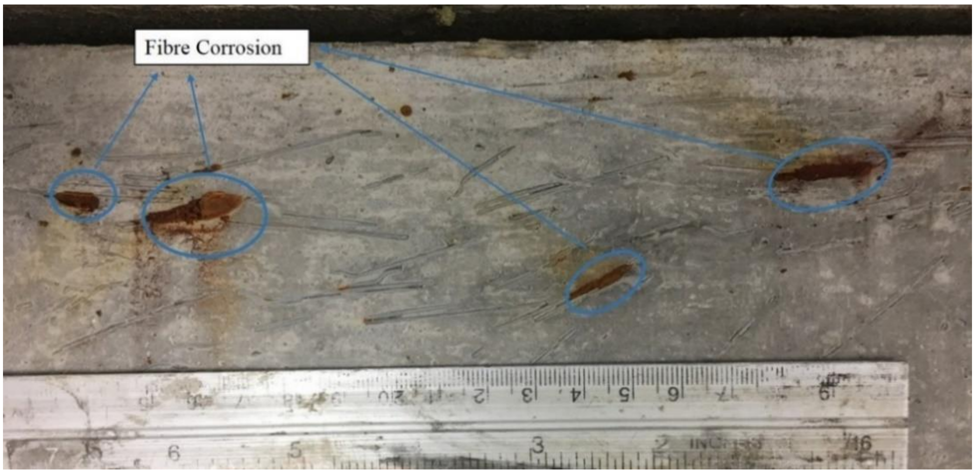

Figure 6.2 Minor corrosion of uncovered steel fibres at the bottom face of the beam

Figure 6.3 Aligned steel fibres at the cracked section of the beam after the bending

6.2.2 Load-Deflection Behaviour and Influence of Fibre Dosage

Structural behaviour of the aligned-fibre-reinforced beams tested in flexure is presented in terms of their measured load-deflection curves at the midspan section in Figure 6.4 for SF1.1, SF1.3 and the reference beam, and Figure 6.5 for SF1.2 respectively. Average values of the measured maximum load resistance, midspan deflection at the maximum load, elastic stiffness as well as the energy absorption capacity for all beams are presented in Table 6.1. For the reference beam, the maximum load resistance was chosen from its yield point.

To carry out direct comparison of the flexural strength between the fibrous beams and the reference beam which was conventionally reinforced with carbon steel rebar, a calibrating method is proposed based on both equivalent mass of steel and equivalent area of steel for the tensile reinforcement. The calibration details are explained in Appendix C.5 while the adjusted values of the maximum load resistance for each type of beam are given in Table 6.1. Concisely, the calibration suggests a safety factor of 1.23 for the alignment effectiveness to clarify the orientation and distribution of the aligned steel fibres. Based on the proposed calibration, for an equivalent addition of steel fibres at 100 kg/m^3, the beam reinforced with aligned steel fibres would usually have a maximum load resistance of between 6.1-8.3 kN while the one with steel bars would be around 17.2 kN. Therefore, at the suggested level of aligning efficiency, the steel fibres can be expected to provide a tensile strength contribution of around 40% of the conventional steel bar. The proposition of the safety factor for alignment effectiveness did not consider the depth of aligned steel fibres and assumed that there were no big gaps of fibres missing within every effective layer.

As shown in Table 6.1, an increased amount of longitudinally aligned steel fibres resulted in an improved flexural load resistance of the beams. When the fibre dosage was increased from two layers of around 80 kg/m^3 (SF1.1) to three layers of around 120 kg/m^3 in total (SF1.2), the maximum load resistance was improved from 6.6 kN to 7.8 kN on average, which was by approximately 20%. Similarly, when the fibre dosage continued to increase from 120 kg/m^3 to 160 kg/m^3 (SF1.3), the maximum load resistance was also improved by slightly over 20%. Therefore, at the range of managed amounts of aligned steel fibres in this study, the flexural strength of the beam was in direct proportion to the fibre dosage. If defining the point where the beam’s load resistance fell below 20% of its maximum capacity as the eventual rupture of the member, the energy absorption of the steel-fibre reinforced beams at ALS can be calculated in terms of the area under their load-deflection curves. It was found that the energy absorption of SF1.2 and SF1.3 both increased by more than 20% compared with SF1.1 and SF1.2 respectively. Therefore, the fibre dosage was also important for the toughness behaviour of the beams. The relations between the fibre dosage and the structural behaviour of the beams are presented in Figure 6.6 and 6.7

in terms of maximum load resistance, midspan deflection, energy absorption capacity and adjusted maximum load at an equivalent dosage of 100 kg/m^3.

As shown, the steel fibre dosage that can be aligned in to the concrete played a significant role in improving the structural behaviour. With increased layers of aligned steel fibres, the beams exhibited enhancements in both strength and toughness. For example, when the addition of steel fibres was increased from 80 kg/m^3 to 160 kg/m^3, the load-carrying capacity and the energy absorption ability at the ALS were improved by nearly 50% and 53% respectively. However, by comparing the calibrated maximum load resistance at an equivalent dosage of 100 kg/m^3, it is found that the addition of highest steel fibre dosage had the lowest equivalent load resistance. In other words, the mobilisation efficiency of aligned fibres in terms of providing flexural strength decreased when a larger amount of fibres was aligned into the concrete. For example, when the total addition was increased from 80 kg/m^3 to 160 kg/m^3, the specific contribution of the aligned fibres per 100 kg/m^3 decreased from 8.3 kN to 6.1 kN, which was by more than 30%. This is because that the strength contribution of each fibre layer is limited by its depth. The closer to the nominal neutral axis the aligned fibre layer is, the less flexural strength these fibres will contribute theoretically under the bending.

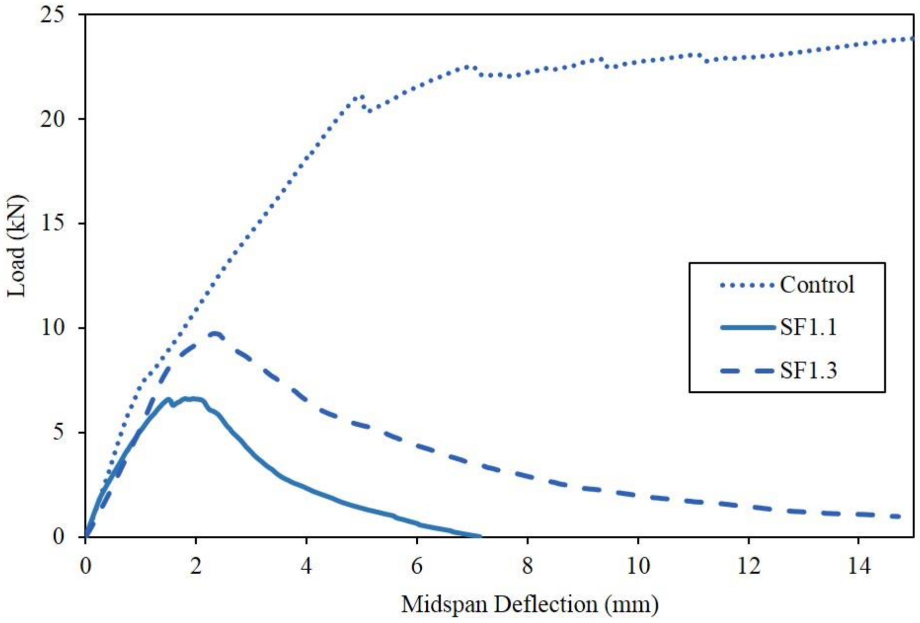

Figure 6.4 Load-deflection curves at midspan of SF1.1, SF1.3 and the control beam

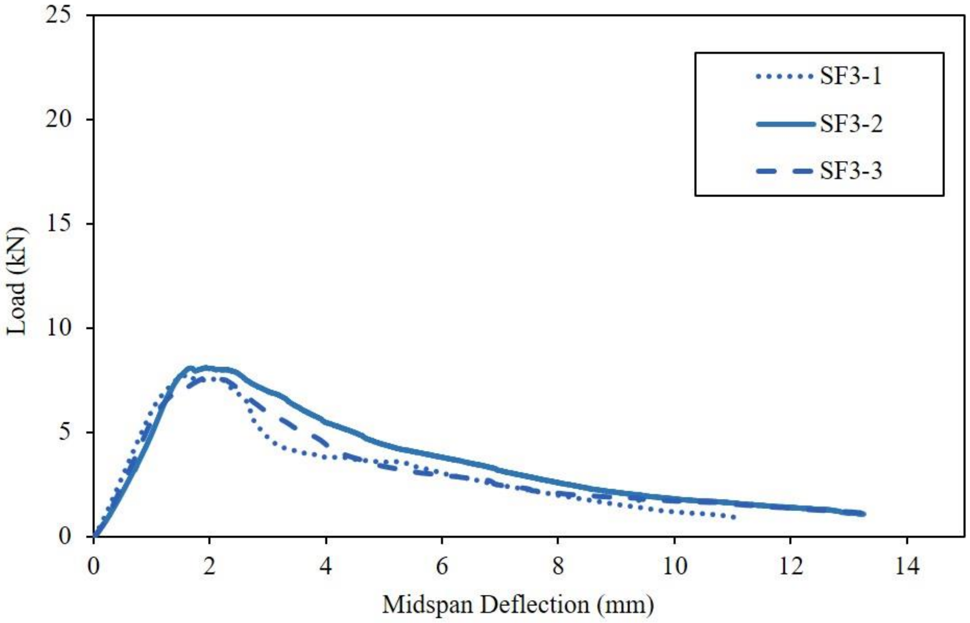

Figure 6.5 Load-deflection curves at midspan of SF3 beams

Table 6.1 Results and calibrated maximum load resistance of aligned-steel-fibre-reinforced beams

Beam Series	Fibre Dosage, kg/m^3	Fibre Layer	Max. Load, kN	Deflection[a], mm	Curve Slope[b]	Energy Absorption[c], N·m	Adjusted Max. Load[d], kN
Control	0	0	21.2	5.0	5.8	41.9	17.2
SF1.1	80	2	6.6	1.8	4.5	17.6	8.3
SF1.2	120	3	7.8	2.0	5.7	21.9	6.5
SF1.3	160	4	9.7	2.3	4.6	26.9	6.1
SF2	80	2	6.0	1.9	5.5	16.6	7.5
SF3	120	3	5.0	2.8	3.7	16.6	4.2
SF4	120	3	8.1	1.8	5.1	22.7	6.8
SF5	120	3	7.9	2.0	5.1	22.3	6.6

[a]: at the maximum load; [b]: elastic stage; [c]: area under the load-deflection curve up until a deflection of 4 mm; [d]: at equivalent 100 kg/m^3 dosage.

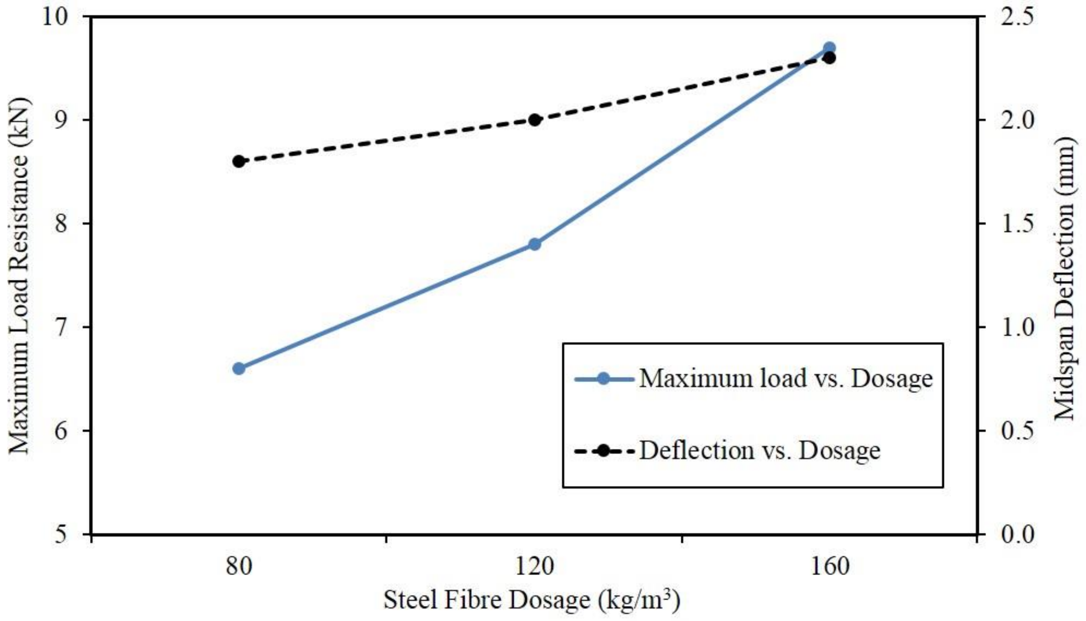

Figure 6.6 Relations between maximum load, deflection and aligned fibre dosage

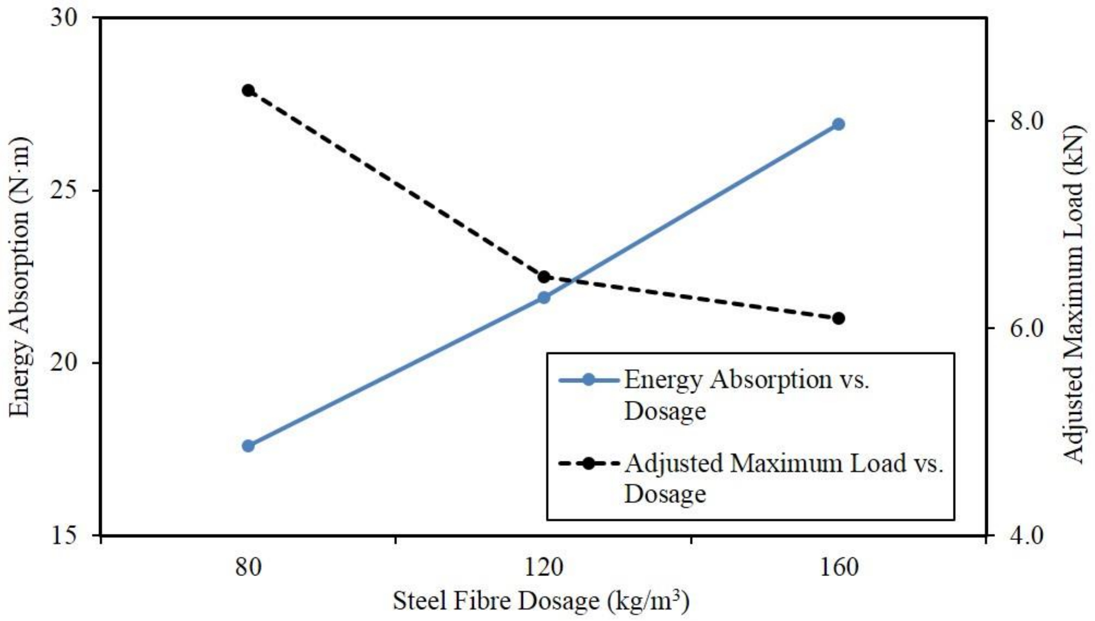

Figure 6.7 Relations between energy absorption, adjusted maximum load and aligned fibre dosage

6.2.3 Shear Behaviour of Aligned Steel Fibres

To compare the shear contribution of aligned steel fibres as well as to avoid the beams reinforced with only steel fibres failing in shear under the bending test, SF1.2 and SF2 were prepared with aligned steel fibres above the nominal neutral axis and with externally fully-wrapped CFRP strands as the shear reinforcement respectively. The steel fibres were aligned above the nominal neutral axis only within the shear spans at an approximate dosage of 20 kg/m^3 per shear span while the CFRP strands were wrapped 100 mm apart at the shear spans. Since both sets of beams did not fail in a shear mode, the shear strength of the aligned steel fibres was not directly measured. However, the failures show that the longitudinally aligned steel fibres were also able to provide required shear resistance. This could be attributed to some fibres perhaps having vertical components in the orientation and consequently providing resistance to the applied shear stress. This distribution issue is more specific discussed in Section 6.4.

6.3 Influence of Concrete Mix (GGBS) and Concrete Strength

GGBS is often used as a material to partly replace cement and to potentially improve the bond of conventional steel rebar in concrete due to its filler effect (Cheng, et al., 2005). For SFRC, addition of GGBS also reportedly (Tuyan & Yazici, 2012; Mo, et al., 2014) increases the fibres’ bond to concrete. Since steel fibres do not yield under the bending, use of GGBS and increase of the concrete strength can possibly enhance the bond between concrete and fibres and, consequently improve the flexural strength behaviour of SFRC.

SF4 beams had a concrete mix of 40% GGBS (160 kg/m^3) while SF1.2, as a control beam, had a fibre addition at the same dosage but a mix of 30% DFA (120 kg/m^3) instead. The concrete strength of both these two mixes was measured to be around 64 MPa. Compared with SF1.2, the structural behaviour of SF4 was only slightly improved (Figure 6.8). More specifically, the load-carrying capacity and the flexural deformation at the failure of SF4 increased by less than 5% and reduced by around 10% respectively. The energy absorption at the ALS (defined as the area under the load-deflection curve) of SF4 was also roughly the same as SF1.2. Therefore, use of GGBS instead of DFA to partly replace the Portland cement was not beneficial on improving the flexure strength of aligned-steel-fibre-reinforced beams. Since steel fibres do not yield at the cracked sections, the load-carrying capacity of the beams should be theoretically related to the bond-to-concrete of the steel fibres. Therefore, it is reasonable to conclude that the increase of the bond by adding the GGBS binder did not contribute to increasing the flexural strength of the beam at the tested fibre dosage.

SF5 beams had a concrete mix with a reduced 0.3 w/c ratio and was measured to have a compressive strength of 80 MPa at 28 days standard curing. As presented in Figure 6.8 of the results from SF1.2, SF4 and SF5, an increase of concrete strength by nearly 20 MPa did not necessarily enhance the beam's structural behaviour. Higher concrete strength and addition of the GGBS binder can both theoretically lead to a stronger fibre-matrix bond. However, increase of the bond appeared to not be a determining factor at an aligned fibre addition of 120 kg/m^3 for concrete stronger than 60 MPa.

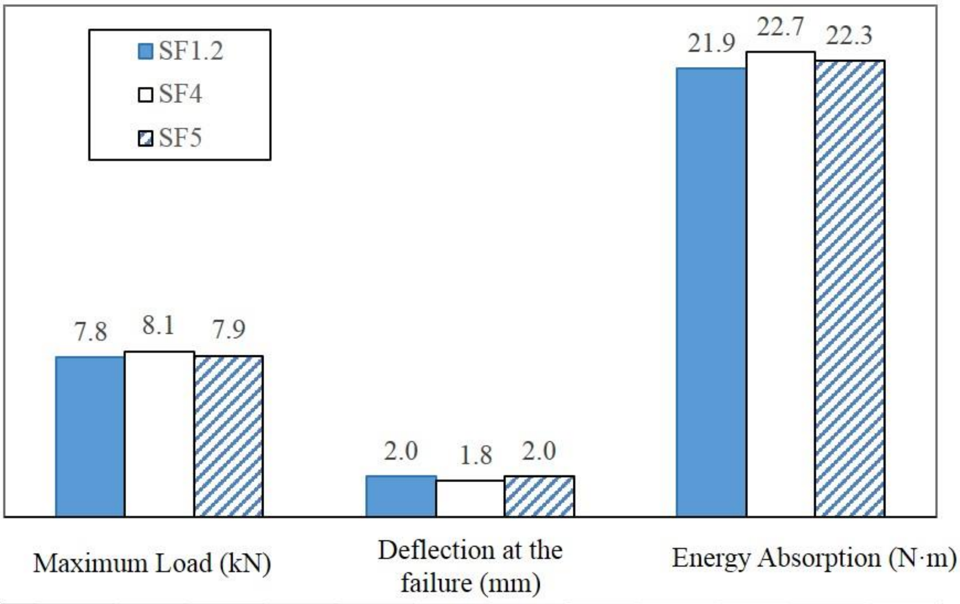

SF1.2: 120 kg/m^3 fibre dosage, 63 MPa concrete strength, 120 kg/m^3 DFA
SF4: 120 kg/m^3 63 MPa 160 kg/m^3 GGBS
SF5: 120 kg/m^3 80 MPa 200 kg/m^3 GGBS

Figure 6.8 Maximum load, deflection at the failure and energy absorption of SF1.2, SF4 and SF5

6.4 Alignment Effectiveness

Compared with SF1.2 beams, SF3 had the same total dosage of 120 kg/m^3 steel fibres in 3 layers but randomly distributed and was measured to have a flexural strength only 60% of, and a flexural deformation 40% greater than, SF1.2 on average (Table 6.1). Therefore, aligning steel fibres in the longitudinal direction of the beam can significantly affect the structural behaviour of the member.

In order to evaluate the distribution of the steel fibres more precisely, examination of the CT reconstruction data is carried out to visualise and analyse the alignment effectiveness within the concrete. The distribution of the steel fibre orientations is calculated using the VGSTUDIO MAX software programme with analysis modules on both space orientation and referencing orientation. Since the X-ray images can be regarded as 3D functions that are twice differentiable in all directions (Krause, et al., 2010), partial second derivatives of intensity is computed for all fibre voxel points by calculating the below Hessian matrix:

$$H = \begin{bmatrix} \frac{\partial^2 I}{\partial x^2} & \frac{\partial^2 I}{\partial x \partial y} & \frac{\partial^2 I}{\partial x \partial z} \\ \frac{\partial^2 I}{\partial y \partial x} & \frac{\partial^2 I}{\partial y^2} & \frac{\partial^2 I}{\partial y \partial z} \\ \frac{\partial^2 I}{\partial z \partial x} & \frac{\partial^2 I}{\partial z \partial y} & \frac{\partial^2 I}{\partial z^2} \end{bmatrix} \qquad \text{Equation 6.1}$$

where H is the Hessian matrix, I is the grayscale sample image matrix, x, y and z are the reference axes.

The fibre orientations can consequently be calculated by computing the eigenvectors and eigenvalues of the Hessian matrix (Oesch, et al., 2018). Based on this calculation method, the Space Orientation Analysis Module determines the mean tensor components of the fibrous composite. Meanwhile, the Referencing Orientation Module provides data of the deviations of the fibres from a selected reference orientation. In this study, the reference orientation was chosen as the longitudinal direction of the beam which was the orientation that the fibres were aligned in (x-axis under the global coordinate system).

The orientation analysis was carried out on cubic samples of both SF1.2 and SF3 beams. Figure 6.9 and 6.10 present the 2D windows of the reference orientation analysis results in colour-coded overlays for the fibres within SF1.2 and SF3 respectively. The deviation of the fibres' orientation from the reference orientation are coded in different colours. The selected reference orientation is the vertical axis in Figure 6.9 and 6.10 (*z*-axis under the sense coordinate system). Therefore, the filaments coded in blue show a small deviation angle and are more parallel to the longitudinal direction while those in red have deviation angles towards 90° and are more perpendicular to the longitudinal direction. As seen, the fibre distribution in SF1.2 is more uniform with most fibres being aligned to a favourable orientation (0-45°) while SF3 is more random and more fibres spread in unfavourable orientations (45-90°). The cumulated deviation angle distributions of the aligned SF1.2 beam and the randomly-spread SF3 beam are also given in cumulated deviation angle vs. content of fibres curves in Figure 6.11. As presented, about 76% of the analysed voxels show a deviation smaller than or equal to 45° from the aligning direction for SF1.2 while it is 64% for SF3.

The mean tensor components and the eigenvalues of the 2 types of fibre distribution are also calculated by computing Equation 6.1 using the programme and given in Table 6.2. The components of the mean orientation tensor for both beams are the highest in the *xx*-axis which represents the *x*-axis in the global coordinate system. However, SF1.2 had a less tensor component in *yy*-axis than SF3 and accordingly can be regarded as having a higher alignment effectiveness. The alignment differentiation contributed to the measured flexural strength difference between the two beams. Additionally, based on the calculated eigenvalues, a safety factor of 1.3 ($1/\lambda_1=1/0.77$) should be recommended for defining the alignment effectiveness manually achieved in this project. This proposed safety factor is dependent on many factors such as the aligning method and the fibre amount. However, the confidence interval of this factor is not achieved in this thesis since here only covered one type of aligning approach with roughly the same amount of fibres each layer.

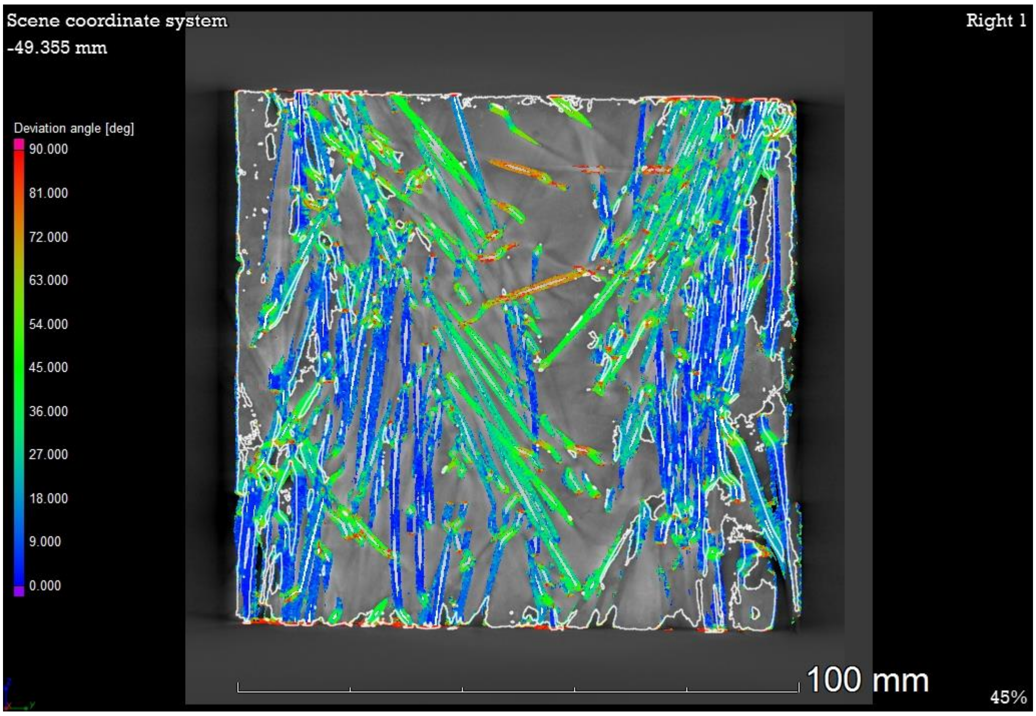

Figure 6.9 2D window of the reference orientation analysis result the fibres within SF1.2 at the depth of 1 mm from the beam bottom

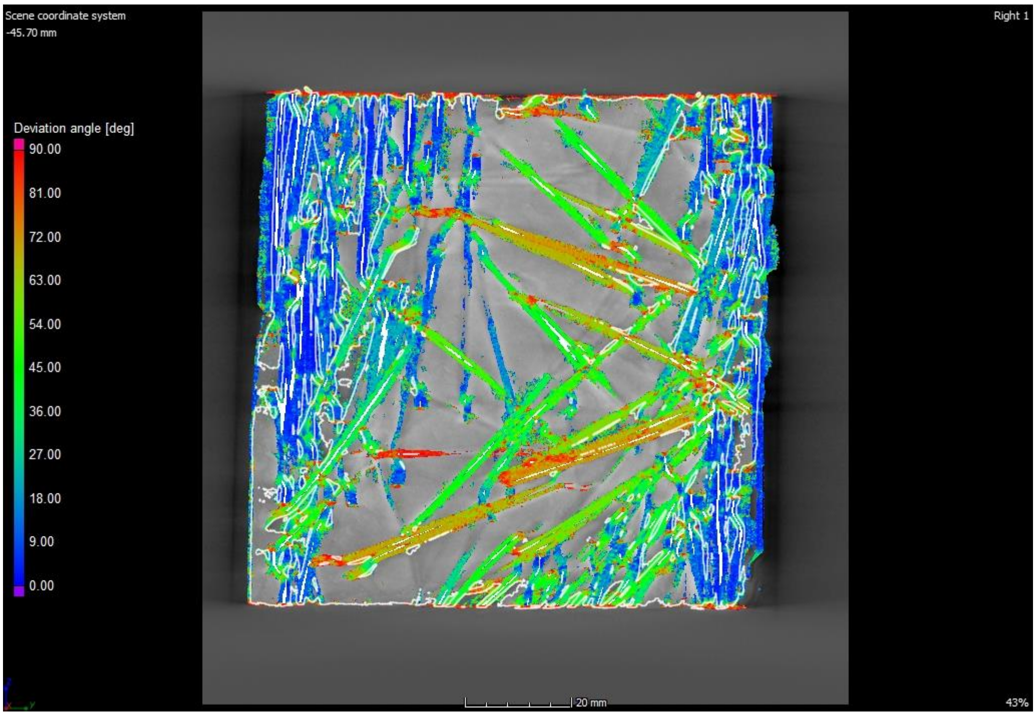

Figure 6.10 2D window of the reference orientation analysis result the fibres within SF3 at the depth of 5 mm from the recognised beam bottom

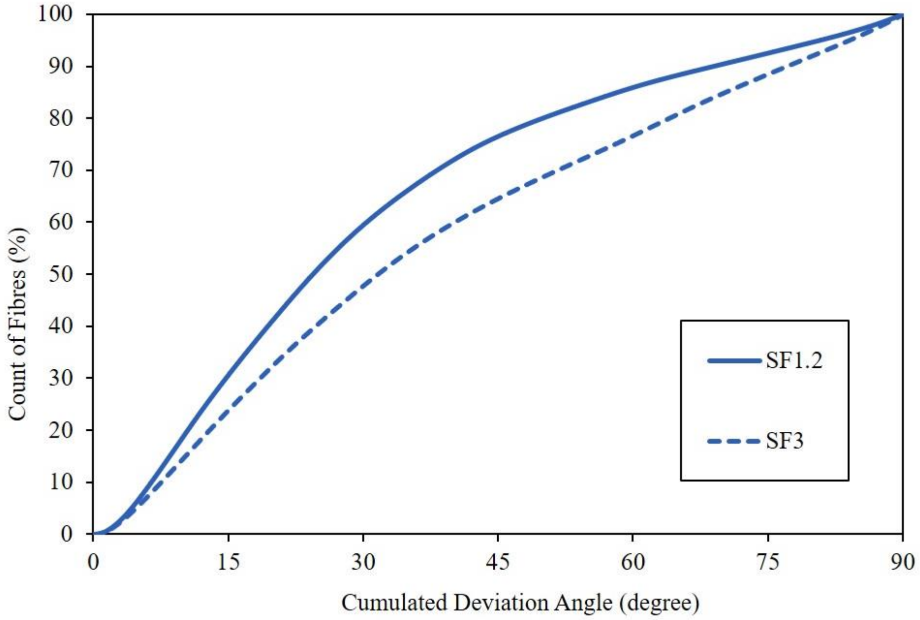

Figure 6.11 Cumulated deviation angle from the beam longitudinal axis of the fibres

Table 6.2 Mean tensor components and eigenvalues of the 2 types of fibre distribution

SF1.2	SF3
Mean tensor components	
$\begin{bmatrix} 0.77 & 0.023 & -0.00068 \\ 0.023 & 0.15 & -0.0023 \\ -0.00068 & -0.0023 & 0.079 \end{bmatrix}$	$\begin{bmatrix} 0.67 & -0.035 & 0.0018 \\ -0.035 & 0.24 & 0.016 \\ 0.0018 & -0.016 & 0.088 \end{bmatrix}$
Eigenvalues	
$[\lambda_1: 0.77, \lambda_2: 0.15, \lambda_3: 0.08]$	$[\lambda_1: 0.65, \lambda_2: 0.24, \lambda_3: 0.06]$

6.5 Flexural Design Consideration

The flexural strength contribution of the longitudinally aligned steel fibres is analysed with consideration of factors such as the fibre dosage, layer numbers and fibre alignment effectiveness. For ordinary SFRC with the fibres added-in during the mix and randomly distributed in the concrete, its flexural strength has been suggested (Kang, et al., 2010) to be calculated with regard to the fibre content as:

$$\sigma_f = A\sigma_{fo}\left(1 - V_{sf}\right) + BV_f\frac{l_{sf}}{d_{sf}}$$ Equation 6.2

where σ_f and σ_{fo} is the flexural strength of concrete with and without fibres respectively, MPa; V_{sf} is the fibre volume fraction, %; l_{sf} and d_{sf} are the length and diameter of the steel fibre respectively, mm; and *A* and *B* are the experimental coefficients.

In the case of flexural members reinforced with aligned steel fibres with multiple layers, the flexural strength contribution of each fibre layer will be different. Therefore, it is hard to determine σ_f exactly. Alternatively, the nominal flexural strength of the fibrous beam under the four-point bending test can be computed as suggested by BS EN 12390-5:2009 (British Standard Insitution, 2009) as:

$$\sigma_f = \frac{F_{max} l_s}{bd^2} \qquad \text{Equation 6.3}$$

where $F_{max}$the maximum load, N; *b* and *d* are the width and depth of the cross-section of the beam respectively, mm; l_s is the spacing between loads (load and support), mm.

For a given fibre geometry (l_{sf}/d_{sf}, the fibre aspect ratio, 55 in this study), σ_f will be solely dependent on V_{sf}. The experiments carried out in this chapter covered a range of the fibre volume fraction of 1.0, 1.5 and 2.0% while the flexural strength can be computed with the measured maximum load resistance. Figure 6.12 shows the relation between the flexural strength calculated using Equation 6.3 and the corresponding fibre content. For the selected type of fibre, the flexural strength is linearly dependent on the fibre volume fraction with very high readability, i.e. the coefficient of determination (R^2) is 0.98. Re-formularising the relationship of the trendline in the format of Equation 6.2, the following Equation 6.4 can be obtained:

$$\sigma_f = 0.2\sigma_{fo}\left(1 - V_{sf}\right) + 1.7V_f \frac{l_{sf}}{d_{sf}} \qquad \text{Equation 6.4}$$

The maximum bending moment at the ULS can then be computed as:

$$M_n = \frac{1}{2}\sigma_f bd^2 \qquad \text{Equation 6.5}$$

For the SLS design, the maximum bending moment can be computed as:

$$M_n = \frac{1}{\alpha}\frac{1}{2}\sigma_f b d^2 \qquad \text{Equation 6.6}$$

where α is the design safety factor and is recommended to be taken as at least 1.3 in regard to the alignment effectiveness analysis ($1/\lambda_1$) previously discussed in Section 6.4.

This analysing method assumes that the theory of the stress distribution for normal SFRC directly applies to flexural concrete members reinforced with aligned steel fibres in order to compute the maximum bending moment. In reality, the flexural strength contribution of each layer was probably digressive because of their reduced depth levels. Published researches (Laranjeira, et al., 2010; Soetens, et al., 2013) showed that macro-steel fibres had a tensile strain of 0.004 at their maximum bond strength to concrete from the pull-out test on single fibre filaments with inclined hooked-ends. It could be at such a strain that the first layer of aligned fibres reached the maximum flexural resistance; meanwhile, the other layers also contributed proportionally. Therefore, the tensile strains of the fibres within each level will be needed in order to compute the corresponding flexural resistance provided by those layers aligned steel fibres. However, this work is not carried out in this thesis limited by time; neither is the validation of the obtained A and B values (which are also dependent on the alignment effectiveness for a given fibre type).

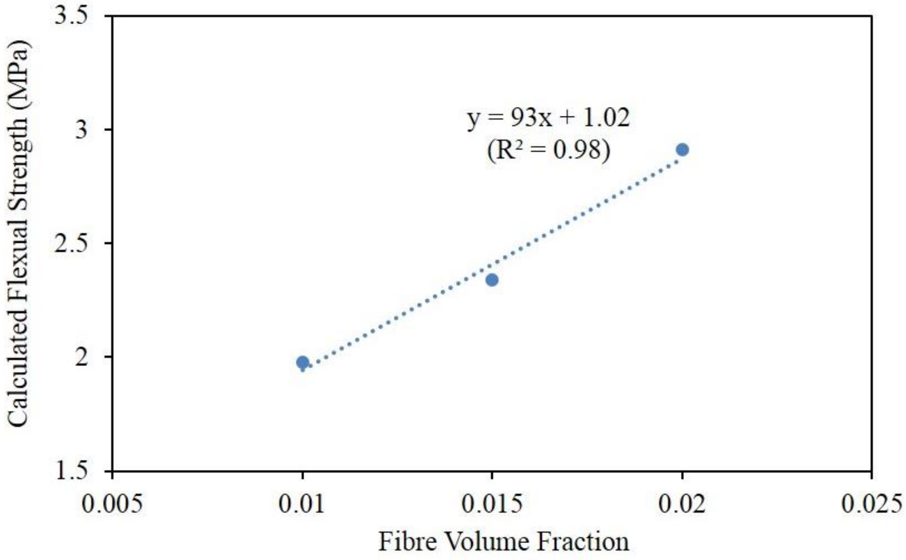

Figure 6.12 Calculated flexural strength vs. fibre volume fraction relationship

6.6 Summary

A method of longitudinally aligning steel fibres with relatively high dosages at different layers during the concrete casting was carried out. Based on this manual aligning method, the structural behaviour of SFRC was investigated using the four-point bending test. It was found that flexural concrete members reinforced with solely aligned steel fibres failed in a flexural mode. The flexural strength provided by these steel fibres is estimated to be able to achieve approximately 40% of conventional steel rebar at equivalently the same amount of steel mass. For concrete with compressive strength over 60 MPa, addition of GGBS instead of DFA and increase of the concrete strength was found unable to improve the flexural strength of the beams reinforced with aligned steel fibres. On the other hand, the flexural strength was measured to be highly dependent on the fibre dosages (number of fibre layers). For the selected type of steel fibres, the maximum bending moment of the beam can be estimated based on the fibre volume fraction (which is also related to the aligned fibre layers in this thesis):

$$M = \frac{1}{2}\sigma_f b d^2$$

$$\sigma_f = 0.2\sigma_{fo}\left(1 - V_f\right) + 1.7V_f \frac{l_f}{d_f}$$

Distribution of the steel fibres was examined with the CT reconstructed 3D images and the alignment effectiveness was calculated in terms of the mean tensor components of the fibrous composite as well as the cumulated deviation angles. It was found that the flexural strength of the beams was significantly sensitive to the fibre orientation. The alignment method applied in this study was able to align 76% of the steel fibres into an angle under or equal to 45° from the longitudinal direction of the beam. The flexural strength of the beam reinforced with aligned steel fibres was also sensitive to the fibre distribution. For example, another alignment method which aligned 64% of the steel fibres into favourable angles produced a beam flexural strength that was approximately only 60% of the former.

Chapter 7 Development of Unconventionally Reinforced WEC Prototype

7.1 Introduction

The WEC prototype was assembled from precast concrete elements and post-tensioned first with steel tendon reinforcement Ø5 mm in diameter. A compressive stress of 1 MPa on average was applied on to the prototype structure with unbonded PT for the assembly. The prototype was then subjected to the three-point bending until a deformation of 10 mm. Behaviour of the prototype under the bending was recorded and compared with numerical modelling results. Reinforcing with novel UHMWPE ropes and testing of the 3D printed beam were also carried out to investigate the feasibility of additive manufacturing.

7.2 Novel Reinforcement Selection

Based on the outputs from previous chapters, a selection of the novel reinforcement to be applied on the concrete WEC prototype was carried out. Applying of the CFRP and GFRP reinforcing bars on the concrete prototype requires them to be specifically manufactured with the suppliers, hence not trialled. A summary of the selection and decision is listed in Table 7.1.

Table 7.1 Selection of novel reinforcement on the 3D printed beam and the prototype

Novel Reinforcement	Application	
	3D Printed Beam	Truss Prototype
CFRP Strands	Useful for providing shear resistance where applicable	Useful for providing shear resistance and extra confinement on connections where applicable
Macro-Synthetic Fibres	Useful for improving toughness but difficult to be added in for printing	Not necessary since prototype will not be loaded to failure
Aligned Steel Fibres	Useful for providing strength but not easy to be aligned during printing	Useful for providing strength
UHMWPE Ropes	Designed to be applied for PT	Can be used for reinforcing and PT

7.3 3D Printed Beam Element Trial

7.3.1 UHMWPE Reinforcing Ropes

Reinforcing and post-tensioning of the WEC prototype (design details in Section 3.10.1) was designed to utilise the UHMWPE ropes. The Marlow® D12 SK99 rope products were planned as the external reinforcement. These ropes (see Figure 7.1) were claimed by the supplier to be manufactured with the Dyneema® SK99 high-modulus polyethylene. As a composite material like FRP, the UHMWPE is also homogeneous and its characteristic properties such as tensile strength and elasticity are dependent on the filament distribution over the cross section. Based on the available technical data (Marlow, 2018) provided by the manufacturer, some of the specifications are computed and presented in Table 7.2.

A prestress of 3.4 MPa is planned to be applied on to the prototype. The value was decided based on numerical modelling (by Dr. L. Zheng, C50 concrete and 3.7 GPa E value) that within the SLS a midspan deflection of 10 mm could be deformed before concrete started to crack under the three-point bending test. The number of ropes required to reinforce and post-tension the prototype can then be determined based on the level of strength for post-tensioning (Table 7.3). However, due to the relatively low stiffness, the elongation of the reinforcing ropes will be proportionately large, which is worth noticing for PT and test. Design of the termination (anchorage) and the PT applying method also need to be solved. Since fibre-reinforced polyethylene is isotropic and weaker in the transverse direction (i.e perpendicular to the fibre reinforcing orientation), clamping the material can potentially lead the material to slip or snap.

Table 7.2 Characteristic properties of the UHMWEP Marlow® D12 SK99 ropes

Property	Data	Source
Diameter, mm	8	Marlow® Web Site
Density, kg/m^3	970	
Average Break Load, kg	7530	
Minimum Break Load, kg	6780	
Elongation at Break, %	3.5	Marlow® Manufacturer
Tensile Strength at Break[a], MPa	1320	Computation with Available Data
Tensile Elasticity until Break[b], GPa	36	

[a]: according to the minimum break load; [b]: possibly not the same for the elastic stage

Figure 7.1 The Marlow® D12 SK99 product as the reinforcing ropes for the prototype

Table 7.3 Number of UHMWPE ropes required for the post-tensioning (3.4 MPa)

Number of Ropes	Load per Rope, kN	Prestress Level[a], %	PT Elongation, %
2	33.2	25	0.9
4	16.6	12	0.4
6	8.3	6	0.2

[a]: without considering prestress losses

7.3.2 3D Printed Element Post-Tensioning and Test

Before post-tensioning with these UHMWPE ropes, the two ends of the 3D printed beam (fabrication details in Section 3.10.2) were cut off by 50 mm to produce smooth surfaces on which steel bearing plates could be applied. This beam was also transversely wrapped with CFRP strands using the same wrapping process described in Section 3.6.3 for shear resistance. Since drying cracks were found in between some printing layers, additional CFRP wraps were applied at the two beam ends and the middle bending zone to prevent possible layer separations during the post-tensioning or testing. The CFRP wrappings and load applying method were schematically presented in Figure 7.2.

The rectangular space through which these UHMWPE ropes were passed located in the centre of the beam cross-section with the concern of preventing possible layer separations during the bending test. This arrangement was used despite being structurally inefficient because of the layer separation risks in the printed beams of the next generation prototype. According to the previous calculations in Table 7.2, a load of approximately 82 kN (20% prestress loss) was required to produce a prestress of 3.4 MPa on the 3D printed beam with the UHMWPE ropes. This load was applied on to the 3D printed beam via hydraulic jacks. Since the termination issue was not solved at the time of testing, these jacks were left in place to keep the post-tension level during the bending test (Figure 7.3)

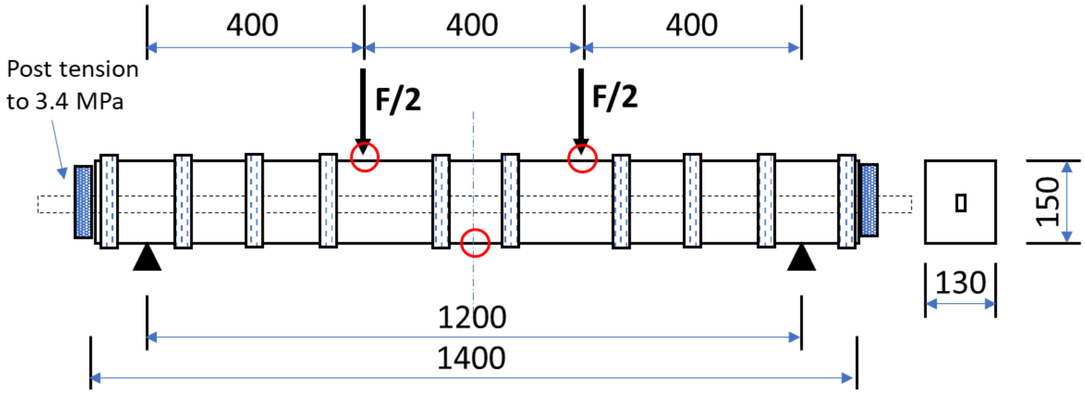

Figure 7.2 Geometric and CFRP wrapping details of the 3D printed beam under the four-point loading test (drawn by Dr. L. Zheng)

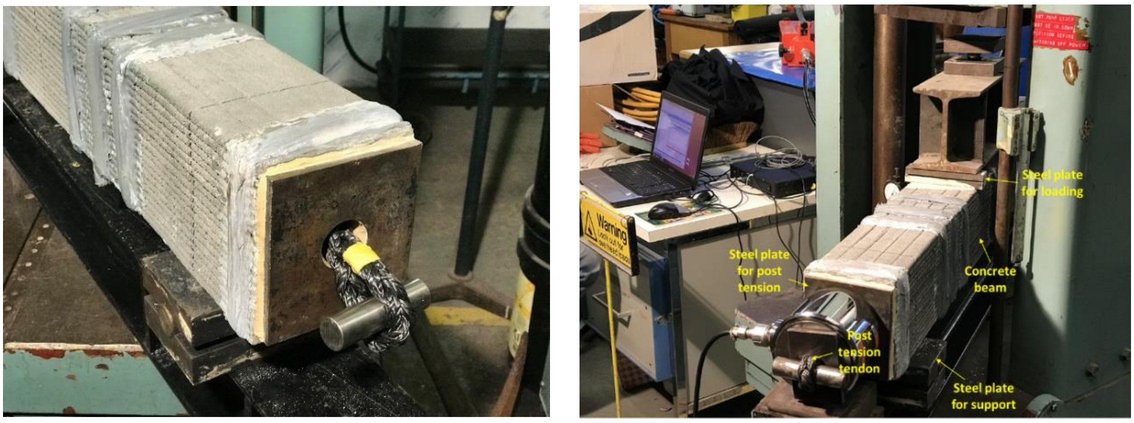

Figure 7.3 Termination of the UHMWPE ropes (left) and applying of the post-tension with the jack (right) (taken and edited by Dr. L. Zheng)

7.4 3D Printed Beam Behaviour

During the bending test, the additive-manufactured beam failed in flexure with a big flexural crack occurrng in the middle bending zone. As shown in Figure 7.4 and 7.5, this crack developed from the bottom to the top face of the beam when the applied load was increasing. Since it was post-tensioned with unbonded UHMPWE ropes, the beam lost its stability when the flexural crack developed across the nominal neutral axis of the beam and exhibited a sudden crush. The recorded load-deflection results are given in Figure 7.6. As presented, the beam deformed nearly linearly up to a load of 20 kN with a deflection of around 0.5 mm. After the linear stage, the beam started to deform plastically and finally resisted a maximum load of almost 30 kN with a deflection of around 3 mm. When the beam reached a deformation of 6 mm, the bending load was gradually released. However, because of that big flexural crack had developed and the unbonded PT system had failed in keeping the prestress, the beam finally collapsed (Figure 7.5) which was reflected as a sharp load drop in the load-deflection curve (Figure 7.6).

Figure 7.4 Crack of the 3D printed beam under the bending at a deflection of 3 mm (taken by Dr. L. Zheng)

Figure 7.5 Crack of the 3D printed beam under the bending at a deflection of 6 mm (taken by Dr. L. Zheng)

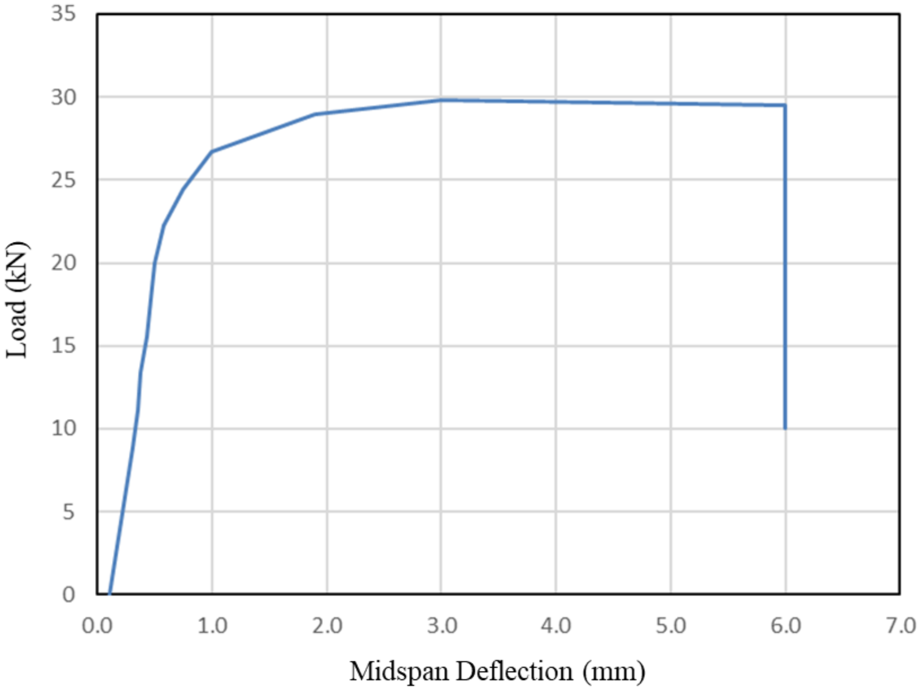

Figure 7.6 The load-deflection curve of the post-tensioned 3D printed beam under the bending test

7.5 Assembly and Test of the Truss Prototype

7.5.1 Initial Assembly

Dowel connectors cut from Ø15 mm and Ø10 mm ribbed carbon steel bars were used for assembling the truss with the Sika AnchorFix®-1 epoxy resin grout. The Ø15 mm dowels were 200 mm in length and used for connecting the longitudinal sections on to the 2 end rings while the Ø10 mm ones were 350 mm in length and for the middle ring. The rings were first joined with dowel connectors and fastened with ratchet straps (Figure 7.7), and left in room temperature for at least 24 hours to allow the grout to set. After curing, the longitudinal beams were assembled on to the 2 end rings vertically (Figure 7.8) followed by the middle ring being lifted up and attached on to the longitudinal sections (Figure 7.8) with these 350 mm dowel connectors staying out (Figure 7.9) for the final joining.

Gaps were observed between some longitudinal sections and the middle ring during the assembly possibly because of the tolerance of concrete elements casting. The gaps that were greater than 3mm were first filled with thin steel plates (Figure 7.10) and then sealed with the epoxy resin grout while those smaller than 3 mm were only sealed with the grout. Six steel confinement bands (Figure 7.11) were also manufactured to externally reinforce the three concrete rings. These Jubilee-Clip-type steel bands were 25 mm in width and 930 mm in inner diameter with an adjustable and securing M12 screw. The AUTOCAD® drawing of the steel bands is shown in Figure 7.12. Considering the load applying method, the end rings and middle ring were confined with 1 and 4 steel bands respectively.

To complete the prototype connecting, the assembled half cage with the middle ring was lifted up and inverted so that these Ø10 mm dowel connectors could be vertically fitted into the plastic dowel sockets of the other half cage. However, because some of the dowel connectors were grouted with slightly inclined angles, the top half cage could only be matched into all 16 embedded sockets by force. As a result, there were relatively small amounts of the epoxy resin grout being injected into these sockets, which could possibly lead to unstable bonding between the dowel connectors and the truss main body. Finally, the vertically assembled prototype truss was rotated by 90° (Figure 7.13) on to the loading supports for further post-tensioning (Figure 7.14) and test.

Figure 7.7 Joining of the ring section with the ratchet strap

Figure 7.8 Assembly of the longitudinal elements on to the ring section vertically (left) and the middle ring on to the erected longitudinal elements (right)

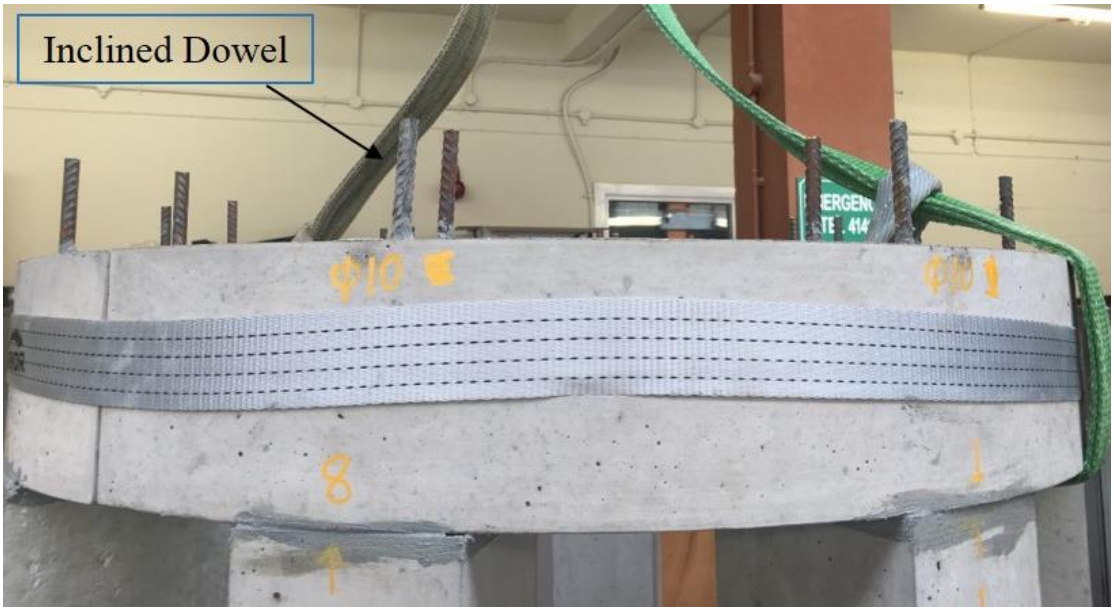

Figure 7.9 The middle dowel connectors staying out for final jointing

Figure 7.10 Gap between the longitudinal element and the middle ring (left), and filling the gap with thin steel plates (right)

Figure 7.11 The manufactured steel band confinement with an adjustable and securing M12 screw

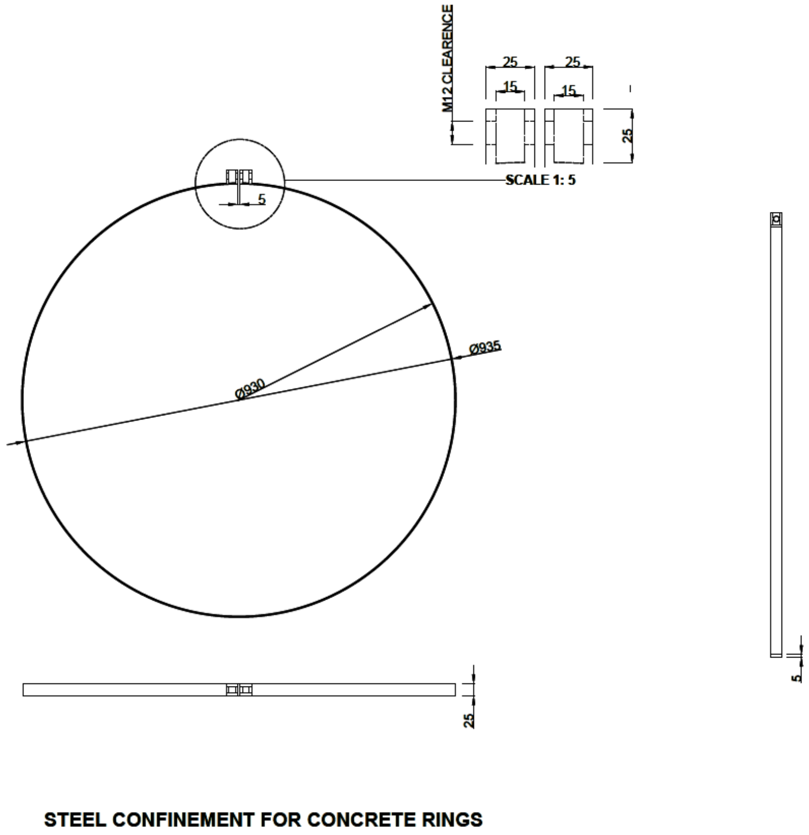

Figure 7.12 AUTOCAD® drawing of the steel confinement band (mm)

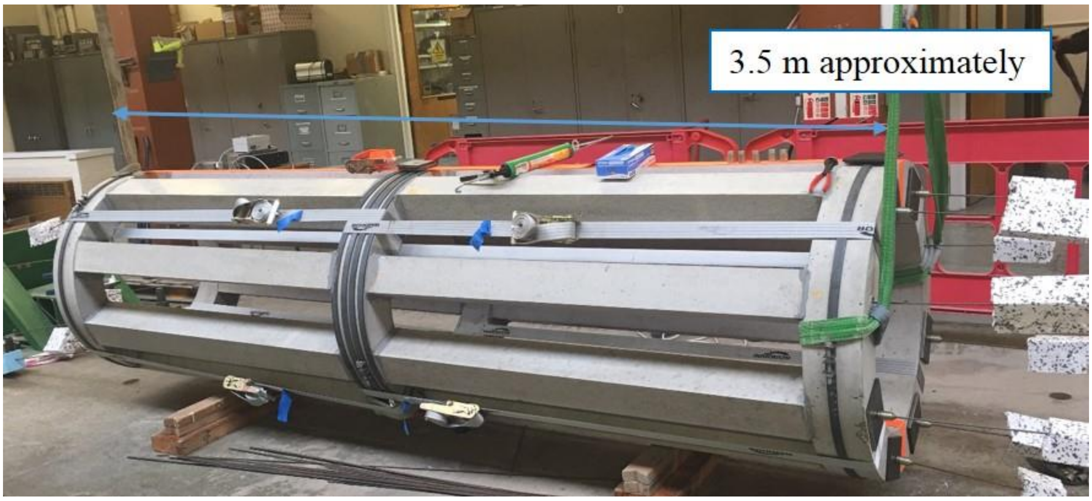

Figure 7.13 The WEC prototype after being rotated to the horizontal testing level

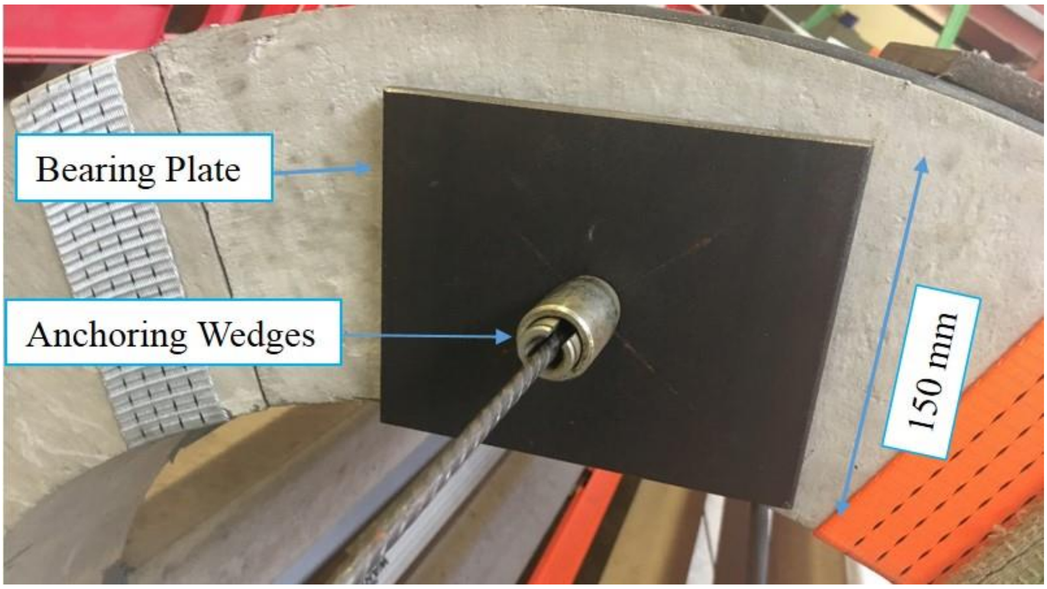

Figure 7.14 PT bearing plate and anchoring wedges (before applying the load)

7.5.2 Post-Tensioning Assembly

Post-tensioning was carried out after the initial assembling. 8 single steel wires (Ø5 mm) were used to prestress the prototype, i.e. one wire located adjacent to each longitudinal section. A compression of 1 MPa was produced by tensioning the steel wires with a 24 kN PT load. This post-tensioning load was computed basing on Eurocode 2 (British Standard Institution, 2005) with a 20% prestress loss rate. The PT load was applied with hydraulic jacks.

7.6 Truss Behaviour and Analysis

7.6.1 Truss Behaviour under Three-Point Bending

Three-point bending test was carried out on the assembled truss prototype as presented in Figure 7.15. The applied load and truss deformation were recorded and analysed with a programmed computer. An electronic dial indicator connected to the computer was used to measure the movement of the loading cell and its measurement was regarded as the deformation of the middle ring. When a deformation of 10 mm was achieved, the applied load was gradually released. The recorded load-deflection results are given in Figure 7.16. The truss resisted a maximum load of 18.5 kN during the test for the deflection of up to 10 mm. However, the truss experienced a linear deforming period before the load of 8 kN and the corresponding deflection was only around 1 mm. Then the truss started to deform nonlinearly until the deflection of 10 mm. A cracking sound was heard at a load of around 10 kN but, due to safety concerns, the cracking was not evaluated during the test. After the load was removed, a residual deflection of around 2.5 mm occurred (Figure 7.16) and no big cracks were observed within the structure.

Figure 7.15 Three-point bending test on the assembled and steel-wire post-tensioned (1 MPa) truss (taken by Dr. L. Zheng)

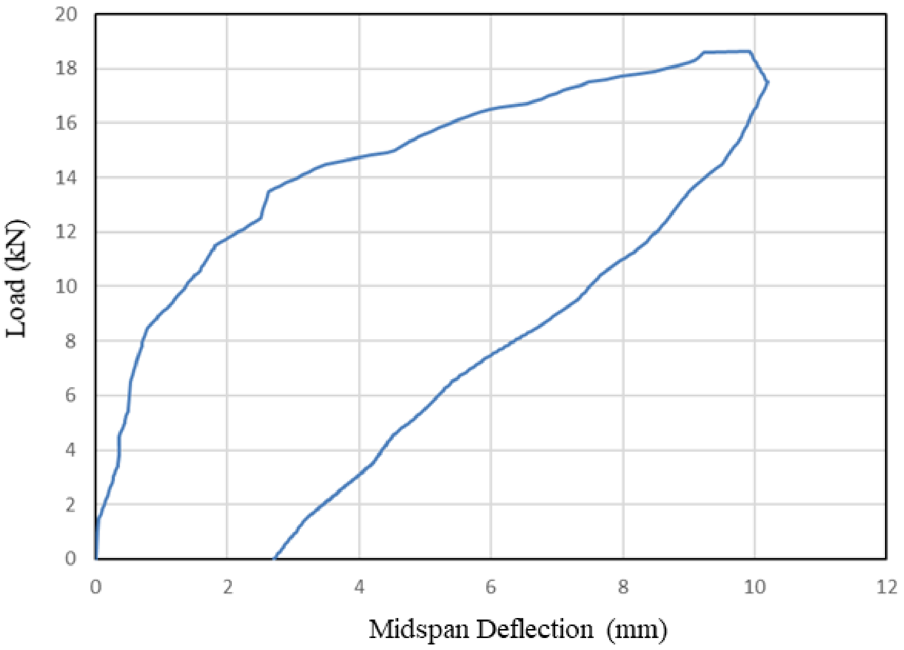

Figure 7.16 The load-deflection response of the truss under the three-point bending

7.6.2 FE Analysis of the Truss Behaviour

FE analysis of the truss reinforced with Ø 5 mm steel tendons and post-tensioned with a stress of 1 MPa was carried out utilising the Abaqus® program. Only a quarter of the truss was created (Figure 7.17) to reduce the simulation as well as computation work since the prototype was structurally symmetric in 3 dimensions.

The concrete damaged plasticity (CDP) model, provided by Abaqus® as one FE analysis software package, was selected for simulating the constitutive behaviour of the prototype. This CDP model combines concepts of isotropic damaged elasticity with isotropic tensile and compressive plasticity to capture the inelastic behaviour of concrete (Sümer & Aktas, 2015). However, this model also requires materials to strain linearly in their elastic stages. As a composite with concrete truss, unbonded steel tendons as well as dowel connectors, the prototype does not fully comply with this requirement. Overall, the analysis is still informative for comparison with experimental results.

On the other hand, an accurate stress distribution analysis across the whole truss section requires the 3D solid element (rather than the simple beam element) to be used as the FE element type. Consequently, a full truss model will need to be created and meshed which will produce too heavy calculation work to carry out for the available computer in the lab. Therefore, it was still the simple beam element and a quarter truss that was used for the modelling.

To compare with physical results, the numerical modelling was run until a deformation of 10 mm. The simulated stress distribution of the model is shown in Figure 7.18 while the simulated load-deflection behaviour is presented in Figure 7.19 in comparison with the measured one. Another simulation was also carried out assuming that the truss was assembled with a post-tension stress of 3.4 MPa (still with steel tendons but Ø 30 mm). This PT stress was selected imitating the case of reinforcing with the UHMWPE ropes. The computed load-deflection curve from this simulation was also given in Figure 7.19.

The area coloured in grey in Figure 7.18 illustrates a distribution of tensile stress greater than 4.5 MPa (i.e. 75% of the concrete tensile strength). These areas are expected to crack under the corresponding bending moment. As shown in Figure 7.19, the measured curve had less stiffness and strength in comparison with the simulated ones. Many reasons could be attributed for this difference. Firstly, the truss assembly accuracy (previously discussed in Section 7.5.1) was restricted by the casting size errors of these elements (Figure 7.10). This could be a major reason that caused the lower global stiffness of the truss (compared with predicted ones) because it prevented the truss from uniformly resisting the bending load. Secondly, the employed CDP model used the provided default material parameters (i.e. C60 concrete rather than C40) and ignored the epoxy resin adhesive in connections. As previously discussed in Section 5.4, using the epoxy resin adhesive to connect concrete elements in the form of the flat face-to-face type of joint limited the flexural load capacity development of the connected members.

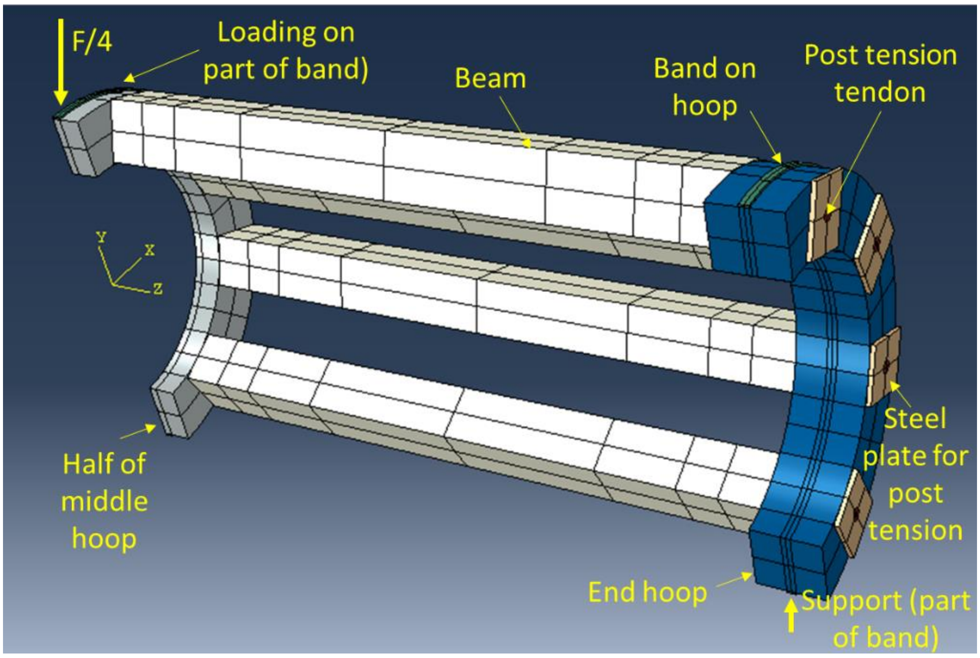

Figure 7.17 Meshing of the prototype (a quarter) and its boundary conditions

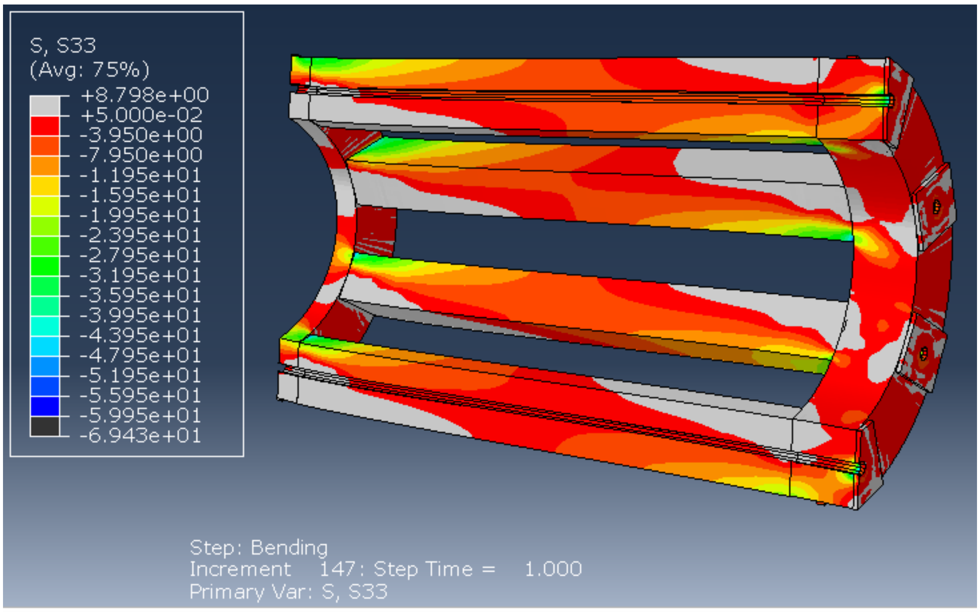

Figure 7.18 Simulated stress distribution of the truss at the deformation of 10 mm (by Dr. L. Zheng)

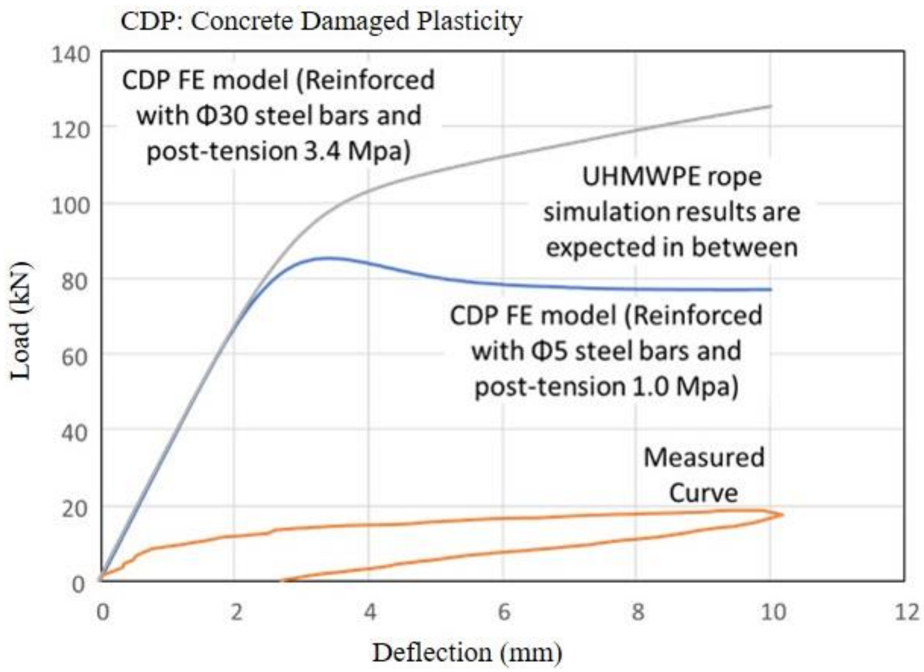

Figure 7.19 FE simulations of the truss under 1 MPa and 3.4 MPa PT in comparison with measured result

7.7 Summary

A WEC prototype was designed and produced from precast concrete elements. Assembly procedures of the precast elements, technical issues and difficulties recognised during the construction were described and discussed. The prototype was connected with dowels and epoxy resin grout, and a small level of prestress (1 MPa). It was noted that matching the dowel connectors into these embedded sockets at the final joining stage was relatively difficult especially when some of the dowel bars were only slightly inclined. The designed longitudinal sleeves for unbonded PT could be problematic for placing reinforcement with large cross-sectional areas because some of them were curved during the precasting and consequently the space was reduced or even blocked. On the other hand, externally strengthening with UHMWPE ropes would be more practicable. However, this was not carried out with the prototype in this study because of the timeline. Reinforcing and post-tensioning with UHMWPE ropes were carried out on the 3D printed beam. Design of the rope anchorage remains unsolved and requires further practical tests.

Both the 3D printed beam and the assembled prototype were subjected to the three-point bending until a deflection of 6 mm and 10 mm respectively. A flexural failure mode was observed for the 3D printed element as well as a sudden collapse when the beam was also wrapped with transverse CFRP strands. The truss resisted a maximum load of 18.5 kN and had a residual deformation of 2 mm after the load was released. Numerical modelling results showed higher stiffness and better strength behaviour of the WEC prototype. This difference could be because of the production and assembly accuracy of the prototype, especially within these dowel connections. Application of the epoxy resin adhesive in the connections also could restrict the strength development of the assembled structure.

Once termination and PT applying techniques are resolved, the WEC prototype can also be reinforced with the UHMWPE ropes and proves the concept of additive manufacturing concrete elements with novel reinforcement for easy-assembly WEC structures. Although the beam was printed without any steel fibre addition, aligning steel fibres longitudinally into the beam appears feasible. These aligned steel fibres can also provide flexural and shear strength contribution. Further experiments also need to be programmed to identify appropriate concrete/mortar mixes to bond the aligned fibres for 3D printing.

Chapter 8 Conclusions and Further Work Recommendations

8.1 Introduction

This PhD research was carried out to investigate novel reinforcement for marine concrete structures and consequently to produce an unconventionally reinforced concrete WEC prototype that could be constructed with a remarkably reduced usage of steel comparing with current wave energy exploiting devices. Experimental conclusions of the structural behaviours of flexural concrete members reinforced with FRPs, synthetic and steel fibres as well as the prototype design and development are presented in this chapter.

8.2 Conclusions

FRP reinforcement bars have the potential to replace conventional steel bars in a concrete WEC structure maintaining the required mechanical properties of strength and toughness. The surface preparation of FRP bars could significantly determine their bond strength to concrete and pull-out failure type. The GFRP bars with a ripped smooth surface presented a bond strength around three times greater than the CFRP ones (with sand coating surface). Both CFRP and GFRP bars were found insensitive to the presence of ions (Cl^- and SO_4^{2-}) in concrete regarding reducing the bond strength or causing material deterioration.

Concrete beams longitudinally reinforced with FRP bars (without shear reinforcement) had reasonably large shear resistance contributed from the uncracked sections. This shear contribution ($V_{c,f}$) was underestimated by the guideline ACI 440.1R-06 (2006) while one modified equation (Equation 4.2) was proposed based on test data from GFRP-reinforced beams for estimating $V_{c,f}$. Concrete beams longitudinally reinforced with GFRP bars and shear reinforcement also had brittle flexural failures.

CFRP strands were measured to have a tensile strength that was only around 20% of that claimed by the supplier. Concrete beams externally strengthened with these CFRP strands (under-reinforced) using the epoxy resin failed in a way that the strands disengaged from the concrete surface. The flexural strength development of beams with a thin epoxy-resin-connected joint (resin layer thickness $\leqslant$30 mm) was restricted by the connection. The bond strength (to concrete) development of the epoxy resin was found relatively sensitive to its curing condition and history. Meanwhile, manually aligning macro-steel fibres by layer within concrete beams enabled them to achieve a flexural strength which was about 40% of that with conventional steel rebar (at equivalently the same amount of steel mass). This manual alignment method could align around 76% of the steel fibres into favourable angles ($\leqslant 45°$ from the longitudinal direction of the beam) while the achieved flexural strength was found very sensitive to the fibre distribution orientations.

Additionally, main conclusions regarding the objectives proposed in Section 1.2 can be outlined as:

Objective (1)

The bond between FRP bars and concrete was found to be related to such parameters as the surface deformation while unrelated to the presence of sea salt ions (Cl^- and SO_4^{2-}). The concrete strength (50-75 MPa) was believed to have no significant influences on the bond of the CFRP bars but might affect the bond strength of GFRP bars. A smooth ribbed surface for GFRP was effective in bonding the concrete while the sand coated surface for CFRP was relatively ineffective although the exterior coating was constructive in terms of maintaining the residual bond strength. Neither GFRP nor CFRP was observed to suffer noticeable deterioration under the seawater exposures. Flexural concrete members only longitudinally reinforced with GFRP bars had shear strengths greater than estimated values from ACI 440.1R-06 (2006). A modification of the estimation was introduced for GFRP bars albeit dependence of FRP surface characterisation for this equation was not verified:

$$V_{c,f} = 0.4 k k_a \sqrt{f_c} b_w d$$

where $k = \sqrt{2\rho_f n_f + (\rho_f n_f)^2} - \rho_f n_f$ and $k_a = 0.03 f_c^{1.25}$

Objective (2)

Flexural concrete members reinforced with GFRP bars were able to achieve the designed ultimate strength but presented brittle failure at the ULS. Meanwhile flexural concrete members externally strengthened with CFRP multi-strands presented lower strength than expected. This was because bonding CFRP on to concrete with the epoxy resin adhesive restricted the strength contribution of the CFRP composite reinforcement. Consequently, the maximum tensile stress provided by the CFRP strands should be decided as:

$$\varepsilon_{fu} = min\{\varepsilon_{epoxy,} \varepsilon_{cfrp}, 0.005\}$$

Load-carrying capacity drops were noticed to exist at the SLS stage for both GFRP and CFRP reinforced beams while for GFRP ones the extent of the initial drop, which usually occurred at the beam's first crack, could be more than 50%. ACI 440.1R-06 (2006) and Pilakoutas et al. (2011) both moderately underestimated the ultimate moment capacity of GFRP-reinforced beams but extremely overestimated that of CFRP-strengthened beams. Additionally, both internal CFRP bars and fully-wrapped CFRP multi-strands were able to provide adequate shear resistance.

The concept of Crack Resistance Indices (CRIs) was introduced to estimate the cracking behaviour of flexural concrete members reinforced with FRPs at their ULS level (CRI_1) and ALS level (CRI_2). Using these 2 parameter systems, the range of serviceability design for an FRP-reinforced beam and its impact tolerance and energy absorption ability under the ALS can be quantitatively calculated.

Objective (3)

Adding macro-synthetic fibres at 20 kg/m^3 during the mix could not remarkably enhance the flexural strength of the beam but could significantly improve the toughness behaviour of the beam at the post-ULS. The toughness improvement was expressed as a CRI_{2E} factor of more than 6.0.

Longitudinally aligning steel fibres with relatively high dosages at different layers during the concrete casting could provide the concrete beams with competitive flexural and shear strengths. The flexural strength was highly dependent on the fibre dosage and the fibre orientation, and could achieve 40% of conventional steel bars at the same amount of mass of steel. Higher concrete strength and addition of GGBS were ineffective in enhancing the flexural strength. For the selected geometric type of steel fibres, the flexural strength of the beam can be computed in terms of the maximum bending moment based on the fibre volume fraction:

$$M_n = \frac{1}{2}\sigma_f b d^2$$

where $\sigma_f = 0.2\sigma_{fo}\left(1 - V_{sf}\right) + 1.7V_{sf}\frac{l_{sf}}{d_{sf}}$

Based on analysis of the 3D reconstructed images, a safety parameter of 1.3 ($1/\lambda_1$) was recommended for defining the alignment effectiveness manually achieved in this project.

Objective (4)

The flat face-to-face type of joint with a thin layer of the epoxy resin around 3 mm as the grouting material was relatively unsatisfactory in structurally connecting concrete beams because of the relatively low elasticity of the adhesive as well as its potentially weak bond of concrete/concrete when the concrete surface was not specifically prepared. The epoxy resin's bond strength between concrete/concrete and concrete/CFRP could be affected by its curing history. Being exposed to water at the early curing stage (within 48 hours) could reduce the bonding effect.

Objective (5)

Design and comparison of the WEC framework was first carried out based on numerical modelling to decide the prototype structure. In the case of precasting concrete elements, this structure was chosen as the circular Vierendeel-truss-type. Assembly of the truss was carried out using dowel connectors and unbonded steel tendons with a 1 MPa prestress. The assembled truss was subjected to the three-point bending up to a deflection of 10 mm. The truss resisted a maximum load of 18.5 kN and presented a residual deflection of 2 mm after the load was released. However the measured strength and stiffness of the truss were both only 20% of what numerically predicated. The 3D printed beam was reinforced with the novel UHMWPE ropes and also subjected to the three-point bending test to investigate the feasibility of additive manufacturing. Application of these novel reinforcement within a concrete WEC could remarkably reduce the usage of steel and consequently lower down the overall cost given the material price difference.

8.3 Recommendations of Further Work

Overall this study has achieved the main aim and objectives projected at the beginning of the programme, albeit there are a number of additional areas for research, development and applications that have not been undertaken within this thesis due to the work timeline. The following fields are outlined as the recommendations for further work and may be considered as a next step in continuing similar areas of research regarding novel concrete reinforcement for WECs:

(1) Testing of CFRP and UHMWPE strengthening products (multi-strands and ropes) is lacking standardised methods. It is worth being developed so that the design of CFRP/UHMPWPE-reinforced concrete members can be addressed accordingly.

(2) The bond strength of epoxy resin between CFRP/concrete was tested as sensitive to water/moisture. Further experiments are suggested to be carried out to examine its responsiveness to the presence of water.

(3) Techniques need to be developed to more effectively distribute aligned steel fibres whist models for calculating the flexural strength of aligned-steel-fibre reinforced beams remain to be advanced with regards to the fibre depths and distributions.

(4) Further research is required to establish design approaches for FRP/UHMWPE-reinforced concrete members so that using these novel reinforcement for the WEC construction can be achieved at a reduced cost.

(5) Anchoring and post-tensioning of the UHMWPE strengthening ropes externally for the WEC prototype remain unsolved. Further trials on such areas are suggested so that development and testing of the prototype can be accomplished.

References

Achillides, Z., 1998. *Bond Behaviour of FRP Bars in Concrete (PhD thesis).* Sheffield: University of Sheffield.

Achillides, Z. & Pilakoutas, K., 2004. Bond Bhaviour of Fibre Reinforced Polymer Bars under Direct Pullout Conditions. *Composites for Construction,* 8(2), pp. 173-181.

Alberti, M., Enfedaque, A., Gálvez, J. & Agrawal, V., 2016. Fibre Distribution and Orientation of Macro-synthetic Polyolefin Fibre Reinforced Concrete Elements. *Construction and Building Materials,* Volume 122, pp. 505-517.

Al-Sunna, R., Kypros, P., Iman, H. & Guadagnini, M., 2012. Deflection Behaviour of FRP Reinforced Concrete Beams and Slabs: An Experimental Investigation. *Composites: Part B,* Volume 43, pp. 2125-2134.

Altun, F., Haktanir, T. & Ari, K., 2007. Effects of Steel Fiber Addition on Mechanical Properties of Concrete and RC Beams. *Construction and Building Materials,* Volume 21, pp. 654-661.

American Concrete Insititute, 2006. *ACI 440.1R-06 Guild for the Design and Constructing of Structural Concrete Reinforced with FRP Bars,* Farmington Hills, MI: ACI Committee 440.

American Concrete Institute, 2004. *ACI 440.3R-04 Guide Test Methods for Fibre-Reinforced Polymer (FRPs) for Reinforcing or Strengthening Concrete Structures,* Farmington Hills, MI: ACI Committee 440.

American Concrete Institute, 2012. *Guide Test Methods for Fiber-Reinforced Polymer (FRP) Composites for Reinforcing or Strengthening Concrete and Masonry Structures,* Farmington Hills, MI: ACI Committee 440.

American Concrete Institute, 2015. *ACI 440.1R-15 Guide for the Design and Constructing of Structural Concrete Reinforced with FRP Bars,* Farmington Hills, MI: ACI Committee 440.

American Concrete Institution, 2004. *ACI 440-4R-04 Prestressing Concrete Structures with FRP Tendons,* Farmington Hills, MI: ACI Committee 440.

American Concrete Institution, 2011. *ACI 440.4R-04 Prestrssing Concrete with FRP Tendons (Reapproved 2011),* Farmington Hills, MI: ACI Committee 440.

America, P., 2019. *Protavic America.* [Online]
Available at: http://www.protavicamerica.com/products/moisture-resistant-epoxy/
[Accessed 21 3 2019].

Andila-Giraldo, O. & Pujol, S., 2019. Failure Mechanisms of Small-Scale Reinforced Concrete Beams Impacted by Soft Missiles. *Structures,* 8, Volume 20, pp. 620-634.

Arias, J. M., Escobar, M. & Vazquez, A., 2012. Ribbed Glass Fibre Reinforced Plastic Rebar Embedded in Concrete- An Experimental Study. *Journal of Composite Materials,* 17(47), pp. 2125-2132.

ASTM International, 2006. *Astm C452 - 06 Standard Test Method for Potential Expansion of Portland-Cement Mortars Exposed to Sulfate,* West Conshohocken, Pennsylvania: ASTM International.

ASTM International, 2017. *ASTM D7565/D7565-10 Standard Test Method for Determining Tensile Properties of Fiber Reinforced Polymer Matrix Composites Used for Strengthening of Civil Structures,* West Conshohocken, Pennsylvania: ASTM International.

Balouch, S. U., Forth, J. P. & Granju, J.-L., 2010. Surface Corrosion of Steel Fibre Reinforced Concrete. *Cement and Concrete Research,* 40(3), pp. 410-414.

Benmokrane, B. et al., 2017. Laboratory Assessment and Durability Performance of Vinyl-Ester,Polyester, and Epoxy Glass-FRP Bars for Concrete Structures. *Composites Part B,* Volume 112, pp. 163-174.

Benmokrane, B., El-Salakawy, E., El-Ragaby, A. & Lackey, T., 2006. Designing and Testing of Concrete Bridge Decks Reinforced with Glass FRP Bars. *Journal of Bridge Engineering,* 11(2), pp. 217-220.

Bristish Standard Institution, 2010. *DD CEN/TS 12390-11:2010 Testing Hardened Concrete. Determination of the Chloride Resistance of Concrete, Unidirectional Diffusion,* London: BSI.

British Standard Insitution, 2009. *BS EN 12390-2: 2009 Testing Hardened Concrete. Making and Curing Specimens for Strength Tests,* London: BSI.

British Standard Insitution, 2009. *BS EN 12390-5:2009 Testing hardened concrete. Flexural strength of test specimens,* London: BSI.

British Standard Instituion, 2016. *BS 8500-1:2015+A1:2016 Concrete. Complementary British Standard to BS EN 206. Method of Specifying and Guidance for the Specifier,* London: BSI.

British Standard Institution, 2002. *bs en 1008: 2002 Mixing water for concrete. Specification for sampling, testing and assessing the suitability of water, including water recovered from processes in the concrete industry, as mixing water for concrete,* London: BSI.

British Standard Institution, 2005. *Eurocode 2 — Design of Concrete Structures Part 2: Concrete Bridges - Design and Detailing Rules,* London: British Standard Institution.

British Standard Institution, 2006. *BS EN 15167-1 Ground Granulated Blast Furnace Slag for Use in Concrete, Mortar and Grout. Definitions, Specifications and Conformity Criteria,* London: BSI.

British Standard Institution, 2011. *BS EN 197-1:201 Cement. Composition, Specifications and Conformity Criteria for Common Cements,* London: BSI.

British Standard Institution, 2012. *BS EN 450-1 Fly Ash for Concrete. Definition, Specifications and Conformity Criteria,* London: BSI.

British Standard Institution, 2012. *BS EN 934-2:2009+A1:2012 Admixtures for Concrete, Mortar and Grout. Concrete Admixtures. Definitions, Requirements, Conformity, Marking and Labelling,* London: BSI.

British Standard Institution, 2013. *BS EN 1097-6 Tests for mechanical and physical properties of aggregates. Determination of particle density and water absorption,* London: BSI.

British Standard Institution, 2013. *BS EN 196-2: 2013 Method of Testing Cement. Chemical Analysis of Cement,* London: BSI.

British Standards Institute, 2002. *BS EN 13706-1: 2002 Reinforced Plastic Composites. Specification for Pultruded Profiles. Designation.,* London: BSI.

British Standards Institute, 2004. *Eurocode 2: Design of Concrete Structures. General Rules and Rules for Buildings.,* London: BSI.

British Standards Institute, 2006. *BS EN 14889-2:2006, Fibres for concrete. Polymer fibres. Definitions, specifications and conformity.,* London: BSI.

British Standards Institute, 2013. *BS 1881-125:2013 Testing Concrete. Methods for Mixing and Sampling Fresh Concrete in the Laboratory,* London: BSI.

British Standards Institution, 2006. *BS EN 14889-1:2006, Fibres for Concrete. Steel Fibres. Definitions, Specifications and Conformity,* London: BSI.

British Standards Institution, 2007. *BS EN 14629:2007 Products and Systems for the Protection and Repair of Concrete Structures. Test Methods. Determination of Chloride Content in Hardened Concrete,* London: BSI.

British Stndard Institution, 2009. *bs en 12350-2: 2009 Testing fresh concrete. Slump-test,* London: BSI.

British Stndard Institution, 2009. *BS EN 12350-3: 2009 Testing fresh concrete. Vebe test,* London: BSI.

Buratti, N., Mazzotti, C. & Savoia, M., 2011. Post-Cracking Behaviour of Steel and Macro-Synthetic Fibre-Reinforced Concretes. *Construction and Building Materials,* Volume 25, pp. 2713-2722.

Canadian Standards Association, 2007. *CAN/CSA-S806-02 Design and Constructing of Building Components with Fibre-Reinforced Polymers,* Mississauga: Canadian Standards Association.

Canadian Standards Association, 2007. *CSA S806-02 Design and Construction of Building Components with Fibre-Reinforced Polymer,* Mississauga: Canadian Standards Association.

Canadian Standards Association, 2010. *CAN/CSA S807-2010: Specification for Fibre-Reinforced Polymers,* Mississauga: CSA.

Ceroni, F., Cosenza, E., Gaetano, M. & Pecce, M., 2006. Durability Issues of FRP Rebars in Reinforced Concrete Members. *Cement & Concrete Composites,* Volume 28, pp. 857-868.

Cheng, A., Huang, R., Wu, J.-K. & Chen, C.-H., 2005. Influence of GGBS on Durability and Corrosion Behaviour of Reinforced Concrete. *Materials Chemistry and Physics,* 93(2-3), pp. 404-411.

Composites UK, 2014. *CompositesUK.* [Online]
Available at:
https://compositesuk.co.uk/system/files/documents/Case%20Study%20-%20West%20Mill%20Bridge.pdf
[Accessed 26 February 2018].

Dai, J.-G., Yokota, H., Iwanami, M. & Kato, E., 2010. Experimental Investigation of the Influence of Moisture on the Bond Behavior of FRP to Concrete Interfaces. *Journal of Composites for Construction,* 14(6), pp. 834-844.

Det Norske Veritas, 2011. *Offshore Standard DNV-OS-C101, Design of Offshore Steel Structures, General,* Oslo: Det Norske Veritas.

Dong, J., Wang, Q. & Guan, Z., 2013. Structural Behaviour of RC Beams with External Flexural and Flexural-Shear Strengthening by FRP Sheets. *Composites: Part B,* Volume 44, pp. 604-612.

Durpray, S. et al., 2010. *The use of concrete in maritime engineering- a good practice guide.* 1st ed. London: CIRIA.

European Committee for Standardisation, 2004. *Eurocode 2: Design of concrete structures - Part 1-1 : General rules and rules for buildings,* Brussels: European Committee for Standardisation.

European Committee for Standardisation, 2010. *CEN/TS 12390-11:2010, Testing Hardened Concrete - Part 11: Determination of the Chloride Resistance of Concrete, Unidirectional Diffusion,* Brussels: European Committee for Standardisation.

European Marine Energy Centre, 2017. *EMEC Orkney.* [Online]
Available at: http://www.emec.org.uk/marine-energy/wave-devices/
[Accessed 21 February 2018].

Feeser, W. K. & Brown, V. L., 2005. *Guide Examples for Design of Concrete Reinforced with FRP Bars.* Kansas City, Missouri, Farmington Hills, Mich.

Feng, P., Meng, X. & Zhang, H., 2015. Mechanical Behavior of FRP Sheets Reinforced 3d Elements Printed with Cementitious Materials. *Composite Structures,* Volume 134, pp. 331-342.

Foti, D., 2011. Preliminary Analysis of Concrete Reinforced with Waste Bottles Pet Fibers. *Construction and Building Materials,* 25(4), pp. 1906-1915.

Frank, E., Hermanutz, F. & Buchmeiser, M. R., 2012. Carbon Fibers: Precursors, Manufacturing and Properties. *Macromolecular Materials and Engineering,* Volume 297, pp. 493-501.

Girgle, F. & Stepanek, P., 2016. An Anchoring Element for Prestressing FRP Reinforcment: Simplified Design of the Anchoring Area. *Materials and Structures,* Volume 49, pp. 1337-1350.

Giuseppe, S., Bencardino, F., Sorrenti, F. & Swamy, N. R., 2015. Structural Effectiveness of FRP Materials in Strengthening RC Beams. *Engineering Structures,* Volume 99, pp. 631-641.

Granju, J.-L. & Balouch, S. U., 2005. Corrosion of steel fibre reinforced concrete from the cracks. *Cement and Concrete Research,* Volume 35, pp. 572-577.

Granju, J.-L. & Balouch, S. U., 2005. Corrosion of Steel Fibre Reinforced Concrete from the Cracks. *Cement and Concrete Research,* 35(3), pp. 572-577.

Gu, Y., Li, M., Wang, J. & Zhang, Z., 2010. Characterization of the Interphase in Carbon Fiber/Polymer Composites Using a Nanoscale Dynamic Mechanical Imaging Technique. *Carbon,* Volume 48, pp. 3229-3235.

Habeeb, M. N. & Ashour, A. F., 2008. Flexural Behavior of Continuous GFRP Reinforced Concrete Beams. *Composites for Construction,* 12(2), pp. 115-124.

Haddad, R. H., Rajai, A.-R., Ghanma, L. & Zaid, N., 2015. Modifying CFRP–Concrete Bond Characteristics from Pull-Out Testing. *Magazine of Concrete Research,* 67(13), pp. 707-717.

Hsie, M., Tu, C. & Song, P., 2008. Mechanical Properties of Polypropylene Hybrid Fiber-Reinforced Concrete. *Materials Science and Engineering A,* Volume 494, pp. 153-157.

Issa, M. A. et al., 2003. Performance of Transverse Joint Grout Materials in Full-Depth Precast Concrete Bridges Deck System. *PCI Journal,* 48(4), pp. 92-103.

Issa, M. S., Metwally, I. M. & Elzeiny, S. M., 2011. Influence of Fibres on Flexual Behaviour and Ductility of Concrete Beams Reinforced with GFRP Rebars. *Engineering Structures*, Volume 33, pp. 1754-1763.

Issa, M. S., Metwally, I. M. & Elzeiny, S. M., 2011. Influence of fibres on flexural and ductility of concrete beams reinforced with GFRP rebars. *Engineering Structures,* Volume 33, pp. 1754-1763.

Jin, F.-L., Li, X. & Park, S.-J., 2015. Synthesis and Application of Epoxy Resins: A Review. *Journal of Industrial and Engineering Chemistry,* Volume 29, pp. 1-11.

Julio, E. N. B. S., Branco, F. A. B. & Silva, V. D., 2005. Concrete-to-Concrete Bond Strength: Influence of an Epoxy-Based Bonding Agent on a Roughened Substrate Surface. *Magazine of Concrete Research,* 57(8), pp. 463-468.

Kang, S.-T., Lee, Y., Park, Y.-D. & Kim, J.-K., 2010. Tensile Fracture Properties of an Ultra High Performance Fibre Reinforced Concrete (UHPFRC) with Steel Fibres. *Composite Strcutures,* Volume 92, pp. 61-71.

Kang, S. T., Yeon, L. B., Kim, J.-K. & Kim, Y. Y., 2011. The Effect of Fibre Distrubution Characteristics on the Flexural Strength of Steel Fibre-Reinforced Unltr High Strength Concrete. *Construction and Building Materials,* Volume 25, pp. 2450-2457.

Khosravi, N., 2017. *Behaviour of Epoxy Filled Flat-Face Joints in Concrete for Wave Energy Converters (Unpublished Doctoral Thesis).* Dundee: The Univeristy of Dundee.

Krause, M. et al., 2010. Determination of the Fibre Orientation in Composites Using the Structure Tensor and Local X-Ray Transform. *Journal of Mateials Science,* 45(4), pp. 888-896.

Laranjeira, F., Molins, C. & Aguado, A., 2010. Predicting the Pullout Response of Inclined Hooked Steel Fibres. *Cement and Concrete Research,* Volume 40, pp. 1471-1487.

Lau, D. & Buyukozturk, O., 2010. Fracture Characterisation of Concrete/Epoxy Interface Affected by Moisture. *Mechanics of Materials,* Volume 42, pp. 1031-1042.

Lenntech, 2018. *Seawater Composition.* [Online]
Available at: https://www.lenntech.com/composition-seawater.htm
[Accessed 4 4 2019].

Litle, W. & Paparoni, M., 1996. Size Effect in Small-Scale Models of Reinforced Concrete Beams. *Journal Proceedings,* Volume 63, pp. 1191-1204.

Lopez, I. et al., 2013. Review of Wave Energy Technologies and the Necessary Power-Equipment. *Renewable and Sustainable Energy Reviews,* Volume 27, pp. 413-434.

Mailvaganam, N. P., 1997. *Effective Use of Bonding Agents,* Ottawa: National Research Council of Canada.

Marlow, 2018. *marlowropes.* [Online]
Available at: https://www.marlowropes.com/technical-data
[Accessed 3 August 2018].

Micelli, F. & Nanni, A., 2004. Durability of FRP Rods for Concrete Structures. *Construction and Building Materials,* Volume 18, pp. 491-503.

Mo, K. H., Yap, K. K. Q., Alengaram, U. J. & Jumaat, M. Z., 2014. The Effect of Steel Fibres on the Enhancement of Flexural and Compressive Toughness and Fracture Charcteristuics of Oil Palm Shell Concrete. *Construction and Buidling Materials,* Volume 55, pp. 20-28.

Nanni, A., De Luca, A. & Zadeh, H. J., 2014. *Reinforced Concrete with FRP Bars: Mechanics and Design.* New York: CRC Press.

Neville, A. M., 2011. *Properties of Concrete.* 5th ed. Edinburgh: Pearson Education Limited.

Ocean Energy Council, 2017. *oceanenergycouncil.* [Online]
Available at: http://www.oceanenergycouncil.com/ocean-energy/wave-energy/
[Accessed 4 Janurary 2018].

Oesch, T., Landis, E. & Kuchma, D., 2018. A Methodology for Quantifying the Imapct of Casting Procedure an Anistropy in Fibre-Reinforced Concrete Using X-Ray CT. *Materials and Structures,* p. 51: 73.

Olivito, R. S. & Zuccarello, F. A., 2010. An Experimental Study on the Tensile Strength of Steel Fiber Reinforced Concrete. *Composites Part B: Engineering,* 41(3), pp. 246-255.

Perez-Collazo, C., Greaves, D. & Iglesias, G., 2015. A review of combined wave and offshore wind energy. *Renewable and Sustainable Energy Reviews,* Volume 42, pp. 141-153.

Pilakoutas, K., Guadagnini, M., Kyriacos, N. & Matthys, S., 2011. Design Guildelines for FRP Reinforced Concrete Structures. *Structures and Buildings,* 164(SB4), pp. 255-263.

Plagué, ,. T., Desmettre, C. & Charron, J.-P., 2017. Influence of Fiber Type and Fiber Orientation on Cracking and Permeability of Reinforced Concrete Under Tensile Loading. *Cement and Concrete Research,* Volume 97, pp. 59-70.

Provatic America, 2019. *Provatic America.* [Online]
Available at: http://www.protavicamerica.com/products/moisture-resistant-epoxy/
[Accessed 21 3 2019].

Randerson, J., 2017. *Marine power: can UK companies rule the waves?.* [Online]
Available at: https://www.theguardian.com/sustainable-business/2017/apr/05/marine-power-can-uk-companies-rule-the-waves

Ratcliffe, R., 2007. Concrete Reinforcement: Fibre Reinforcement Steel versus Macro (Structural) Synthetic. *Concrete Engineering International,* 11(1), pp. 14-16.

Savvilotidou, M., Vassilopoulos, A. P., Frigione, M. & Keller, T., 2017. Effects of Aging in Dry Environment on Physical and Mechanical Properties of A Cold-Curing Structural Epoxy Adhesive for Bridge Construction. *Construction and Building Materials,* Volume 140, pp. 552-561.

Schmidt, J. W., Taljsten, B., Bennitz, A. & Pedersen, H., 2009. *FRP Tendon Anchorage in Post-Tensioned Concrete Strcutures.* Cape Town, Taylor & Francis Group, pp. 1181-1186.

Schöck, 2017. *Schöck Ltd.* [Online]
Available at: https://www.schoeck.co.uk/en-gb/combar-material
[Accessed 24 January 2018].

Sen, R., 2015. Developments in the Durability of FRP-Concrete Bond. *Construction and Building Materials,* Volume 78, pp. 112-125.

SH Structures, 2018. *SHStructure.com.* [Online]
Available at: http://www.shstructures.com/projects/m8-harthill-services-footbridge/
[Accessed 22 February 2018].

Slowik, M., 2014. Shear Failure Mechanism in Concrete Beams. *Procedia Materials Science,* Volume 3, pp. 1977-1982.

Soetens, T., Van Gysel, A., Matthys, S. & Taerwe, L., 2013. A Semi-Analytical Model to Predict the Pull-Out Behaviour of Inclined Hooked-End Steel Fibres. *Construction and Building Materials,* Volume 43, pp. 253-265.

Song, Z., 2014. *Enhance the Service Life of Concrete Exposed to Chloride Attack (Doctoral Thesis).* Dundee: University of Dundee.

Soudki, K., El-Salakaway, E. & Craig, B., 2007. Behaviour of CFRP Strengthened Reinforced Concrete Beams in Corrosive Environment. *Composites for Construction,* 11(3), pp. 291-298.

Sümer, Y. & Aktas, M., 2015. Defining parameters for concrete damage plasticity model. *Challenge Journal of Structural Mechanics,* Volume 1, pp. 149-155.

Tata Steel, 2018. *Tata Steel Europe.* [Online]
Available at: https://www.tatasteeleurope.com/en/markets/engineering/strip/price-lists
[Accessed 23 May 2018].

The Concrete Society, 2007. *Technical Report No. 63 Guildance for the Design of Steel-Fibre-Reinforced Concrete,* Surrey: The Concrete Society.

The Concrete Society, 2007. *Technical Report No. 65 Guidance on the Use of Macro-Synthetic-Fibre-Reinforced Concrete,* Surrey: The Concrete Society.

The Concrete Society, 2012. *Technical Report No. 55 Design Guidance for Strengthening Concrete Structures Using Fibre Composite materials,* Surrey: The Concrete Society.

The Scottish Goverment, 2017. *Scottish Goverment.* [Online]
Available at: http://www.gov.scot/Topics/Business-Industry/Energy/Energy-sources/19185
[Accessed 03 Janurary 2018].

Theriault, M. & Benmokrane, B., 1998. Effetcs of FRP Reinforcement Ratio and Concrete Strength on Flexural Behaviour of Concrete Beams. *Journal of Composites for Construction,* Volume 2, pp. 7-15.

Thomas, J. & Ramaswamy, A., 2007. Mechanical Properties of Steel Fibre-Reinforced Concrete. *Journal of Materials in Civil Engineering,* 19(5), pp. 385-392.

Torrents, J. et al., 2012. Inductive Method for Assessing the Amount and Orientation of Steel Fibre in Concrete. *Materials and Structures,* Volume 45, pp. 1577-1592.

Torres, L., Kyriacos, N. & Pilakoutas, K., 2012. Design Procedure and Simplified Equations for the Flexual Capacity of Concrete Members Reinforced with Fibre-Reinforced Polymer Bars. *Structural Concrete,* 13(2), pp. 119-129.

Toutanji, H. & Ortiz, G., 2001. The Effects of Surface Preparation on the Bond Interface Between FRP Sheets and Concrete Members. *Composute Structures,* Volume 53, pp. 457-462.

Triantafillou, T. & Matthys, S., 2013. Fibre-Reinforced Polymer Reinforcement Entres fib Model Code 2010. *Structural Concrete,* 14(4), pp. 335-342.

Tureyen, K. A. & Frosch, R. J., 2002. Shear Tests of FRP-Reinforced Concrete Beams without Stirrups. *ACI Strcutural Journal,* 99(4), pp. 427-434.

Tuyan, M. & Yazici, H., 2012. Pull-Out Behaviour of Single Steel Fibre from Sifcon Matrix. *Construction and Building Materials,* Volume 35, pp. 571-577.

Wang, H. & Belarbi, A., 2011. Ductility Characteristics of Fibre-Reinforced-Concrete Beams Reinforced with FRP Rebars. *Construction and Building Materials,* Volume 25, pp. 2391-2401.

Wave Energy Scotland, 2016. *Wave Energy Scotland: Materials Landscaping Study -- Final Report,* s.l.: s.n.

Wave Energy Scotland, 2016. *waveenergyscotland.* [Online]
Available at: http://www.waveenergyscotland.co.uk/news-events/dismantling-pelamis-p2-001-in-orkney/
[Accessed 20 August 2018].

Wave Energy Scotland, 2017. *Polyshell.* [Online]
Available at:
http://www.waveenergyscotland.co.uk/programmes/details/materials/polyshell/
[Accessed 20 August 2018].

Westman, M. P. et al., 2010. *Natural Fiber Composites: A Review,* Washington: Pacific Northwest National Laboratory.

West, R. P., 2003. *Design Issues in the Alignment of Steel Fibres in Concrete Slabs Using A Magnetic Fin.* Dundee, Thomas Telford.

West, R. P., Zhang, S. & Mandl, J., 2005. *Aligning Long Steel Fibres in Fresh Concrete.* Dundee, Thomas Telford.

Wilson, W. & O'Flaherty, T., 2016. *Effect of Steel Fibre Dosage on the Behaviour of Ultra High Performance Fibre Reinforced Concrete Beams and Slabs.* Glaway, Civil Engineering Research in Irland Conference.

Wirth, K., 2019. *Geochemical Instrumentation and Analysis.* [Online]
Available at:
https://serc.carleton.edu/research_education/geochemsheets/techniques/XRF.html
[Accessed 12 5 2019].

Yang, F., Lin, Z. & Yang, M., 2016. Bond Mechanism and Bond Strength of GFRP Bars to Concrete: A Review. *Composites Part B,* Issue 98, pp. 56-69.

Yang, J.-M., Min, K.-H., Shin, H.-O. & Yoon, Y.-S., 2012. Effect of Steel and Synthetic Fibres on Flexural Behaviour of High-Strength Concrete Beams Reinforced with FRP Bars.. *Composites: Part B,* Volume 43, pp. 1077-1086.

Yazici, S., Inan, G. & Tabak, V., 2007. Effect of Aspect Ratio and Volume Fraction of Steel Fiber on the Mechanical Properties of SFRC. *Construction and Building Materials,* Volume 21, pp. 1250-1253.

Yin, S. et al., 2015. Use of Macro Plastic Fibres in Concrete: A Review. *Construction and Building Materials,* Volume 93, pp. 180-188.

Zafar, A., Bertocco, F., Schjodt-Thomsen, J. & Rauhe, J. C., 2012. Investigation of the Long Term Effects of Moisture on Carbon Fibre and Epoxy Matrix Composites. *Composites Science and Technology,* Volume 72, pp. 656-666.

Zhou, Y. et al., 2015. Bond Behavior of FRP-to-Concrete Interface under Sulfate Attack: An Experimental Study and Modeling of Bond Degradation. *Construction and Building Materials,* Volume 85, pp. 9-21.

Appendix A

A.1 Concrete Mixes and Compressive Strength

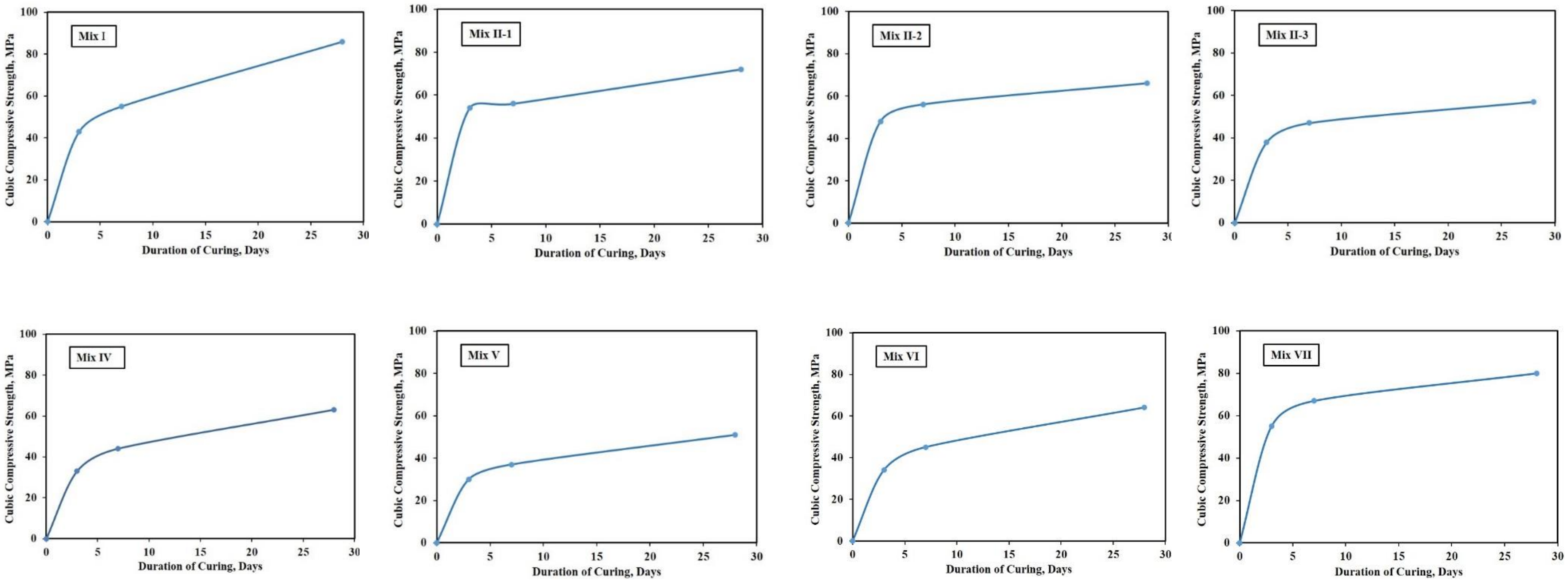

Note: Mix III-1 and III-2 were only measured 28-days' compressive strength; therefore, not plotted.

Figure A.1 Development of the compressive strength for concrete mixes

A.2 Unidirectional Chloride Diffusion Predetermination Test

Determination of the unidirectional chloride penetration of concrete Mix I was carried out in accordance with CEN/TS 12390-11: 2010 (Bristish Standard Institution, 2010). In this study, 3 concrete cubes 100 mm in dimension were cut individually with a wet tile saw into 2 subparts by 20 : 80 mm in the orientation perpendicular to the casting direction. The 20 mm blocks were used to measure the chloride resistance. Each block was first immersed into demineralised water in a container in order to be vacuum saturated. The saturation process was maintained for 3 hours. Afterwards, the 3 blocks were dried and sealed with wax on all surfaces except the sawn one then placed in to the saturated calcium hydroxide ($Ca(OH)_2$) solution for 18 hours. Finally, the blocks were transferred to the 1 mol/l Cl^- exposure solution which was produced by dissolving 234 g sodium chloride into 4 litres of demineralised water. Figure A.2 shows the arrangement of the blocks under the exposure with the unsealed sawn face of each block directly being exposed to the Cl^- solution. The exposure was at a constant temperature of 20 ± 2°C and lasted for 45 days.

After the exposure, the concrete blocks were dry ground on the unsealed sawn face with an electrical grinder. The grinding was carried out within 8 hours of removing the blocks from the exposure solution and performed on the central area with a boundary of at least 10 mm away from the concrete surfaces. 10 grams of concrete dust were collected from each block within a layer less than 2 mm deep from the surface. Table 3.4 (in Section 3.3) lists the chemical reagents that were used during the chloride measurement and the surface chloride content of Mix I was measured to be 0.53% by mass of concrete on average.

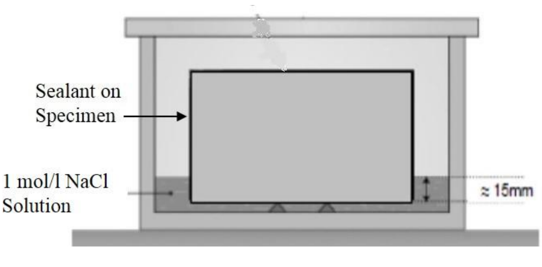

Figure A.2 Arrangement of the block under exposure (Bristish Standard Institution, 2010)

A.3 Calculation of the Addition of Gypsum

ASTM C452-06: 2006 (ASTM International, 2006) requires the content of SO_3 to be 7% by mass of cement and gypsum for testing the potential expansion of PC mortars exposed to sulphate. However, the computing method for the amount of the gypsum proposed by this standard was used for this calculation. The gypsum amount needed for addition can be calculated in terms of percentage of the cement amount with the following equations:

$$\text{cement}, \% = \frac{g-7.0}{g-c} \times 100 \qquad \text{Equation A.3.1}$$

$$\text{gypsum}, \% = \frac{7.0-c}{g-c} \times 100 \qquad \text{Equation A.3.2}$$

where, g is the SO_3 content of the PC, %; c is the SO_3 content of the gypsum, %.

In this study, the PC cement had a SO_3 content of 2.6% based on the XRF measurement while the gypsum had a SO_3 content of 44.0% as claimed by the supplier. Hence:

g = 44.0; c = 2.6

$$\text{cement}, \% = \frac{g-7.0}{g-c} \times 100 = \frac{44.0-7.0}{44.0-2.6} \times 100 = 89.4\%$$

$$\text{gypsum}, \% = \frac{c-7.0}{g-c} \times 100 = \frac{7.0-2.6}{44.0-2.6} \times 100 = 10.6\%$$

Therefore, $\frac{gypsum}{cement} = \frac{10.6}{89.4} = 0.119 = 11.9\%$

For concrete Mix III-2 with a cement proportion of 422 kg/m^3, addition of the gypsum is:

Addition of gypsum = $422\ kg/m^3 \times 0.119 =$ **50 kg/m^3**

A.4 Trial Mixes of Synthetic-Fibre-Reinforced Concrete

The synthetic fibre dosage needs to be relatively large in order to provide post-crack load resistance and reduce failure brittleness while on the other hand, addition of large amounts of fibres during mixing usually causes rheological problems. Therefore, a series of trial mixes was carried out to figure out a balance between these two requirements.

Table A.1 shows the trialled mixes with varied free water and synthetic fibre proportions as well as the measured slump results. All the mixes used 70% PC+ 30% DFA and granite aggregates. Details of these materials as well as the macro-synthetic fibre were provided in Section 3.3.1 and 3.3.3 respectively. The mixing of Trial 1 was found extremely coarse and dry (Figure A.3) and had a slump of almost 0 which indicated that the fresh concrete had nearly no flowability. Therefore, the free water content for Trial II was increased to 190 kg/m^3 with proportionally reduced amounts of cement and aggregates so that the w/c ratio remained 0.43. It was found that the workability for Trial 2 increased but it was still hard to mould and compact the fresh concrete. It appeared that the addition would have no chance to approach 80 kg/m^3 even though addition of steel fibres at such a dosage or over 80 kg/m^3 is relatively usual. This could be because the macro-synthetic fibres were taking up a substantial volume in the mixes due to their relatively light density and consequently the fresh concrete became insupportable to flow and compact. Trial III had a significantly reduced PC fibre dosage of 20 kg/m^3 and produced a mix with acceptable and practicable workability (Figure A.3). Albeit still coarse, this mix could be handled for moulding. Hence, the mix proportions of Trial 3 were decided to be used for this study.

Table A.1 Trial mix proportions and measured slumps for addition of synthetic fibres

Mix	w/c Ratio	Mix Proportions, kg/m^3				Measured Slump, mm
		Water	Cement	Aggregate	Fibres	
Trial I	0.43	170	400	1810	80	<1
Trial II		190	447	1743	80	<1
Trial III		190	447	1771	20	20

Figure A.3 The fresh mixed concrete of Trial I in the pan before the slump test (left), and slump test for the mix of Trial II (right)

Appendix B

B.1 Experimental Results from Pull-Out Test

Table B.1 Experimental results from the pull-out test on GFRP and CFRP bars

Bar Type	w/c Ratio	Addition	Bond Stress, MPa				Slip, mm	Gradient	
			$\tau_{0.05}$	$\tau_{0.10}$	$\tau_{0.25}$	τ_{max}	s_{max}	k1	k2
GFRP	0.45	-	0.3	0.7	1.9	28.4	5.5	5.4	-12.5
			-	-	0.9	27.3	4.9	5.6	-5.8
			-	0.3	1.4	24.1	4.5	5.5	-9.1
CFRP	0.45	-	0.1	0.4	0.7	7.1	2.5	1.7	-0.3
			0.1	0.5	1.4	5.9	3.2	1.7	-0.2
			0.2	0.6	0.8	7.6	4.5	1.8	-0.4
	0.40	-	0.1	0.6	1.8	6.6	7.1	2.0	-
			0.1	0.6	1.8	6.0	3.0	1.9	-
	0.50	-	0.2	0.6	1.7	7.5	3.4	2.6	-
			0.1	0.4	1.6	11.6	8.3	2.8	-
			0.1	0.1	1.3	8.8	3.3	3.2	-
GFRP	0.45	Chloride	-	0.3	1.4	30.1	5.8	2.5	-1.7
			-	0.2	1.1	27.3	5.1	2.6	-1.3
			-	0.2	1.2	31.1	5.6	2.8	-1.7
	0.47	Sulphate	-	0.3	1.4	23.3	4.0	2.9	-1.7
			-	0.3	1.4	26.9	4.9	2.8	-1.4
			-	0.2	1.1	29.2	5.7	2.6	-1.0
CFRP	0.45	Chloride	-	0.3	1.5	7.5	3.6	3.9	-
			0.1	0.4	1.1	7.6	3.7	2.0	-
			0.1	0.5	2.0	10.6	6.2	4.4	-
	0.47	Sulphate	0.1	0.3	1.4	6.3	2.6	2.5	-
			0.1	0.3	1.4	5.0	2.1	3.0	-
			0.2	0.7	1.8	7.8	4.1	3.3	-

B.2 Experimental Results from the Three-Point Bending Test

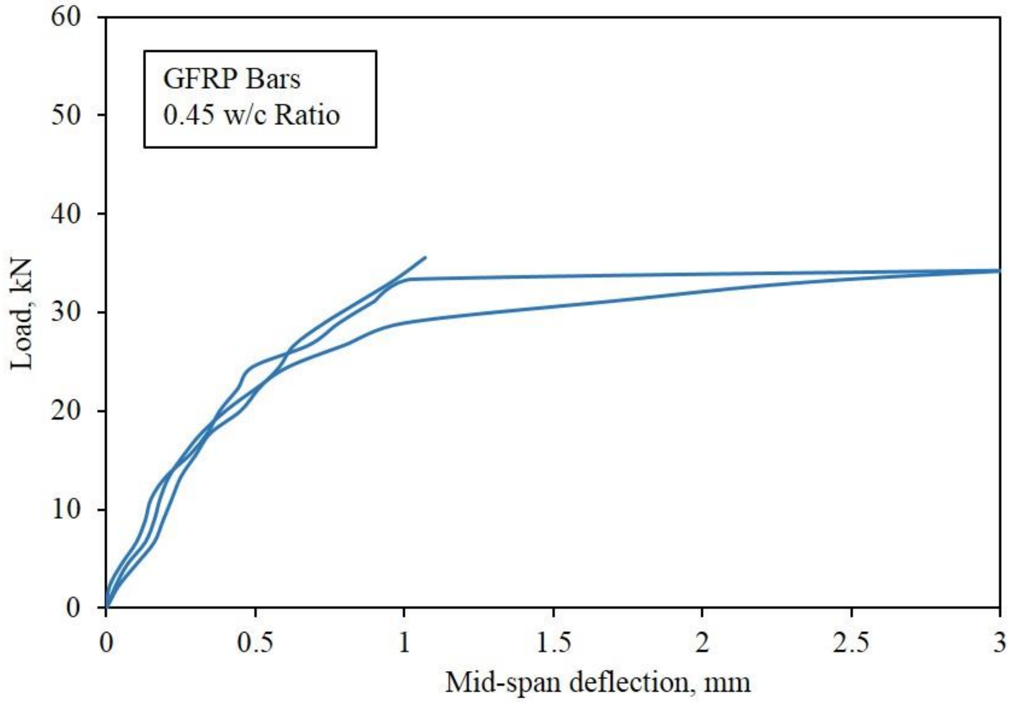

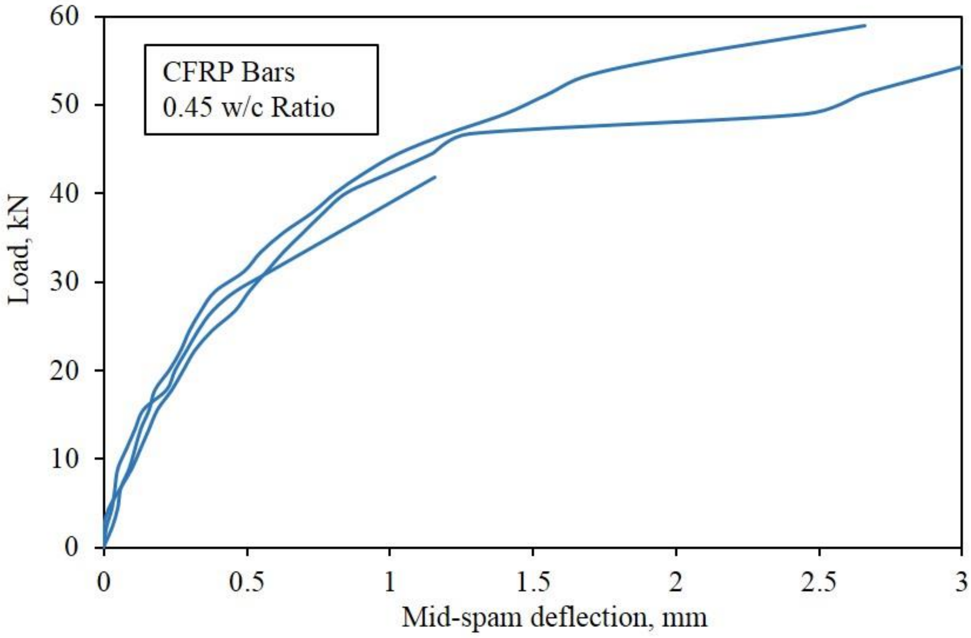

Figure B.1 Applied load vs. midspan deflection curves from the three-point bending test on beams reinforced with GFRP bars (above) and CFRP bars (below)

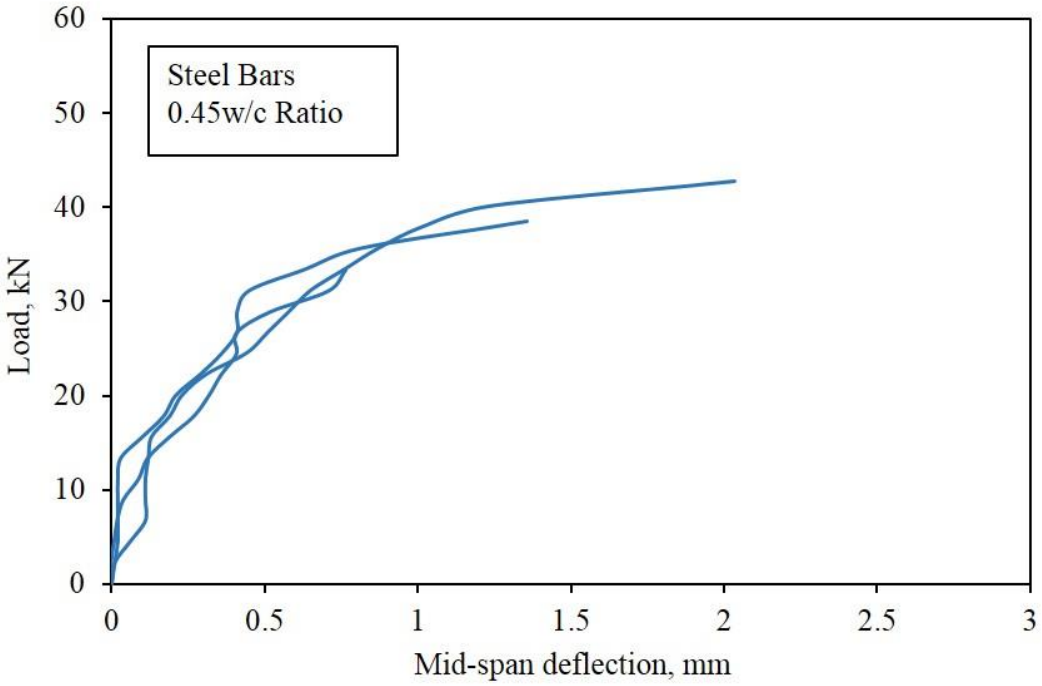

Figure B.2 Applied load vs. midspan deflection curves from the three-point bending test on beams reinforced with steel bars

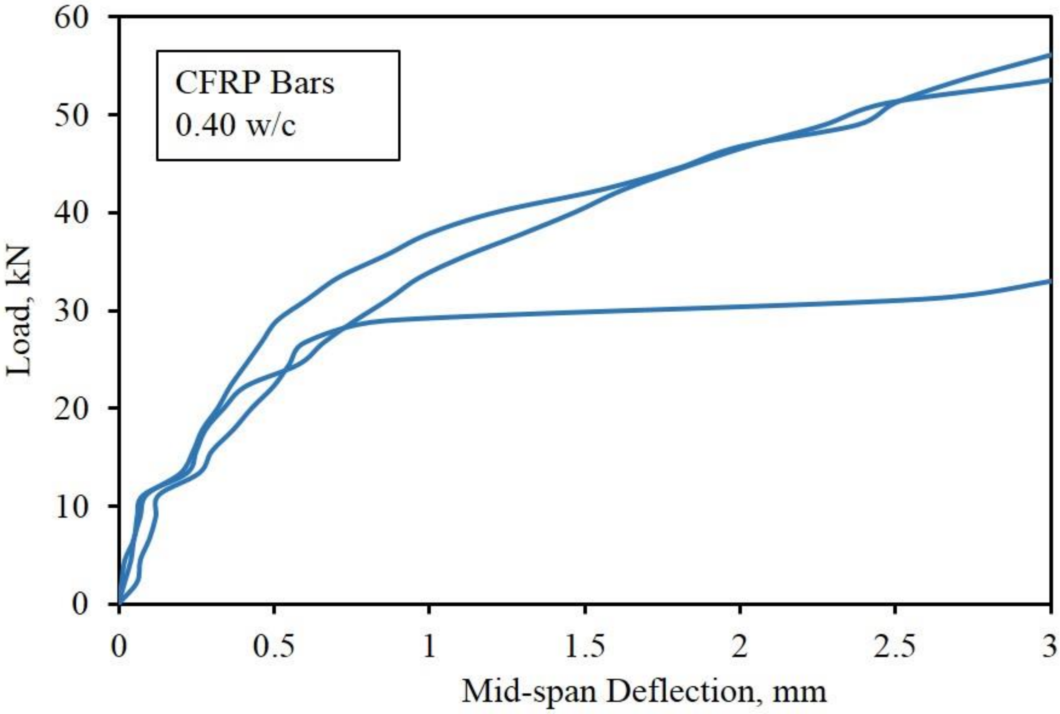

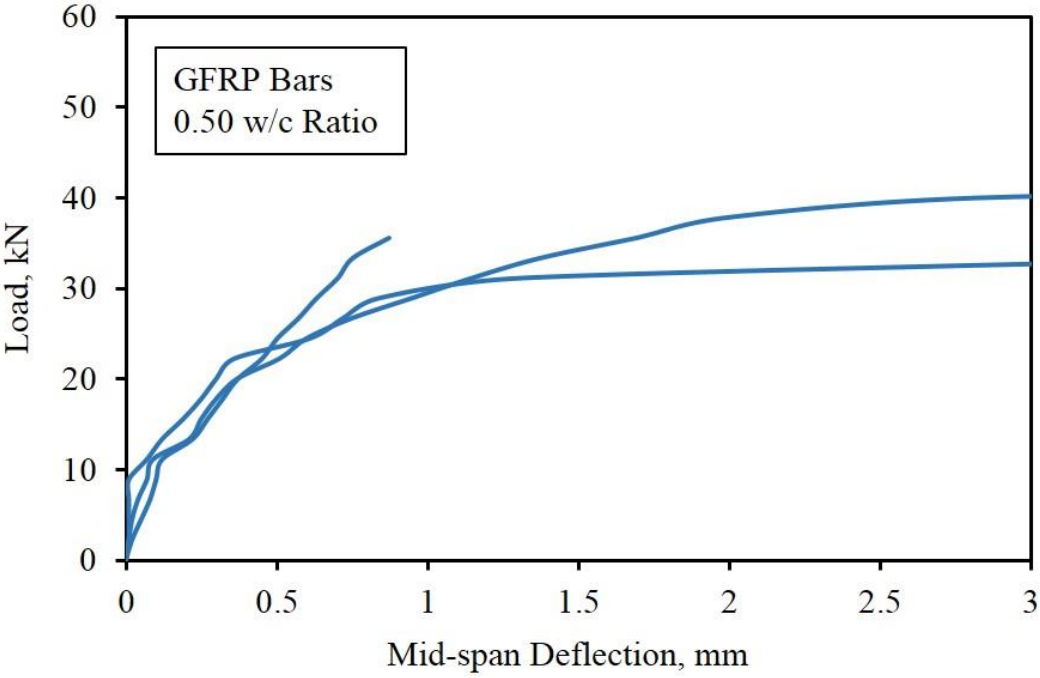

Figure B.3 Applied load vs. midspan deflection curves from the three-point bending test on beams reinforced with GFRP bars for concrete of 0.40 (above) and 0.50 (below) w/c ratio

Appendix C

C.1 Calculations of Prediction of the Ultimate Moment

Part A: ACI 440.1R-06 (2006) Method

(1) Beam Reinforced with GFRP Bars

Material Properties:

Characteristic strength of concrete C50/60,

Design strength of concrete $f_c' = 50 \times 0.9 = 45\ MPa$;

Elastic modulus of GFRP $E_f = 60\ GPa$;

Ultimate tensile strength of GFRP $f_{fu} = 1000$ N/mm^2,

Short-term design tensile strength of GFRP $f_f = \frac{1000}{1.3} = 769$ N/mm^2;

$\beta_1 = 0.70$; $\varepsilon_{cu} = 0.003$.

Reinforcement Condition:

The balanced reinforcement ratio for beams reinforced with GFRP bars:

$$\rho_b = 0.85\frac{f_c'}{f_f}\beta_1\frac{E_f \cdot \varepsilon_{cu}}{E_f \cdot \varepsilon_{cu} + f_f} = 0.85 \times \frac{45}{769} \times 0.70 \times \frac{60\times10^3 \cdot 0.003}{60\times10^3 \cdot 0.003 + 769} = \quad \mathbf{0.007}$$

The reinforcement ratio of the GFRP-reinforced beams: $\rho_f = \frac{A_f}{bd} = \frac{100.5}{100\times75} =$ **0.013**

Therefore, the GFRP-reinforced beams were **over-reinforced**.

Ultimate Moment Resistance and Reinforcement Ultimate Strain:

Tensile stress of the GFRP rebar at failure:

$$f_f = \sqrt{\frac{(E_f\varepsilon_{cu})^2}{4} + \frac{0.85\beta_1 f_c}{\rho_f}E_f\varepsilon_{cu}} - 0.5E_f\varepsilon_{cu} = 558\ N/mm^2 < f_{fu} = 1000\ N/mm^2;$$

$$a = \frac{A_f f_f}{0.85 f_c b} = \frac{100.5\times550}{0.85\times50\times100} = 13.2mm,$$

$$M_n = A_f f_f\left(d - \frac{a}{2}\right) = 100.5 \times 550\left(75 - \frac{13.2}{2}\right) = \quad \mathbf{3.8\ kN\cdot m}$$

$$\varepsilon_{fu} = \frac{f_f}{E_f} = \frac{550}{60\times10^3} = \quad \mathbf{0.009}$$

(2) Beams Strengthened with External CFRP Strands

Material Properties:

Characteristic strength of concrete C50/60 (C40/50 for the fibrous concrete)

Design strength of concrete $f_c' = 50 \times 0.9 = 45\ MPa$;

Elastic modulus of GFRP $E_f = 230\ GPa$;

Ultimate tensile strength of CFRP $f_{fu} = 2100$ N/mm^2,

Short-term design tensile strength of CFRP $f_f = \frac{2100}{1.3} = 1615\ N/mm^2$;

Reinforcement Condition:

The balanced reinforcement ratio for beams strengthened with external CFRP strands:

$\rho_b = 0.85\frac{f_c'}{f_f}\beta_1\frac{E_f\cdot\varepsilon_{cu}}{E_f\cdot\varepsilon_{cu}+f_f} = 0.85\times\frac{45}{1615}\times 0.70\times\frac{230\times10^3\cdot 0.003}{230\times10^3\cdot 0.003+1615} =$ **0.005**

For beams strengthened with one longitudinal CFRP strand: $\rho_f = \frac{A_f}{bd} = \frac{28}{100\times100} =$ **0.003**

Therefore, they were **under-reinforced**.

For beams strengthened with two longitudinal CFRP strands: $\rho_f = \frac{A_f}{bd} = \frac{28\times2}{100\times100} =$ **0.006**

Therefore, they were slightly **over-reinforced**

For beams strengthened with three longitudinal CFRP strands: $\rho_f = \frac{A_f}{bd} = \frac{28\times3}{100\times100} =$ **0.009**

Therefore, they were **over-reinforced**.

Ultimate Moment Resistance & Reinforcement Ultimate Strain:

$\varepsilon_{cu} = 0.003.$

(2-1) Beams strengthened with one longitudinal CFRP strand (CC1 & CC2.1)

$\beta_1 = 0.70$ (CC2.1)

$\varepsilon_{fu} = \frac{f_{fu}}{E_f} = \frac{2100}{230\times10^3} = 0.009$

$c_b = \frac{\varepsilon_c}{\varepsilon_{fu}+\varepsilon_c}d = \frac{0.003}{0.009+0.003}\times 100 = 25\,mm$

$M_n = A_f f_{fu}\left(d-\frac{\beta_1 c_b}{2}\right) = 28\times2100\times\left(100-\frac{0.70\times25}{2}\right) =$ **5.4 kN·m**

$\beta_1 = 0.75$ (CC1)

$M_n = A_f f_f\left(d-\frac{\beta_1 c_b}{2}\right) = 28\times2100\times\left(100-\frac{0.75\times25}{2}\right) =$ **5.3 kN·m**

(2-2) Beams strengthened with two longitudinal CFRP strands (CC2.2)

$\beta_1 = 0.70;$

Tensile stress of the CFRP strands at failure:

$f_f = \sqrt{\frac{(E_f\varepsilon_{cu})^2}{4}+\frac{0.85\beta_1 f_c}{\rho_f}E_f\varepsilon_{cu}} - 0.5E_f\varepsilon_{cu} = 1537\,N/mm^2 < f_{fu} = 2100\,N/mm^2;$

$a = \frac{A_f f_f}{0.85 f_c b} = \frac{56\times1537}{0.85\times50\times100} = 20.3\,mm$

$M_n = A_f f_f\left(d-\frac{a}{2}\right) = 56\times1537\times\left(100-\frac{20.3}{2}\right) =$ **7.7 kN·m**

$\varepsilon_{cu} = \frac{f_f}{E_f} = \frac{1537}{230\times10^3} =$ **0.007**

(2-3) Beams strengthened with three longitudinal CFRP strands (CC2.3)

$\beta_1 = 0.70;$

Tensile stress of the GFRP rebar at failure:

$f_f = \sqrt{\frac{(E_f\varepsilon_{cu})^2}{4}+\frac{0.85\beta_1 f_c}{\rho_f}E_f\varepsilon_{cu}} - 0.5E_f\varepsilon_{cu} = 1204\,N/mm^2 < f_{fu} = 2100\,N/mm^2;$

$a = \frac{A_f f_f}{0.85 f_c' b} = \frac{84 \times 1204}{0.85 \times 50 \times 100} = 23.8\ mm$

$M_n = A_f f_f \left(d - \frac{a}{2}\right) = 84 \times 1129 \times \left(100 - \frac{24.8}{2}\right) =$ **8.9 kN·m**

$\varepsilon_{cu} = \frac{f_f}{E_f} = \frac{1129}{230 \times 10^3} =$ **0.005**

Part B: Pilakoutas et al. (2011) Method

(Material properties are the same as aforementioned unless otherwise specified)

(1) Beam Reinforced with GFRP Bars

$\beta_1 = 0.80; \eta = 1.0$

Tensile stress of the GFRP rebar at failure:

$\varepsilon_f = \sqrt{\frac{\varepsilon_{cu}^2}{4} + \frac{\eta \beta_1 f_c}{\rho_f E_f} \varepsilon_{cu}} - 0.5\varepsilon_{cu} = \sqrt{\frac{0.003^2}{4} + \frac{1.0 \times 0.80 \times 50}{0.013 \times 60 \times 10^3} 0.003} - 0.5 \times 0.003 =$ **0.011**

$\mathrm{a} = \beta_1 \frac{\varepsilon_{cu}}{\varepsilon_f + \varepsilon_{cu}} d = 0.80 \times \frac{0.003}{0.011 + 0.003} \times 75 = 12.9\ mm$

$M_n = \eta f_c b a \left(d - \frac{a}{2}\right) = 1.0 \times 50 \times 100 \times 12.9 \times \left(75 - \frac{12.9}{2}\right) =$ **4.4 kN·m**

$f_f = \varepsilon_f E_f = 0.011 \times 60 \times 10^3 = 660\ N/mm^2 < f_{fu} = 1000\ N/mm^2;$

(2) Beams Strengthened with External CFRP Strands

(2-1) Beams strengthened with one longitudinal CFRP strand (CC1 & CC2.1)

Based on the calculating method suggested by Pilakoutas et al. (2011), the compressive strain of concrete at failure $\varepsilon_c = 0.001$

$\varepsilon_{fu} = \frac{f_{fu}}{E_f} = \frac{2100}{230 \times 10^3} = 0.009$

$c = \frac{\varepsilon_c}{\varepsilon_{fu} + \varepsilon_c} d = \frac{0.001}{0.009 + 0.001} \times 100 = 10.0mm$

$M_n = A_f f_{fu} \left(d - \frac{\beta_1 c}{2}\right) = 28 \times 2100 \times \left(100 - \frac{1.0 \times 10.0}{2}\right) =$ **5.6 kN·m**

(2-2) Beams strengthened with two longitudinal CFRP strands (CC2.2)

$\beta_1 = 0.80; \eta = 1.0$

Tensile stress of the CFRPs strands at failure:

$\varepsilon_f = \sqrt{\frac{\varepsilon_{cu}^2}{4} + \frac{\eta \beta_1 f_c}{\rho_f E_f} \varepsilon_{cu}} - 0.5\varepsilon_{cu} = \sqrt{\frac{0.003^2}{4} + \frac{1.0 \times 0.80 \times 50}{0.006 \times 230 \times 10^3} 0.003} - 0.5 \cdot 0.003 =$ **0.008**

$\mathrm{a} = \beta_1 \frac{\varepsilon_{cu}}{\varepsilon_f + \varepsilon_{cu}} d = 0.80 \times \frac{0.003}{0.008 + 0.003} \times 75 = 16.4\ mm$

$M_n = \eta f_c b a \left(d - \frac{a}{2}\right) = 1.0 \times 50 \times 100 \times 18.0 \times \left(75 - \frac{16.4}{2}\right) =$ **5.5 kN·m**

$f_f = \varepsilon_f E_f = 0.008 \times 230 \times 10^3 = 1840\ N/mm^2 < f_{fu} = 2100\ N/mm^2;$

(2-3) Beams strengthened with three longitudinal CFRP strands (CC2.3)

Tensile stress of the CFRPs strands at failure:

$\varepsilon_f = \sqrt{\frac{{\varepsilon_{cu}}^2}{4} + \frac{\eta\beta_1 f_c}{\rho_f E_f}\varepsilon_{cu}} - 0.5\varepsilon_{cu} = \sqrt{\frac{0.003^2}{4} + \frac{1.0\times0.80\times50}{0.009\times230\times10^3}0.003} - 0.5\cdot0.003 =$ **0.006**

$\text{a} = \beta_1 \frac{\varepsilon_{cu}}{\varepsilon_f + \varepsilon_{cu}} d = 0.80 \times \frac{0.003}{0.006+0.003} \times 75 = 20.0\ mm$

$M_n = \eta f_c ba\left(d - \frac{a}{2}\right) = 1.0 \times 50 \times 100 \times 20.0 \times \left(75 - \frac{20.0}{2}\right) =$ **6.5 kN·m**

$f_f = \varepsilon_f E_f = 0.006 \times 230 \times 10^3 = 1380\ N/mm^2 < f_{fu} = 2100\ N/mm^2;$

C.2 Calculations of Prediction of Shear Resistance

The shear resistance contribution of uncracked concrete and longitudinal FRP rebar is computed according to Equation 4.2:

Characteristic cylindrical strength of concrete in compression $f_c = 50\ MPa$;

Elastic modulus of concrete $E_c = 5000\sqrt{50} = 35\ MPa$; $\rho_f = 0.013$; $n_f = \frac{E_f}{E_c} = \frac{60}{35} = 1.71.$

$k = \sqrt{2\rho_f n_f + (\rho_f n_f)^2} - \rho_f n_f = \sqrt{2\cdot0.013\cdot1.71 + (0.013\cdot1.71)^2} - 0.013\cdot1.71 = 0.19$

$k_a = 0.03 f_c^{1.25} = 0.03 \times 50^{1.25} = 3.99$

$V_{c,f} = 0.4kk_a\sqrt{f_c}b_w d = 0.4 \times 0.19 \times 3.99\sqrt{50} \times 100 \times 75 = 16000N =$ **16.0 kN**

The shear resistance contribution of the FRP shear reinforcement is computed according to Equation 6.3 and 6.4:

(a) for GC1 beams with CFRP bar ‘sticks’ shear reinforcement

$f_{fv} = 0.004E_f = 0.004 \times 130 \times 10^3 = 520\ MPa$

$V_f = \frac{1}{s}A_{fv}f_{fv}d = 50.2 \times 520 \times 75 \times \frac{1}{70} = 27900\ N =$ **27.9 kN**

(b) for GC2 beams with CFRP strands shear reinforcement

$f_{fv} = 0.004E_f = 0.004 \times 230 \times 10^3 = 920\ MPa$

$V_f = \frac{1}{s}A_{fv}f_{fv}d = 28.0 \times 920 \times 100 \times \frac{1}{70} = 36800\ N =$ **36.8 kN**

C.3 Analysis of CT Scanned Images of CFRP Strand and Aligned Steel Fibres

Visualisation of the void distribution and calculation of the void volume fraction is carried out with the Porosity/Inclusion Analysis (VGDefx/only threshold) module. The sample was registered as a simple object. To produce the surface determination, the grey values of the background and the material were defined manually by selecting related example areas while the isosurface value was also slightly adjusted based on the suggested level (Figure C.1). The porosity calculation was carried out with the determinate surface while the analysis area was the ‘internal cleaning, all’ mode.

Visualisation and calculation of the steel fibre distribution was carried out with the Fibre Composite Material Analysis module using the same methods for object registration and surface determination as the CFRP. Both the absolute 3D orientations and deviation from a defined orientation (the alignment direction) were analysed. The gradient threshold was selected as 3.00 by inspecting the preview analysis area (Figure C.2) and the first analysis results to avoid calculating noise in addition to the fibres.

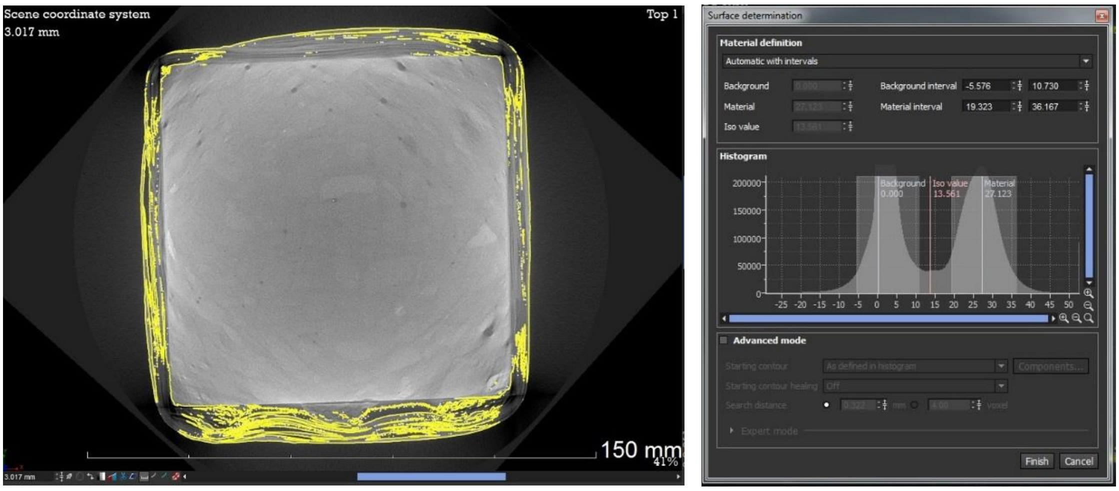

Material definition
Automatic with intervals
Background 0.000
Material 27.123
Iso value 13.561
Background interval -5.576 10.730
Material interval 19.323 36.167
Background 0.000
Iso value 13.561
Material 27.123
☐ Advanced mode
Starting contour: As defined in histogram
Starting contour healing: Off
Search distance ● 0.322 mm ○ 4.00 voxel
Expert mode

Figure C.1 Surface determination of the reconstructed CFRP sample

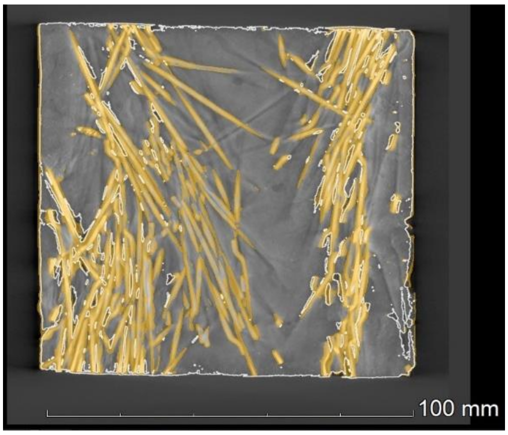

Figure C.2 Preview of analysis area (in yellow) after the gradient threshold selection

C.4 Post-Tensioning of Concrete Reinforced with GFRP

The 3 post-tensioned beams had the same reinforcing conditions for both main bars and shear links as GC1 beams in Section 5.2 and failed in a similar flexural failure mode as the latter. The PT beams developed big flexural cracks within the pure bending zone that spread approaching the top face. Crush of concrete from under the 2 load-applying points also occurred possibly due to the beams being over-reinforced as well as post-tensioned. A typical failure of the post-tensioned beam is shown in Figure C.3. The PT beams had a load resistance of 17.2 kN at their first crack on average, which was approximately 30% higher than the non-stressed GC1 beams. Hence, the post-tensioning behaved effectively in retarding the crack development albeit it was considered as unsuccessful during the experiment. However, the maximum load resistance of PT beams was relatively lower than GC1 and more varied individually. This might be attributed to the failure of applying the post-tension during test. Since insufficient debond might have caused material break partially happening in the tensile GFRP rebar, the flexural strength of these beams was also affected. This break might not be too severe to reduce early strength behaviour of the beams and, as a result, their strength at first crack was still improved.

Figure C.3 Crack and failure of one post-tensioned beam reinforced with GFRP

C.5 Calibration of Load Resistance of Steel-Fibre-Reinforced Beams

The calibration is carried out on two beams that are assumed to have one Ø10 mm tensile steel rebar and aligned steel fibres 100 kg/m^3 in dosage (without consideration of the layer depths) separately.

For the fibrous beam, the equivalent area of steel for the tensile reinforcement is computed as:

The cross-sectional area of each filament, $A_{fibre} = \frac{1}{4}\pi d_{fibre}^2 = \frac{1}{4}\pi \cdot 1^2 = 0.785\ mm^2$

Two safety factors are proposed to define the alignment of the steel fibres: α_1 and α_2. Factor α_1 describes the favourable orientations in terms of providing tensile resistance and is taken as 1.5 while factor α_2 describes the fibre distribution of being overlapped to make the layer continuous and is taken as 1.3. According to the manufacturer, there were roughly 3200 fibre filaments per kg of steel fibres. Hence, the quantity of steel fibres that are effective in providing tensile strength within a unit length is,

$$100\ kg \cdot m^{-3} \times 1m \times 0.1m \times 0.1m \times 3200 \times \frac{50mm}{1000mm} \times \frac{1}{\alpha_1} = 123$$

The equivalent area of steel for the tensile reinforcement is,

$A_{eq} = 123 A_{fibre} \frac{1}{\alpha_2} = 123 \times 0.785 \times \frac{1}{1.5} =$ **64.4 mm^2;**

For the beam reinforced with carbon steel rebar, the equivalent mass of steel for the tensile reinforcement is calculated as:

The cross-sectional area of the Ø10 mm bar, $A_f = \frac{1}{4}\pi d_f^2 = \frac{1}{4}\pi \cdot 10^2 = 78.5\ mm^2$

The factors α_1 and α_2 are also applied here for comparison. Therefore, the steel rebar equivalently equals to a steel fibre dosage of,

$D_{eq} = A_f l \rho_s \alpha_1 \alpha_2 \frac{1}{V} = 78.5 \times 10^{-6} \times 1.0 \times 8050 \times 1.5 \times 1.3 \times \frac{1}{1 \times 0.1 \times 0.1} =$ **123 kg/m^3**

The results and the ratios of equivalent area and mass of steel are summarised in Table C1. Both methods give a rebar/fibre ratio of approximately 1.22. Therefore, a conservative calibration factor α of **1.23** is used to modify the measured flexural strength results.

Table C.1 Calibrated results of mass and area of steel for the tensile reinforcement

Steel Reinforcement	100 kg/m^3 Steel Fibres, mm^2	Ø10 mm Steel Rebar, kg/m^3	Rebar/Fibre Ratio
Area or Equivalent area	64.4 (Eq.)	78.5	1.22
Mass or Equivalent mass	100	123.2(Eq.)	1.23

Eq.: equivalent